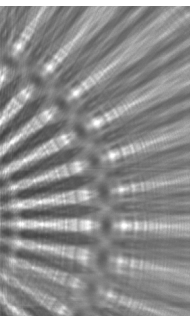


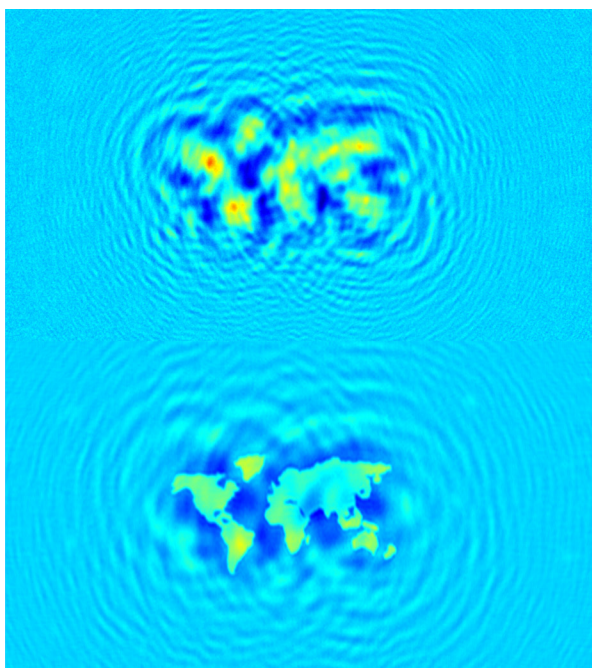


Göttingen Series in  
X-ray Physics



Matthias Bartels  
Cone-beam x-ray phase contrast  
tomography of biological samples

Optimization of contrast,  
resolution and field of view



Universitätsverlag Göttingen





Matthias Bartels

Cone-beam x-ray phase contrast tomography of biological samples

This work is licensed under the [Creative Commons](https://creativecommons.org/licenses/by-sa/3.0/) License 3.0 “by-sa”, allowing you to download, distribute and print the document in a few copies for private or educational use, given that the document stays unchanged and the creator is mentioned.



Published in 2013 by Universitätsverlag Göttingen  
as Volume 13 in the series „Göttingen series in x-ray physics“

---

Matthias Bartels

Cone-beam x-ray phase  
contrast tomography of  
biological samples

Optimization of contrast,  
resolution and field of view

Göttingen series in x-ray physics  
Volume 13



Universitätsverlag Göttingen  
2013

## Bibliographische Information der Deutschen Nationalbibliothek

Die Deutsche Nationalbibliothek verzeichnet diese Publikation in der Deutschen Nationalbibliographie; detaillierte bibliographische Daten sind im Internet über <http://dnb.ddb.de> abrufbar.

### *Address of the Author*

Dr. Matthias Bartels

e-mail: [Matthias.Bartels@phys.uni-goettingen.de](mailto:Matthias.Bartels@phys.uni-goettingen.de)

Dissertation

for the award of the degree

“Doctor rerum naturalium”

of the Georg-August-Universität Göttingen

Referent: Prof. Dr. Tim Salditt

1. Korreferent: PD Dr. Timo Aspelmeier

2. Korreferent: Prof. Dr. Martin Müller

This work is protected by German Intellectual Property Right Law.

It is also available as an Open Access version through the publisher's homepage and the Online Catalogue of the State and University Library of Goettingen (<http://www.sub.uni-goettingen.de>). Users of the free online version are invited to read, download and distribute it.

Layout: Matthias Bartels

Cover: Jutta Pabst

Cover image: Matthias Bartels

© 2013 Universitätsverlag Göttingen

<http://univerlag.uni-goettingen.de>

ISBN: 978-3-86395-134-4

ISSN: 2191-9860

## **Preface of the series editor**

The Göttingen series in x-ray physics is intended as a collection of research monographs in x-ray science, carried out at the Institute for X-ray Physics at the Georg-August-Universität in Göttingen, and in the framework of its related research networks and collaborations.

It covers topics ranging from x-ray microscopy, nano-focusing, wave propagation, image reconstruction, tomography, short x-ray pulses to applications of nanoscale x-ray imaging and biomolecular structure analysis.

In most but not all cases, the contributions are based on Ph.D. dissertations. The individual monographs should be enhanced by putting them in the context of related work, often based on a common long term research strategy, and funded by the same research networks. We hope that the series will also help to enhance the visibility of the research carried out here and help others in the field to advance similar projects.

Prof. Dr. Tim Salditt, Editor  
Göttingen February 2011



# Contents

<b>Introduction</b>	<b>1</b>
<b>1 Two-dimensional x-ray propagation imaging</b>	<b>5</b>
1.1 Propagation of x-rays in free space	6
1.1.1 Wave equations in free space	6
1.1.2 Angular spectrum approach	7
1.1.3 Paraxial Helmholtz equation	9
1.1.4 Fresnel diffraction	10
1.1.5 Fraunhofer diffraction	12
1.1.6 Fresnel scaling theorem	12
1.1.7 Numerical implementation of Fresnel diffraction	14
1.2 X-ray interaction with matter	15
1.2.1 Wave equations in the presence of matter	15
1.2.2 Refractive index for X-rays	16
1.2.3 The projection approximation	17
1.2.4 Phase shift and absorption within objects	19
1.3 Contrast formation and imaging regimes	20
1.3.1 Contrast transfer function	21
1.3.2 Transport-of-intensity equation	22
1.3.3 Imaging regimes	23
1.4 Effective near field and empty beam division	25
1.5 Coherence	26
1.6 Radiation damage and dose	30
<b>2 Solving the phase problem</b>	<b>31</b>
2.1 Holographic reconstruction	32
2.2 Transport-of-intensity equation	35
2.2.1 Pure phase object	37
2.2.2 Treatment of absorption	38
2.3 Contrast transfer function	41
2.3.1 Pure phase object	41
2.3.2 Treatment of absorption	44
2.4 Iterative algorithms	44
2.4.1 Gerchberg-Saxton-Fienup type algorithms	46
2.4.1.1 Gerchberg-Saxton algorithm	46

---

2.4.1.2	Error reduction algorithm . . . . .	47
2.4.1.3	Hybrid Input-Output algorithm . . . . .	48
2.4.2	Newton Methods . . . . .	50
2.5	Hybrid approaches . . . . .	51
<b>3</b>	<b>Three-dimensional x-ray propagation imaging</b>	<b>53</b>
3.1	Fourier slice theorem . . . . .	55
3.2	Filtered backprojection . . . . .	56
3.3	Cone-beam tomography . . . . .	57
3.4	Reconstruction and visualization software . . . . .	58
<b>4</b>	<b>Implementation of x-ray propagation imaging</b>	<b>59</b>
4.1	X-ray detectors . . . . .	59
4.2	Laboratory setup JuLiA . . . . .	60
4.3	GINIX at beamline P10 of PETRA III . . . . .	62
4.3.1	Coherence Beamline P10 . . . . .	62
4.3.2	GINIX . . . . .	63
4.3.3	X-ray waveguides . . . . .	66
4.3.4	Original waveguide configuration . . . . .	69
4.3.5	Optimized waveguide configuration . . . . .	70
4.3.6	KB configuration . . . . .	72
4.4	Beamline ID22NI of the ESRF . . . . .	76
4.5	Distance calibration . . . . .	79
4.5.1	Distance calibration with periodic structure . . . . .	79
4.5.2	Distance calibration using holographic reconstruction . . . . .	81
<b>5</b>	<b>Three-dimensional imaging of rodent cochlea</b>	<b>83</b>
5.1	Challenges of cochlear imaging . . . . .	84
5.2	Experiment . . . . .	85
5.2.1	Experimental setup . . . . .	85
5.2.2	Sample preparation and mounting . . . . .	86
5.2.3	Alignment of rotation axis . . . . .	89
5.3	Data analysis . . . . .	91
5.3.1	Phase and tomographic reconstruction . . . . .	91
5.3.2	Threshold based segmentation of bone . . . . .	93
5.4	Results . . . . .	94
5.4.1	Solid target source . . . . .	94
5.4.2	Liquid metal jet source . . . . .	98
5.4.3	Optimizing spatial resolution . . . . .	99
5.4.4	Space estimation for intra-cochlear implants . . . . .	105
5.5	Summary . . . . .	106



---

<b>6</b>	<b>Three-dimensional imaging of mouse nerves</b>	<b>107</b>
6.1	Experiments . . . . .	108
6.1.1	Experimental setup I . . . . .	108
6.1.2	Experimental setup II . . . . .	109
6.1.3	Experimental setup III . . . . .	109
6.1.4	Sample preparation and mounting . . . . .	110
6.1.4.1	Immersion fixation . . . . .	110
6.1.4.2	Mounting of immersion fixated samples . . . . .	110
6.1.4.3	EPON-embedding of immersion fixated samples . . . . .	112
6.1.4.4	High pressure freezing and EPON-embedding . . . . .	113
6.1.4.5	Light- and electron microscopy . . . . .	113
6.2	Data analysis . . . . .	114
6.2.1	Treatment of raw data . . . . .	114
6.2.2	Phase retrieval . . . . .	117
6.2.3	Single-distance phase retrieval . . . . .	117
6.2.4	Multi-distance phase retrieval . . . . .	120
6.2.5	Tomographic reconstruction . . . . .	122
6.3	Results . . . . .	122
6.3.1	Unstained nerves . . . . .	122
6.3.2	Osmium tetroxide stain . . . . .	123
6.3.3	Higher spatial resolution for imaging of optical nerves . . . . .	127
6.3.4	High resolution imaging using high pressure freezing . . . . .	129
6.4	Summary . . . . .	134
<b>7</b>	<b>Three-dimensional density contrast of <i>Deinococcus radiodurans</i></b>	<b>135</b>
7.1	Experiment . . . . .	136
7.1.1	Experimental setup . . . . .	136
7.1.2	Sample preparation and mounting . . . . .	137
7.2	Data analysis . . . . .	138
7.2.1	Treatment of raw data . . . . .	138
7.2.2	Phase retrieval and automatic support determination . . . . .	141
7.3	Results . . . . .	141
7.3.1	2D phase reconstruction . . . . .	141
7.3.2	Three-dimensional mass density . . . . .	144
7.3.3	Dose and resolution . . . . .	144
7.4	Summary . . . . .	146
<b>8</b>	<b>Towards higher resolution</b>	<b>147</b>
8.1	Imaging of <i>Dictyostelium discoideum</i> cells . . . . .	147
8.1.1	Sample preparation . . . . .	147
8.1.2	Experimental setup . . . . .	147
8.1.3	Empty beam and drift correction . . . . .	149
8.1.4	Astigmatism . . . . .	151
8.1.5	Phase reconstruction . . . . .	152
8.1.6	Dose and resolution . . . . .	154

8.2	Optimized waveguide configuration . . . . .	155
8.2.1	Imaging of a test structure at 13.8 keV . . . . .	155
8.2.1.1	Experimental setup . . . . .	155
8.2.1.2	Raw data treatment . . . . .	156
8.2.1.3	Phase reconstruction . . . . .	158
8.2.1.4	Resolution . . . . .	161
8.2.2	Imaging of <i>Deinococcus radiodurans</i> at 13.8 keV . . . . .	161
8.2.2.1	Experimental setup and raw data treatment . . . . .	162
8.2.2.2	Phase reconstruction . . . . .	162
8.2.2.3	Dose and resolution . . . . .	164
8.2.3	Imaging of <i>Deinococcus radiodurans</i> at 7.9 keV . . . . .	166
8.2.3.1	Experimental setup and raw data treatment . . . . .	166
8.2.3.2	Phase reconstruction . . . . .	168
8.2.3.3	Resolution and dose . . . . .	170
8.3	Summary . . . . .	171
	<b>Conclusion</b>	<b>173</b>
	<b>Appendix</b>	<b>175</b>
A.1	Fourier analysis . . . . .	175
A.1.1	Fourier transform . . . . .	175
A.1.2	Properties of the Fourier transform . . . . .	175
A.1.3	Fourier transform of the Dirac delta function . . . . .	177
A.2	Free space propagation of conjugate objects . . . . .	177
A.3	Spatial resolution . . . . .	178
	<b>Bibliography</b>	<b>199</b>
	<b>List of Publications</b>	<b>201</b>
	<b>Danksagung</b>	<b>203</b>
	<b>Curriculum vitae</b>	<b>207</b>

## Introduction

Three-dimensional information on opaque objects can be obtained by the remarkable technique of computed tomography (CT) [37, 96]. From a set of projection images collected at incremental angles around a common rotation axis, a three-dimensional reconstruction of the investigated object can be computed [175].

X-ray CT based on classical radiography constitutes an indispensable tool in clinics. Contrast arises from attenuation of an x-ray beam penetrating the examined object. While clinical CT commonly obtains millimeter sized voxels<sup>1</sup>, micro-CT is suitable for *in vivo* small animal imaging with voxel sizes below  $(100\ \mu\text{m})^3$  [95, 3] based on a magnifying (or cone-beam) geometry [38]. While highly mineralized structures such as bone yield considerable contrast, absorption cross-sections of lighter elements which constitute soft tissue are small and the contrast is weak. As a matter of fact, x-ray imaging is not limited to absorption contrast since an x-ray wavefield traversing an object experiences a phase shift related to the decrement of the object's complex index of refraction. By exploiting the phase shift, high contrast for soft tissue structures can be achieved. However, phase imaging is challenging since one cannot measure the phase of an x-ray wave field directly.

In this work cone-beam propagation-based phase contrast [193, 218, 32, 139, 171, 84] (also denoted as x-ray propagation imaging) is applied to biological samples ranging from micrometer sized single cells over multi-cellular tissue to entire millimeter sized organs. While length scales comprising three orders of magnitude are bridged, with spatial resolutions ranging from tens of nanometers to few micrometers, the underlying concept of image formation remains unaffected. A partially coherent divergent x-ray beam traverses the specimen and the modified wave field behind the sample propagates to the detection plane where a magnified Fresnel diffraction pattern (hologram) is recorded. Then, suitable numerical phase retrieval methods are applied to reconstruct the phase shift and absorption induced by the specimen [34, 83, 81, 157, 60, 54]. Finally, combination with tomography yields three-dimensional quantitative density information of the investigated object [138, 33].

---

<sup>1</sup> A voxel (volumetric pixel) is a volume element defined on a three-dimensional Cartesian grid. A pixel is a picture element defined on a two-dimensional Cartesian grid.

The basic concept of cone-beam x-ray propagation imaging is based on only three ingredients: source, sample and detector. Nonetheless, geometric parameters, instrumentation, source and detector properties, sample preparation, data processing and phase retrieval vary significantly from specimen to specimen. In this work the imaging process is optimized with respect to contrast, resolution and field of view for a broad range of biological samples.

As a prerequisite, in chapter 2 aspects of scalar diffraction theory in free space and matter are reviewed and contrast formation in two-dimensional x-ray propagation is discussed. Chapter 3 is devoted to phase retrieval methods. Relevant approaches with their assets and limitations are introduced and applied to simulated data. The important concept of tomography is outlined in chapter 4. A major task is the experimental realization and optimization of three-dimensional x-ray propagation imaging for different sample characteristics. Chapter 5 embraces the experimental setups and discusses applied improvements.

Chapter 6 reports imaging results on mouse and rat cochlea which constitute the largest samples studied in this work. Detailed knowledge about the delicate and complex cochlea morphology is necessary to understand malformations caused by genetic defects, to improve the treatment of hearing diseases and to optimize the design of cochlear implants. For macroscopic objects, grating-based interferometry has recently attracted increased attention [215, 40, 146, 168, 188] and efforts currently aim at clinical applications [197, 44]. Nevertheless, grating-based phase contrast imaging with compact sources [170, 13, 169, 115, 50] is limited to spatial resolutions above 30  $\mu\text{m}$ . For many biological and biomedical applications higher resolution is required, e.g. to resolve thin membranes or nerve fibres within rodent cochlea. As shown by synchrotron radiation studies [177, 176], x-ray propagation imaging is well suited for cochlea imaging as it circumvents invasive sample preparation associated with classical histology [129], optical coherence tomography [220], orthogonal-plane optical fluorescence [213] and magnetic resonance imaging [202] (e.g. slicing [129], staining [129, 202, 213], dehydrating [129], opening the bony cochlea wall [220]). However, the (limited) availability of third generation synchrotron facilities inhibits wide-spread applications. As an important step towards routine non-destructive 3D determination of rodent cochlear structures, x-ray phase-contrast tomography is realized by means of compact laboratory microfocus sources [139, 171, 84, 218] and optimized for imaging of functional soft tissue within the bony cochlear capsule.

In chapter 7 three-dimensional imaging of uncut mouse nerves is assessed. While multiple scattering, fluorescence staining and resolution issues pose harsh limits to visible light microscopy studies, preparation difficulties and limited penetration depth restrict the application of electron microscopy. Destructive serial block-face scanning electron microscopy capable of measuring larger volumes at high resolution requires extensive accumulation times [42, 112, 142]. On the contrary, high penetration depth of x-rays and zooming capabilities of cone-beam propagation imaging [145] offer the unique potential to examine large sample volumes with spatial resolution in the hundred nanometer range and reasonable accumulation times. In a series of experiments different preparation techniques, experimental

setups and reconstruction methods are examined for mouse nerves of the central and peripheral nervous system.

Chapter 8 is devoted to three-dimensional imaging of unstained biological cells. Transmission electron microscopy of cells relies on sectioning and sophisticated sample preparation steps such as fixation, dehydration and plastic embedment along with heavy metal staining. Super-resolution fluorescence microscopy techniques which localize isolated fluorescent protein markers in 3D with a resolution of few tens of nanometers have recently been developed [98, 167]. However, not all structural problems can be solved based on the distribution of fluorescence markers. Quantitative three-dimensional determination of local density is a case in point. Coherent lensless x-ray imaging offers the unique potential for quantitative three-dimensional density determination by means of quantitative phase reconstruction schemes [35, 100, 131, 153, 189, 195, 216]. Quantitative imaging of bacterial *Deinococcus radiodurans* in two [65] and three dimensions [216] was recently performed by means of ptychographic scanning coherent diffraction imaging [181, 182, 51, 201]. To prevent structural changes due to radiation damage as observed in the ptychographical study [216], propagation imaging based on x-ray waveguides is applied here as a dose-efficient alternative approach.

Chapter 9 presents experiments aiming at cellular imaging with a spatial resolution better than 100 nm. An optimized synchrotron setup for two-dimensional waveguide-based x-ray propagation imaging is developed, based on recent progress in waveguide fabrication as well as optimized geometry and detector parameters. Future experimental upgrades towards high resolution three-dimensional imaging are briefly discussed. Finally, chapter 10 closes with a short summary of obtained results.

To conclude, the goal of this work is the optimization of cone-beam x-ray propagation imaging in terms of contrast, spatial resolution and field of view for three-dimensional imaging of biological samples of various sizes.



# 1 Two-dimensional x-ray propagation imaging

A major goal of this work was to investigate how x-ray propagation imaging can be used to determine structural information of biological and biomedical samples. While relevant length scales, data processing and instrumentation may vary significantly from specimen to specimen, the generic setup and the underlying concept of image formation as depicted in **Fig. 1.1** remains unaffected.

At first, a **divergent x-ray beam** is generated and the x-ray wave field propagates from the source over a distance  $z_1$  to a plane where the specimen is located. **Propagation in free space** is introduced in this chapter. The complex wave field can be calculated numerically for any plane, provided that the wave field is known in a single plane. The incident wave field traverses the specimen of thickness  $t$ . The concepts of **paraxial approximation** and **projection approximation** describe how modifications of the x-ray wave field are related to the refractive index  $n(\mathbf{r})$  of the specimen. Next, the modified wave field propagates over a distance  $z_2$  to the detection plane. Detection of x-ray wave fields is limited to intensity measurements. Therefore, phase information of the wave field is lost, a phenomenon denoted as the **phase problem**. A major challenge in x-ray propagation imaging is the recovery of phase information using suitable numerical **phase**

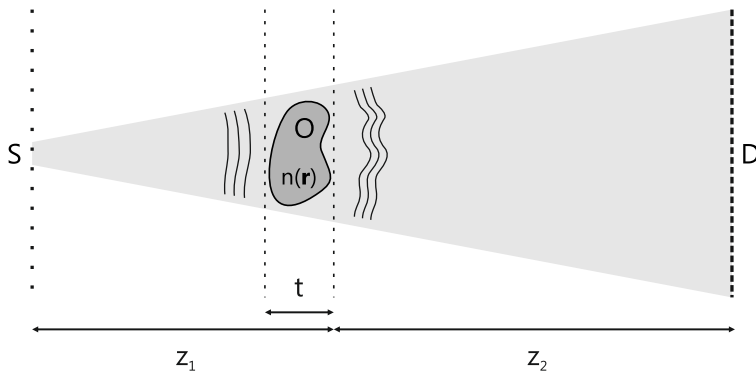


**Figure 1.1:** Generic setup of an x-ray propagation imaging experiment. A divergent beam is created by an x-ray source (S) and propagates over a distance  $z_1$  to the object plane. The beam interacts with the object (O) of thickness  $t$  and refractive index  $n(\mathbf{r})$ . The modified wave field propagates over a distance  $z_2$  and is measured by an x-ray detector.

**reconstruction** techniques. Methods applied in this work rely either on multiple measurements with the specimen located in different planes along the optical axis or useful *a priori* knowledge about the investigated sample. The information content of x-ray propagation imaging experiments turns out to be the **complex index of refraction** *projected* along the optical axis. The *three-dimensional* index of refraction can be reconstructed by combining x-ray propagation imaging with tomography, as discussed in chapter 3.

## 1.1 Propagation of x-rays in free space

### 1.1.1 Wave equations in free space

The spatial and temporal evolution of electromagnetic fields in free space constitutes an important part of the image formation process in x-ray propagation imaging. To study this process we start with Maxwell's equations in the absence of matter (see e.g. [20, 164]):

$$\nabla \cdot \mathbf{E}(\mathbf{r}, t) = 0, \quad (1.1)$$

$$\nabla \cdot \mathbf{B}(\mathbf{r}, t) = 0, \quad (1.2)$$

$$\nabla \times \mathbf{E}(\mathbf{r}, t) + \partial_t \mathbf{B}(\mathbf{r}, t) = \mathbf{0}, \quad (1.3)$$

$$\nabla \times \mathbf{B}(\mathbf{r}, t) - \epsilon_0 \mu_0 \partial_t \mathbf{E}(\mathbf{r}, t) = \mathbf{0}. \quad (1.4)$$

The set of partial differential equations governs the evolution of electric field  $\mathbf{E}(\mathbf{r}, t)$  and magnetic induction  $\mathbf{B}(\mathbf{r}, t)$  at any point in space  $\mathbf{r} = (x, y, z) \in \mathbb{R}^3$  and time  $t$ .<sup>1</sup> The constants  $\epsilon_0 = 8.854 \cdot 10^{-12} \text{ AsV}^{-1}\text{m}^{-1}$  and  $\mu_0 = 4\pi \cdot 10^{-7} \text{ VsA}^{-1}\text{m}^{-1}$  define the electrical permittivity and magnetic permeability in vacuum, respectively. Based on equations (1.1-1.4), two wave equations for  $\mathbf{E}(\mathbf{r}, t)$  and  $\mathbf{B}(\mathbf{r}, t)$  can be derived [164]:

$$(\epsilon_0 \mu_0 \partial_t^2 - \nabla^2) \mathbf{E}(\mathbf{r}, t) = \mathbf{0} \quad (1.5)$$

$$(\epsilon_0 \mu_0 \partial_t^2 - \nabla^2) \mathbf{B}(\mathbf{r}, t) = \mathbf{0}. \quad (1.6)$$

Equations (1.5, 1.6) constitute six scalar equations with identical structure. We neglect polarisation effects and describe the electromagnetic field by a single complex scalar field  $\Psi(\mathbf{r}, t)$ , which obeys the **scalar (d'Alambert) wave equation**

$$\boxed{(\epsilon_0 \mu_0 \partial_t^2 - \nabla^2) \Psi(\mathbf{r}, t) = 0.} \quad (1.7)$$

<sup>1</sup> SI units are used throughout this text. Bold letters represent vector quantities.



To determine the speed of propagation of an electromagnetic field, a time-dependent monochromatic plane wave with angular frequency  $\omega$  is considered

$$\begin{aligned}\Psi_{\omega}^{(\text{PW})}(\mathbf{r}, t) &= a \cdot \exp[i\varphi(\mathbf{r}, t)] \\ &= a \cdot \exp[i(\mathbf{k} \cdot \mathbf{r} - \omega t + \varphi_0)] \\ &= \Psi_{\omega}^{(\text{PW})}(\mathbf{r}) \cdot \exp(-i\omega t),\end{aligned}\tag{1.8}$$

where  $\mathbf{k} \in \mathbb{R}^3$  is the wave vector,  $k = |\mathbf{k}| = \frac{2\pi}{\lambda}$  the wave number,  $\lambda$  the wavelength,  $\varphi_0$  a real constant,  $|\Psi_{\omega}^{(\text{PW})}(\mathbf{r})| = a$  the amplitude and  $\varphi(\mathbf{r}, t)$  the phase of the wave. The plane wave  $\Psi_{\omega}^{(\text{PW})}(\mathbf{r}, t)$  is a solution to the scalar vacuum wave equation (1.7), if

$$\epsilon_0 \mu_0 = \frac{k^2}{\omega^2}.$$

Wave fronts of the plane wave travel with the vacuum phase velocity

$$c := \omega/k = \frac{1}{\sqrt{\epsilon_0 \mu_0}},$$

which was experimentally found to correspond to the speed of light in vacuum [164]. While monochromatic plane waves constitute an idealisation, any electromagnetic field in a given volume of free space described by a scalar function  $\Psi(\mathbf{r}, t)$  can be spectrally decomposed as a superposition of monochromatic fields [164]

$$\Psi(\mathbf{r}, t) = \frac{1}{\sqrt{2\pi}} \int_0^{\infty} \psi_{\omega}(\mathbf{r}) \exp(-i\omega t) d\omega.\tag{1.9}$$

Here, the harmonic time dependence  $\exp(-i\omega t)$  of each monochromatic component of the field was separated from the stationary spatial wave function  $\psi_{\omega}(\mathbf{r})$ , similar to equation (1.8) for the case of a plane wave. To determine under which circumstances the decomposition represents a solution to the vacuum wave equation, we insert equation (1.9) into the d'Alambert wave equation (1.7). The order of integration and differentiation is interchanged, differentiation is performed with respect to time and the time-independent **Helmholtz equation** [164] is obtained

$$\boxed{(\nabla^2 + k^2) \psi_{\omega}(\mathbf{r}) = 0},\tag{1.10}$$

with  $k = \frac{\omega}{c}$ . The Helmholtz equation governs the spatial evolution of the stationary wave function  $\psi_{\omega}(\mathbf{r})$ , corresponding to a given monochromatic component of the spectral decomposition.<sup>2</sup>

### 1.1.2 Angular spectrum approach

We investigate how a given monochromatic wave field with spatial wave function  $\psi(\mathbf{r})$  propagates from a plane perpendicular to the optical axis at  $z = 0$  to another

<sup>2</sup> For the sake of convenience, we will henceforth drop the explicit index and let  $\psi(\mathbf{r})$  denote a monochromatic component, corresponding to an angular frequency  $\omega$ .

plane at  $z > 0$  along the optical axis  $z$ , following the description in [164]. The time-independent plane wave  $\psi^{(\text{PW})}(\mathbf{r}) = \exp(i\mathbf{k} \cdot \mathbf{r})$ , propagating along the wave vector  $\mathbf{k} = (k_x, k_y, k_z) \in \mathbb{R}^3$  is a solution to the Helmholtz equation (1.10), provided that  $k_x^2 + k_y^2 + k_z^2 = k^2 = \frac{\omega^2}{c^2}$ . With lateral coordinates in planes perpendicular to the optical axis  $\mathbf{r}_\perp := (x, y)$ , the plane wave solutions to the Helmholtz equation can be rewritten as

$$\psi^{(\text{PW})}(\mathbf{r}_\perp, z) = \exp[i\mathbf{k}_\perp \cdot \mathbf{r}_\perp] \exp\left[iz\sqrt{k^2 - k_\perp^2}\right]. \quad (1.11)$$

Further elementary solutions to the Helmholtz equation are given by time independent spherical waves for all  $\mathbf{r} \in \mathbb{R}^3 \setminus \{\mathbf{r}_0\}$

$$\psi^{(\text{SW})}(\mathbf{r}) = \frac{1}{|\mathbf{r} - \mathbf{r}_0|} \exp(ik|\mathbf{r} - \mathbf{r}_0|). \quad (1.12)$$

Spherical waves can be regarded as concentric spheres of constant phase around a central point  $\mathbf{r}_0$ , without a distinct direction of propagation.

To construct general solutions, we take advantage of the Helmholtz equation's linearity and the invariance of vacuum with respect to translational shifts. Therefore, propagation of wave fields along the optical axis  $z$  in vacuum can be considered a linear translational-invariant system with  $\psi(\mathbf{r}_\perp, 0)$  as input signal and  $\psi(\mathbf{r}_\perp, z)$  as output signal. Such a system is characterized by its transfer function or its impulse response [187, 68, 211]. Equation (1.11) already constitutes a solution to the problem of determining the harmonic field  $\psi^{(\text{PW})}(\mathbf{r}_\perp, z)$  in a plane  $z > 0$ , given the harmonic field  $\psi^{(\text{PW})}(\mathbf{r}_\perp, 0) = \exp[i\mathbf{k}_\perp \cdot \mathbf{r}_\perp]$  at  $z = 0$ , namely by multiplication with the transfer function

$$H_z(\mathbf{k}_\perp) = \exp\left[iz\sqrt{k^2 - k_\perp^2}\right], \quad (1.13)$$

which is known as the free space propagator [164]. According to the Fourier theorem (section A.1.1), any input field  $\psi(\mathbf{r}_\perp, 0)$  can be decomposed into its spectral harmonic components

$$\psi(\mathbf{r}_\perp, 0) = \frac{1}{2\pi} \int \tilde{\psi}(\mathbf{k}_\perp, 0) \exp[i\mathbf{k}_\perp \cdot \mathbf{r}_\perp] d\mathbf{k}_\perp. \quad (1.14)$$

Here,  $\tilde{\psi}(\mathbf{k}_\perp, 0)$  denotes the two-dimensional Fourier transform of  $\psi(\mathbf{r}_\perp, 0)$  with respect to lateral coordinates  $x$  and  $y$ . By applying the transfer function (1.13) to each spectral harmonic component, the wave field propagated over a distance  $z$  is obtained as

$$\psi(\mathbf{r}_\perp, z) = \frac{1}{2\pi} \int H_z(\mathbf{k}_\perp) \tilde{\psi}(\mathbf{k}_\perp, 0) \exp[i\mathbf{k}_\perp \cdot \mathbf{r}_\perp] d\mathbf{k}_\perp \quad (1.15)$$

$$= \frac{1}{2\pi} \int \tilde{\psi}(\mathbf{k}_\perp, 0) \exp\left[iz\sqrt{k^2 - k_\perp^2}\right] \exp[i\mathbf{k}_\perp \cdot \mathbf{r}_\perp] d\mathbf{k}_\perp. \quad (1.16)$$

Since each individual plane wave propagates into direction  $(\mathbf{k}_\perp, \sqrt{k^2 - k_\perp^2})$  the decomposition (1.16) is also called an **angular spectrum** of plane waves. With the notation  $\mathcal{F}_\perp$  and  $\mathcal{F}_\perp^{-1}$  for Fourier transform and Fourier back transform with respect to lateral coordinates, **free space propagation** of electromagnetic fields in vacuum reads

$$\psi(\mathbf{r}_\perp, z) = \mathcal{F}_\perp^{-1} \left[ \exp\left(iz\sqrt{k^2 - k_\perp^2}\right) \mathcal{F}_\perp[\psi(\mathbf{r}_\perp, 0)] \right]. \quad (1.17)$$

For notational convenience, free space propagation in vacuum over a distance  $z$  can be described by the operator

$$\mathcal{D}_z = \mathcal{F}_\perp^{-1} \exp\left(iz\sqrt{k^2 - k_\perp^2}\right) \mathcal{F}_\perp \quad (1.18)$$

acting on a given wave field. For  $k_\perp^2 > k^2$ , the exponential term of the transfer function is real-valued and describes a damping factor  $\exp[-z\sqrt{k_\perp^2 - k^2}]$  which decays to zero within few wavelengths. This non-propagating solution is called an evanescent wave. Relation  $k_\perp^2 > k^2$  corresponds to spatial frequencies  $\nu_\perp > \lambda^{-1}$  [187]. Hence, the spatial bandwidth of light propagation in vacuum is limited to about  $\lambda^{-1}$ . X-rays with wavelengths on the order of  $1 \text{ \AA} = 10^{-10} \text{ m}$ , therefore have the potential for substantial higher resolution compared to optical microscopy, even if resolution is still restricted to the 10 nm range [27, 196, 102], due to the lack of efficient focusing optics [183, 120, 143] and for biological material ultimately by radiation damage [97, 190].

Equation (1.17) already suffices to numerically implement free space propagation efficiently using discrete Fourier transforms. However, it is rewarding to apply further assumptions on the wave fields, namely to apply the paraxial approximation.

### 1.1.3 Paraxial Helmholtz equation

If the wave front normals of a wave field form small angles with respect to a given optical axis, we call the wave field paraxial. A paraxial wave

$$\psi(\mathbf{r}) = A(\mathbf{r}) \cdot \exp(ikz) \quad (1.19)$$

can be constructed by modulating a plane wave  $\exp(ikz)$ , which rapidly oscillates along the optical axis, with a slowly varying complex envelope  $A(\mathbf{r})$ . Without loss of generality we chose the optical axis to be the  $z$ -axis. Substitution of the ansatz above into the Helmholtz equation (1.10) yields [164]

$$(2ik\partial_z + \nabla_\perp^2 + \partial_z^2) A(\mathbf{r}) = 0, \quad (1.20)$$

with the transverse Laplacian in lateral coordinates  $\nabla_\perp^2 = \partial_x^2 + \partial_y^2$ . The assumption that  $A(\mathbf{r})$  varies slowly with  $z$  boils down to neglecting the second derivative with respect to  $z$  to arrive at the **homogenous paraxial Helmholtz equation** [187]

$$\boxed{(2ik\partial_z + \nabla_{\perp}^2) A(\mathbf{r}) = 0.} \quad (1.21)$$

An elementary solution to (1.21) can be found by regarding a spherical wave  $\psi^{(\text{SW})}(\mathbf{r})$  (1.12) emanating at  $\mathbf{r}_0 = 0$ . Assuming small angles with  $\theta^2 = (x^2 + y^2)/z^2 \ll 1$  we approximate  $r = |\mathbf{r}|$  as

$$r = \sqrt{x^2 + y^2 + z^2} = z\sqrt{1 + \theta^2} = z\left(1 + \frac{\theta^2}{2} - \mathcal{O}(\theta^4)\right) \quad (1.22)$$

$$\approx z\left(1 + \frac{\theta^2}{2}\right) = z + \frac{x^2 + y^2}{2z}. \quad (1.23)$$

Insertion of equation (1.23) into the phase of the spherical wave and using the first order approximation  $r \approx z$  for the amplitude  $1/r$  yields

$$\psi^{(\text{SW,P})}(r) = \frac{1}{z} \exp(ikz) \exp\left[ik\frac{r_{\perp}^2}{2z}\right]. \quad (1.24)$$

One finds that the paraxial approximation of a spherical wave  $\psi^{(\text{SW,P})}(r)$ , also called paraboloidal wave, obeys the paraxial Helmholtz equation (1.21). Note that a Gaussian beam which is well suited to describe the wavefield behind a single-mode x-ray waveguide [56, 57] also constitutes a solution to the paraxial Helmholtz equation.

#### 1.1.4 Fresnel diffraction

In the following, the paraxial approximation is applied to the angular spectrum solution (1.17) of the Helmholtz equation. If the given wave field is paraxial, all non-negligible plane wave components will form a small angle with respect to the optical axis, which is expressed by [164]

$$|\psi(\mathbf{r}_{\perp}, 0)| > 0 \text{ only for } k_{\perp}^2 \ll k^2. \quad (1.25)$$

Equivalently, the given wave field varies considerably only over lateral length scales which are not smaller than  $a_{\min}$ , with [61, 164]

$$a_{\min} \gg \lambda \Leftrightarrow k_{\perp}^2 \ll k^2. \quad (1.26)$$

In the case of a paraxial field, we can approximate the root in the transfer function  $H_z(\mathbf{k}_{\perp})$  (1.13)

$$\sqrt{k^2 - k_{\perp}^2} = k - \frac{k_{\perp}^2}{2k} + \mathcal{O}(k_{\perp}^4) \quad (1.27)$$

$$\simeq k - \frac{k_{\perp}^2}{2k}, \quad (1.28)$$

and obtain the binomial approximation

$$H_z^F(\mathbf{k}_\perp) \simeq \exp(ikz) \exp\left(\frac{-izk_\perp^2}{2k}\right). \quad (1.29)$$

Insertion into equation (1.17) yields

$$\boxed{\psi(\mathbf{r}_\perp, z) \simeq \exp(ikz) \mathcal{F}_\perp^{-1} \left[ \exp\left(\frac{-izk_\perp^2}{2k}\right) \mathcal{F}_\perp(\psi(\mathbf{r}_\perp, 0)) \right]}. \quad (1.30)$$

Equation (1.30) describes propagation of paraxial wave fields in vacuum, also known as the **Fresnel approximation of free space propagation** or simply **Fresnel diffraction**. The corresponding Fresnel diffraction operator is denoted as

$$\mathcal{D}_z^F = \exp(ikz) \mathcal{F}_\perp^{-1} \exp\left(\frac{-izk_\perp^2}{2k}\right) \mathcal{F}_\perp. \quad (1.31)$$

As mentioned in section 1.1.2, the process of free space propagation from one plane to another can be considered as a linear translation-invariant system. Therefore, it can be described by its impulse response  $h(\mathbf{r}_\perp, z)$  via a convolution [68, 187]:

$$\psi(\mathbf{r}_\perp, z) = \psi(\mathbf{r}_\perp, 0) \otimes h(\mathbf{r}_\perp, z). \quad (1.32)$$

As can be seen by rewriting equation (1.30) as

$$\psi(\mathbf{r}_\perp, z) \simeq \mathcal{F}_\perp^{-1} [\mathcal{F}_\perp \mathcal{F}_\perp^{-1} [H_z^F(\mathbf{k}_\perp)] \mathcal{F}_\perp(\psi(\mathbf{r}_\perp, 0))], \quad (1.33)$$

and applying the convolution theorem (A.11), the Fresnel approximation  $h^F(\mathbf{r}_\perp, z)$  of the impulse response is given by [187, 164]:

$$h^F(\mathbf{r}_\perp, z) \simeq \frac{1}{2\pi} \mathcal{F}_\perp^{-1} [H_z^F(\mathbf{k}_\perp)] \quad (1.34)$$

$$= \frac{1}{2\pi} \exp(ikz) \mathcal{F}_\perp^{-1} \left[ \exp\left(\frac{-izk_\perp^2}{2k}\right) \right] \quad (1.35)$$

$$= -\frac{ik \exp(ikz)}{2\pi z} \exp\left(\frac{ikr_\perp^2}{2z}\right). \quad (1.36)$$

Hence, we obtain the following **convolution formulation of Fresnel diffraction**:

$$\psi(\mathbf{r}_\perp, z) \simeq -\frac{ikz \exp(ikz)}{2\pi z} \int \psi(\mathbf{r}'_\perp, 0) \exp\left[\frac{ik(r_\perp - r'_\perp)^2}{2z}\right] d\mathbf{r}'_\perp. \quad (1.37)$$

We now discuss the equation above from a physical point of view. Diverging paraboloidal waves which obey the paraxial Helmholtz equation as we have shown above, emanate at each point  $(\mathbf{r}'_\perp, 0)$  in the input plane with the complex amplitude

$\psi(\mathbf{r}'_{\perp}, 0)$ . In the output plane at  $z > 0$ , all contributions of each individual paraboloidal waves are summed up to obtain the value  $\psi(\mathbf{r}_{\perp}, z)$  at each point  $(\mathbf{r}_{\perp}, z)$ . It is worthwhile to note that the convolution formulation of Fresnel diffraction (1.37) is equal to the Fresnel approximation of the Rayleigh-Sommerfeld diffraction formula [68], which in turn is the mathematical formulation of the Huygens-Fresnel principle.

### 1.1.5 Fraunhofer diffraction

By expanding the quadratic term in the convolution formulation of Fresnel diffraction (1.37) and switching the notation for  $\mathbf{r}_{\perp}$  and  $\mathbf{r}'_{\perp}$ , one obtains [164]

$$\psi(\mathbf{r}'_{\perp}, z) \simeq -\frac{ik \exp(ikz)}{2\pi z} \exp\left[\frac{ikr'^2}{2z}\right] \int \psi(\mathbf{r}_{\perp}, 0) \exp\left[\frac{ikr_{\perp}^2}{2z}\right] \exp\left[-ik \frac{\mathbf{r}_{\perp} \cdot \mathbf{r}'_{\perp}}{z}\right] d\mathbf{r}_{\perp}. \quad (1.38)$$

Next, we assume that the incident field  $\psi(\mathbf{r}_{\perp}, 0)$  only varies significantly within an area of diameter  $d$ . If the propagation distance  $z$  is much larger than  $d$ , more precisely if the dimensionless **Fresnel number** [164]

$$F := \frac{d^2}{\lambda z} \quad (1.39)$$

is small ( $F \ll 1$ ), the spherical phase term inside the integral can be neglected. The remaining integral is proportional to a two-dimensional Fourier transform (A.1) of the incident field  $\psi(\mathbf{r}_{\perp}, 0)$  with respect to angular spatial frequencies  $\mathbf{k}_{\perp} = \frac{k\mathbf{r}_{\perp}}{z}$ , known as the **far field** or **Fraunhofer diffraction** formula

$$\psi(\mathbf{r}'_{\perp}, z) \simeq -\frac{ik \exp(ikz)}{2\pi z} \exp\left[\frac{ikr'^2}{2z}\right] \mathcal{F}_{\perp} [\psi(\mathbf{r}_{\perp}, 0)]_{\mathbf{k}_{\perp} = \frac{k\mathbf{r}'_{\perp}}{z}}. \quad (1.40)$$

### 1.1.6 Fresnel scaling theorem

This section addresses the question, how the propagation of a **divergent wave field** can be described. We follow the arguments in [61], while a similar derivation restricted to ideal spherical waves can be found in [164]. Consider a paraxial divergent wave field  $\psi(\mathbf{r}_{\perp}, 0)$  at  $z = 0$  with radius of curvature  $z_1$ , similar to a paraboloidal wave (1.24) emanating at  $z = -z_1$ , with an additional nearly planar complex envelope  $\psi^{(P)}(\mathbf{r}_{\perp}, 0)$ . This may be expressed by separating the spherical part from the envelope

$$\psi(\mathbf{r}_{\perp}, 0) = \psi^{(P)}(\mathbf{r}_{\perp}, 0) \exp\left[\frac{ikr_{\perp}^2}{2z_1}\right]. \quad (1.41)$$

Propagation to a plane at  $z = z_2 > 0$  can be achieved by inserting the ansatz above into equation (1.38), yielding

$$\psi(\mathbf{r}'_{\perp}, z_2) = A(z_2) \exp\left[\frac{ikr'^2_{\perp}}{2z_2}\right] \int \psi^{(P)}(\mathbf{r}_{\perp}, 0) \exp\left[\frac{ikr^2_{\perp}}{2}\left(\frac{1}{z_1} + \frac{1}{z_2}\right)\right] \exp\left[-ik\frac{\mathbf{r}_{\perp} \cdot \mathbf{r}'_{\perp}}{z_2}\right] d\mathbf{r}'_{\perp} \quad (1.42)$$

with  $A(z_2) = -ik \exp(ikz_2)/2\pi z_2$ . By introducing the **geometric magnification** factor<sup>3</sup>

$$M := \frac{z_1 + z_2}{z_2}, \quad (1.43)$$

we find that

$$\frac{1}{z_1} + \frac{1}{z_2} = \frac{M}{z_2}, \quad (1.44)$$

as well as

$$|A(z_2/M)| = M|A(z_2)| \quad (1.45)$$

and write the amplitude of  $\psi(\mathbf{r}'_{\perp}, z_2)$  as

$$|\psi(\mathbf{r}'_{\perp}, z_2)| = \left| \frac{1}{M} A\left(\frac{z_2}{M}\right) \right| \left| \int \psi^{(P)}(\mathbf{r}_{\perp}, 0) \exp\left[\frac{ikr^2_{\perp}}{2z_2/M}\right] \exp\left[-ik\frac{\mathbf{r}_{\perp} \cdot (\mathbf{r}'_{\perp}/M)}{z_2/M}\right] d\mathbf{r}'_{\perp} \right|. \quad (1.46)$$

Next, regard the propagation of a wave field which is identical to the planar envelope  $\psi^{(P)}(\mathbf{r}_{\perp}, 0)$  over a distance  $z = z_2/M$ . The amplitude evaluated at lateral position  $\mathbf{r}'_{\perp}/M$  then reads

$$\left| \psi^{(P)}\left(\frac{\mathbf{r}'_{\perp}}{M}, \frac{z_2}{M}\right) \right| = \left| A\left(\frac{z_2}{M}\right) \right| \left| \int \psi^{(P)}(\mathbf{r}_{\perp}, 0) \exp\left[\frac{ikr^2_{\perp}}{2z_2/M}\right] \exp\left[-ik\frac{\mathbf{r}_{\perp} \cdot (\mathbf{r}'_{\perp}/M)}{z_2/M}\right] d\mathbf{r}'_{\perp} \right|. \quad (1.47)$$

By comparing equations (1.46, 1.47) and defining the **effective propagation distance**

$$z_{eff} := \frac{z_2}{M} \quad (1.48)$$

one arrives at the **Fresnel scaling theorem**

$$\boxed{|\psi(\mathbf{r}'_{\perp}, z_2)| = \frac{1}{M} |\psi^{(P)}(\mathbf{r}'_{\perp}/M, z_{eff})|}. \quad (1.49)$$

Hence, apart from a constant multiplicative factor the amplitude of the divergent field  $\psi$  propagated over a distance  $z_2$  at lateral position  $\mathbf{r}'_{\perp}$  is equal to the amplitude of the planar part  $\psi^{(P)}$  propagated over the distance  $z_{eff}$ , evaluated at  $\mathbf{r}'_{\perp}/M$  [171, 39].

<sup>3</sup> We will henceforth use the term magnification for both, the process of enlarging the appearance of something and the enlargement itself, quantified by the factor M.

### 1.1.7 Numerical implementation of Fresnel diffraction

Free space propagation over a distance  $z$  of an incident paraxial wave field  $\psi(\mathbf{r}_\perp, 0)$  with x-ray wavelength  $\lambda = 2\pi/k$  in vacuum can be described by the Fresnel diffraction operator  $\mathcal{D}_z^{\mathcal{F}}$  (1.31)

$$\mathcal{D}_z^{\mathcal{F}} = a \cdot \mathcal{F}_\perp^{-1} \exp\left(\frac{-iz(k_x^2 + k_y^2)}{2k}\right) \mathcal{F}_\perp, \quad (1.50)$$

with  $a = \exp(ikz)$ . In most cases, analytical calculation of  $\psi(\mathbf{r}_\perp, z)$  is not possible and numerical implementation of equation (1.50) is required. To this end, we introduce the discrete representation  $\psi(n_x\Delta x, n_y\Delta y, z)$  of  $\psi(\mathbf{r}_\perp, z)$ , with sampling interval lengths  $\Delta x$ ,  $\Delta y$ , number of pixels  $N_x$ ,  $N_y$  and grid indices  $n_{x/y} = [0, N_{x/y} - 1] \in \mathbb{N}_0$  for the horizontal and vertical direction, respectively. The discrete representation of free space propagation of  $\psi(\mathbf{r}_\perp, 0)$  to a plane at  $z > 0$  then reads

$$\psi(n_x\Delta x, n_y\Delta y, z) = a \cdot \text{IDTF} \left[ \exp\left(\frac{-iz(n_x^2\Delta k_x^2 + n_y^2\Delta k_y^2)}{2k}\right) \text{DTF}[\psi(n_x\Delta x, n_y\Delta y, 0)] \right], \quad (1.51)$$

with the sampling interval  $\Delta k$  in Fourier space and the two-dimensional discrete Fourier transform (DTF) and its inverse (IDTF). With the reciprocity relations

$$\Delta k_x \Delta x = 2\pi/N_x \quad (1.52)$$

$$\Delta k_y \Delta y = 2\pi/N_y \quad (1.53)$$

and the **discrete Fresnel numbers**

$$F_x^1 = \frac{(\Delta x)^2}{\lambda z}, \quad (1.54)$$

$$F_y^1 = \frac{(\Delta y)^2}{\lambda z}, \quad (1.55)$$

the complex exponential in (1.51) can be written as

$$\exp\left(\frac{-iz(n_x^2\Delta k_x^2 + n_y^2\Delta k_y^2)}{2k}\right) = \exp\left(-\frac{i\pi n_x^2}{N_x^2 F_x^1}\right) \exp\left(-\frac{i\pi n_y^2}{N_y^2 F_y^1}\right). \quad (1.56)$$

Therefore, Fresnel diffraction of a given wave field with a discrete  $N_x \times N_y$  pixel representation only depends on the *combination* (1.54, 1.55) of wavelength, propagation distance and pixel size. If necessary to ensure proper sampling of the complex exponential (1.56) at smaller Fresnel numbers [210], the incident wave field is embedded in a larger array using symmetric padding (mirror reflections at the borders or replicate of the border values).



## 1.2 X-ray interaction with matter

We are now equipped with numerical and analytical tools to describe the evolution of x-ray wave fields in free space. However, structural information of investigated samples can only be obtained due to x-ray interaction with matter. In this section, propagation of x-rays in the presence of matter is discussed and the **projection approximation** which relates properties of an object to phase and amplitude modulations of the incident wave field is introduced.

### 1.2.1 Wave equations in the presence of matter

Starting with Maxwells equations in the presence of uncharged, non-conducting, non-magnetic, static and isotropic material

$$\nabla \cdot [\epsilon(\mathbf{r}) \cdot \mathbf{E}(\mathbf{r}, t)] = 0 \quad (1.57)$$

$$\nabla \cdot \mathbf{B}(\mathbf{r}, t) = 0 \quad (1.58)$$

$$\nabla \times \mathbf{E}(\mathbf{r}, t) + \partial_t \mathbf{B}(\mathbf{r}, t) = \mathbf{0} \quad (1.59)$$

$$\nabla \times \mathbf{B}(\mathbf{r}, t) - \mu_0 \epsilon(\mathbf{r}, t) \partial_t \mathbf{E}(\mathbf{r}, t) = \mathbf{0}, \quad (1.60)$$

and assuming that the electric permittivity  $\epsilon(\mathbf{r}, t)$  of the medium varies slowly on length scales comparable to the wavelength, the scalar wave equation reads [164]

$$(\epsilon(\mathbf{r})\mu_0\partial_t^2 - \nabla^2) \Psi(\mathbf{r}, t) = 0. \quad (1.61)$$

With the definition of the **refractive index**

$$n(\mathbf{r}) = \sqrt{\frac{\epsilon(\mathbf{r})}{\epsilon_0}}$$

the wave equation in the presence of a medium can be written as

$$\left( \frac{n^2(\mathbf{r})}{c^2} \partial_t^2 - \nabla^2 \right) \Psi(\mathbf{r}, t) = 0. \quad (1.62)$$

Plane waves  $\psi^{(\text{PW})}(\mathbf{r}, t)$  (1.8) constitute an elementary solution, if

$$k^2 = n^2(\mathbf{r}) \frac{\omega^2}{c^2} = n^2(\mathbf{r}) k_0^2, \quad (1.63)$$

with  $k_0 = \frac{2\pi}{\lambda_0}$  denoting the wave number in vacuum. With respect to vacuum, the wavelength  $\lambda = \lambda_0/n(\mathbf{r})$  and the phase velocity  $v = \omega/k = c/n(\mathbf{r})$  are altered within the medium. Following the angular spectrum approach as outlined in the case of vacuum in section 1.1.2, we can write the time-independent **inhomogenous Helmholtz equation** [164] as

$$\boxed{(\nabla^2 + n^2(\mathbf{r})k^2) \psi(\mathbf{r}) = 0.} \quad (1.64)$$

With the approximation of the slowly varying envelope, outlined in section 1.1.3, the **paraxial Helmholtz equation in the presence of matter** [187] reads

$$\boxed{(2ik\partial_z + \nabla_{\perp}^2 + k^2 [n^2(\mathbf{r}) - 1]) A(\mathbf{r}) = 0.} \quad (1.65)$$

### 1.2.2 Refractive index for X-rays

Since interaction of X-rays with matter is rather weak, the refractive index is commonly expressed in the form [1]

$$n(\mathbf{r}) = 1 - \delta(\mathbf{r}) + i\beta(\mathbf{r}) \quad (1.66)$$

with  $\delta(\mathbf{r})$  and  $\beta(\mathbf{r})$  being real positive numbers much smaller than unity (e.g. **Fig. 1.2 a**). X-ray interaction with matter can primarily be attributed to bound electrons in shells of atoms and therefore  $\delta(\mathbf{r})$  and  $\beta(\mathbf{r})$  relate to the electron density of the medium. Close to resonance energies the energy-dependent dispersion correction of the atomic scattering factor cannot easily be predicted theoretically. However, away from resonance edges the decrement  $\delta(\mathbf{r})$  of the refractive index can approximately be expressed in terms of the electron density  $\rho_e(\mathbf{r})$  and the Thomson scattering length  $r_e$  [1]

$$\delta(\mathbf{r}) \simeq \frac{2\pi r_e}{k^2} \rho_e(\mathbf{r}). \quad (1.67)$$

Throughout this work, hard x-rays with photon energies between  $\hbar\omega = E = 7.9$  keV and  $E = 17$  keV are used<sup>4</sup>. The resonance energies for most prevalent

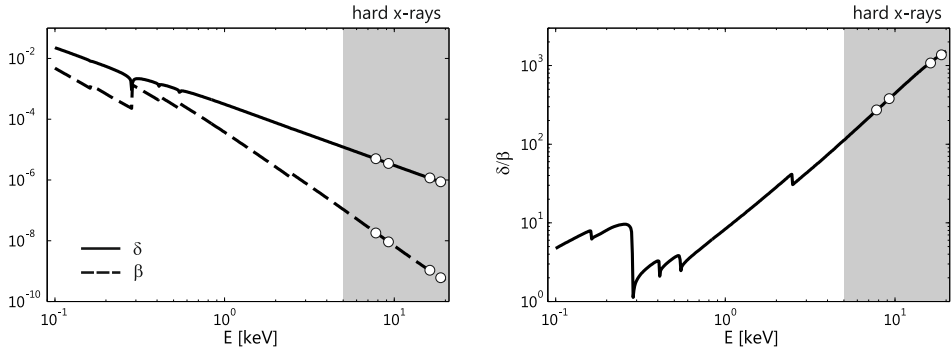


**Figure 1.2:** (a) Real and imaginary part of the refractive index  $n = 1 - \delta + i\beta$  for a model biological specimen with empirical formula  $\text{H}_{50}\text{C}_{30}\text{N}_9\text{O}_{10}\text{S}_1$  and mass density  $1.35 \text{ g/cm}^3$  [97] at different x-ray photon energies. (b) Ratio  $\delta/\beta$ , corresponding to the values shown in (a). Photon energies  $E \in \{7.9, 9.25, 13.8, 17\}$  keV used for experiments in this work are indicated with circles. Data obtained from [89].

<sup>4</sup> We define the hard x-ray range in this work as photon energies above 5 keV.

atoms in biological materials lie outside this energy range, as shown in **Fig. 1.2** for a model biological material consisting of H, C, N, O and S atoms. Therefore, in the context of this work, equation (1.67) is well justified [31]. In the case of a multi-elemental material, the electron density is further related to the atomic number  $Z_j$  and relative atomic mass  $A_j$ <sup>5</sup> of the  $j$ -th element. Taking the molar fractions  $p_j$  of each element into account, equation (1.67) can be written in terms of the mass density  $\rho_m$

$$\delta(\mathbf{r}) \simeq \frac{2\pi r_e}{k^2 u} \rho_m(\mathbf{r}) \frac{\sum_j p_j Z_j}{\sum_j p_j A_j}. \quad (1.68)$$

For low- $Z$  elements except for hydrogen, one finds the quotient  $Z/A \simeq 1/2$ . As the mass fraction of hydrogen atoms in most biological materials is rather small, one may approximate

$$\delta(\mathbf{r}) \simeq \frac{\pi r_e}{k^2 u} \rho_m(\mathbf{r}). \quad (1.69)$$

For the imaginary part  $\beta(\mathbf{r})$  no simple relation to the materials electron density exists. However, away from absorption edges we can approximate  $\beta(\mathbf{r})$  for a single-elemental material [1] as

$$\beta \propto Z^4 E^{-4}. \quad (1.70)$$

This compares to

$$\delta \propto Z E^{-2}, \quad (1.71)$$

as can be seen in equation (1.68) for the case of a single element. Note that both  $\delta(\mathbf{r})$  and  $\beta(\mathbf{r})$  are several orders of magnitude below unity for hard x-rays (e.g. **Fig. 1.2 a**). Therefore, we can neglect terms of second order and mixed terms in  $n^2(\mathbf{r})$  and write

$$n^2(\mathbf{r}) \simeq 1 - 2\delta(\mathbf{r}) + 2i\beta(\mathbf{r}). \quad (1.72)$$

### 1.2.3 The projection approximation

Consider the situation of an x-ray wave field traversing an object of thickness  $\Delta t$  for the case of a paraxial incoming field  $\psi(\mathbf{r}) = A(\mathbf{r}) \cdot \exp(ikz)$ , as outlined in section 1.1.3. Inserting equation (1.72) into the paraxial Helmholtz equation (1.65) yields

$$(2ik\partial_z + \nabla_{\perp}^2 + k^2 [2i\beta(\mathbf{r}) - 2\delta(\mathbf{r})]) A(\mathbf{r}) \simeq 0. \quad (1.73)$$

The **projection approximation** corresponds to the limit of geometrical optics and assumes that all changes to the wave field due to sample interaction are accumulated along streamlines of the unscattered beam [164] as depicted in **Fig.**

<sup>5</sup> The relative atomic mass is a dimensionless quantity, expressed in units of the unified atomic mass unit  $1u \simeq 1.661 \cdot 10^{-27}$  kg

**1.3.** It is valid if the radius of the first Fresnel zone  $\sqrt{\lambda z}$  corresponding to Fresnel diffraction inside the object is small compared to the smallest non-negligible lateral length scale  $\Delta r_{\perp}$  of the object [31, 171, 39]

$$\sqrt{\lambda_0 \Delta t} < \Delta r_{\perp}. \quad (1.74)$$

If  $\Delta r_{\perp}$  is regarded as resolution of the imaging system, the maximum thickness of the object  $\Delta t$  for the projection approximation to hold is

$$\Delta t < \frac{\Delta r_{\perp}^2}{\lambda_0}. \quad (1.75)$$

If the conditions above are violated, one may use multi-slice methods (see e.g. [200]) or solve the inhomogenous Helmholtz equation by means of finite difference calculations (see e.g. [56]). If the conditions are fulfilled, we account for the projection approximation by neglecting the transverse Laplacian in equation (1.73) [164] and write

$$\partial_z A(\mathbf{r}) \simeq -ik [\delta(\mathbf{r}) - i\beta(\mathbf{r})] A(\mathbf{r}). \quad (1.76)$$

Solving the boundary value problem for the above partial differential equation (1.76) yields [164]

$$A(\mathbf{r}_{\perp}, \Delta z) \simeq A(\mathbf{r}_{\perp}, 0) \exp \left[ -ik \int_0^{\Delta t} [\delta(\mathbf{r}) - i\beta(\mathbf{r})] dz \right]. \quad (1.77)$$

With  $\psi(\mathbf{r}_{\perp}, 0) = A(\mathbf{r}_{\perp}, 0)$  and  $\psi(\mathbf{r}_{\perp}, \Delta t) = A(\mathbf{r}_{\perp}, \Delta t) \exp(ik\Delta t)$  the wave field behind the object reads

$$\boxed{\psi(\mathbf{r}_{\perp}, \Delta t) \simeq \exp(ik\Delta z) \psi(\mathbf{r}_{\perp}, 0) \exp \left[ -ik \int_0^{\Delta t} [\delta(\mathbf{r}) - i\beta(\mathbf{r})] dz \right]}. \quad (1.78)$$

For convenience we introduce the **illumination function** [61, 182]

$$P(\mathbf{r}_{\perp}) := \psi(\mathbf{r}_{\perp}, 0) \quad (1.79)$$

and the **object transmission function**

$$O(\mathbf{r}_{\perp}) := \exp \left[ -ik \int_0^{\Delta t} [\delta(\mathbf{r}) + -i\beta(\mathbf{r})] dz \right] \quad (1.80)$$

and rewrite equation (1.78) as

$$\psi(\mathbf{r}_{\perp}, \Delta t) \simeq \exp(ik\Delta t) P(\mathbf{r}_{\perp}) O(\mathbf{r}_{\perp}). \quad (1.81)$$

With the definitions

$$\bar{\delta}(\mathbf{r}_\perp) := \int_0^{\Delta t} \delta(\mathbf{r}) dz \quad (1.82)$$

$$\bar{\beta}(\mathbf{r}_\perp) := \int_0^{\Delta t} \beta(\mathbf{r}) dz \quad (1.83)$$

the object transmission function reads

$$O(\mathbf{r}_\perp) = \exp[-k\bar{\beta}(\mathbf{r}_\perp)] \exp[-ik\bar{\delta}(\mathbf{r}_\perp)]. \quad (1.84)$$

For a homogenous object with constant index of refraction  $n = 1 - \delta + i\beta$  and projected thickness  $T(x, y)$ , the object transmission function can be written as

$$O(\mathbf{r}_\perp) = \exp[-k\beta T(\mathbf{r}_\perp)] \exp[-ik\delta T(\mathbf{r}_\perp)]. \quad (1.85)$$

### 1.2.4 Phase shift and absorption within objects

In the framework of paraxial approximation and projection approximation, the imaginary part  $\beta(\mathbf{r})$  of the refractive index is related to the amplitude  $a(\mathbf{r}_\perp)$  of the object transmission function (1.84) by

$$a(\mathbf{r}_\perp) = |O(\mathbf{r}_\perp)| = \exp[-k\bar{\beta}(\mathbf{r}_\perp)] \quad (1.86)$$

$$\Leftrightarrow \bar{\beta}(\mathbf{r}_\perp) = -\frac{\ln(a(\mathbf{r}_\perp))}{k}. \quad (1.87)$$

By taking the squared modulus of equation (1.81) and identifying  $I(\mathbf{r}) = |\psi(\mathbf{r})|^2$  with the intensity we find the familiar Beer-Lambert law

$$I(\mathbf{r}_\perp, \Delta z) = I(\mathbf{r}_\perp, 0) \exp[-\mu T(\mathbf{r}_\perp)], \quad (1.88)$$

for an object composed of a single material with constant  $\beta(\mathbf{r}) = \beta$ , projected thickness  $T(\mathbf{r}_\perp)$  along the  $z$  direction and linear attenuation coefficient

$$\mu = 2k\beta. \quad (1.89)$$

While the imaginary part accounts for absorption within the sample, the decrement  $\delta(\mathbf{r})$  of the refractive index is related to a phase shift (1.84)<sup>6</sup>

$$\varphi(\mathbf{r}_\perp) = \varphi(O(\mathbf{r}_\perp)) = -k\bar{\delta}(\mathbf{r}_\perp) \quad (1.90)$$

$$\Leftrightarrow \bar{\delta}(\mathbf{r}_\perp) = -\varphi(\mathbf{r}_\perp)/k. \quad (1.91)$$

<sup>6</sup> The operator  $\varphi(f)$  is defined here as  $\varphi(f) = \phi$  for  $f = a \cdot \exp(i\phi)$ . Apart from periodicity in  $2\pi$ , the phase may be identified with the argument of the object transmission function, i.e.  $\varphi(O(\mathbf{r}_\perp)) = \arg(O(\mathbf{r}_\perp))$ .

Hence, the *projected* refractive index  $\bar{n}(\mathbf{r}_\perp) = 1 - \bar{\delta} + i\bar{\beta}$  can be obtained using equations (1.87, 1.91) by determining phase and amplitude of the object transmission function.

We note that  $\delta$  is up to 3 orders of magnitude larger than  $\beta$  [147] as shown for a typical biological material in **Fig. 1.2 b**. Together with the proportionalities (1.70, 1.71) and equations (1.86, 1.90) it is evident that, especially for thin specimens composed of light biological materials, the induced phase shift at high photon energies will typically be much stronger than the attenuation of the x-ray wave field. However, thicker specimens or biological samples which incorporate high- $Z$  elements will result in notable absorption. Therefore, an x-ray imaging technique capable of exploiting both effects is desirable. The following sections discuss how contrast formation in x-ray propagation imaging meets this requirement and how the desired information can be retrieved from measurable data.

### 1.3 Contrast formation and imaging regimes

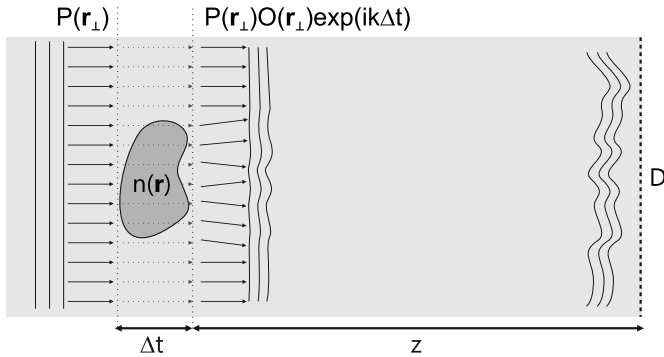


**Figure 1.3:** Contrast formation in x-ray propagation imaging. According to the projection approximation, changes to the incident wave field  $P(\mathbf{r}_\perp)$  due to an object with refractive index  $n(\mathbf{r})$  are accumulated along streamlines of the unscattered beam. These changes are described by the object transmission function  $O(\mathbf{r}_\perp)$ . The wave field behind the object is subject to Fresnel diffraction  $\mathcal{D}$ . In the case of plane wave illumination, the intensity detected in a plane at distance  $z$  behind the object is described by  $|\mathcal{D}_z \{O(\mathbf{r}_\perp)\}|^2$ .

**Fig. 1.3** depicts an idealized situation of a monochromatic plane wave with  $P(\mathbf{r}_\perp) = 1$  traversing a sample at plane  $z = 0$  with object transmission function  $O(\mathbf{r}_\perp)$  and thickness  $\Delta t$ . Assuming the projection approximation (1.81) to hold, the wave field right behind the object can be expressed as

$$\psi(\mathbf{r}_\perp, 0) \simeq \exp(ik\Delta t)O(\mathbf{r}_\perp). \quad (1.92)$$

The intensity  $I(\mathbf{r}_\perp, z)$  of the wave field propagated to a plane  $z > 0$  can be expressed using the Fresnel diffraction operator  $\mathcal{D}_z$  (1.31)

$$I(\mathbf{r}_\perp, z) = |\psi(\mathbf{r}_\perp, z)|^2 = |\mathcal{D}_z \{\psi(\mathbf{r}_\perp, 0)\}|^2 = |\mathcal{D}_z \{O(\mathbf{r}_\perp)\}|^2. \quad (1.93)$$

### 1.3.1 Contrast transfer function

For a weakly interacting object with  $\mu(\mathbf{r}_\perp) \ll 1$  and  $|\varphi(\mathbf{r}_\perp)| \ll 1$ , Taylor expansion to first order of the object transmission function (1.84) yields

$$O(\mathbf{r}_\perp) \simeq 1 - k\bar{\beta}(\mathbf{r}_\perp) - ik\bar{\delta}(\mathbf{r}_\perp) \quad (1.94)$$

$$= 1 - \mu(\mathbf{r}_\perp) + i\varphi(\mathbf{r}_\perp). \quad (1.95)$$

The propagated wave field  $\psi(\mathbf{r}_\perp, z)$  is calculated as

$$\psi(\mathbf{r}_\perp, z) = \mathcal{D}_z \{O(\mathbf{r}_\perp)\} \quad (1.96)$$

$$= \mathcal{F}^{-1} [\exp(-i\chi) \mathcal{F}(1 - \mu(\mathbf{r}_\perp) + i\varphi(\mathbf{r}_\perp))], \quad (1.97)$$

using  $\mathcal{D}_z$  (1.31) with  $\chi(\mathbf{k}_\perp, z) = zk_\perp^2/2k$ . Following equation (1.93), global phase factors were dropped since they do not contribute to the intensity. For the sake of convenience, the dependence on lateral coordinates  $\mathbf{r}_\perp$  and angular spatial frequencies  $\mathbf{k}_\perp$  as well as propagation distance  $z$  are omitted in the following lines. With  $\exp(-i\chi) = \cos \chi - i \sin \chi$  the propagated wave field can be expressed as

$$\psi = 1 + \mathcal{F}^{-1} [(\cos \chi - i \sin \chi) (i\tilde{\varphi} - \tilde{\mu})], \quad (1.98)$$

where  $\tilde{\varphi}$  and  $\tilde{\mu}$  denote the Fourier transforms of  $\varphi$  and  $\mu$ , respectively. Using the Fourier transform convolution theorem (A.11), equation (1.98) can be expressed as

$$\psi = 1 + \varphi \otimes \mathcal{F}^{-1}(\sin \chi) - \mu \otimes \mathcal{F}^{-1}(\cos \chi) - i\mu \otimes \mathcal{F}^{-1}(\sin \chi) + i\varphi \otimes \mathcal{F}^{-1}(\cos \chi). \quad (1.99)$$

The intensity  $|\psi|^2$  to first order in  $\varphi$  and  $\mu$  then reads [171]

$$|\psi|^2 \simeq 1 + 2\varphi \otimes \mathcal{F}^{-1}(\sin \chi) - 2\mu \otimes \mathcal{F}^{-1}(\cos \chi) \quad (1.100)$$

and can be expressed as  $\tilde{I}(\mathbf{k}_\perp, z) = \mathcal{F} \left( |\psi(\mathbf{r}_\perp, z)|^2 \right)$  in Fourier space

$$\tilde{I}(\mathbf{k}_\perp, z) \simeq 2\pi\delta_{\text{D}}(\mathbf{k}_\perp) + 2\tilde{\varphi}(\mathbf{k}_\perp) \sin [\chi(\mathbf{k}_\perp, z)] - 2\tilde{\mu}(\mathbf{k}_\perp) \cos [\chi(\mathbf{k}_\perp, z)], \quad (1.101)$$

using the Fourier pair (A.22) for the Dirac delta function  $\delta_{\text{D}}$ . In terms of spatial frequencies  $(\nu_x, \nu_y) = (k_x, k_y)/2\pi$  with  $\chi(\nu, z) = \pi\lambda z\nu^2$  equation (1.101) can be written as [139, 171]

$$\tilde{I}(\nu_x, \nu_y, z) \simeq \delta_{\text{D}}(\nu_x, \nu_y) + 2\tilde{\varphi}(\nu_x, \nu_y) \sin [\chi(\nu, z)] - 2\tilde{\mu}(\nu_x, \nu_y) \cos [\chi(\nu, z)]. \quad (1.102)$$

Here, the scaling property (A.20) of the delta function  $\delta_{\mathbb{D}}$  was used. Under certain conditions, the weak object approximation which was used to derive expression (1.102) can be relaxed. The assumption of slowly varying phase

$$|\varphi(\mathbf{r}_{\perp}) - \varphi(\mathbf{r}_{\perp} + \lambda z \mathbf{k}_{\perp}/2\pi)| \ll 1. \quad (1.103)$$

is sufficient for the case of a pure phase object ( $\mu(\mathbf{r}_{\perp}) = 0$ ) [72] or for a homogeneous object with  $\delta \propto \beta$  and weak absorption ( $\mu(\mathbf{r}_{\perp}) \ll 1$ ) [207]. Equation (1.102) constitutes an important step towards understanding the contrast formation in x-ray propagation imaging. The intensity is given by amplitude and phase of the object transmission function, however *filtered* by the oscillating terms  $\sin[\chi(\nu, z)]$  and  $\cos[\chi(\nu, z)]$  in Fourier space, which are denoted **phase contrast transfer functions (PCTF)** and **amplitude contrast transfer functions (ACTF)**, respectively. The contrast transfer functions are of oscillatory nature as shown in **Fig. 1.4** for the reduced radial spatial frequency  $\sqrt{\lambda z} \nu$  [171]. At a given propagation distance  $z$ , the intensity carries zero information about the phase of the object transmission function for spatial frequencies  $\nu_0 = \sqrt{n/\lambda z}$ , since  $\sin[\chi(\nu_0, z)] = 0$  for  $\nu_0$  with  $n \in \mathbb{N}$ . Correspondingly, for  $\cos[\chi(\nu_0, z)] = 0$  no information of the amplitude at spatial frequencies  $\nu_0 = \sqrt{(n+1/2)/\lambda z}$  is transferred.

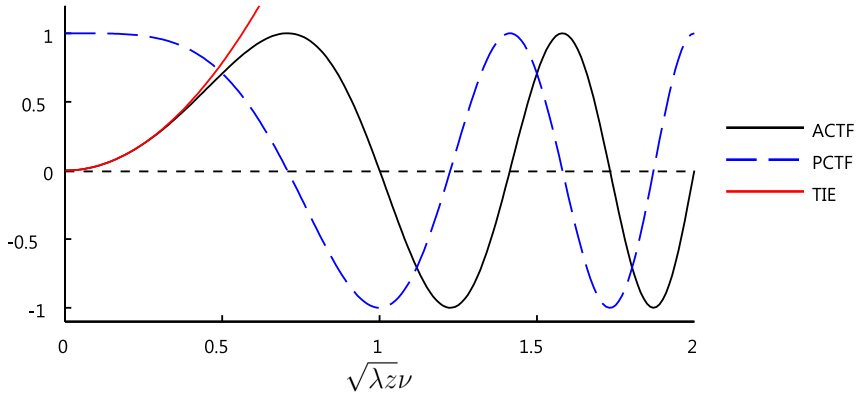


**Figure 1.4:** Phase contrast transfer function (PCTF) and amplitude transfer function (ACTF) of x-ray propagation imaging for a weak object. PCTF and ACTF are zero for  $\nu_0 = \sqrt{n/\lambda z}$  and  $\nu_0 = \sqrt{(n+1/2)/\lambda z}$  with  $n \in \mathbb{N}$ , respectively. The contrast transfer at small propagation distances as assumed by the transport-of-intensity equation (TIE) is shown for a pure phase object.

### 1.3.2 Transport-of-intensity equation

Another approach to understand contrast formation of free space propagation is to write the homogenous paraxial Helmholtz equation (1.21) in terms of intensity  $I(\mathbf{r})$  and phase  $\varphi(\mathbf{r})$  of the spatial part of a paraxial wave field  $\mathbf{A}(\mathbf{r}) = \sqrt{I(\mathbf{r})} \exp(i\varphi(\mathbf{r}))$

$$(2ik\partial_z + \nabla_{\perp}^2) \sqrt{I(\mathbf{r})} \exp(i\varphi(\mathbf{r})) = 0. \quad (1.104)$$



After simplifications, the imaginary part results in a second-order elliptic partial differential equation

$$\nabla_{\perp} \cdot (I(\mathbf{r})\nabla_{\perp}\phi(\mathbf{r})) = -k\frac{\partial I(\mathbf{r})}{\partial z}, \quad (1.105)$$

known as the **transport-of-intensity equation (TIE)** [198, 83, 199]. This continuity equation describes the conservation of optical energy of a paraxial wave field as it propagates over an infinitesimal distance  $\partial z$  [164]. If the transverse gradient of the intensity or phase is small, one may approximate the left side of equation (1.105) by

$$\nabla_{\perp} \cdot (I(\mathbf{r})\nabla_{\perp}\phi(\mathbf{r})) = I(\mathbf{r})\nabla_{\perp}^2\phi(\mathbf{r}) + \nabla_{\perp}I(\mathbf{r})\nabla_{\perp}\phi(\mathbf{r}) \quad (1.106)$$

$$\simeq I(\mathbf{r})\nabla_{\perp}^2\phi(\mathbf{r}). \quad (1.107)$$

Note that the intensity right behind an object illuminated with a plane wave  $\exp(i\varphi(\mathbf{r}))$  is given by the amplitude of the object transmission function,  $I(\mathbf{r}_{\perp}, z) = |O(\mathbf{r}_{\perp})|$ . As discussed in section (1.4), on certain conditions a non-uniform illumination can be normalized and treated as plane wave illumination. In that case, the above approximation holds for objects with slowly varying absorption. Using the finite-difference approximation for sufficiently small propagation distances  $\Delta z$

$$\frac{\partial I(\mathbf{r}_{\perp}, z)}{\partial z} \simeq \frac{\partial I(\mathbf{r}_{\perp}, z + \Delta z) - \partial I(\mathbf{r}_{\perp}, z)}{\Delta z}, \quad (1.108)$$

and inserting equations (1.106-1.108) into the TIE (1.105) yields the **weak object TIE**

$$\frac{I(\mathbf{r}_{\perp}, z + \Delta z)}{I(\mathbf{r}_{\perp}, z)} \simeq 1 - \frac{\Delta z}{k} \nabla_{\perp}^2 \phi(\mathbf{r}_{\perp}, z). \quad (1.109)$$

The intensity of the wave field propagated by a small distance  $\Delta z$  and normalized by the intensity of the non-propagated wave field, thus deviates from unity by a term proportional to the local curvature in the phase of the non-propagated wave. Importantly, a similar relation (replacing  $k$  by a spectrally weighted sum) holds for polychromatic x-rays [218, 171] making it an important approach for phase-contrast imaging in the laboratory based on microfocus x-ray sources.

### 1.3.3 Imaging regimes

Due to complex amplitude and contrast transfer of free space propagation (1.102), distinct imaging regimes can be identified. Based on equation (1.93) the intensity in any plane  $z > 0$  can be simulated for a given object transmission function with pixel side lengths  $\Delta x$ ,  $\Delta y$  and number of pixels  $N_x$ ,  $N_y$  by means of numerical implementation of Fresnel diffraction as described in section 1.1.7. For the sake of convenience, we assume  $\Delta x = \Delta y$ ,  $N_x = N_y$ . As already shown for the transition to Fraunhofer diffraction (1.40), the relevant quantity determining the degree of diffraction for a given feature of lateral extent  $d$  of the object transmission function is the Fresnel number (1.39). Consistently, for numerical implementations

the *discrete* Fresnel number (1.54)  $F^1 = \frac{\Delta x^2}{\lambda z}$  is sufficient to calculate Fresnel diffraction of a given incident wave field (see equation 1.56). Since a typical object comprises structures on several different length scales, a reasonable definition of imaging regimes has to be linked to a certain feature size  $d$ . We define a typical feature size  $d = 10\Delta x$  [117] and the corresponding discrete Fresnel number

$$F^{10} = \frac{(10\Delta x)^2}{\lambda z} = 100 \cdot F^1. \quad (1.110)$$

**Fig. 1.5** shows the simulated intensity along the optical axis  $z$  for different values of  $F^{10}$  for a simulated object consisting of pure amplitude and pure phase structures as well as mixed structures with both, absorption and phase contributions. The maximum (relative) phase shift was set to  $-\pi/4$  and the minimal amplitude transmission was 0.5. Right behind the object, phase contrast transfer is zero while amplitude transfer is one. Consequently, in the **contact image** only absorbing structures are visible (**a**), in agreement with the transport-of-intensity equation (1.109) for  $\Delta z = 0$ . With increasing propagation distance and decreasing Fresnel numbers, phase contrast arises due to diffraction especially for high spatial frequencies, as expressed by the transverse Laplacian of the phase in equation (1.109). Since edges constitute high spatial frequencies one may speak of phase contrast in **edge-enhancement** mode [33]. Low spatial frequencies, which represent the global shape of the object, are not yet subject to strong diffraction, as expected from the shape of the PCTF (equation (1.102) and **Fig. 1.4**). Therefore, at  $F^{10} \simeq 10$  the object is well recognized (**b**) and one often speaks of the **direct contrast**. By further increasing the propagation distance, the intensity loses more and more resemblance with the object (**c-f**). The finite-difference approximation (1.108) for the TIE breaks down and the phase and amplitude CTFs oscillate rapidly as a function of spatial frequency (**Fig. 1.4**). This so called **holographic regime** is further subdivided into the near and far holographic regime for Fresnel numbers  $F^{10} \simeq 1$  and  $F^{10} \lesssim 0.1$ , respectively.

Imaging techniques in the aforementioned regimes, which are subsumed as the **near field**, are often called x-ray propagation based phase contrast, x-ray inline holography or **x-ray propagaton imaging**. Intensity distributions in the near field will be termed (Fresnel) **diffraction patterns**, holographic intensity distributions or simply **holograms**.

Eventually, for *discrete* Fresnel numbers  $F^{10} \ll 0.1$  the *physical* Fresnel number corresponding to the extent of the object and the beam is much smaller than unity. The intensity is therefore described by Fraunhofer diffraction (1.40), i.e. the Fourier Transform of the object transmission function. Imaging techniques in the **Fraunhofer regime** or **far field** are referred to as **coherent x-ray diffractive imaging** (CDI) [141, 28]. In recent years, a particular variant of CDI, denoted as ptychography, has created broad interest and various applications in x-ray microscopy and coherent x-ray beam characterisation [182, 181, 133, 200, 65, 66, 216, 43, 150]. A detailed discussion of CDI techniques is deliberately omitted in this work. Instead, the focus is on applying x-ray propagation imaging for three-dimensional structure determination of various biological samples, especially of

various lateral extent. In the respective chapters CDI and ptychographic methods will be referred to for comparison and discussed in the related context.

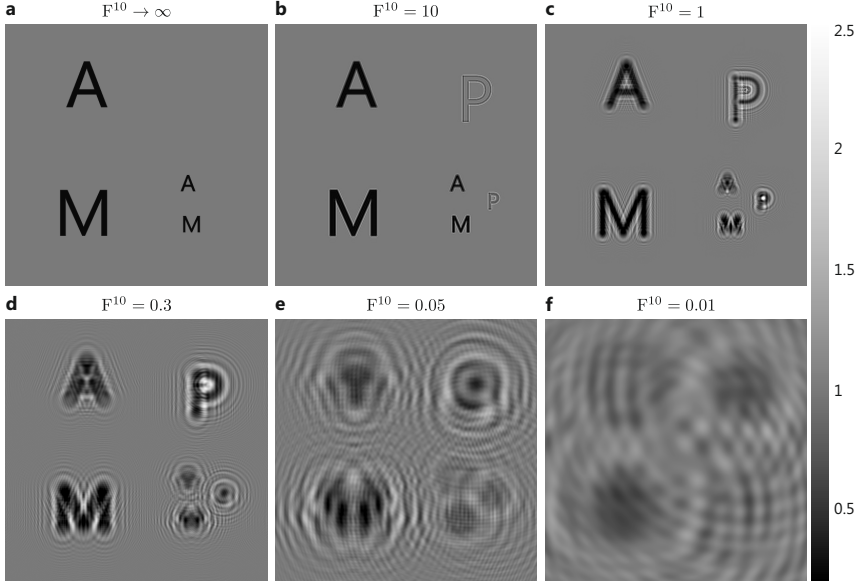


**Figure 1.5:** Simulated intensity distributions for an object consisting of pure amplitude ('A'), pure phase ('P') as well as mixed structures ('M') with both, absorption and phase contributions at different values of  $F^{10}$ . The maximum phase shift is  $-\pi/4$ , the minimal amplitude transmission is 0.5.

## 1.4 Effective near field and empty beam division

For an x-ray propagation imaging experiment as simulated in the previous section with a pixel size of  $\Delta x = 100$  nm and a typical hard x-ray wavelength of  $\lambda = 1$  Å, the corresponding Fresnel numbers  $F^{10} \in [10, 0.1]$  are obtained at propagation distances  $z \in [10^{-3}, 10^{-6}]$  m. Thus, a suitable two-dimensional detector has to be placed down to 1  $\mu$ m behind the sample to access the *physical* near field, which seems rather unfeasible. More importantly, the obtainable spatial resolution is limited to the physical pixel size, more precisely the point spread function of the detector which is at best 300 nm [35] for current detector technology. However, based on the Fresnel scaling theorem (1.49) it is possible to access the *effective* near field using a nearly spherical illumination function  $P(\mathbf{r}_\perp) = P^{(P)}(\mathbf{r}_\perp) \exp\left[\frac{ikr_\perp^2}{2z_1}\right]$  at plane  $z = 0$ . The intensity of the illumination function recorded at  $z = z_2$  thus reads

$$I(\mathbf{r}'_\perp, z_2) = |\mathcal{D}_z \{P(\mathbf{r}'_\perp)\}|^2 = \frac{1}{M^2} \left| \mathcal{D}_{z_{\text{eff}}} \left\{ P^{(P)}(\mathbf{r}'_\perp/M) \right\} \right|^2 =: I^{(E)}(\mathbf{r}_\perp, z_{\text{eff}}), \quad (1.111)$$

with  $\mathbf{r}_\perp = \mathbf{r}'_\perp/M$ . As no object is placed in the beam,  $I^{(E)}(\mathbf{r}_\perp, z_{\text{eff}})$  will henceforth be called the **empty beam**. The recorded intensity with an object placed into the beam at  $z = 0$  can equivalently be written as

$$I(\mathbf{r}_\perp, z_{\text{eff}}) := \frac{1}{M^2} \left| \mathcal{D}_{z_{\text{eff}}} \left\{ O(\mathbf{r}'_\perp/M) P^{(P)}(\mathbf{r}'_\perp/M) \right\} \right|^2, \quad (1.112)$$

If the propagation of both, the nearly planar envelope of the illumination function and the object transmission function can be separated approximately by means of a multiplication, i.e. if

$$\left| \mathcal{D}_{z_{\text{eff}}} \left\{ P^{(P)}(\mathbf{r}_\perp) O(\mathbf{r}_\perp) \right\} \right|^2 \simeq \left| \mathcal{D}_{z_{\text{eff}}} \left\{ P^{(P)}(\mathbf{r}_\perp) \right\} \right|^2 \cdot \left| \mathcal{D}_{z_{\text{eff}}} \left\{ O(\mathbf{r}_\perp) \right\} \right|^2 \quad (1.113)$$

a relation similar to (1.93) can be derived

$$\begin{aligned} \bar{I}(\mathbf{r}_\perp, z_{\text{eff}}) &= \frac{I(\mathbf{r}_\perp, z_{\text{eff}})}{I^{(E)}(\mathbf{r}_\perp, z_{\text{eff}})} = \frac{\frac{1}{M^2} \left| \mathcal{D}_{z_{\text{eff}}} \left\{ O(\mathbf{r}_\perp) P^{(P)}(\mathbf{r}_\perp) \right\} \right|^2}{\frac{1}{M^2} \left| \mathcal{D}_{z_{\text{eff}}} \left\{ P^{(P)}(\mathbf{r}_\perp) \right\} \right|^2} \\ &\simeq \frac{\left| \mathcal{D}_{z_{\text{eff}}} \left\{ P^{(P)}(\mathbf{r}_\perp) \right\} \right|^2 \cdot \left| \mathcal{D}_{z_{\text{eff}}} \left\{ O(\mathbf{r}_\perp) \right\} \right|^2}{\left| \mathcal{D}_{z_{\text{eff}}} \left\{ P^{(P)}(\mathbf{r}_\perp) \right\} \right|^2} \\ &\simeq \left| \mathcal{D}_{z_{\text{eff}}} \left\{ O(\mathbf{r}_\perp) \right\} \right|^2. \end{aligned} \quad (1.114)$$

The result states that as long as approximation (1.113) holds, the squared modulus of the propagated object transmission function is given by the **normalized intensity**  $\bar{I}(\mathbf{r}_\perp, z_{\text{eff}})$  [61]. Importantly, due to geometric demagnification, the effective propagation distance  $z_{\text{eff}} = z_2/M$  and effective pixel size  $\Delta x_{\text{eff}} = \Delta x/M$  allow to access the effective near field of the object transmission function with a sampling not restricted to the physical pixel size of the detector. The equivalence of equation (1.114) with respect to equation (1.93) suggests the term **effective plane wave geometry**. Numerical simulations and reconstruction techniques suitable for parallel beams are directly applicable to the experimental situation of x-ray propagation imaging by switching to the effective plane wave geometry.

## 1.5 Coherence

So far we have discussed x-ray propagation imaging with deterministic monochromatic wave fields with measurable intensity  $I(\mathbf{r}, t) = |\Psi(\mathbf{r}, t)|^2$ . Realistic x-ray wave fields are of intrinsic random character as they are created by non-deterministic processes with random quantum mechanical and thermal effects influencing the photon emission. Thus, a given x-ray wave field  $\Psi(\mathbf{r}, t)$  is a stochastic function in space and time and we define the **mean intensity**

$$I(\mathbf{r}) = \langle |\Psi(\mathbf{r}, t)|^2 \rangle_{\mathcal{E}} = \langle |\Psi(\mathbf{r}, t)|^2 \rangle_T = \lim_{T \rightarrow \infty} \frac{1}{2T} \int_{-T}^T |\Psi(\mathbf{r}, t)|^2 dt. \quad (1.115)$$

Replacing the ensemble average with the time average is justified for statistically stationary wave fields [187] with the benefit that the resulting term can approximately be measured in an experiment. Contrast formation in x-ray propagation imaging is based on intensity measurements of a wave field which propagated in free space to the detection plane. The Hygens-Fresnel interpretation of the wave field in the detection plane is a superposition of diverging paraboloidal waves emanating at each point in the input plane (see section 1.1.4). Thus, contrast arises due to interference effects which for stochastic x-ray wave fields depend on the two-point correlation function

$$\Gamma(\mathbf{r}_1, \mathbf{r}_2, \tau) = \langle \Psi(\mathbf{r}_1, t + \tau) \Psi^*(\mathbf{r}_2, t) \rangle, \quad (1.116)$$

known as the **mutual coherence function** [187, 164]. The mean intensity  $I(\mathbf{r}_1, t) = \Gamma(\mathbf{r}_1, \mathbf{r}_1, 0)$  is a special case of the mutual coherence function and the **complex degree of coherence** is defined as

$$\gamma(\mathbf{r}_1, \mathbf{r}_2, \tau) = \frac{\Gamma(\mathbf{r}_1, \mathbf{r}_2, \tau)}{\sqrt{\Gamma(\mathbf{r}_1, \mathbf{r}_1, 0)\Gamma(\mathbf{r}_2, \mathbf{r}_2, 0)}} = \frac{\Gamma(\mathbf{r}_1, \mathbf{r}_2, \tau)}{\sqrt{I(\mathbf{r}_1)I(\mathbf{r}_2)}}. \quad (1.117)$$

Monochromatic wave fields  $\Psi(\mathbf{r}, t) = \sqrt{I(\mathbf{r})} \cdot \exp[i(\varphi(\mathbf{r}) - \omega t)]$  as used in the previous chapters have a complex degree of coherence

$$\gamma(\mathbf{r}_1, \mathbf{r}_2, \tau) = \exp[i(\varphi(\mathbf{r}_1) - \varphi(\mathbf{r}_2) - \omega \tau)] \quad (1.118)$$

with unit modulus and hence full coherence for all space-time points. Realistic x-ray wave fields may be modelled as **quasi monochromatic wave fields** defined as a superposition of monochromatic components [164]

$$\Psi(\mathbf{r}, t) = \frac{1}{\sqrt{2\pi}} \int_{\omega=\bar{\omega}-\Delta\omega/2}^{\omega=\bar{\omega}+\Delta\omega/2} \psi(\mathbf{r}) \exp(-i\omega t) d\omega, \quad (1.119)$$

with non-zero monochromatic components within a narrow spectral range  $[\bar{\omega} - \Delta\omega/2, \bar{\omega} + \Delta\omega/2]$  around a mean angular frequency  $\bar{\omega}$  with  $\Delta\omega \ll \bar{\omega}$ . With  $\delta\omega = \omega - \bar{\omega}$  the integral above reads

$$\Psi(\mathbf{r}, t) = \exp(-i\bar{\omega}t) \mathcal{A}(\mathbf{r}, t) \quad (1.120)$$

with the complex envelope

$$\mathcal{A}(\mathbf{r}, t) = \frac{1}{\sqrt{2\pi}} \int_{\delta\omega=-\Delta\omega/2}^{\delta\omega=\Delta\omega/2} \psi_{\bar{\omega}+\delta\omega}(\mathbf{r}) \exp(-i\delta\omega t) d(\delta\omega). \quad (1.121)$$

Since the quasi monochromatic wave field is restricted to a narrow spectral range with  $\Delta\omega \ll \omega$ ,  $\mathcal{A}(\mathbf{r}, t)$  varies slowly compared to the harmonic factor  $\exp(-i\bar{\omega}t)$  [164]. However, variations in phase and amplitude of the complex envelope are expected to manifest in varying interference patterns with respect to time. Consequently, it can be shown that the complex degree of coherence for quasi monochromatic wave fields satisfies [164]

$$|\gamma(\mathbf{r}_1, \mathbf{r}_2, \tau)| \leq 1. \quad (1.122)$$

While coherence of a wave field is expressed as correlations between points in space *and* time it is worthwhile to study spatial and temporal correlations separately. First, we regard spatial correlations of wave fields for a fixed lag time  $\tau$ . For  $\tau = 0$  the mutual coherence function is denoted as the **mutual intensity** [164]

$$\Gamma(\mathbf{r}_1, \mathbf{r}_2) = \langle \Psi(\mathbf{r}_1, t) \Psi^*(\mathbf{r}_2, t) \rangle. \quad (1.123)$$

For quasi monochromatic wave fields the mutual coherence function can be written as a product

$$\Gamma(\mathbf{r}_1, \mathbf{r}_2, \tau) \approx \exp(-i\bar{\omega}\tau) \Gamma(\mathbf{r}_1, \mathbf{r}_2), \quad (1.124)$$

where the spatial coherence properties are described completely by the mutual intensity [187]. An important peculiarity of spatial coherence is that spatial correlations of a wave field can be induced by free-space propagation. This property is quantified by the **van Cittert-Zernike theorem** [223]. A given intensity distribution  $I(\mathbf{s}_\perp, 0) = I(s_x, s_y, 0)$  with zero spatial coherence corresponding to a small monochromatic source with lateral extent  $d$  yields a mutual intensity of

$$\Gamma(\mathbf{r}_{\perp,1}, \mathbf{r}_{\perp,2}, z) \propto \mathcal{F}_\perp[I(\mathbf{s}_\perp)](\mathbf{k}_\perp = \bar{k}(\mathbf{r}_{\perp,1} - \mathbf{r}_{\perp,2})/z) \quad (1.125)$$

in the far field of the source at  $z \gg r$  [156]. Thus, the mutual intensity relates to the Fourier transform of the lateral intensity distribution of the incoherent source. For a Gaussian source (for the sake of simplicity in one dimension) with standard deviation  $\sigma$  and peak intensity  $I_0$

$$I(s_x, 0) = \frac{I_0}{\sqrt{2\pi}\sigma} \exp\left[-\frac{s_x^2}{2\sigma^2}\right] \quad (1.126)$$

the van Cittert-Zernike theorem states

$$|\Gamma(x_1, x_2, z)| \propto I_0 \exp\left[-\frac{\bar{k}^2 \sigma^2 (x_1 - x_2)^2}{2z^2}\right]. \quad (1.127)$$

We define the **spatial coherence length**<sup>7</sup>  $l_s$  as the  $1/\sqrt{e}$ -decay half-length of  $|\Gamma(x_1, x_2, z)|$  and obtain for the Gaussian source

$$l_s = \frac{z}{\bar{k}\sigma}. \quad (1.128)$$

Therefore, a larger spatial coherence length can be generated by choosing an x-ray source with smaller standard deviation  $\sigma$  of the intensity distribution or by increasing the distance  $z$  to the source. Note that for x-ray propagation imaging it is not necessary to illuminate the entire object coherently [171]. For example, the microfous arrangement used in chapter 5 with a source size of about  $6 \mu\text{m}$  (FWHM) exhibits a spatial coherence length off only about  $1 \mu\text{m}$  at typical source-sample distances of  $z_1 = 80 \text{ mm}$ . Still, phase contrast arises for high spatial frequencies.

<sup>7</sup> Prefactors vary in the literature.

On the contrary, coherent x-ray diffraction microscopy in the Fraunhofer far field poses more stringent requirements on spatial coherence.

To study the influence of the spectral bandwidth of a quasi monochromatic wave field we consider the special case of the mutual coherence function for  $\mathbf{r}_1 = \mathbf{r}_2$ , namely the **temporal coherence function** [187]

$$\Gamma(\tau) = \langle \Psi(\mathbf{r}_1, t + \tau) \Psi^*(\mathbf{r}_1, t) \rangle. \quad (1.129)$$

The modulus of the complex degree of temporal coherence

$$\gamma(\tau) = \frac{\Gamma(\tau)}{\Gamma(0)} \quad (1.130)$$

is a measure for correlation of the wave field at a given point in space for two points in time separated by a lag time  $\tau$ . For a spectral density with Lorentzian shape with bandwidth  $\Delta\omega$ , the modulus of the temporal coherence function can be written as  $|\gamma(\tau)| = \exp(-\tau/\tau_c)$  with **coherence time**  $\tau_c$  as defined by the  $1/e$ -decay of  $|\gamma(\tau)|$  [209], corresponding to a **longitudinal coherence length**  $l_l = c\tau_c$  [187].

Partial longitudinal coherence is expected to limit the resolution of x-ray propagation imaging experiments. To this end, we consider the oscillating terms  $\tilde{\varphi} \sin(\chi)$  and  $\tilde{\mu} \cos(\chi)$  of the contrast transfer functions (1.102) with  $\chi = \pi z \lambda \nu^2$ . The spectral bandwidth of the wave field with a wavelength spread of  $\Delta\lambda$  may be neglected if  $\Delta\chi = \pi z \nu^2 \Delta\lambda \ll \pi$  for all  $\nu$ . This condition is fulfilled if [34, 184]

$$\epsilon = \Delta\lambda z \nu_{\max}^2 = \frac{\Delta\lambda}{\lambda} \frac{\lambda z}{4\Delta r^2} \ll 1, \quad (1.131)$$

with  $\nu_{\max} = 1/(2\Delta r)$  being the highest spatial frequency corresponding to a resolution of  $\Delta r$ . For the parameters of beamline ID22 at the ESRF (see section 4.4) with  $\Delta\lambda/\lambda = 1.6 \cdot 10^{-2}$  one obtains  $\epsilon = 1.75$ , assuming a half-period resolution of  $\Delta r = 100$  nm and typical effective propagation distances of  $z_{\text{eff}} = 60$  mm. Therefore, the medium monochromaticity of the pink x-ray beam may set an upper limit for the obtainable spatial resolution. On the contrary, the Coherence Beamline P10 (see section 4.3) provides high monochromaticity of  $\Delta\lambda/\lambda = 10^{-4}$  based on a double-crystal monochromator. High resolution imaging at the optimized waveguide configuration of the GINIX setup at beamline P10 (see section 4.3.5) is achieved for relatively small propagation distances of  $z_{\text{eff}} = 8$  mm at effective pixel sizes of  $p_{\text{eff}} = 10$  nm. This yields values of  $\epsilon = 0.04 - 0.08 \ll 1$  at photon energies in the range of 7.9 – 15 keV for a half-period resolution of  $\Delta r = 20$  nm. Thus, the longitudinal coherence is sufficient for high resolution x-ray propagation imaging at the GINIX setup.

## 1.6 Radiation damage and dose

Radiation damage of biological samples due to ionizing radiation is a critical issue which sets an upper limit to the obtainable resolution in lensless coherent x-ray imaging [97, 190]. The 'primary' process of radiation damage starts with energy deposition by photoelectric absorption of x-ray photons and subsequent bond breaking due to expelled core shell electrons. 'Secondary' damage processes are based on reactions of diffusing atomic and molecular radicals [111, 149]. Thus, radiation damage effects are expected to increase with increasing number of absorbed photons. The deposited energy is quantified by the dose  $D$  defined as energy per unit mass ( $\text{Gy} = \text{J/kg}$ ) and is related to the incident photon fluence  $F_0$  which is defined as the number of photons per unit area. According to Beer-Lambert's law the fluence decreases at depth  $t$  to  $F = F_0 \exp(-\mu t)$  with linear attenuation coefficient  $\mu = 2k\beta$ . Hence, the number of photons absorbed per unit area at the surface is  $[\partial F/\partial t]_{t=0} = \mu F_0$  and the surface dose  $D$  for x-ray photons with energy  $h\nu$  is

$$D = \frac{\mu F_0 h\nu}{\rho_m} \quad (1.132)$$

for an object with mass density  $\rho_m$  [97]. Radiation damage can be considered at different length scales. While order in protein crystals can be destroyed at dose values of  $10^7$  Gy [88], the **maximum tolerable dose**  $D_{\text{tol}}$  for biological materials at lower resolution may be higher especially if fixation methods which suppress secondary damage processes are employed, as for example freeze-drying or cryo-fixation. Empirical studies suggest an approximate linear relationship between  $D_{\text{tol}}$  and spatial resolution  $\Delta r$  of the form

$$D_{\text{tol}}[\text{Gy}] \approx 10^8 \cdot \Delta r[\text{nm}], \quad (1.133)$$

for frozen-hydrated samples under cryo-conditions [97]. A successful and meaningful imaging experiment with resolution  $\Delta r$  demands that the **required dose for imaging**  $D_{\text{req}}$  is below or equal the maximum tolerable dose of the specimen at that resolution. It can be expected that the required dose depends on the imaging method [99] as well as on sample properties [97]. For coherent x-ray diffraction imaging in the far field the following relation was proposed

$$D_{\text{req}} = \frac{25\mu h\nu}{\rho_m} \frac{1}{r_e^2 \lambda^2 |\rho|^2 |\Delta r^4|}, \quad (1.134)$$

with classical electron radius  $r_e$  and complex electron density  $\rho = k(\beta + i\delta)/(r_e \lambda)$  [97]. The equation states that the required dose scales with the fourth power of the requested spatial resolution. For cryo-fixation an upper limit for typical biological samples is currently estimated to be at about 10 nm [97].



## 2 Solving the phase problem

As shown in the previous sections, an x-ray propagation imaging experiment can be described by equation (1.93), namely

$$I(\mathbf{r}_\perp, z) = |\mathcal{D}_z \{O(\mathbf{r}_\perp)\}|^2. \quad (2.1)$$

The experimental situation of cone-beam illumination is accounted for by switching to an effective plane wave geometry (section 1.4). If  $\mathcal{D}_z \{O(\mathbf{r}_\perp)\}$  would be accessible by a measurement, a simple free space backpropagation  $\mathcal{D}_{-z} \{O(\mathbf{r}_\perp)\}$  would yield the complex object transmission function  $O(\mathbf{r}_\perp)$  and quantitative imaging could be implemented in a straight forward manner. However, the intensity  $|\mathcal{D}_z \{O(\mathbf{r}_\perp)\}|^2$  is the measurable physical quantity and phase information is therefore lost. This phenomenon is called **phase problem** of lensless coherent x-ray imaging or non-crystallographic phase problem [164]. A key aspect for successful imaging is to recover the lost phase information, a process also termed **phase retrieval** or **phase reconstruction**. Various methods to solve the phase problem have been proposed (see [156] for a recent review). In this chapter, relevant methods for phase retrieval in the near field are discussed. Simulations were carried out to elucidate assets and limitations of each approach and to verify the numerical implementations which were applied to experimental data recorded at varying configurations of source, detector, geometry and sample characteristics. To this end, holograms of pure phase objects were simulated with object transmission function

$$O(\mathbf{r}_\perp) = \exp[-i\varphi(\mathbf{r}_\perp)], \quad (2.2)$$

and maximum phase shift  $\varphi_{\max} = \max(\varphi(\mathbf{r}_\perp)) = \pi/4$  or  $\varphi_{\max} = \pi/20$ . Absorbing objects were simulated as homogenous objects

$$O(\mathbf{r}_\perp) = a(\mathbf{r}_\perp) \cdot \exp[-i\varphi(\mathbf{r}_\perp)], \quad (2.3)$$

$a(\mathbf{r}_\perp) = \exp[-\varphi(\mathbf{r}_\perp)/\kappa]$ . The ratio  $\kappa = \delta/\beta$  of decrement and imaginary part of the refractive index was set to  $\kappa = 10^3$ . **Fig. 2.1** shows simulated holograms for an object with  $\varphi_{\max} = \pi/4$  and  $\kappa = 10^3$  at different Fresnel numbers  $F^{10} = [80, 10, 2, 0.5]$ . Since holograms with  $\varphi_{\max} = \pi/20$  and for pure phase objects appear very similar, they are not shown explicitly. Phase retrieval methods presented in this chapter are based either on the transport-of-intensity equation (1.105), the contrast transfer functions (1.102), (iterative) use of the Fresnel diffraction operator (1.31), or a hybrid of those approaches.

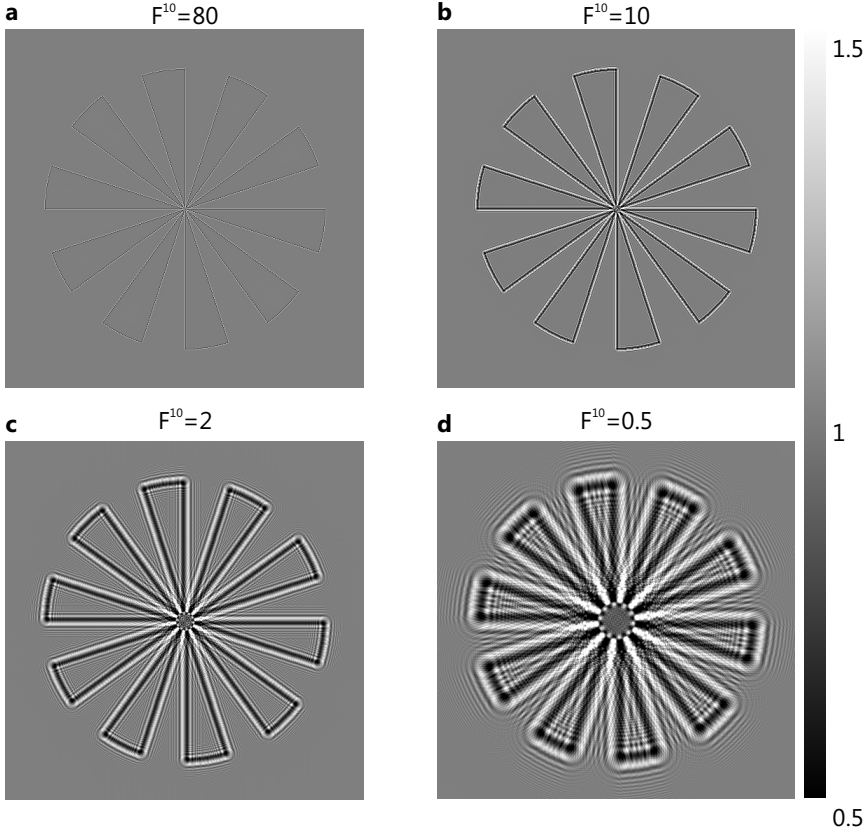


**Figure 2.1:** Simulated intensity distribution for an object with maximum phase shift  $\pi/4$  and maximal absorption of 0.8%, corresponding to  $\delta/\beta = 10^3$  at Fresnel numbers (a)  $F^{10} = 80$ , (b)  $F^{10} = 10$ , (c)  $F^{10} = 2$  and (d)  $F^{10} = 0.5$ .

## 2.1 Holographic reconstruction

The simplest form of phase reconstruction dates back to Garbors idea of in-line holography [59] for which he received the Nobel prize in 1971. The general principle is to encode phase information by intensity measurement  $I$  of the coherent interference pattern between sample wave  $S$  and a reference wave  $R$

$$I = |R + S|^2 = |R|^2 + R^*S + RS^* + |S|^2. \quad (2.4)$$

Treating the measured intensity  $I$  as a pure absorption object transmission function (either numerically or for visible light by recording  $I$  with a photographic

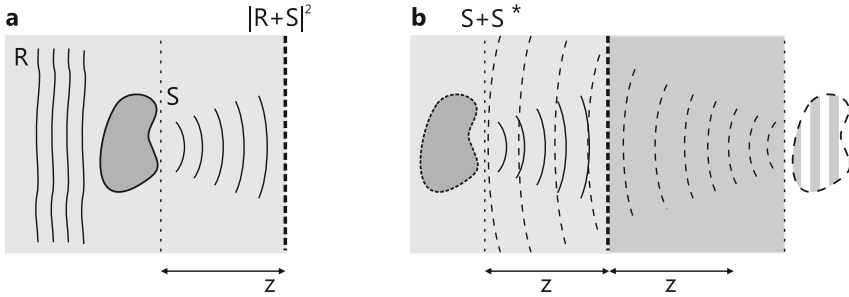


**Figure 2.2:** (a) In-line holographic recording. The interference pattern of reference wave  $R$  and sample wave  $S$  is recorded. (b) Holographic reconstruction. The complex sample wave  $S$  appears in focus while it is disturbed by the defocused twin image corresponding to the conjugate wave  $S^*$ .

plate), a subsequent illumination with the same reference wave yields a wave field  $H$  proportional to

$$H \propto R|R|^2 + |R|^2S + R^2S^* + R|S|^2. \quad (2.5)$$

Each of the four terms in  $H$  represent a beam emerging from the hologram. The second term is proportional to the sample wave  $S$ . The first and last term are modified versions of the reference wave and the third term is a beam that corresponds to the conjugate version of the sample wave  $S^*$ . If the experiment is designed in a way that reference and object beam form significantly different angles with the plane where the hologram is recorded, it is possible to separate the virtual, real and reference waves. This enables the reconstruction of the wave field scattered by the sample as if the sample was still present.

Even though reference beam holography was demonstrated for x-rays [57], x-ray propagation imaging corresponds to the original scheme of **in-line holography** as proposed by Gabor [59] depicted in **Fig. 2.2**. It is assumed that the scattered wave is produced by the reference wave itself, provided the sample is weakly interacting with object transmission function  $O(\mathbf{r}_\perp, 0) \simeq 1 + \delta O(\mathbf{r}_\perp, 0)$  and  $|\delta O(\mathbf{r}_\perp, 0)| \ll 1$ . We assume a plane wave illumination or equivalently demand that approximation (1.4) for empty beam correction holds. The recorded intensity then reads

$$\begin{aligned} I(\mathbf{r}_\perp, z) &= |\mathcal{D}_z \{O(\mathbf{r}_\perp, 0)\}|^2 \simeq |\mathcal{D}_z \{1 + \delta O(\mathbf{r}_\perp, 0)\}|^2 \\ &\simeq 1 + \delta O(\mathbf{r}_\perp, z) + \delta O^*(\mathbf{r}_\perp, z) + |\delta O(\mathbf{r}_\perp, z)|^2 \\ &\simeq 1 + \delta O(\mathbf{r}_\perp, z) + \delta O^*(\mathbf{r}_\perp, z). \end{aligned} \quad (2.6)$$

We have neglected  $|\delta O(\mathbf{r}_\perp, z)|^2$  due to  $|\delta O(\mathbf{r}_\perp, 0)| \ll 1$ . Historically,  $I(\mathbf{r}_\perp, z)$  was recorded on a photographic film for optical light and the reconstruction was performed by illumination of the developed film with the same reference wave. Here

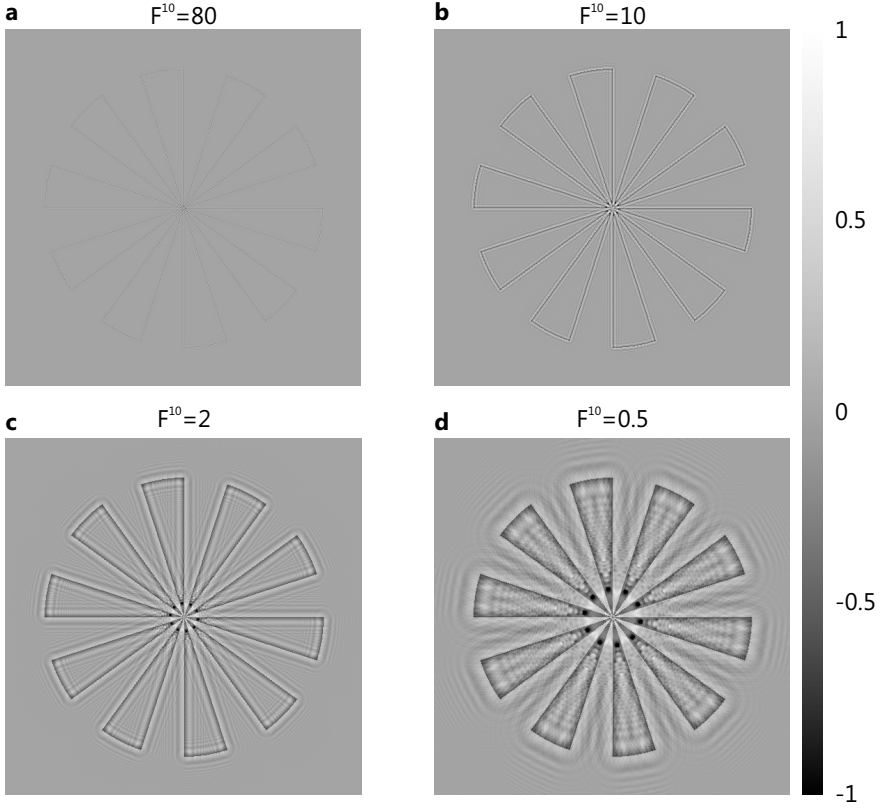


**Figure 2.3:** Phase distributions obtained by holographic reconstructions of simulated holograms (**Fig. 2.1**) for an object with maximum phase shift  $\pi/4$  and maximal absorption of 0.8%, corresponding to  $\delta/\beta = 10^3$ . At large Fresnel numbers the small propagation distance  $z$  yields a twin images  $\delta O^*(\mathbf{r}_\perp, 2z)$  similar to the hologram which is dominating the reconstruction. At smaller Fresnel numbers (larger  $z$ ) the twin image gets more and more out of focus and the reconstruction resembles the object more closely.

we have  $I(\mathbf{r}_\perp, z)$  as a discrete representation recorded by x-ray detectors. Consequently, **holographic reconstruction** is implemented numerically by simple back-propagation of  $I(\mathbf{r}_\perp, z)$  using the Fresnel diffraction operator  $\mathcal{D}_z^{\mathcal{F}}$

$$\mathcal{D}_{-z}^{\mathcal{F}}[I(\mathbf{r}_\perp, z)] \simeq \exp(-ikz) + \delta O(\mathbf{r}_\perp, 0) + \mathcal{D}_{-z}^{\mathcal{F}}[\delta O^*(\mathbf{r}_\perp, z)]. \quad (2.7)$$

While the first term is constant in lateral coordinates, the second term corresponds to a reconstruction of the object transmission function. To interpret the third term, we note that the complex conjugate wave field of an incident wave field  $f(\mathbf{r}_\perp)$  propagated over a distance  $z$  is identical to the wave field obtained by propagation

of the complex conjugate incident field  $f^*(\mathbf{r}_\perp)$  over the negative distance  $-z$  (see section A.2)

$$\mathcal{D}_z^{\mathcal{F}}[f(\mathbf{r}_\perp)]^* = \mathcal{D}_{-z}^{\mathcal{F}}[f^*(\mathbf{r}_\perp)]. \quad (2.8)$$

The third term in (2.7) can then be written as

$$\begin{aligned} \mathcal{D}_{-z}^{\mathcal{F}}[\delta O^*(\mathbf{r}_\perp, z)] &= \mathcal{D}_{-z}^{\mathcal{F}}[\mathcal{D}_z^{\mathcal{F}}[\delta O(\mathbf{r}_\perp, 0)]^*] \\ &= \mathcal{D}_z^{\mathcal{F}}[\mathcal{D}_z^{\mathcal{F}}[\delta O(\mathbf{r}_\perp, 0)]]^* \\ &= \mathcal{D}_{2z}^{\mathcal{F}}[\delta O(\mathbf{r}_\perp, 0)]^* \end{aligned} \quad (2.9)$$

$$= \delta O^*(\mathbf{r}_\perp, 2z) \quad (2.10)$$

and the reconstructed wave field reads

$$\mathcal{D}_{-z}^{\mathcal{F}}[I(\mathbf{r}_\perp, z)] \simeq \exp(-ikz) + \delta O(\mathbf{r}_\perp, 0) + \delta O^*(\mathbf{r}_\perp, 2z). \quad (2.11)$$

The reconstruction of the focussed image  $\delta O(\mathbf{r}_\perp, 0)$  is thus disturbed by  $\delta O^*(\mathbf{r}_\perp, 2z)$ . The so called twin image constitutes the complex conjugate of the wave field which emerges when propagating the object transmission function over a (defocus) distance  $2z$ . This phenomenon, as illustrated in **Fig 2.2 b**, is known as the **twin image problem** of in-line holography. Especially for small propagation distances  $z$  the twin image  $\delta O^*(\mathbf{r}_\perp, 2z)$  is similar to the recorded hologram  $|1 + \delta O(\mathbf{r}_\perp, z)|^2$  and dominates the reconstruction, as shown in **Fig. 2.3** for a simulated object with maximum phase shift  $\pi/4$  and maximal absorption of 0.8%, corresponding to  $\delta/\beta = 10^3$ . For larger propagation distances  $z$  (small Fresnel numbers), the twin image gets more and more defocused and the reconstruction resembles the object more closely, however still severely disturbed.

## 2.2 Transport-of-intensity equation

The transport-of-intensity equation (TIE, equation 1.105) relates the change of intensity along the optical axis to intensity and phase of the wave field in a plane perpendicular to the optical axis. In the absence of intensity zeroes, the TIE has a unique solution for the phase up to a constant additive number [82]. TIE-based phase retrieval [198, 199] was one of the first methods suggested and applied for x-ray phase-contrast imaging [218, 81, 165, 157, 75, 84]. Compatibility with polychromatic x-rays [218, 171] renders TIE-based methods particularly interesting for cone-beam imaging applications with microfocus x-ray sources [139, 138]. Given a pure phase object, the TIE can be solved for the phase in a straight forward manner [22] while handling of absorption requires the presence of a homogenous object [163, 79, 139], the assumption of weak absorption [71, 70, 79] or measurements in two different planes along the optical axis [84, 157, 165].

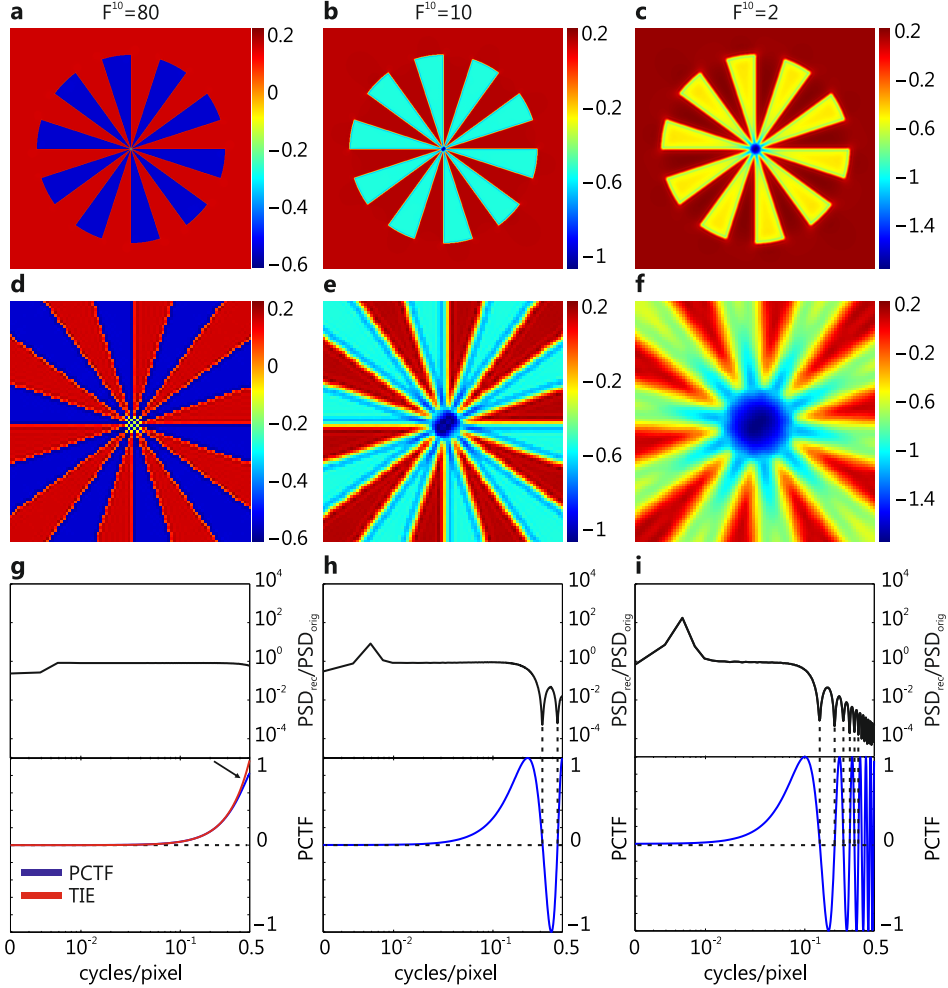


**Figure 2.4:** (a-c) Phase reconstructions based on the pure phase TIE of simulated intensities for a pure phase object with maximum phase shift  $\pi/4$  at different Fresnel numbers  $F^{10} = [80, 10, 2]$ . (d-f) Magnified view (by a factor of six) of the central part of the images shown in (a-c). (g-i) Ratio  $\text{PSD}_{\text{rec}}/\text{PSD}_{\text{orig}}$  (black) of the azimuthally averaged power spectral densities (PSD) of reconstructed and original phase distribution, along with the corresponding phase contrast transfer functions (PCTF, blue). For large Fresnel numbers, the reconstruction is accurate up to the point where phase contrast transfer assumed for the TIE (red) deviates significantly from the PCTF. At smaller Fresnel numbers reconstructions are disturbed by zero crossings of the PCTF.

### 2.2.1 Pure phase object

For a pure phase object with  $I(\mathbf{r}_\perp, 0) = |O(\mathbf{r}_\perp)| = 1$  equation (1.109) simplifies to the **pure phase TIE**

$$I(\mathbf{r}_\perp, z) \simeq 1 - \frac{z}{k} \nabla_\perp^2 \varphi(\mathbf{r}_\perp), \quad (2.12)$$

with  $\varphi(\mathbf{r}_\perp) = \varphi(O(\mathbf{r}_\perp))$ . Here we switched variables  $\Delta z \rightarrow z$  and  $z \rightarrow 0$  without loss of generality. For comparison, the contrast transfer function (1.102) of a pure phase object with  $\tilde{\mu}(\nu_x, \nu_y) = 0$  reads

$$\tilde{I}(\nu_x, \nu_y, z) \simeq \delta_D(\nu_x, \nu_y) + 2\tilde{\varphi}(\nu_x, \nu_y)\chi(\nu, z), \quad (2.13)$$

when the assumption of a small propagation distance is taken into account by approximating [139, 171]

$$\sin[\chi(\nu, z)] \approx \chi(\nu, z). \quad (2.14)$$

Fourier backtransform of equation (2.13) then consistently yields the pure phase object TIE (2.12) as can be seen in **Fig. 1.4**. If  $I(\mathbf{r}_\perp, z)$  is known, the phase distribution can be calculated by

$$\varphi(\mathbf{r}_\perp) = -\frac{k}{z} \nabla_\perp^{-2} (I(\mathbf{r}_\perp, z) - 1). \quad (2.15)$$

By use of the Fourier representation for the inverse Laplacian  $\nabla_\perp^{-2}$  [164]

$$\nabla_\perp^{-2} = -\mathcal{F}^{-1} \left[ \frac{1}{k_x^2 + k_y^2} \mathcal{F} \right] \quad (2.16)$$

the following solution is obtained [22]

$$\varphi(\mathbf{r}_\perp) = -\frac{k}{z} \mathcal{F}^{-1} \left[ \frac{\mathcal{F}[I(\mathbf{r}_\perp, z) - 1]}{\mathbf{k}_\perp^2} \right], \quad (2.17)$$

which can be implemented by means of discrete Fourier transforms. The original algorithm suggested by Bronnikov [22] was developed as an approach to combine phase retrieval and tomography. Since filtering for phase retrieval and filtering for tomography (see chapter 3, equation (3.18)) both take place in Fourier space, one can save two Fourier transforms and merge the operations into one step. This is possible for all phase retrieval algorithms based on Fourier transforms [24, 123] but for data analysis it is typically more convenient to separate these two steps. Thus, equation (2.17) can be considered the phase retrieval part of the original algorithm [22]. To illustrate the dependence on the discrete Fresnel number (1.54)  $F^1 = \frac{\Delta x^2}{\lambda z}$  we assume again  $\Delta x = \Delta y$ ,  $N_x = N_y$  and introduce the dimensionless reciprocal variable  $\mathbf{q}_\perp = \Delta x \cdot \mathbf{k}_\perp$ . Then, equation (2.17) can be written as

$$\varphi(\mathbf{r}_\perp) = -2\pi F^1 \mathcal{F} \left[ \frac{\mathcal{F}[I(\mathbf{r}_\perp, z) - 1]}{\mathbf{q}_\perp^2} \right]. \quad (2.18)$$

**Fig. 2.4** shows phase reconstructions based on equation (2.18) for simulated intensity distributions of a pure phase object with maximum phase shift  $\pi/4$  at different discrete Fresnel numbers  $F^{10} = [80, 10, 2]$ . For a large Fresnel number  $F^{10} = 80$  corresponding to small propagation distances, the reconstructed phase agrees well with the original phase of the simulated object. Accurate reconstruction is also evidenced by the azimuthally averaged power spectral density (PSD) which is nearly identical to the original (**g**). Only at higher spatial frequencies the approximation (2.14)  $\sin[\chi(\nu, z)] \approx \chi(\nu, z)$  fails and small deviations in the PSD are visible (arrow in (**g**)). For smaller Fresnel numbers the intensity gets more and more holographic (compare **Fig. 2.1 b,c**), the finite difference approximation for  $\partial I(\mathbf{r}_\perp z)/\partial z$  breaks down and the reconstruction gets blurred and inaccurate (**b,c**). A comparison of the corresponding PSD with the original reveals that zeroes in the phase contrast transfer function (PCTF) disturb the reconstruction (**h,i**).

### 2.2.2 Treatment of absorption

While the pure phase TIE (2.12) delivers accurate reconstructions at large Fresnel numbers it fails for non-zero absorption. The Fourier filter (2.16) exhibits large values for low spatial frequencies  $\mathbf{k}_\perp$ . For large Fresnel numbers mainly low frequencies of the amplitude are transferred corresponding to the amplitude transfer function (1.4). As a consequence, the reconstruction is severely disturbed by low frequency artifacts as can be seen in **Fig. 2.5** for an object with maximum phase shift  $\pi/4$  and maximum absorption of 0.8%, corresponding to  $\delta/\beta = 10^3$ . However, for slowly varying absorption the weak object TIE (1.109) is valid. If  $I(\mathbf{r}_\perp, 0)$  is obtained in a second measurement the phase can be calculated by [23]

$$\varphi(\mathbf{r}_\perp) = -2\pi F^1 \mathcal{F} \left[ \frac{\mathcal{F}[I(\mathbf{r}_\perp, z)/I(\mathbf{r}_\perp, 0) - 1]}{\mathbf{q}_\perp^2} \right]. \quad (2.19)$$

The assumption of slowly varying absorption can further be discarded by an alternative formulation of the TIE (1.105) due to Paganin and Nugent [165, 164]. On the assumption, that a scalar potential  $\xi(\mathbf{r}_\perp)$  with

$$I(\mathbf{r}_\perp, 0) \nabla_\perp \varphi(\mathbf{r}_\perp) \approx \nabla_\perp \xi(\mathbf{r}_\perp) \quad (2.20)$$

exists, the following expression for the phase can be obtained

$$\begin{aligned} \varphi(\mathbf{r}_\perp) &= -k \nabla_\perp^{-2} \left[ \nabla_\perp \cdot \left( \frac{1}{I(\mathbf{r}_\perp, 0)} \nabla_\perp \left[ \nabla_\perp^{-2} \frac{\partial}{\partial z} I(\mathbf{r}_\perp, 0) \right] \right) \right] \\ &\simeq -k \nabla_\perp^{-2} \left[ \nabla_\perp \cdot \left( \frac{1}{I(\mathbf{r}_\perp, 0)} \nabla_\perp \left[ \nabla_\perp^{-2} \frac{I(\mathbf{r}_\perp, z) - I(\mathbf{r}_\perp, 0)}{z} \right] \right) \right]. \end{aligned} \quad (2.21)$$

The validity of approximation (2.20) related to the existence of phase vortices is discussed in detail in [165]. Note that for slowly varying absorption,  $I(\mathbf{r}_\perp, 0)$  may be moved inside of the gradient and inverse Laplacian. With  $\nabla_\perp \cdot \nabla_\perp = \nabla_\perp^2$  one inverse Laplacian is cancelled out and the equation gets identical to the weak



object TIE (1.109) when variables are switched ( $\Delta z \rightarrow z$  and  $z \rightarrow 0$ ). Equation (2.21) allows to calculate the phase of a mixed phase and amplitude object based on two separate intensity measurements. However, a second measurement of the contact image  $I(\mathbf{r}_\perp, 0)$  is experimentally challenging for cone-beam geometry, as it requires to bring the object very close to the x-ray source or to the detector, in order to achieve a vanishing effective propagation distance  $z_{\text{eff}} = z_1 z_2 / (z_1 + z_2)$ . Both options may be impossible due to space constraints or the fact that large magnification is needed to achieve sufficient sampling. Therefore, it is desirable to reconstruct the phase distribution approximately from a single measurement of an absorbing object. To this end, the **modified Bronnikov algorithm** (MBA)

$$\varphi(\mathbf{r}_\perp) \simeq -2\pi F^1 \mathcal{F}^{-1} \left[ \frac{\mathcal{F}[I(\mathbf{r}_\perp, z) - 1]}{\mathbf{q}_\perp^2 + \alpha} \right] \quad (2.22)$$

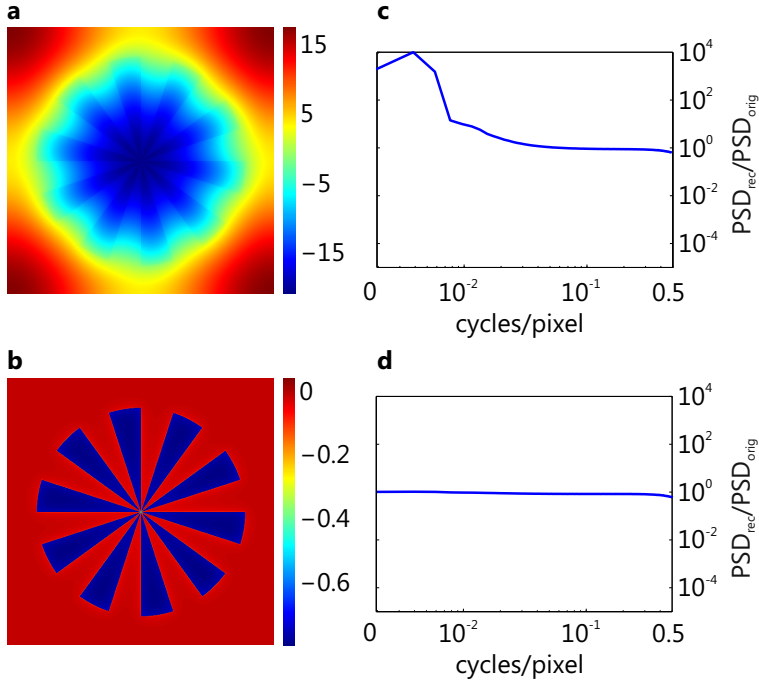


**Figure 2.5:** (a) Phase reconstruction based on the pure phase TIE of a simulated hologram at Fresnel number  $F^{10} = 80$  (Fig. 2.1 a) for an object with maximum phase shift  $\pi/4$  and maximal absorption of 0.8%, corresponding to  $\delta/\beta = 10^3$ . The reconstruction exhibits strong low frequency artifacts. (b) Phase reconstruction using the modified Bronnikov algorithm with regularisation parameter  $\alpha = 4\pi F^1 \beta/\delta$ , circumventing the low frequency artifact. (c,d) Ratio of the azimuthally averaged power spectral densities (PSD) of the reconstructed and original phase distribution. (c) Introduction and (d) suppression of low frequency artifacts is evident.

with a rather arbitrary regularization parameter  $\alpha$  was suggested [70, 71] as an extension of the pure phase object algorithm (2.17). The parameter  $\alpha$  substitutes the singularity at  $\mathbf{q}_\perp = \mathbf{0}$  with the value  $1/\alpha$  and stabilized the reconstruction at low spatial frequencies. For  $\alpha = 0$  the algorithm is identical to the pure phase object case (2.17), while for  $\alpha \rightarrow \infty$  the Fourier filter effectively vanishes and the recovered phase is identical to the measured intensity distribution (apart from scaling). Therefore, the regularisation parameter has to be chosen semi-empirically [70] by evaluating the quality of the phase reconstruction. Another approach is based on the assumption of a homogenous object composed of a **single material** with  $\kappa = \delta/\beta$ , yielding the exact expression [163]

$$\varphi(\mathbf{r}_\perp) = \frac{\kappa}{2} \cdot \ln \left( \frac{4\pi F^1 \beta}{\delta} \mathcal{F}^{-1} \left[ \frac{\mathcal{F}[I(\mathbf{r}_\perp, z)]}{\mathbf{q}_\perp^2 + 4\pi F^1/\kappa} \right] \right). \quad (2.23)$$

Note the similar structure of the single-material approach (SMO) compared to the MBA (2.22). Especially the Fourier filter is identical to the SMO filter for  $\alpha = 4\pi F^1/\kappa$ . Hence, both algorithms typically lead to similar results [24] with differences depending on the compositions of the object [18]. Most importantly, for both algorithms the assumption of a homogenous or semi-homogenous object ( $\delta \propto \beta$  with varying density of the material) should be met. Otherwise both algorithms produce artifacts such as blurring [18]. The similarity between SMO and MBA motivates the choice of  $\alpha = 4\pi F^1/\kappa$  for the latter. Indeed, another algorithm for homogenous objects based on the contrast transfer function simplifies to the MBA formula in the case of a weakly absorbing and slowly varying object transmission function [79], again with  $\alpha = 4\pi F^1/\kappa$ . Applying the MBA algorithm with this regularisation parameter successfully removes the low frequency artifacts for the simulated object as shown in **Fig. 2.5 c**. Even though  $\alpha = 4\pi F^1/\kappa$  is a good starting point, for experimental data the regularisation parameter is chosen by means of visual inspection since homogeneity is not strictly met and other experimental imperfections have to be regularized as well. Because of the restrictive validity conditions of low absorbing or semi-homogenous objects, SMO and MBA may result in blurred reconstructions for actual inhomogenous objects with significant absorption. As an alternative approach the **Bronnikov aided correction** (BAC) was suggested [219], based on the weak object TIE (1.109), solved for the intensity  $I(\mathbf{r}_\perp, 0)$  in the sample plane

$$I(\mathbf{r}_\perp, 0) = \frac{I(\mathbf{r}_\perp, z)}{1 - \frac{z}{k} \nabla_\perp^2 \tilde{\varphi}(\mathbf{r}_\perp)}. \quad (2.24)$$

An approximation of the phase distribution  $\tilde{\varphi}(\mathbf{r}_\perp)$  is obtained by applying the MBA (2.22). Then, the approximated phase  $\tilde{\varphi}(\mathbf{r}_\perp)$  is used to calculate the intensity of an hypothetical pure phase object

$$C(\mathbf{r}_\perp) = 1 - \gamma \nabla_\perp^2 \tilde{\varphi}(\mathbf{r}_\perp) \quad (2.25)$$

and to reconstruct the absorption signal

$$I(\mathbf{r}_\perp, 0) = \frac{I(\mathbf{r}_\perp, z)}{C(\mathbf{r}_\perp)}, \quad (2.26)$$

where  $z/k$  was replaced by an  $\alpha$ -dependent control parameter  $\gamma$  [219]. Both parameters  $\alpha$  and  $\gamma$  are chosen based on visual inspection. The BAC parameter  $\gamma$  is selected in a way that the correction signal  $C(\mathbf{r}_\perp)$  compensates the edge-enhancement in  $I(\mathbf{r}_\perp, z)$ . Reconstruction of objects with non-negligible absorption has proven to show more details than MBA phase reconstruction [219]. Note that the reconstructed absorption signal is not equal to the measurements of classical absorption radiography since the BAC implicitly utilized  $\delta \propto \beta$  and the complementary behaviour of absorption and phase contrast transfer of Fresnel diffraction (1.102).

## 2.3 Contrast transfer function

Phase retrieval based on the TIE is limited to the edge-detection regime with small propagation distances, i.e. large Fresnel numbers  $F^{10} \gg 1$ , as demonstrated in **Fig. 2.4**. The validity of the contrast transfer function (1.102) is not subject to this limitation. Instead, it is based on linearization of the object transmission function justified for weak absorption and slowly varying phase [72]. To fill up information not transmitted by the transfer functions at distinct spatial frequencies, a through-focus variation method developed for electron transmission microscopy [36] was adapted by Cloetens et al. [34] for the case of hard x-ray imaging. By recording several holograms at suitable different Fresnel numbers [222] zero crossings of the PCTF are effectively circumvented and quantitative reconstructions in 3D are achievable [35, 33]. For the case of pure phase or homogenous objects, single-distance CTF methods were proposed [207, 77, 80].

### 2.3.1 Pure phase object

For the sake of simplicity, we restrict the following derivation to one dimension, with the two-dimensional case being a trivial generalisation. The contrast transfer function (1.102) for a pure phase object, i.e.  $\mu(x) = 0$ , reads

$$\tilde{I}(\nu, z) \simeq \delta_D(\nu) + 2\tilde{\varphi}(\pi\lambda z\nu^2) \sin[\pi\lambda z\nu^2]. \quad (2.27)$$

zeroes in the PCTF due to the sinusoidal term motivate intensity recordings at several planes along the optical axis to fill up the Fourier space for all spatial frequencies. Reconstruction of the phase  $\varphi(\nu)$  from a set of  $N$  intensity distributions measured at propagation distances  $z_m$  with  $m = 1 \dots N$  is then performed by least square minimization of the difference between measured intensities  $\tilde{I}^{(\text{exp})}(\nu, z_m)$  and intensities  $\tilde{I}^{(\text{approx})}(\nu, z_m)$  corresponding to  $\tilde{\varphi}(\nu)$  [36, 34]. We define the cost function in Fourier space

$$S_c = \frac{1}{N} \sum_{m=1}^N \int d\nu |\tilde{I}^{(\text{exp})}(\nu, z_m) - \tilde{I}^{(\text{approx})}(\nu, z_m)|^2 \quad (2.28)$$

$$= \frac{1}{N} \sum_{m=1}^N \int d\nu |\tilde{I}^{(\text{exp})}(\nu, z_m) - 2\tilde{\varphi}(\pi\lambda z\nu^2) \sin[\pi\lambda z\nu^2] - \delta_D(\nu)|^2 \quad (2.29)$$

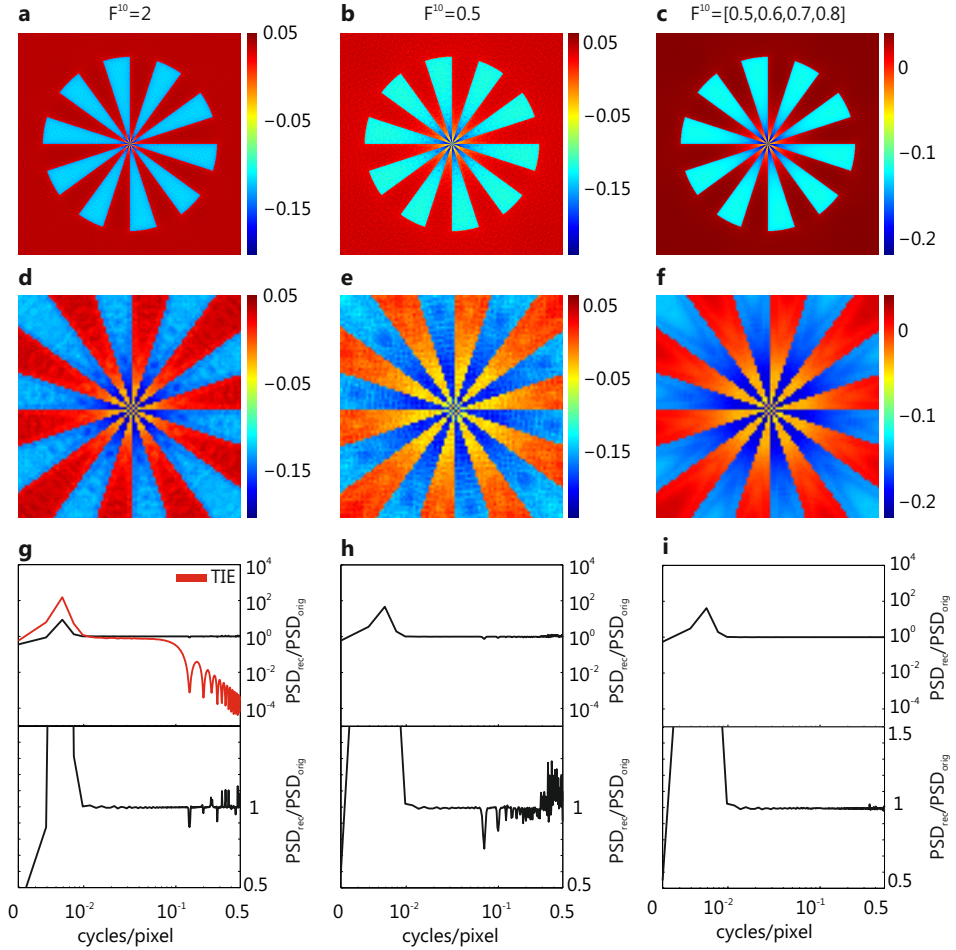


**Figure 2.6:** Phase reconstructions based on the CTF approach of simulated holograms for a pure phase object with maximum phase shift  $\pi/20$  at Fresnel numbers (a)  $F^{10} = 2$ , (b)  $F^{10} = 0.5$  and (c)  $F^{10} = [0.5, 0.6, 0.7, 0.8]$ . (d-f) Magnified view (by a factor of six) of the central part of the images shown in (a-c). (g-i) Ratio  $\text{PSD}_{\text{rec}}/\text{PSD}_{\text{orig}}$  of the azimuthally averaged power spectral densities (PSD) of reconstructed and original phase distribution along (only in g) with the corresponding ratio for the TIE-based reconstruction (Fig. 2.4 c,f,i). The ratio is shown on a logarithmic scale (top) and on a linear scale (bottom) with adjusted ordinate scaling. Compared to the TIE reconstruction, zero crossings of the phase contrast transfer function produce only minor deviations from the original PSD visible as artifacts in d,e. By using four distances, high frequency artifacts are removed (f) yielding a PSD in good agreement with the original, except for the low frequencies.

and calculate the minimum  $\partial S_c / \partial \tilde{\varphi} = 0$ , yielding

$$\tilde{\varphi}(\nu) = \frac{\sum_{m=1}^N \tilde{I}^{(\text{exp})}(\nu, z_m) \sin[\pi \lambda z \nu^2]}{\sum_{m=1}^N 2 \sin^2[\pi \lambda z \nu^2]}. \quad (2.30)$$

The phase distribution can thus be obtained from a sum of measured intensity distributions filtered in Fourier space by contrast transfer related sinusoidal terms. In two dimensions we get

$$\varphi(\mathbf{r}_\perp) = \mathcal{F}^{-1} \left[ \frac{\sum_{m=1}^N \mathcal{F}[I^{(\text{exp})}(\mathbf{r}_\perp, z_m)] \cdot \sin[\mathbf{q}_\perp^2 / F^1 4\pi]}{\sum_{m=1}^N 2 \sin^2[\mathbf{q}_\perp^2 / F^1 4\pi]} \right]. \quad (2.31)$$

The denominator is zero at  $\mathbf{q}_\perp = \mathbf{0}$  for all  $F^1$  and can also vanish for non-zero spatial frequencies [222]. To account for this, for residual absorption and for experimental imperfections, a frequency dependent regularisation parameter  $\alpha(\mathbf{q}_\perp)$

$$\alpha(\mathbf{q}_\perp) = \alpha_1 \cdot f(\mathbf{q}_\perp) + \alpha_2 \cdot (1 - f(\mathbf{q}_\perp)) \quad (2.32)$$

with

$$f(\mathbf{q}_\perp) = (1 - \text{erf}[(\mathbf{q}_\perp^2 - q_{\text{cut}})/\sigma_\alpha]) / 2 \quad (2.33)$$

is added [222]

$$\varphi(\mathbf{r}_\perp) = \mathcal{F}^{-1} \left[ \frac{\sum_{m=1}^N \mathcal{F}[I^{(\text{exp})}(\mathbf{r}_\perp, z_m)] \cdot \sin[\mathbf{q}_\perp^2 / F^1 4\pi]}{\sum_{m=1}^N 2 \sin^2[\mathbf{q}_\perp^2 / F^1 4\pi] + \alpha(\mathbf{q}_\perp)} \right]. \quad (2.34)$$

For a single distance equation (2.31) simplifies to

$$\varphi(\mathbf{r}_\perp) = \mathcal{F}^{-1} \left[ \frac{F[I^{(\text{exp})}(\mathbf{r}_\perp, z_m)] \cdot \sin[\mathbf{q}_\perp^2 / F^1 4\pi]}{2 \sin^2[\mathbf{q}_\perp^2 / F^1 4\pi] + \alpha(\mathbf{q}_\perp)} \right], \quad (2.35)$$

in agreement to what has been derived in [77, 80]. **Fig. 2.6 a,b** shows phase reconstructions based on a single simulated hologram of a pure phase object with maximum phase shift  $\varphi_{\text{max}} = \pi/20$  at respective Fresnel number  $F^{10} = 2$  ( $\alpha_1 = 10^{-10}$ ,  $\alpha_2 = 10^{-4}$ ) and  $F^{10} = 0.5$  ( $\alpha_1 = 10^{-10}$ ,  $\alpha_2 = 10^{-3}$ ). Compared to the TIE reconstruction at  $F^{10} = 2$  (**Fig. 2.4 c,f,i**), zero crossings of the PTCF produce only minor deviations from the original PSD, even for a smaller Fresnel number  $F^{10} = 0.5$  (**b**). However, artifacts associated with deviations in Fourier space are visible in magnified views of the reconstructed phase maps (**d,e**). Application of multi-distance phase retrieval ( $\alpha_1 = 10^{-10}$ ,  $\alpha_2 = 10^{-3}$ ) expressed by equation (2.31) for simulated holograms at  $F^{10} = [0.5; 0.6; 0.7; 0.8]$  effectively removes these artifacts (**c,f**) yielding a PSD in good agreement with the original (**i**), expect for low frequencies for which phase contrast transfer vanishes. However, the CTF approach relies on the assumption of slowly varying phase. By increasing the maximum phase shift of the simulated object to  $\varphi_{\text{max}} = \pi/4$  additional artifacts are introduced as shown in **Fig 2.7**.

### 2.3.2 Treatment of absorption

Small absorption effects can be treated by appropriate choice of the low frequency regularisation parameter  $\alpha_1$  in equation (2.32). However, similar to the TIE case, assumption of homogeneity can advantageously be incorporated in the reconstruction process. Consider the contrast transfer function (1.102) for an object with slowly varying phase and weak absorption

$$\tilde{I}(\nu, z) \simeq \delta_{\text{D}}(\nu) + 2\tilde{\varphi}(\pi\lambda z\nu^2) \sin[\pi\lambda z\nu^2] - 2\tilde{\mu} \cos[\pi\lambda z\nu^2]. \quad (2.36)$$

For a homogenous object with  $\kappa = \delta/\beta$  we get

$$\tilde{I}(\nu, z) \simeq \delta_{\text{D}}(\nu) + 2\tilde{\varphi}(\pi\lambda z\nu^2) \sin[\pi\lambda z\nu^2] + \frac{2}{\kappa}\tilde{\varphi} \cos[\pi\lambda z\nu^2] \quad (2.37)$$

$$\simeq \delta_{\text{D}}(\nu) + 2\tilde{\varphi}(\pi\lambda z\nu^2) \left( \sin[\pi\lambda z\nu^2] + \frac{1}{\kappa} \cos[\pi\lambda z\nu^2] \right). \quad (2.38)$$

Consequently,  $\partial S_c/\partial\tilde{\varphi} = 0$  yields [31]

$$\varphi(\mathbf{r}_{\perp}) = \mathcal{F}^{-1} \left[ \frac{\sum_{m=1}^N \mathcal{F}[I^{(\text{exp})}(\mathbf{r}_{\perp}, z_m)] \cdot \left( \sin[\mathbf{q}_{\perp}^2/F^1 4\pi] + \frac{1}{\kappa} \cos[\mathbf{q}_{\perp}^2/F^1 4\pi] \right)}{\sum_{m=1}^N 2 \left( \sin[\mathbf{q}_{\perp}^2/F^1 4\pi] + \frac{1}{\kappa} \cos[\mathbf{q}_{\perp}^2/F^1 4\pi] \right)^2 + \alpha(\mathbf{q}_{\perp})} \right]. \quad (2.39)$$

For a single distance this simplifies to

$$\varphi(\mathbf{r}_{\perp}) = \mathcal{F}^{-1} \left[ \frac{\mathcal{F}[I^{(\text{exp})}(\mathbf{r}_{\perp}, z_m)]}{2 \left( \sin[\mathbf{q}_{\perp}^2/F^1 4\pi] + \frac{1}{\kappa} \cos[\mathbf{q}_{\perp}^2/F^1 4\pi] \right) + \alpha(\mathbf{q}_{\perp})} \right], \quad (2.40)$$

in agreement to what has been derived in [207].

## 2.4 Iterative algorithms

The approaches above using TIE and CTF are based on linearization of Fresnel diffraction. Hence, they are limited to the validity range of the respective approximations, i.e. small propagation distances for the TIE and weak absorption as well as slowly varying phase for the CTF. To account for the full nonlinear process of image formation, iterative algorithms are particularly well suited. Reconstruction by iterated projections was introduced by Gerchberg and Saxton (GS) in the context of electron microscopy [60]. Extensions of the original scheme, known as the error-reduction (ER) and hybrid input-output (HIO) algorithms, were proposed by Fienup [53]. The Gerchberg-Saxton-Fienup (GSF) type of algorithms were developed for the case where diffraction pattern and image plane are related via a Fourier transform. Therefore, they found application in the field of x-ray coherent diffraction imaging (CDI) [141]. For x-ray propagation imaging in the holographic regime they can be applied by replacing Fourier transforms by Fresnel diffraction operators [76, 63]. A wide variety of iterative projection algorithms exists to date (see e.g. [46, 134] for an overview). Another approach to solve the inverse problem of Fresnel diffraction are non-linear regularisation methods [191, 41, 94].

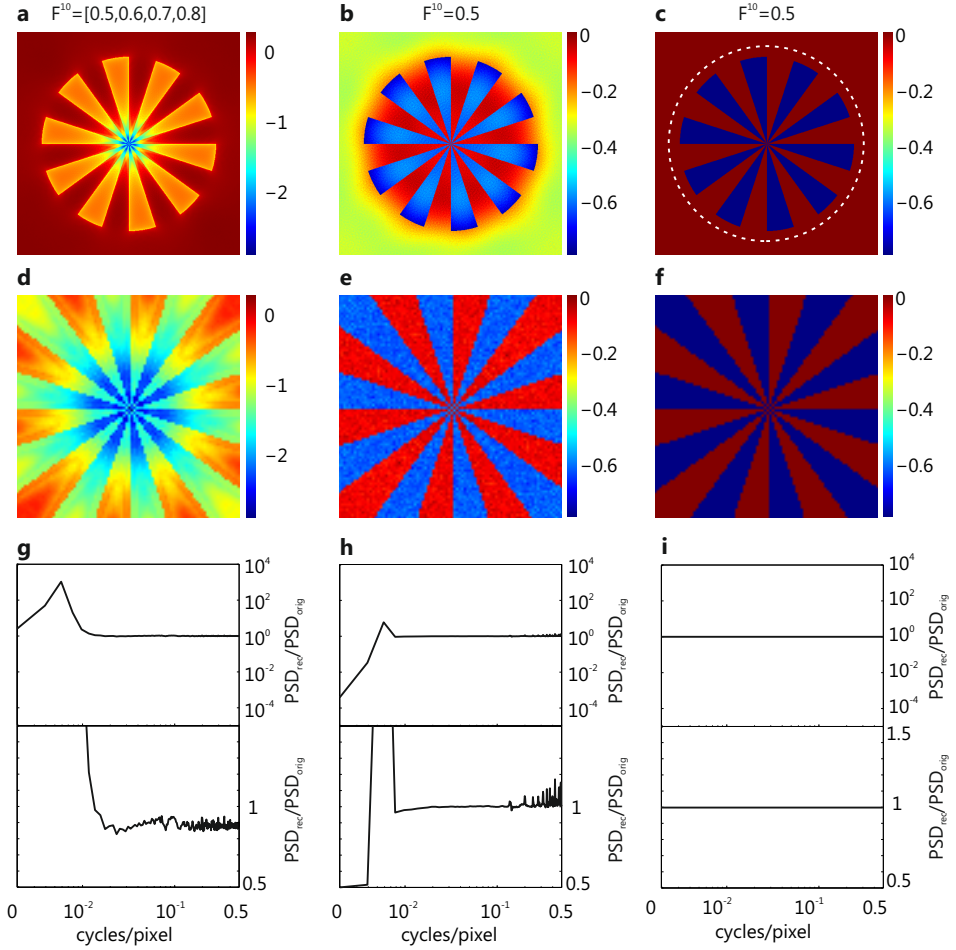


**Figure 2.7:** Phase reconstructions of a simulated hologram for a pure phase object with maximum phase shift  $\pi/4$  at Fresnel number  $F^{10} = 0.5$ . (a) Reconstruction based on the CTF approach. (b) GS reconstruction obtained from  $2 \cdot 10^4$  iterations. (c) Reconstruction based on a modified HIO scheme. The support is indicated by the dashed circle. (d-f) Magnified view (by a factor of six) of the central part of the images shown in (a-c). (g-i) Ratio  $\text{PSD}_{\text{rec}}/\text{PSD}_{\text{orig}}$  of the azimuthally averaged power spectral densities (PSD) of reconstructed and phase distribution. The ratio is shown on a logarithmic scale (top) and on a linear scale (bottom) with adjusted ordinate scaling. Due to violation of the slowly varying phase assumption, the CTF method introduces artifacts. The modified HIO reconstruction recovers the phase distribution at all spatial frequencies to a very high accuracy.

### 2.4.1 Gerchberg-Saxton-Fienup type algorithms

The following algorithms can be interpreted as iterative maps onto constraint sets [46]. We introduce the space  $\mathcal{E}$  of discrete representations of two-dimensional complex wave fields  $\psi := \psi(n_x, n_y) := \psi(n_x \Delta x, n_y \Delta y)$ , with sampling interval lengths  $\Delta x, \Delta y$ , number of pixels  $N_x, N_y$  and grid indices  $n_{x/y} = [0, N_{x/y} - 1] \in \mathbf{N}_0$ . A constraint set is a subspace  $\mathcal{C} \in \mathcal{E}$  of wave fields which obey a certain condition. An element  $\psi_C \in \mathcal{C}$  is assigned to a given  $\psi \in \mathcal{E}$  by the constraint map  $P_C$

$$P_C : \mathcal{E} \setminus \{0\} \rightarrow \mathcal{C} : \psi \rightarrow \psi_C. \quad (2.41)$$

A reasonable constraint  $P_{C_1}$  is for example compatibility of the wave field with the measured data in the detection plane. *A priori* information about the sample could constitute a second constraint  $P_{C_2}$ , e.g. requirement of unit amplitude in the case of pure phase objects. Then, a solution to the phase retrieval problem has to be an element of the intersection  $\mathcal{C}_\cap = \mathcal{C}_1 \cap \mathcal{C}_2$ . The algorithms presented in this section aim at finding an element  $\psi \in \mathcal{C}_\cap$  by iterative application of constraint maps. Note that depending on the constraints and especially in the presence of noise, the intersection  $\mathcal{C}_\cap$  may be empty and only approximate solutions to the problem can be obtained.

#### 2.4.1.1 Gerchberg-Saxton algorithm

Consider the situation of two normalized intensity distributions  $I_1 := |\psi|^2$  and  $I_2 := |\Psi|^2 := |\mathcal{D}_z[\psi]|^2$  of a wave field, known in two respective planes  $\Sigma_1$  and  $\Sigma_2$  perpendicular to the optical axis and separated from each other by a distance  $z > 0$ . The two constraints of the Gerchberg-Saxton (GS) algorithm [60] are compatibility of the wave field  $\psi$  with the respective intensity distributions  $I_1$  and  $I_2$ . To this end, a given wave field  $\psi_n$  corresponding to iteration  $n$  is propagated to plane  $\Sigma_2$ :

$$\Psi_n = \mathcal{D}_z[\psi_n]. \quad (2.42)$$

The phase of the wave field is retained while the amplitude is replaced by the known amplitude  $\sqrt{I_2}$ :

$$\Psi'_n = \sqrt{I_2} \frac{\Psi_n}{|\Psi_n|}. \quad (2.43)$$

Backpropagation yields a wave field  $\psi'_n$  in  $\Sigma_1$  compatible with  $I_2$

$$\psi'_n = \mathcal{D}_{-z}[\Psi'_n]. \quad (2.44)$$

The constraint map corresponding to the operations above

$$P_M[\psi_n] = \mathcal{D}_{-z} \left[ \sqrt{I_2} \frac{\mathcal{D}_z[\psi_n]}{|\mathcal{D}_z[\psi_n]|} \right] := \psi'_n \quad (2.45)$$

is denoted as the **modulus constraint** operation. Compatibility with intensity distribution  $I_1$  is achieved by

$$P_1[\psi'_n] = \sqrt{I_1} \frac{\psi'_n}{|\psi'_n|} := \psi_{n+1} \quad (2.46)$$



The GS algorithm is described by iterative application of operations  $P_1$  and  $P_M$ :

$$\psi_{\text{sol}} = (P_1 P_M)^{N_{\text{it}}} [\psi_0], \quad (2.47)$$

with number of iterations  $N_{\text{it}}$ . The algorithm is stopped either after a fixed number of iterations  $N_{\text{it}}$  or when the misfit or **reconstruction error**

$$d^2(|\Psi_n|^2) := \frac{1}{(N_x N_y)} \sum_{(n_x, n_y)} (|\Psi_n(n_x, n_y)|^2 - I_2(n_x, n_y))^2 \quad (2.48)$$

between the measured and predicted intensities in  $\Sigma_2$  reaches a predefined threshold  $d \leq d_{\text{stop}}$ . One can set random values of phase and amplitude [164] for the **initial guess**  $\psi_0$  or incorporate *a priori* information as obtained for example from an approximate phase reconstruction using TIE approaches [76]. It has been shown that the misfit  $d$  decreases monotonically for the GS, i.e. each iteration  $\psi_{n+1}$  will have an equal or smaller reconstruction error than  $\psi_n$  [60]. **Convergence** in a wider sense is achieved if further iterations will not have an effect on the estimated wave field. This may take a large number or even an infinite number of iterations. Note further that convergence does not imply a correct solution. The GS algorithm can be applied for phase retrieval even for the case of a single intensity measurement  $I_2$ . With the assumption of a pure phase object we get

$$I_1 = |\psi|^2 = |O|^2 = 1 \quad (2.49)$$

for x-ray propagation imaging with normalized intensities. Hence, the intensity distributions  $I_1$  and  $I_2$  are known and the GS scheme can be applied. **Fig. 2.7 b** shows the phase reconstruction of a simulated hologram for a pure phase object with maximum phase shift  $\pi/4$  at  $F^{10} = 0.5$  after  $N_{\text{it}} = 2 \cdot 10^4$  iterations of the GS algorithm. An initial guess  $\psi_0$  with random phase and amplitude modulation was used<sup>1</sup>

$$\psi_0 = \exp(iR_1(x_n, y_n) - R_2(x_n, y_n)), \quad (2.50)$$

with equally distributed pseudo-random numbers  $R_{1/2}(x_n, y_n)$  on the interval  $[-0.5, 0.5]$ . Compared to the CTF reconstruction which breaks down for strong phase shift, fewer artifacts are visible. However, deviations in the PSD are visible at spatial frequencies which are not constrained by the PCTF (not shown) and most prominent at low spatial frequencies.

#### 2.4.1.2 Error reduction algorithm

The error reduction algorithm (ER) by Fienup [53] is designed for phase reconstruction of a wave field  $\psi$  from a single measurement of the modulus  $I_2$  of its Fourier transform. In this work, it is particularly relevant for determining the wave field exiting an x-ray waveguide in  $\Sigma_1$  by measuring the waveguide far field in  $\Sigma_2$  [119, 120]. We define the support  $\mathcal{S}$  of  $\psi$  in  $\Sigma_1$  as the set

<sup>1</sup> For the present case of a pure phase object one could also use an amplitude of unity.

$\mathcal{S} := \{(n_x, n_y) | \psi(n_x, n_y) \neq 0\}$  of points where the wave field is non-zero. If  $\mathcal{S}$  is known for some reason the **support constraint** operation can be defined as

$$P_S[\psi'_n] := \begin{cases} \psi'_n(n_x, n_y) & (n_x, n_y) \in \mathcal{S} \\ 0 & (n_x, n_y) \notin \mathcal{S} \end{cases} := \psi_{n+1}. \quad (2.51)$$

In other words, the support constraint sets the wave field to zero for all points outside the support, where the wave field is expected to vanish. The ER algorithm is described by iterative application of support and magnitude constraint operations  $P_S$  and  $P_M$ :

$$\psi_{\text{sol}} = (P_S P_M)^{N_{\text{it}}}[\psi_0], \quad (2.52)$$

with number of iterations  $N_{\text{it}}$ . As for the GS algorithm it is stopped either after a fixed number of iterations  $N_{\text{it}}$  or when the reconstruction error  $d$  reaches a predefined threshold  $d \leq d_{\text{stop}}$ . Since the support is typically not exactly known, a final application of  $P_M$  makes the result consistent with the data. As for the GS algorithm the error decreases monotonically with each iteration [54].

### 2.4.1.3 Hybrid Input-Output algorithm

The monotonic decrease of the misfit  $d$  between measured and predicted intensities may cause the ER and GS algorithms to be trapped in local minima of the complex error landscape defined by  $d$ . To circumvent stagnation in local minima the Hybrid-Input-Output (HIO) algorithm constructs a new iterate  $\psi_{n+1}$  as a linear combination of the input  $\psi_n$  and output  $\psi'_n$  of the latest modulus constraint operation [53]. We will discuss a modified version (mHIO) of the original scheme well adapted to x-ray propagation imaging of pure phase object [63, 76]. in the case of known intensity  $I_2 := |\Psi|^2 := |\mathcal{D}_z[\psi]|^2$  in the detection plane  $\Sigma_2$  and known support  $\mathcal{S}$  in the sample plane  $\Sigma_1$ . For x-ray propagation imaging we use an alternative definition of support as the set  $\mathcal{S} := \{(n_x, n_y) | O(n_x, n_y) \neq 1\}$  of all points where the object transmission function  $O$  induces a phase or amplitude modulation of the incident wave field. The algorithm is initialized with a random or structured initial guess  $\psi_0$ . The first (recurring) operation is the application of the modulus constraint on the current guess  $\psi_n$

$$\psi'_n = P_M[\psi_n]. \quad (2.53)$$

The next iterate  $\psi_{n+1}$  is then constructed by [76]

$$|\psi_{n+1}| = |\psi| - \beta \cdot (|\psi'| - 1) \quad (2.54)$$

and [63]

$$\varphi(\psi_{n+1}) = \begin{cases} \varphi(\psi_n(n_x, n_y)) - \gamma \cdot \varphi(\psi'(n_x, n_y)) & (n_x, n_y) \notin \mathcal{S} \\ \min[\varphi(\psi_n(n_x, n_y)), 0] & (n_x, n_y) \in \mathcal{S}. \end{cases} \quad (2.55)$$

Equation (2.54) slowly pushes the amplitude to unity as expected for a pure phase object, controlled by parameter  $\beta$  with  $0 < \beta \leq 1$ . The phase however is pushed

slowly towards zero outside the support, controlled by  $0 < \gamma \leq 1$  of equation (2.55). These operations resemble the real space update of the original HIO scheme [54]. Constraining the phase shift within the support to negative values by equation (2.55) incorporates the *a priori* knowledge that the object has only positive electron density. This corresponds to the positivity constraint in coherent x-ray diffraction imaging. Setting the upper limit of phase shifts to zero is valid since any constant phase factor in the sample plane is in agreement with measured intensity data. In contrast to the GS and ER algorithm, the error of the HIO algorithm can increase. Especially in the presence of noise the mHIO error might grow without bound. To account for experimental noise and to stabilize the reconstruction, a modified modulus constraint operation as described in [63] is used:

$$P_M[\psi_n] = \mathcal{D}_{-z} \left[ \sqrt{(1 - \frac{D}{d})I_2 + \frac{D}{d} |\Psi_n|^2} \frac{\Psi_n}{|\Psi_n|} \right] := \psi'_n, \quad (2.56)$$

with  $\Psi_n = \mathcal{D}_z[\psi_n]$ . The squared amplitude in detection plane  $\Sigma_2$  is constructed as a linear combination of the measured intensity  $I_2$  and currently guessed intensity  $|\Psi_n|^2$ . Depending on the misfit

$$d^2(|\Psi_n|^2) := \frac{1}{(N_x N_y)} \sum_{(n_x, n_y)} (|\Psi_n(n_x, n_y)|^2 - I_2(n_x, n_y))^2, \quad (2.57)$$

guessed and measured intensity distributions are weighted according to the ratio  $D/d$ . The parameter  $D$  is closely related to the standard deviation of the normalized intensity [63]. The expected misfit of an ideal reconstruction is

$$\langle d^2(|\Psi_n|^2) \rangle = \left\langle \frac{1}{(N_x N_y)} \sum_{(n_x, n_y)} (|\Psi_n(n_x, n_y)|^2 - I_2(n_x, n_y))^2 \right\rangle \quad (2.58)$$

$$= \frac{1}{(N_x N_y)} \sum_{(n_x, n_y)} \langle (I_2(n_x, n_y) - I_2(n_x, n_y))^2 \rangle \quad (2.59)$$

$$= \frac{1}{(N_x N_y)} \sum_{(n_x, n_y)} \sigma^2(n_x, n_y) \quad (2.60)$$

$$= \bar{\sigma}^2, \quad (2.61)$$

with the standard deviation  $\sigma(n_x, n_y)$  of intensity  $I_2(n_x, n_y)$  at each point  $(n_x, n_y)$ . A natural choice of  $D$  is thus  $D = \sqrt{\bar{\sigma}^2}$ . As long as the misfit is larger than what could be achieved ideally, the reconstruction is altered. Otherwise, if  $d \leq D$  the reconstruction is stopped to prevent overfitting of noise. Since  $I_2(n_x, n_y) = I_2^{(\text{raw})}(n_x, n_y)/I^{(\text{E})}(n_x, n_y)$  is the ratio of recorded raw intensity  $I_2^{(\text{raw})}$  and empty beam intensity  $I^{(\text{E})}$  (see section 1.4), the values of  $\sigma(n_x, n_y)$  depend on the expectation values and noise characteristics of recorded hologram and empty beam. A good estimate for  $D$  is the standard deviation of a histogram of normalized intensity values outside the support area [61]. For experimental data  $D$  is adjusted

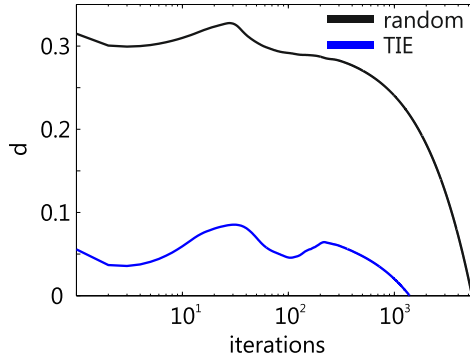


**Figure 2.8:** Misfit  $d$  between reconstructed and measured holographic intensity distribution for phase reconstruction with a modified HIO scheme. The hologram was simulated for a pure phase object with maximum phase shift  $\pi/4$  at Fresnel number  $F^{10} = 0.5$ . An initial guess based on a TIE reconstruction (blue curve) reduces the number of necessary iterations compared to a random initial guess (black curve), here by a factor of about four.

both by monitoring the trajectory of the misfit and by visual inspection of the reconstructed phase distribution.

**Fig. 2.7 c** shows the phase reconstruction of a simulated hologram for a pure phase object with maximum phase shift  $\pi/4$  at Fresnel number  $F^{10} = 0.5$  using the modified HIO algorithm. An initial guess  $\psi_0$  with random phase and amplitude values (see equation 2.50) and a parameter  $D = 10^{-4}$  was used. After  $N_{\text{it}} = 5405$  iterations the reconstruction stopped. The trajectory of the misfit  $d(|\Psi_n|^2)$  (**Fig. 2.8**) shows that the mHIO escaped local minima before the error decreased monotonically towards the final reconstruction. The reconstructed phase resembles the original phase distribution almost perfectly (**c,f**). No deviations in the azimuthally averaged PSD are visible (**i**). Importantly, the algorithm has reconstructed spatial frequencies which are unconstrained in plane  $\Sigma_2$  due to zeroes in the PCTF based on the knowledge of support and the intensity distribution in  $\Sigma_1$ . This effect can partially be seen for the high frequencies of the GS reconstruction (**b,e,h**) and can be attributed to bandwidth-extrapolation due to analyticity of the Fourier transform of complex two-dimensional functions with compact support [63, 68, 7].

#### 2.4.2 Newton Methods

The inverse problem of finding the sample plane wave field from measured intensity data can be formulated as an operator equation

$$F(u) = g, \quad (2.62)$$

with the unknown complex wavefield  $u \in \mathcal{B} \subset L^2(\mathbb{R})$  in the sample plane, the measured (normalized) intensity distribution  $g \in L^1(\mathbb{R})$  and a non-linear operator

$F : \mathcal{B} \rightarrow L^1(\mathbb{R}^2)$ . The operator describes *a priori* constraints and the image formation process consisting of Fresnel diffraction and application of the squared modulus. The inverse problem is typically ill-posed since a strict solution does not have to exist due to noisy data or inconsistent constraints. Also, a solution might not be unique or might not depend continuously on the data. Therefore, regularization is required [203]. A common method to solve nonlinear ill-posed operator equations is the iteratively regularized Gauss-Newton method (IRGN) [5, 4, 15, 107] given by

$$u_{n+1} \in \operatorname{argmin}_{u \in \mathcal{B}} \mathcal{S}[g, F(u_n) + F'(u_n, u - u_n)] + \alpha_n \mathcal{R}(u_0), \quad (2.63)$$

with the data misfit functional  $\mathcal{S}(g, \hat{g}) = |g - \hat{g}|^2$ , Fréchet derivative  $F'(u)$  of  $F$  at  $u^2$ , initial guess  $u_0$ , penalty term  $\mathcal{R}(u_0) = |u - u_0|^2$  and regularisation parameters  $\alpha_n$ , which satisfy

$$\alpha_0 \leq 1, \quad \alpha_n \searrow 0, \quad 1 \leq \frac{\alpha_n}{\alpha_{n+1}} \leq C, \quad \text{for all } n \in \mathbb{N}. \quad (2.64)$$

The algorithm was implemented in MATLAB<sup>3</sup> by Thorsten Hohage and colleagues at the Institut für Numerische und Angewandte Mathematik of the University of Göttingen. The *a priori* information of a pure phase object with a compact support is incorporated in the forward operator. In each Newton step a convex minimization problem has to be solved. This is achieved by a conjugate gradient method [91]. A recent generalization to general data misfit functionals  $\mathcal{S}(g, F(u_n) + F'(u_n, u - u_n))$  enables to take noise statistics explicitly into account, as shown for the relevant case of Poisson noise [94]. However, in the present case of normalized holograms we assume normal distributed noise and apply the original IRGN method. The algorithm was tested for noise-free data with the regularization parameters  $\alpha_n$  set to zero. Reconstruction of a simulated hologram at Fresnel number  $F^{10} = 0.5$  of a pure phase object with maximum phase shift  $\pi/4$  essentially looked the same as the original object (data not shown). No deviations in the PSD were present and zeroes in the PCTF were filled up in agreement to what was obtained for the mHIO algorithm (see **Fig. 2.7 c,f,i**). For noise-free data an initial guess with unit intensity and zero phase shift was sufficient. Choosing a CTF reconstruction as initial guess as used in chapter 8 for experimental data, also resulted in an artifact free reconstruction.

## 2.5 Hybrid approaches

Due to the fact that all phase retrieval methods come with their respective limitations, several combinations were proposed. As shown by Gureyev [76], it is particularly efficient to use a TIE solution as an initial guess for iterative refinement with GSF-type algorithms [158]. **Fig. 2.8** demonstrates this for the modified

<sup>2</sup> A derivaton of the Fréchet derivative of the Fresnel diffraction intensity operator can be found in [191]

<sup>3</sup> MATLAB is a commercial software package developed by The MathWorks, Inc.

HIO scheme. Compared to random initialisation, an initial guess based on an MBA phase reconstruction reduces the number of iterations needed to achieve a certain misfit (here  $d = 10^{-4}$ ) by a factor of about four. The observed phase maps were almost identical (the result for random initialisation is shown in **Fig. 2.7 c,f,i**). For non-ideal and noisy experimental data an initial guess based on a deterministic (but approximate) phase retrieval is expected to influence the reconstruction quality in addition to the reduced number of iterations. In the same manner, single distance CTF solutions could also be used as an initial guess. Indeed, CTF reconstructions are often regarded as approximate solutions and iteratively refined [34, 33] by means of a maximum likelihood method, which minimizes the difference between measured and calculated diffraction patterns [36]. It has been shown that the CTF does not coincide with the TIE in the limit of small propagation distances [73]. An iterative mixed approach was developed as an attempt to combine CTF and TIE in order to extend the validity range to large propagation distances and strong absorption [73]. However, phase retrieval for mixed objects with considerable absorption is still a challenge (especially for non-homogenous objects) and an active area of research [125, 124].

Recently, a promising deterministic approach for phase retrieval of arbitrary objects was developed by Krenkel et al. [117] as a combination of TIE and holographic reconstruction which the authors termed Holo-TIE. It is based on the fact that equation (2.21) does not impose any restriction on the object transmission function. Due to the finite-difference approximation of the derivative with respect to  $z$  (1.108), the TIE is typically seen to be restricted to the edge-detection regime and large Fresnel numbers (e.g. [123, 163, 139, 24]). This holds only if one of the planes is chosen to be the sample plane. However, equation (2.21) is valid for any pair of closely separated planes. By measuring the intensities  $I_1$  and  $I_2$  in two planes at  $z$  and  $z + \Delta z$  in the holographic regime, an approximate phase distribution

$$\tilde{\varphi}(\mathbf{r}_\perp, z) = -k \nabla_\perp^{-2} \left[ \nabla_\perp \cdot \left( \frac{1}{I_1(\mathbf{r}_\perp, z)} \nabla_\perp \left[ \nabla_\perp^{-2} \frac{I(\mathbf{r}_\perp, z + \Delta z) - I(\mathbf{r}_\perp, z)}{\Delta z} \right] \right) \right]. \quad (2.65)$$

and hence, the complex wave field in one of the planes can be calculated. A subsequent simple backpropagation then yields the complex wave field in the object plane and therefore the object transmission function [117, 204]

$$O(\mathbf{r}_\perp) = \mathcal{D}_{-z} \left\{ \sqrt{I_1(\mathbf{r}_\perp, z)} \exp[i\tilde{\varphi}(\mathbf{r}_\perp, z)] \right\}. \quad (2.66)$$

Again, the Holo-TIE solution can be refined iteratively by means of GSF type algorithms [117]. A limitation of Holo-TIE may be the need for smooth illumination functions and high photon flux in order for the difference image not to be deteriorated by noise and low frequency variations. However, in combination with tomography it has the unique potential for deterministic quantitative 3D structure determination of mixed objects without any *a priori* information on the sample.

### 3 Three-dimensional x-ray propagation imaging

As discussed in the previous chapters, x-ray propagation imaging with suitable phase retrieval yields the amplitude  $a(\mathbf{r}_\perp) = \exp[-k\bar{\beta}(\mathbf{r}_\perp)]$  and phase  $\varphi(\mathbf{r}_\perp) = -k\bar{\delta}(\mathbf{r}_\perp)$  of the object's two-dimensional complex transmission function (1.80). The aim of **tomography** is to determine three-dimensional information of the object from a set of two-dimensional images recorded at different rotation angles. The mathematical foundation of this method was developed by Radon in 1917 [175]. For the experimental realisation [37, 96] Cormack and Hounsfield received the Nobel prize in 1979. The discussion mainly follows [103] and we start by writing the definitions (1.82,1.83) of  $\bar{\delta}(\mathbf{r}_\perp)$  and  $\bar{\beta}(\mathbf{r}_\perp)$  for a plane of constant  $y^1$

$$\bar{\delta}_y(x) = -\varphi_y(x)/k = \int_0^z \delta_y(x, z) dz \quad (3.1)$$

$$\bar{\beta}_y(x) = -\ln[a_y(x)]/k = \int_0^z \beta_y(x, z) dz. \quad (3.2)$$

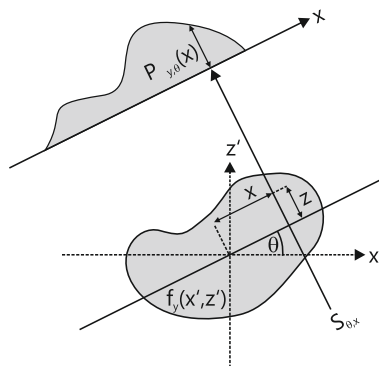


**Figure 3.1:** Projection  $P_{y,\theta}(x)$  of a function  $f_y(x', z')$  at angle  $\theta$ .

<sup>1</sup> The index  $y$  indicates that the respective function is dependent on variable  $y$  but handled as a parameter here, since it is constant.

We introduce the coordinate system of the object  $(x', y', z')$  which is rotated around the  $y$  axis against the laboratory system by an angle  $\theta$

$$\begin{bmatrix} x \\ y \\ z \end{bmatrix} = \begin{bmatrix} \cos \theta & 0 & \sin \theta \\ 0 & 1 & 0 \\ -\sin \theta & 1 & \cos \theta \end{bmatrix} \begin{bmatrix} x' \\ y' \\ z' \end{bmatrix}. \quad (3.3)$$

The inverse rotation matrix is obtained by switching  $\theta \rightarrow -\theta$ . Let  $f_y(x, z)$  be a function describing either  $\delta_y(x, z)$  or  $\beta_y(x, z)$ . Then, equations (3.1,3.2) are identical to what is defined a projection  $P_{y,\theta}(x)$  of  $f_y(x', z')$  at angle  $\theta$

$$P_{y,\theta}(x) = \int_{S_{\theta,x}} f_y(x', z') dz, \quad (3.4)$$

with the integral over straight lines  $S_{\theta,x}$  which obey  $x' \cos \theta + z' \sin \theta = x$  (**Fig. 3.1**). The integral transform into the space of all such straight lines in  $\mathbb{R}^2$

$$P_y(\theta, x) = \mathcal{R}f = \int f_y((-z \sin \theta + x \cos \theta), (+z \cos \theta + x \sin \theta)) dz \quad (3.5)$$

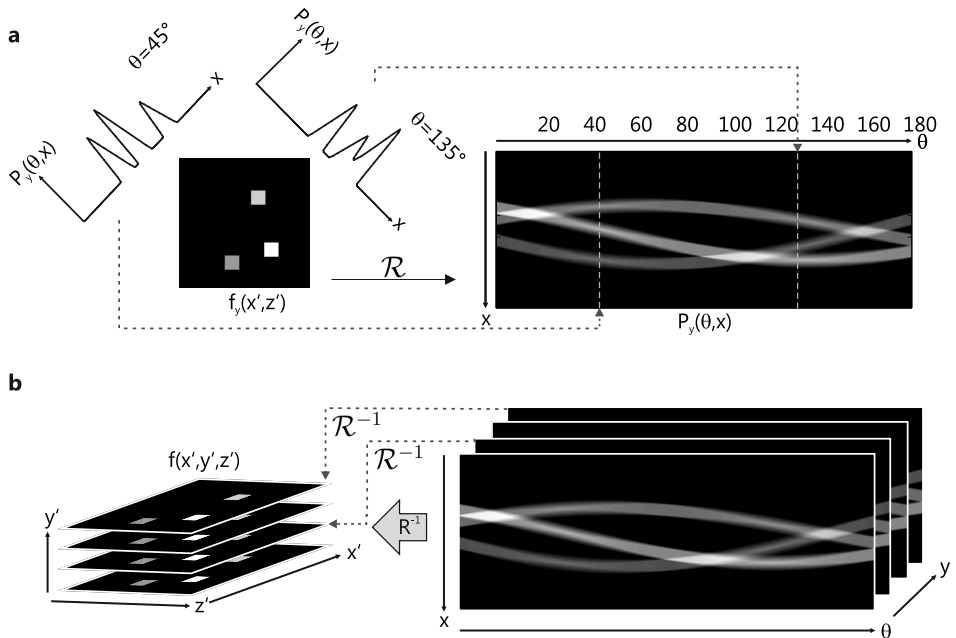


**Figure 3.2:** (a) A function  $f_y(x', z')$  and the corresponding sinogram  $P_y(\theta, x)$  along with two projections at angles  $\theta = [45, 135]^\circ$ . (b) From a  $y$ -stack of sinograms  $P_y(\theta, x)$  the three-dimensional function  $f(x', y', z')$  is reconstructed by a series of inverse Radon transforms  $\mathcal{R}^{-1}$ .



given by the operator  $\mathcal{R}$  is denoted as two-dimensional **Radon transform** [175]. Based on the fact that a Dirac delta function is transformed by  $\mathcal{R}$  into a function which can be expressed by a sinusoid,  $P_y(\theta, x)$  is often called a **sinogram** (**Fig. 3.2 a**). Since the sinogram  $P_y(\theta, x)$  corresponds to the phase or amplitude of the two-dimensional object transmission function evaluated in a plane  $y$ , it can be obtained experimentally by solving the phase problem for different rotation angles. Applying an inverse Radon transform  $\mathcal{R}^{-1}$  then yields the two-dimensional function

$$f_y(x', z') = \mathcal{R}^{-1} P_y(\theta, x). \quad (3.6)$$

for a plane of constant  $y$ . By evaluating several planes,  $f(x', y', z')$  and therefore the three-dimensional index of refraction  $n(\mathbf{r}) = 1 - \delta(\mathbf{r}) + i\beta(\mathbf{r})$  within the object can be obtained (**Fig. 3.2 b**). The essential theorem for inverting the Radon transform is outlined in the next section.

### 3.1 Fourier slice theorem

Insertion of equation (3.5) into the one-dimensional Fourier transform  $\tilde{P}_y(\theta, \nu)$  of  $P_y(\theta, x)$  with respect to the second argument yields

$$\begin{aligned} \tilde{P}_y(\theta, \nu) &= \int P_y(\theta, x) \exp(-i2\pi\nu x) dx \\ &= \iint f_y((-z \sin \theta + x \cos \theta), (+z \cos \theta + x \sin \theta)) \exp[-i2\pi\nu x] dz dx. \end{aligned} \quad (3.7)$$

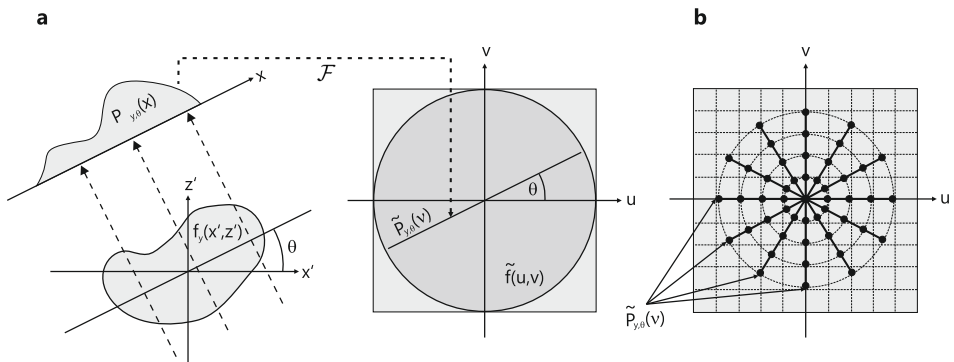


**Figure 3.3:** (a) Fourier slice theorem. The one-dimensional Fourier transform  $\tilde{P}_y(\theta, \nu)$  of a projection  $P_y(\theta, x)$  at angle  $\theta$  equals a slice through the two-dimensional Fourier transform  $\tilde{f}_y(\nu \cos \theta, \nu \sin \theta)$  of the corresponding function  $f(x', z')$ . (b) The fast Fourier transform is defined on a cartesian grid while the Fourier slices are obtained on a polar grid.

Switching to the coordinate system of the object results in

$$\begin{aligned}\tilde{P}_y(\theta, \nu) &= \iint f_y(z', x') \exp[-i2\pi\nu(x' \cos \theta + z' \sin \theta)] dz' dx' \\ &= \iint f_y(z', x') \exp[-i2\pi\nu \cos \theta x'] \exp[-i2\pi\nu \sin \theta z'] dz' dx'.\end{aligned}\quad (3.8)$$

We identify the two-dimensional Fourier transform of  $f_y$  and write the **Fourier slice theorem** as [103]

$$\boxed{\tilde{P}_y(\theta, \nu) = \tilde{f}_y(\nu \cos \theta, \nu \sin \theta).} \quad (3.9)$$

The one-dimensional Fourier transform of a projection is identical to a slice at the respective rotation angle through the two-dimensional Fourier transform of the corresponding function (**Fig. 3.3 a**). Therefore, the inverse Radon transform seems analytically fairly simple. If several projections are known, the two-dimensional information in Fourier space  $\tilde{f}_y(u, v)$  can be filled up slice by slice. Then, by an inverse Fourier transform the two-dimensional function  $f_y(x', z')$  can be reconstructed. A numerical implementation of such a **direct Fourier method** is however aggravated by the fact that the Fast Fourier transform is defined on a rectangular grid, while the Fourier slices are known on a polar grid (**Fig. 3.3 b**). Interpolation between the two coordinate systems in Fourier space can result in strong artifacts in real space [103]. Therefore, to date the most widely used method for tomographic reconstruction is **filtered backprojection**.

## 3.2 Filtered backprojection

The inverse two-dimensional Fourier transform of  $f_y(x', z')$

$$f_y(x', z') = \int_{-\infty}^{\infty} \int_{-\infty}^{\infty} \tilde{f}_y(u, v) \exp(i2\pi(ux' + vz')) du dv \quad (3.10)$$

can be written in polar coordinates

$$u = \nu \cos \theta \quad (3.11)$$

$$v = \nu \sin \theta \quad (3.12)$$

as

$$f_y(x', z') = \int_0^{2\pi} \int_0^{\infty} \tilde{f}_y(\theta, \nu) \exp(i2\pi\nu(x' \cos \theta + z' \sin \theta)) \nu d\nu d\theta. \quad (3.13)$$

With the relation

$$\tilde{f}_y(\theta + \pi, \nu) = \tilde{f}_y(\theta, -\nu), \quad (3.14)$$

the integral over  $2\pi$  can be split up and written as

$$f_y(x', z') = \int_0^{\pi} \int_{-\infty}^{\infty} \tilde{f}_y(\theta, \nu) |\nu| \exp(i2\pi\nu(x' \cos \theta + z' \sin \theta)) d\nu d\theta. \quad (3.15)$$

Using the Fourier slice theorem (3.9) one obtains

$$f_y(x', z') = \int_0^\pi \left[ \int_{-\infty}^{\infty} \tilde{P}_y(\theta, \nu) |\nu| \exp(i2\pi\nu(x' \cos \theta + z' \sin \theta)) d\nu \right] d\theta. \quad (3.16)$$

This integral may be expressed as [103]

$$f_y(x', z') = \int_0^\pi Q_y(\theta, x' \cos \theta + z' \sin \theta) d\theta \quad (3.17)$$

with

$$Q_y(\theta, x) = \int_{-\infty}^{\infty} \tilde{P}_y(\theta, \nu) |\nu| \exp(i2\pi\nu x) d\nu. \quad (3.18)$$

The definition of  $Q_y(\theta, x)$  motivates the term **filtered projection**, since the projection  $P_y(\theta, x)$  is filtered in Fourier space with a frequency filter  $|\nu|$ . The frequency filter  $|\nu|$  may also be understood intuitively by considering the polar grid sampling in Fourier space which gets sparser for higher spatial frequencies (**Fig. 3.3 b**). Equation (3.17) describes contribution of the filtered projections for each angle  $\theta$  to the values of  $f_y(x', z')$ . For all coordinates  $(x', z')$  with  $x' \cos \theta + z' \sin \theta = x$ , a constant value of  $Q_y(\theta, x)$  is added to  $f_y(x', z')$ . Since the relation  $x' \cos \theta + z' \sin \theta = x$  describes lines which form an angle  $\theta$  with respect to the  $x'$ -axis, this process may be interpreted as smearing back the values of  $Q_y(\theta, x)$ , hence the term **backprojection**. A numerical implementation still has to handle interpolation from polar to cartesian grids, but the interpolation now takes place in real space and produces less pronounced artifacts.

### 3.3 Cone-beam tomography

In the sections above, a parallel beam geometry was assumed. This allowed to treat each  $y$ -plane separately and the three-dimensional problem was divided into a set of methodological identical two-dimensional reconstructions. X-ray propagation imaging with geometric magnification is based on a cone-beam illumination. Depending on resolution, sample thickness and cone angle this simplification is no longer justified and the backprojection cannot be performed in parallel planes. Instead, a three-dimension reconstruction has to be performed. Feldkamp, Davis and Kress (FDK) developed an approximate solution to the problem by means of three-dimensional filtered backprojection [52]. The FDK algorithm weights and filters each projection according to its relative location to the central plane of the illumination cone. Then, each weighted and filtered projection is backprojected into the three-dimensional volume. Artifacts appear for voxels with increasing distance to the central plane because a circular orbit does not ensure that all voxels are seen from all angles. This effect is aggravated by large cone angles [208]. Since projections in cone-beam geometry are integrals over tilted fan beams, a scan range over 180 degrees as in parallel beam tomography is not sufficient. For a fan beam, a minimal complete dataset consists of 180 degrees plus fan angle to

ensure that all pixels are seen from all angles. However, a minimal complete dataset contains partially redundant data and cannot be reconstructed in a straightforward manner. By applying a suitable weighting function to the sinogram, known as Parker weights [166], reconstruction of a minimal complete dataset can be performed by means of filtered backprojection. In this work, experiments exhibit only small cone angles below 10 degrees and minimal artifacts associated with cone-beam reconstruction are expected [95].

### 3.4 Reconstruction and visualization software

An efficient numerical implementation of tomography should utilize the fact that (cone-beam) filtered backprojection can be highly parallelized. For some experiments huge datasets of up to 2000 projections and more than  $10^9$  voxels have to be processed. To this end, a commercial software package (Ultra Fast ConeBeam Reconstruction Software, Bronnikov Algorithms, Netherlands) was customized and implemented into the phase retrieval and data analysis chain. An interface was written which handles the access to the C++ DLL (dynamic link library) of the program via MATLAB. A computer with two Intel XEON processors (2,4 Ghz), 96 Gbyte DDR3 RAM, Zotec GeForce GTX 285 graphics card and two SAS hard discs in RAID0 configuration was set up to process huge datasets and to ensure reasonable reconstruction times. A typical cone-beam reconstruction of a dataset with  $2048^3$  voxels from over 1000 projections takes about one hour. Analysis and visualisation of the three-dimensional data was performed using Avizo Fire 7 (Visualisation Science Group) installed on the same computer to allow fast feedback on the reconstruction quality. Data recorded at the ID22NI beamline was reconstructed using a software package (PyHST [29]) which is installed on the ESRF beamline server and remotely accessible. Small parallel beam datasets with less than  $10^7$  voxels were reconstructed with a MATLAB implementation of filtered backprojection.

## 4 Implementation of x-ray propagation imaging

As outlined in the previous chapters, an x-ray propagation imaging experiment consists of three ingredients: source, sample and detector. In this work, compact x-ray sources based on electron impact were used for laboratory experiments. Highly focused undulator beams produced at synchrotron storage rings were used for fast measurements and x-ray waveguides provided highly coherent beams with small lateral source dimensions needed for high resolution imaging. Motorized stages for sample positioning along and perpendicular to the optical axis as well as for tomographic scans and a variety of x-ray detectors were provided by the respective instruments.

### 4.1 X-ray detectors

A crucial device for x-ray propagation imaging is the detector. Several types of x-ray detectors exist, each with its specific advantages and limitations. The spatial resolution for example is limited by the pixel size or more precisely the point spread function. The available number of pixels limits the field of view in x-ray propagation imaging while sensitivity, noise characteristics and dynamical range are further important parameters which influence image quality. Hence, different kinds of detectors were used to account for the various experimental conditions.

#### Single-photon counting device

Single-photon counting detectors, also termed pixel detectors, deliver a high dynamic range while having zero read-out noise. The main drawback of these detectors are the relatively large pixel dimensions. The Pilatus 300k [21] (Dectris, Switzerland) and the Maxipix [173, 172] (ESRF, France) have pixel sizes of 172  $\mu\text{m}$  and 55  $\mu\text{m}$ , respectively. The Pilatus with its high dynamical range (maximum flux of  $\gtrsim 2 \times 10^6$  photons/s/pixel [205]) and large active area ( $84 \times 107 \text{ mm}^2$ ) is used for flux calibrations and recording of highly divergent x-ray waveguide far fields. The Maxipix offers a very high frame rate of up to 300 Hz and is used for waveguide based imaging. However, these pixel detectors consist of several modules each having only a very limited number of pixels and insensitive inter-module gaps.

#### Charged-coupled devices

Direct illuminated charged-coupled devices (CCD) offer medium sized pixels of few tens of micrometers and a large number of pixels. The direct-illumination CCD

used here (LCX, Princeton Instruments) has  $1340 \times 1300$  pixels,  $20 \mu\text{m}$  in size. However, the dynamical range is limited to about 100 photons per pixel. Therefore, several accumulations are needed for a certain signal level. Since the readout time of the LCX is 1.8 seconds [155], this results in a rather ineffective measurement for intense x-ray beams where only short exposure times are necessary.

### Scintillator-based devices

To date, the highest spatial resolution for x-ray detection is achieved with scintillator based detector systems. The incoming x-ray photons are converted into visible light photons by a scintillating crystal. Then, the optical photons are recorded using detector technology for visible light. Two basic principles are commonly used, the scintillator is either imaged by an optical microscope or bonded onto optical fibres. The spatial resolution of such a combined detector system is characterized by the point spread function (PSF) of the scintillator, aberrations of the optics and the PSF of the optical detector. Two fibre-coupled scintillator-based detectors with a custom scintillator ( $15 \mu\text{m}$  GdOS:Tb, Photonic Science) and  $6.54 \mu\text{m}$  pixel size were used. The detector connected to a CCD ( $1040 \times 1388$  pixels, X-ray Mini FDI, Photonic Science) is termed FDI, the detector connected to an sCMOS-Chip ( $1080 \times 1920$  pixels, Photonic Science) is termed sCMOS. Two different high resolution detector systems were used, based on optical microscopes built by Optique Peter (France). The first detector system (termed PCO here) uses a  $20 \mu\text{m}$  thick LuAG:Ce scintillating screen (Crytur, Czech Republic), magnifying objective lenses (x4, x10, x20, Olympus, Germany) and a PCO.2000 CCD (PCO, Germany) with  $2048 \times 2048$  pixels,  $7.4 \mu\text{m}$  in size. Depending on the objective lense, the detector system is termed PCOx4, PCOx10 or PCOx20. The standard deviation of the PSF reaches values down to  $1.1 \mu\text{m}$ . The second system (termed FReLoN here) uses a fast readout and low noise CCD (FReLoN 4m, ESRF [121]) with  $2048 \times 2048$  pixel,  $24 \mu\text{m}$  in size. The  $20 \mu\text{m}$  thick LSO:Tb scintillating screen is imaged with a x10 objective and a x3.1 eyepiece, resulting in a pixel size of  $756 \text{ nm}$ .

## 4.2 Laboratory setup JuLiA

Experiments aiming at a spatial resolution in the micrometer range for millimeter sized objects were carried out at the laboratory instrument for phase-contrast microtomography called “**J**ust a **L**iquid **A**node” (JuLiA). The instrument was set up by the author at the Institute for X-ray Physics of the University of Göttingen and is described in detail in [9]. Since a few modifications of the initial setup were necessary to increase performance and flexibility and in particular to allow tomography in the inverse geometry (see section 5.4.3), main components of the instrument as used in this work (**Fig. 4.1**) are described in the following.

The x-ray source is a JXS R5 prototype (Excillum, Sweden) which can be equipped either with a cooled solid metal target to operate as a standard microfocus source at  $60 \text{ kVp}$  and  $0.07 \text{ mA}$  current or with a galinstan (GaInSn alloy) liquid-metal-

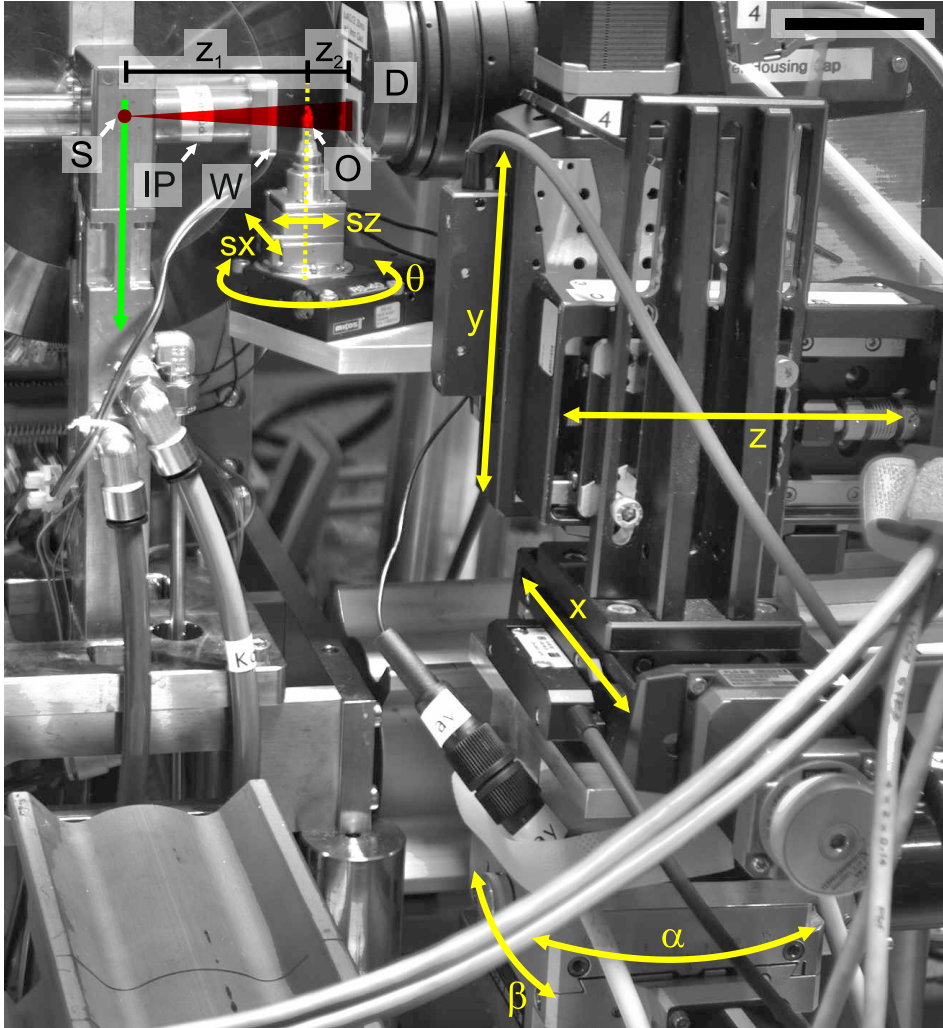


**Figure 4.1:** Main components of the instrument for phase-contrast microtomography (JuLiA). X-rays are created at the interaction point of electron beam (not shown) with the liquid metal jet (green). The object (O) is placed in the x-ray cone-beam (red) at a distance  $z_1$  from the source (S). The detector (D, here the PCO is installed) is placed at a distance  $z_2$  from the object. An intermediate piece made of copper (IP) prevents the heated window (W) from being short circuited by galinstan debris created by the metal jet. The object is aligned in the axis of rotation (dashed yellow line) by two compact translations ( $s_x, s_y$ ). The sample tower allows to position the axis of rotation in the beam ( $x, y, z$ ) and align it perpendicular to the optical axis (angles  $\alpha$  and  $\beta$ ). Tomography is then performed by rotating the object with respect to  $\theta$  by a compact rotation stage. Scale bar, 50 mm.

jet anode [87, 162] which provides roughly 10 times higher brilliance operating at 60 kVp and up to 0.7 mA current. The characteristic photon energy is 17.5 keV (Mo- $K_\alpha$ ) for the solid target and 9.25 keV (Ga- $K_\alpha$ ) for the liquid target. Typical source sizes are 6  $\mu\text{m} \times 6 \mu\text{m}$  for the solid and 4  $\mu\text{m} \times 7 \mu\text{m}$  for the liquid anode (FWHM, h.  $\times$  v.). In the liquid-metal-jet configuration, a heated debris window is installed to prevent galinstan from covering the x-ray output window. However, during operation galinstan debris often caused a short circuit and consequently a failure of the heater, limiting the use for long tomographic measurements. To overcome this limitation an intermediate piece of copper was fabricated to increase the distance of the output window from the liquid-metal-jet (**Fig. 4.1**). Current market-ready versions of the source do not suffer from this phenomenon. Indeed, a MetalJet D2 (Excillum, Sweden) with minimal maintenance and increased stability is currently being installed as an update for the JuLiA instrument.

Positioning of detector and sample tower along the optical axis is facilitated with an aluminum profile (X95, Linos, Germany) allowing highest flexibility. The detectors FDI, sCMOS, PCO and LCX are implemented in the control software and can easily be switched. The sample tower (**Fig. 4.1**) consists of 3 translational stages with optical encoders (PLS-85, Micos, Germany) and a two-segment cradle (5203.10, Huber, Germany) to align the axis of rotation (angles  $\alpha$  and  $\beta$ ) in the beam. To allow small source-detector distances down to 85 mm, a compact rotation stage (RS-40, Micos, Germany) was chosen along with two compact linear nano positioners with optical encoders (ANPx101/NUM, Attocube, Germany), mounted on top of the rotation stage for alignment of the sample into the axis of rotation.

### 4.3 GINIX at beamline P10 of PETRA III

A major goal of this work was the implementation and improvement of x-ray propagation imaging techniques at the *Göttingen Instrument for Nano-Imaging with X-rays* (GINIX) [106, 105, 104] which is installed at the P10 beamline of the new third generation synchrotron source PETRA III at DESY (Deutsches Elektronen-Synchrotron, Hamburg) and operated by the *Institute for X-ray Physics* of the *University of Göttingen*. The unique design with a circumference of 2304 m makes PETRA III the most brilliant storage ring light source worldwide [55, 6, 14].

#### 4.3.1 Coherence Beamline P10

The *Coherence Beamline* P10 consists of front-end (FE), optics hutch (OH) and the first and second experimental hutches (EH1 and EH2). It is designed to utilize the high coherent flux for investigation of sample dynamics by x-ray photon correlation spectroscopy and for coherent lensless imaging of micro- and nanostructures. For that purpose, the beam can be brought to different experimental endstations. For the sake of simplicity, in **Fig. 4.2** only beamline components relevant for propagation imaging with the GINIX setup are shown, while a comprehensive



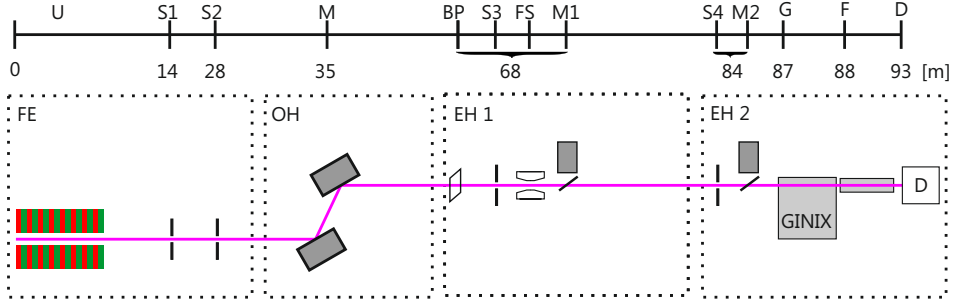


**Figure 4.2:** Components of the P10 coherence beamline at PETRA III relevant for propagation imaging with their respective distances from the undulator source. Front-end (FE) with primary (S1) and secondary (S2) slits. Optics hutch (OH) with high-heat load double-crystal Si(111) monochromator (M). First experimental hutch (EH1) with beam position monitor (BP), slits (S3), fast shutter (FS) and beam intensity monitor (M1). Second experimental hutch (EH2) with slits (S4), beam intensity monitor (M2), GINIX setup (G), flight path (F) and detector bench (D).

description of the beamline components can be found in [225, 104, 226]. The 5 m long U29 undulator is installed in a low- $\beta$  section of the ring providing an x-ray source only  $85 \mu\text{m} \times 14 \mu\text{m}$  in size (FWHM, h. $\times$ v.) with a divergence of  $28 \mu\text{rad} \times 3.7 \mu\text{rad}$  ( $1\sigma$ , h. $\times$ v.) [226, 14]. After the primary and secondary slits of the front-end, the optics hutch contains a high-heat load double-crystal Si(111) monochromator with a spectral bandwidth of  $\Delta E/E = 10^{-4}$ . A mirror for pink beam operation, i.e. using only the intrinsic monochromaticity of the undulator harmonic without double-crystal monochromator, is foreseen. The feedback signal of the beam position monitor (FMB Oxford, UK) in EH1 serves to stabilize the pitch of the second monochromator crystal. An intensity monitor behind a set of pink beam compatible in-vacuum slits is installed in both experimental hutches. Exposure times down to a few milliseconds are enabled by a piezo-driven fast shutter system (FPS400M, Cedrat Technologies, France) mounted in EH1.

### 4.3.2 GINIX

The GINIX setup is located on an optical table in EH2 (see **Fig. 4.2**) which can be moved into the beam. Apart from the initial configuration as a dedicated x-ray waveguide-based imaging endstation [104], the modular design enables various applications, covering scanning nano-diffraction, scanning transmission x-ray microscopy (STXM), ptychographic CDI [66, 217] as well as fullfield x-ray propagation imaging [117] and tomography [12, 158]. While sample positioning and mounting of additional optical elements vary for different configurations, all GINIX setups share certain key components (**Fig. 4.3 a**). The central optical element is the non-dispersive Kirkpatrick-Beaz (KB) mirror system, composed of two ellip-

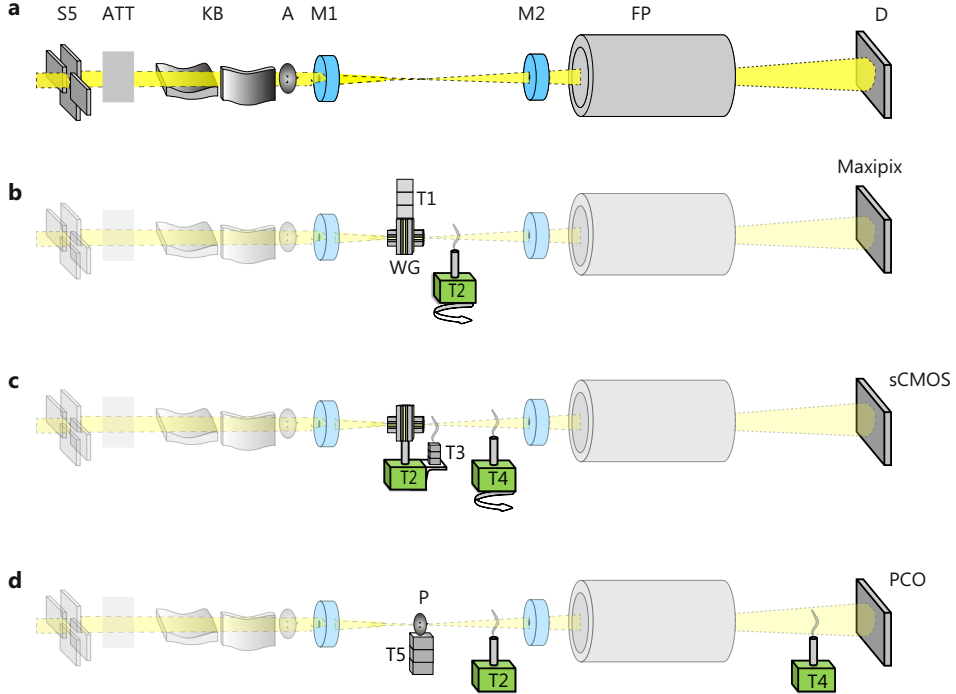


**Figure 4.3:** Different imaging configurations of the GINIX setup. (a) Key components shared by all experiments with KB mirror entrance slits (S5), attenuators (ATT), KB mirror system (KB), aperture (A), first (M1) and second (M2) on-axis optical microscopes, evacuated flight path (FP) and detector bench (D). (b) Waveguide imaging configuration with miniaturized waveguide (WG, 35 nm guiding core) positioning tower (T1), tomography sample tower (T2) and Maxipix detector. (c) Optimized waveguide imaging configuration. The WG is aligned with the actual sample tower (T2). Samples for 2D imaging are mounted on a miniaturized  $xyz$  nano-positioner (T3) with crossed-roller slides and large travel range on top of T2. For tomography another sample tower (T4) is installed. The sCMOS detector is well suited to WGs with larger guiding core dimensions (50 – 100 nm) and increased photon flux (d) KB imaging configuration. A pinhole (P) is aligned in the focal plane by  $xyz$  positioners (T5) and acts as a low-pass filter. Samples are placed on the actual sample tower (T2) for high magnification or on the second tomography tower (T4) installed between flight path and detector for quasi-parallel imaging. The high photon flux allows to install a high resolution detector (PCO).

tically shaped mirrors in orthogonal arrangement [110] with a focal plane about 87 m behind the source. The first mirror (polished by WinlightX, France) focuses the beam in vertical direction (vertical mirror) with a focal length of  $f = 302$  mm, and an incidence angle of  $\theta = 3.954$  mrad at the center of the mirror. To increase reflectivity at higher photon energies a 35 nm thick Pd layer was coated onto the mirror (WinlightX). The second mirror (polished by JTEC, Japan and coated with 55 nm Pd by Axo Dresden, Germany) focuses the beam in horizontal direction (horizontal mirror) with a focal length of  $f = 200$  mm and an incidence angle of  $\theta = 4.05$  mrad at the center of the mirror. The maximum deviation of the elliptical shape (peak to valley) was measured by optical metrology to be 13.9 nm and 4.8 nm for the vertical and horizontal mirror, respectively. Coating and geometry of the mirrors allow for efficient hard x-ray focusing up to 13.9 keV. A comprehensive description of the mirrors can be found in [104, 105]. To reduce beam-induced degradation, the KB system is operated at ultrahigh vacuum. Wavefront changes due to x-ray windows of the vacuum vessel are minimized by using 1  $\mu\text{m}$  thick  $\text{Si}_3\text{N}_4$  membranes (7 mm  $\times$  7 mm, Silson, UK). The geometric acceptance of the KB system is set by the incidence angles and length of the mirror substrates to about 400  $\mu\text{m}$   $\times$  400  $\mu\text{m}$  resulting in focus sizes down to about 200 nm  $\times$  200 nm with a flux larger than  $10^{11}$  ph/s [185]. The illumination of the mirror system is controlled via slit systems S3 and S4 in EH1 and EH2 and by two pairs of hybrid metal single-crystal blades (Xenocs, France) mounted on the optical table in front of the vacuum vessel (S5). Coherent illumination of the mirrors is achieved by closing the slit gaps of S5 in front of the mirrors and enables ptychographic applications and reconstruction of the intensity distribution in the focal plane [66, 217]. The controllable numerical aperture of the mirrors results in adjustable focus sizes in the range of 250 – 500 nm [66]. This enables versatile possibilities to use the high coherent flux of the P10 beamline. The unfocussed and partially focussed components of the beam are blocked by a 450  $\mu\text{m}$  thick W foil while the focused beam passes through an aperture (A) of 1 mm diameter. To reduce photon flux for alignment or to minimize radiation damage of samples and detectors, a set of attenuators (PF4, Xia, USA) is installed in front of the KB system. An on-axis optical microscope (M1, Optique Peter, France) with a working distance of 50 mm and a tilted drilled mirror (1.5 mm inner diameter) facilitates alignment of optical elements like waveguides, pinholes or soft edges in the x-ray beam. A second on-axis optical microscope (M2, Bruker AXS, USA) with a working distance of 32 mm and a drilled objective (1.2 mm inner diameter) is used to align and observe samples while they are exposed to x-rays. Reduction of air scattering and absorption behind the sample is achieved by a vacuum flight path either with a 1  $\mu\text{m}$  thick  $\text{Si}_3\text{N}_4$  membrane (5 mm  $\times$  5 mm, Silson, UK) or a 50  $\mu\text{m}$  thick polyimide foil (25 mm diameter) as entrance window and a 75  $\mu\text{m}$  thick polyimide foil (135 mm diameter) as exit window. The motorized detector bench is positioned about 5 m behind the x-ray focus and can be equipped with up to four different area detectors at a time.

Based on experimental experience gained during this work, positioning of sample and optical elements was modified and improved compared to the initial GINIX

setup described in [104], resulting in three main imaging configurations (**Fig. 4.3**). One configuration aims at propagation imaging with the pure KB beam, the others are tailored to waveguide-based imaging.

### 4.3.3 X-ray waveguides

While the focus of the KB mirror system delivers a high photon flux, the partial spatial coherence [185] and a focal size of  $S \geq 200$  nm limits the achievable resolution, contrast and dose efficiency in x-ray propagation imaging. Moreover, high frequency variations in the KB far field (**Fig. 4.4 a**) violate assumption (1.113) needed for empty beam correction (**Fig. 4.8**), owing to considerable intensity in the tails of the focus (see **Fig. 4.9** and [66]). X-ray waveguides on the other hand act as coherence and spatial filters, since only a limited number of modes can propagate inside the waveguide [170, 101, 58, 160, 161, 25, 122]. Recently, high transmission planar waveguides [186] were combined in a crossed geometry yielding almost fully coherent [185] hard x-ray beams confined in two dimensions below 15 nm [119, 118]. Two-dimensional x-ray propagation imaging of eukariotic cells was previously achieved [63] using waveguides and a similar KB setup at beamline ID22NI of the ESRF. Implementation of waveguide-based x-ray propagation imaging at GINIX and extending it to three dimensions was a major goal of this work.

Four waveguides of two different types (see **Tab. 4.1** for relevant parameters) were used in front-coupling mode [57, 159]: three crossed multilayer waveguides (XWG1-XWG3) [119, 120, 186] and one bonded lithographic channel waveguide (BWG) [66, 85, 152]. Crossed multilayer waveguides (XWG) consist of two pla-

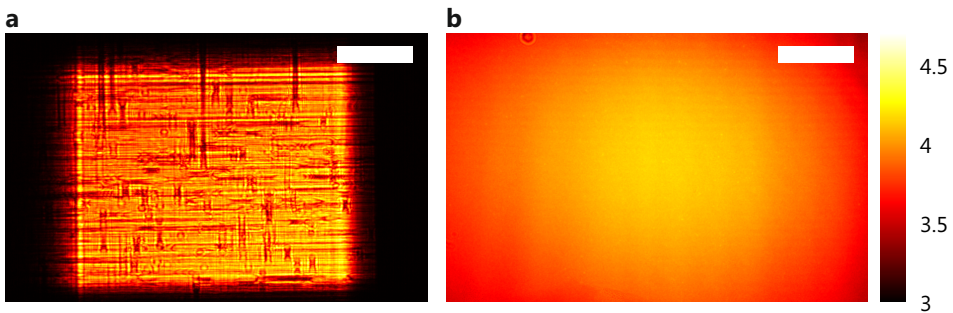


**Figure 4.4:** (a) KB farfield intensity distribution at 13.6 keV photon energy recorded within 0.1 seconds using the sCMOS camera about 5 m behind the focus. The primary beam was attenuated by a factor of about 370 using 100  $\mu\text{m}$  thick W. Prominent high frequency variations are visible. (b) The farfield of a crossed x-ray waveguide (XWG3) exhibits no high spatial frequencies but a smooth intensity distribution. However, no attenuators were used within the 10 second exposure, due to the reduced photon flux compared to the pure KB beam. Logarithmic color coding. Scale bars, 2 mm.

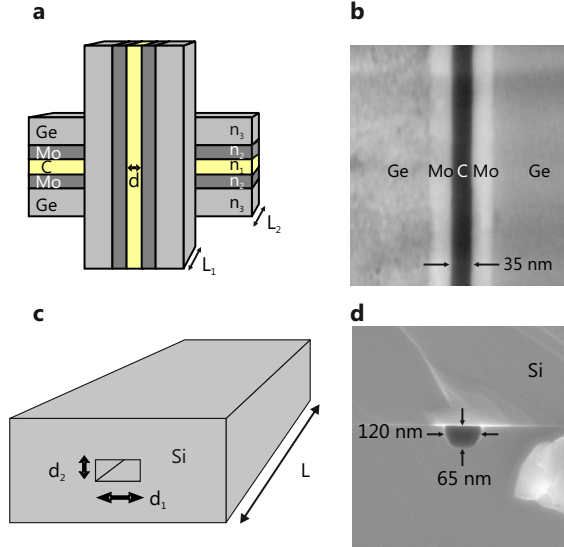


**Figure 4.5:** (a) Sketch of a crossed x-ray waveguide consisting of two one-dimensional waveguide slices of lengths  $L_1$  and  $L_2$  and a transmission optimized sputtered thin film sequence Ge/Mo/C/Mo/Ge. (b) Scanning electron micrograph (SEM) of a single waveguide slice with guiding layer thickness  $d = 35$  nm. (c) Sketch of a lithographic channel waveguides with length  $L$  and guiding core dimensions  $d_1$  and  $d_2$ . (d) SEM image of the exit surface of an air-filled bonded silicon channel waveguide with core dimensions  $d_1 = 120$  nm,  $d_2 = 65$  nm and length  $L = 1$  mm.

nar waveguide slices each with a sputtered thin film sequence Ge/Mo/C/Mo/Ge optimized for transmission at photon energies of 11.5 – 18 keV. The Mo interlayers between a C guiding layer and the strongly absorbing Ge cladding significantly enhance transmission and enable smaller confinement of modes compared to single-material waveguides [186]. Even though layer thicknesses of 18 nm and 9 nm were achieved [117], here  $d = 35$  nm or  $d = 59$  nm was chosen for the diameter of the guiding layer to ensure sufficient photon flux for imaging applications. **Fig. 4.5 a,b** shows a sketch of the XWG design along with a scanning electron micrograph revealing the multilayer structure corresponding to a slice of XWG1/2. For lower photon energies (here 7.9 keV) empty (air) channels are favourable. Recently, channel waveguides in silicon wafers with sub-100 nm lateral dimensions were realised [64, 85, 152] based on e-beam lithography and wafer-bonding [113, 174]. **Fig. 4.5 c,d** shows a sketch of the channel waveguide design along with a scanning electron micrograph of the exit surface of BWG<sup>1</sup>. Far field intensity distributions of each waveguide are shown in **Fig. 4.6 a-d**. They were recorded at the respective photon energies (**Tab. 4.1**) with a Pilatus pixel detector (see section

<sup>1</sup> The channel used here corresponds to channel G23 of wafer dw8-TG in [85].

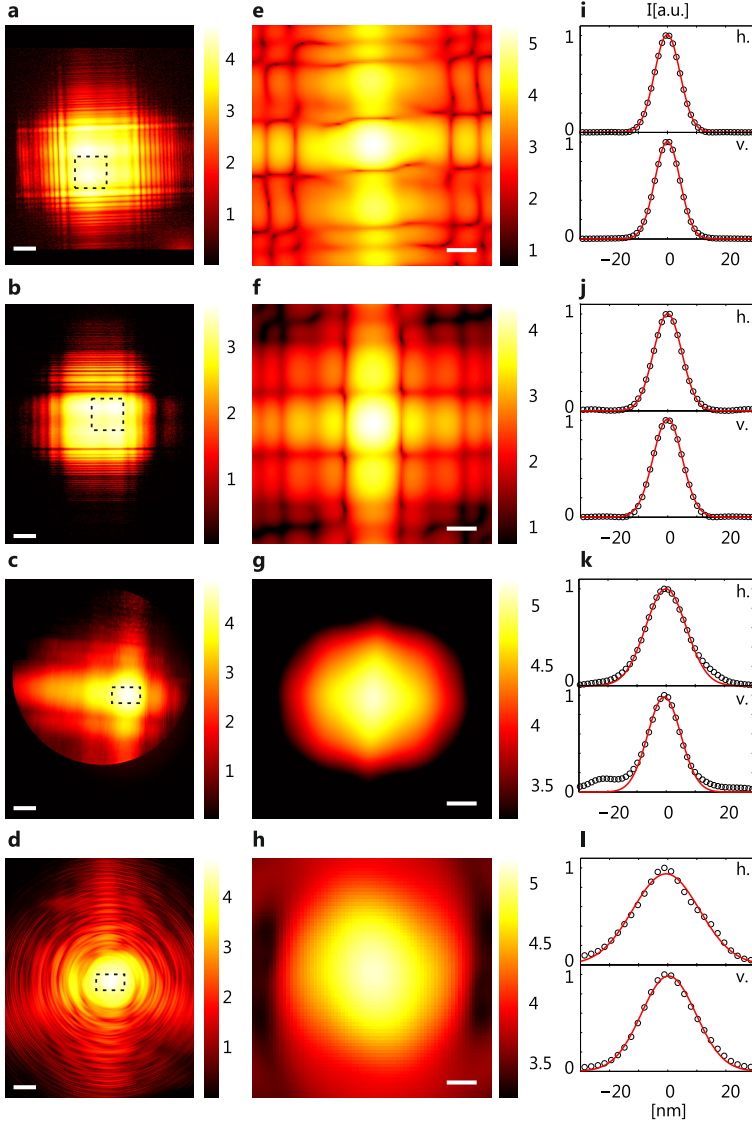


**Figure 4.6:** Logarithmic far field intensity distributions of waveguide (a) XWG1, (b) XWG2, (c) XWG3 and (d) BWG. (e-h) Reconstructed near field intensity using the ER algorithm, logarithmic color coding. The gaussian initial guess has a standard deviation of twice the size of the autocorrelation function (FWHM). (i-j) Gaussian fits to the central peak of the near field intensity (h.  $\times$  v.). Scale bars, (a) 10 nm, (b) 20 nm.

	$\sigma$	XWG1	XWG2	XWG3	BWG
AC, FWHM [nm]	-	$17 \times 20$	$23 \times 20$	$41 \times 34$	$58 \times 51$
ER, FWHM [nm]	1	$9.8 \times 9.6$	$10.9 \times 11.3$	$14 \times 11$	$19.8 \times 16.8$
ER, FWHM [nm]	$2 \cdot \text{AC}$	$10.3 \times 10.1$	$11.4 \times 11.8$	$16 \times 13$	$27 \times 22$
$d_1 \times d_2$ [nm]		$35 \times 35$	$35 \times 35$	$59 \times 59$	$120 \times 65$
$L_1/L_2$ [ $\mu\text{m}$ ]		400/207	220/270	385/379	-
$L$ [ $\mu\text{m}$ ]		607	490	764	1000
$I$ [ph/s]		$2 \cdot 10^7$	$1 \cdot 10^8$	$5 \cdot 10^8$	$2 \cdot 10^9$
$E$ [keV]		15	13.8	13.6	7.9

**Table 4.1:** X-ray waveguide parameters with lateral dimensions  $d_{1/2}$ , lengths  $L_{1/2}$ , total length  $L$ , maximum photon flux  $I$  and photon energy  $E$ . An upper limit for beam confinement is set by the autocorrelation (AC), a lower limit by ER reconstruction of the near field intensity distribution using a gaussian initial guess with standard deviation  $\sigma$  and a rectangular support with 200 nm side length.

4.1) about 5 m behind the waveguide exit. To fill in missing information in the inter-module gaps of the Pilatus detector, two measurements with the detector at two different lateral positions were combined into a single image. For XWG3, a  $\text{Si}_3\text{N}_4$  membrane was glued on a round aperture and used as entrance window of the flight path resulting in dark regions outside the central waveguide cone (c). The photon flux exiting the waveguide was measured by integrating the far field intensity distribution recorded with the single-photon counting detector. A lower limit for the lateral extension of the near field intensity distribution is set by the size  $s_{\text{AC}}$  (FWHM) of Gaussian fits to the two-dimensional autocorrelation along the vertical and horizontal direction, respectively. A more precise measure for the beam confinement is obtained by reconstructing the complex wave field right behind the waveguide exit (e-f) using the ER algorithm (see section 2.4.1.2) and subsequent Gaussian fitting of the central peak. Since the result of phase reconstruction by means of ER depends on the initial guess, the ER algorithm was run with two different initial guesses. A two-dimensional Gaussian with standard deviation  $\sigma = 1$  nm was used to reconstruct an upper limit while a standard deviation twice the size of the autocorrelation function  $\sigma = 2s_{\text{AC}}$  was used to get a more conservative value. The support was set to a rectangle with 200 nm side lengths. Results are tabulated in **Tab. 4.1**.

#### 4.3.4 Original waveguide configuration

For high geometric magnifications  $M = 1 + z_2/z_1$  the sample has to approach the x-ray waveguide exit very closely. At the same time, the waveguide has to be

aligned in three translational and two rotational degrees of freedom in addition to the degrees of freedom needed for sample alignment and tomographic scans. Therefore, sample and waveguide mounting and positioning is a challenging design parameter. The original configuration of GINIX [104] (**Fig. 4.3 b**) was used for three-dimensional imaging of bacterial cells (see chapter 7). A set of miniaturized piezo-driven stick-slip positioners with optical encoders (ANPx101/NUM, ANPx51/NUM, ANPz101/NUM, ANR101/NUM, ANGp101/NUM, attocube systems, Germany) which are mounted upside down onto an additional piezo stage (P-622.ZCD, Physik Instrumente, Germany) provide the degrees of freedom needed for waveguide alignment (T1 in **b**) [104]. A crossed x-ray waveguide with guiding layer thickness  $d = 35 \text{ nm}$  (XWG1/2) was placed into the focal plane of the KB mirrors. Small source sizes are evidenced by large divergence angles (**Fig. 4.6 a,b**). For both waveguides Gaussian fits (**Fig. 4.6 i,j**) to the central peak of the ER reconstructions (**Fig. 4.6 e,f**) give a source size (FWHM) below  $12 \text{ nm} \times 12 \text{ nm}$  (**Tab. 4.1**). The sample is mounted on top of an air bearing rotation stage (UPR-160 AIR, Micos, Germany) of a dedicated sample tower (T2 in **Fig. 4.3 b**) for precise tomographic scans. In case of large samples or asymmetric sample mounts, rough lateral alignment above the rotation axis is facilitated by a manual table. Precise positioning is carried out with an  $xyz$  piezo stage (NanoCube P-615, Physik Instrumente, Germany) with  $350 \mu\text{m} \times 350 \mu\text{m} \times 250 \mu\text{m}$  travel range. The rotation unit is moved along the optical axis (about 200 mm travel range) and relative to the x-ray beam by a combined  $xyz$  stage (HPS-170, UPL-160, Micos, Germany). A manual stage for angular alignment of the rotation axis was added to the instrument. However, for convenient use a motorised version of the stage is foreseen as a future upgrade. This configuration of waveguide and sample positioning circumvents the spatial constraints present in previous experiments [119, 63] and allows to bring the sample as close to the waveguide exit as needed, a compact sample environment provided. Magnified in-line holograms were recorded with the Maxipix pixel detector.

### 4.3.5 Optimized waveguide configuration

Even though the original waveguide configuration enables three-dimensional x-ray propagation imaging of biological cells (see chapter 7) several improvements were implemented. First of all, the waveguide positioning system exhibits major drawbacks. Alignment of the small x-ray waveguide channels is aggravated by the lack of reproducibility for repeated scans and parasitic side movements of the positioners [104]. More importantly, long-term stability of the waveguide position relative to the KB focus could not be achieved. The stacking of positioners resulted in an arrangement sensitive to small motions due to thermal drift and vibrations. Upside down mounting of the slip-stick positioners may have also favoured unwanted drifts. As a result, the intensity of the waveguide beam fluctuated significantly (**Fig. 4.7 a**). Lateral shifts between waveguide entrance and KB focus in turn involved varying waveguide far field intensity distributions. Hence, severe empty beam correction problems occurred, creating a need for elaborate data analysis



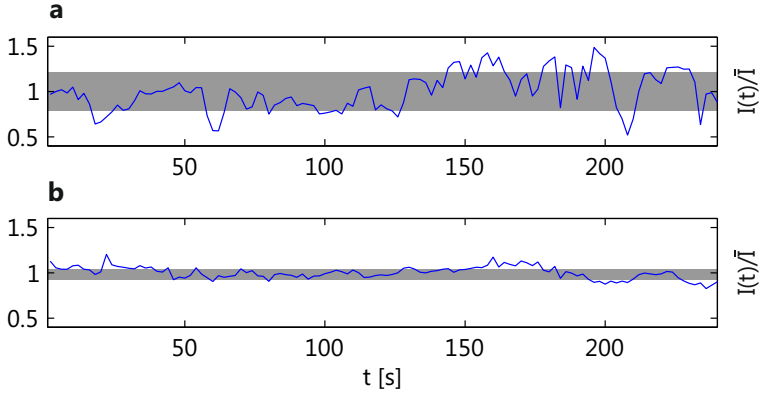


**Figure 4.7:** (a) Intensity fluctuations of a WG beam (XWG2) in the original WG setup. Every two seconds, the integral intensity  $I(t)$  was measured with one second dwell time. The mean intensity is  $\bar{I} = 6 \cdot 10^7$  ph/s, the relative fluctuation  $\sigma/(\bar{I}) = 21\%$ , with standard deviation  $\sigma$ . (b) The same measurement (XWG3) for the optimized WG setup with a mean intensity  $\bar{I} = 2 \cdot 10^8$  ph/s and reduced relative fluctuation of  $\sigma/(\bar{I}) = 6\%$ .

and filtering (see section 7) and limiting the spatial resolution. In addition, the intensity often dropped by an order of magnitude within few minutes, demanding frequent realignment of the waveguide. Moreover, relative movements of waveguide and sample lead to washed out holograms and degraded spatial resolution. Considerable improvements in positioning stability could be achieved by mounting the waveguides on top of the robust sample tower (see **Fig. 4.3 c**) resulting in less fluctuation of the beam intensity (**Fig. 4.7 b**). In addition, the scanning capabilities of the  $xyz$  piezo stage enabled a significantly faster alignment, which was essential to examine new waveguide fabrication techniques and to characterize waveguide channels of different thicknesses and lateral dimensions. Important conclusions could be drawn from experiments performed with the original configuration using waveguides with guiding core dimensions of 35 nm. First, beam confinement well below the guiding core dimensions was achieved (see **Tab. 4.1**) due to the different modes propagating in the waveguide [119, 120]. However, the achieved spatial resolution in imaging applications was considerably lower (see section 7). Due to relatively low photon flux in the order of  $10^7$  photons per second the highly sensitive and noise-free Maxipix detectors was used. The rather large pixel size of  $55 \mu\text{m}$  demands for geometric magnifications of  $M \approx 2000$  to achieve effective pixel sizes in the order of 25 nm (needed for 50 nm full-period resolution for the optimistic case of sampling-limited spatial resolution). This can only be achieved if the sample is moved as close as 2–3 mm to the waveguide exit. While it was possible to do so, the corresponding effective propagation distance of about 2–3 mm ( $z_{\text{eff}} \approx z_1$  for large  $M$ ) resulted in decreased contrast as expected from the PCTF (1.102). Stability issues as stated above degraded the achievable res-

olution especially at long exposure times according to the low photon flux. To circumvent these limitations, an optimized waveguide-detector combination was devised. Based on the fact that the x-ray beam is confined below the waveguide core dimensions, this parameter was relaxed to 60–100 nm (see **Tab. 4.1**, XWG3 and BWG). The resulting x-ray sources, still with lateral dimensions well below 30 nm × 30 nm, showed increased photon flux of up to  $2 \cdot 10^9$  photons per second, which is two orders of magnitude above the achievement in the first experiment. This gain in photon flux allowed to take advantage of the high resolution provided by a scintillator-based and fibre-coupled sCMOS detector (see 4.1). The small pixel size of 6.54 μm requires only a geometric magnification of  $M \approx 650$  to achieve 10 nm sampling of the magnified holograms. This results in a source-sample distance of  $z_1 \approx 8$  mm which allows convenient sample chambers and positioning but most importantly higher contrast due to increased effective propagation distances  $z_{\text{eff}} \approx z_1 \approx 8$  mm compared to the original configuration<sup>2</sup>. The influence of these experimental adjustments on the achievable spatial resolution and contrast is discussed in chapter 8. With the sample tower (T2) occupied by the waveguide, the need for alternative sample positioning arises. For that purpose, a miniaturized *xyz* nano-positioner (SLC-1730, SmarAct, Germany) with crossed-roller slides and optical encoders was installed on top of the rotation stage (T3 in **Fig. 4.3 c**) next to the *xyz* piezo stage used for waveguide alignment. The large travel range of 21 mm × 21 mm × 21 mm and the small minimum step size of 50 nm has proven an ideal combination for high resolution two-dimensional imaging (see chapter 8). For tomographic measurements another sample tower (T4) was mounted on the optical table. A precision rotation stage (PRS-110, Micos, Germany) is placed onto a stack of linear positioners (PLS-85, Micos, Germany). The large travel range of about 200 mm along the optical axis enables high resolution as well as medium resolution and large field of view scans. Two goniometer stages (WT-85 and WT-100, Micos, Germany) below the rotation unit facilitate angular alignment of the rotation axis while a goniometer (MS-1006, Huber, Germany) above the rotation stage is used to center and orient the sample with respect to the axis of rotation.

#### 4.3.6 KB configuration

X-ray waveguides with their small guiding core dimensions and consequently small source sizes have proven an ideal quasi-point source for propagation imaging (see chapters 6,7,8 and [63, 12]). However, the need for sufficient motorized degrees of freedom for waveguide alignment and long-term stability issues along with the reduced photon flux raises the question, whether the pure KB beam of beamline P10 can be used as a source for x-ray propagation imaging with short exposure times [145]. The focal size of about 200 nm would facilitate spatial resolutions below those currently achieved by parallel beam imaging [35]. To this end, waveguides

<sup>2</sup> Since the PCTF is a function of  $\nu^2 z$ , contrast changes differently for different spatial frequencies. However, for a given  $z$  contrast is weak for spatial frequencies below the first maximum of the PCTF at  $\nu = \sqrt{0.5/\lambda z}$ .

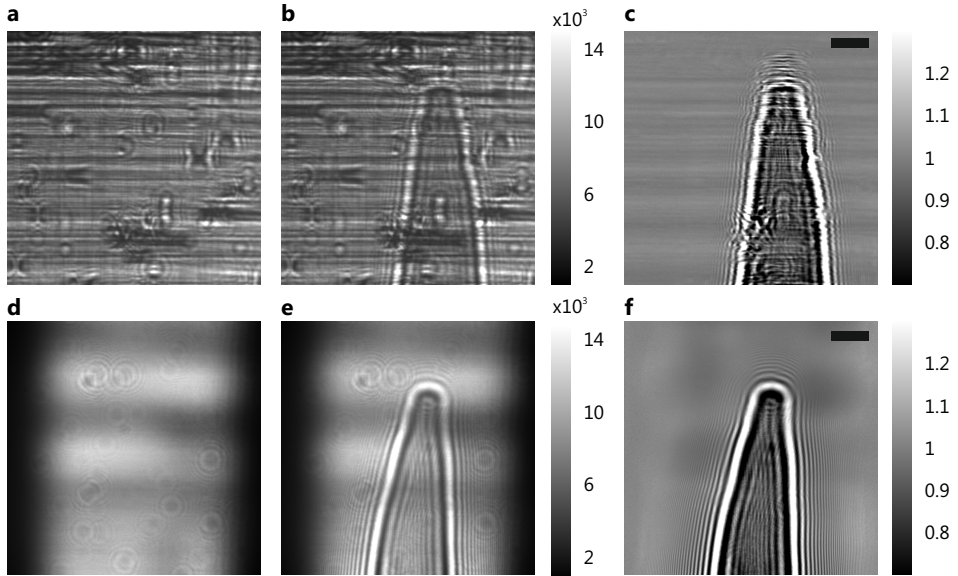


**Figure 4.8:** (a) Empty beam intensity of a pure KB beam at photon energy of 7.9 keV. (b) Hologram of a biological specimen (*C. elegans*). (c) Normalized intensity showing artifacts associated with features in the KB far field. (d-f) Empty beam, hologram and normalized intensity for a similar specimen using a low-pass filtered KB beam (1.4 μm pinhole). Scale bars, 20 μm.

are removed (**Fig. 4.3 d**) and the sample is mounted on the dedicated sample tower (T2). For large field of view imaging at lower resolution, sample tower T4 which was mounted on the optical table in the optimized waveguide configuration can be installed between flight path and detector bench (compare **Fig. 4.3 c,d**). The high photon flux of the KB beam enables fine sampling of holographic fringes based on the high resolution of few micrometers provided by the PCO detector system (see section 4.1).

**Fig. 4.8 a-c** shows empty beam, hologram and normalized intensity for a biological specimen (EPON-embedded *C. elegans*, see [158] for details on sample preparation) at  $z_1 = 0.19$  m recorded within 2 seconds using the PCOx4 at  $z_2 = 5.49$  m. In the domain where the object is located, prominent artifacts in the normalized intensity (**c**) appear which are in strong correlation to the features of the structured KB far field (**a**). While the assumption (1.113) for empty beam correction is exact for an ideal plane wave and experimentally proves to be sufficiently fulfilled for smooth x-ray waveguide far fields, it is obviously violated here for high frequency modulations of the illumination function. Based on the fact that smooth waveguide far fields yield good results, improvement of empty beam correction can be expected if high frequency variations of the KB far field are suppressed. To this end, we note that the Fraunhofer far field intensity is the Fourier transform

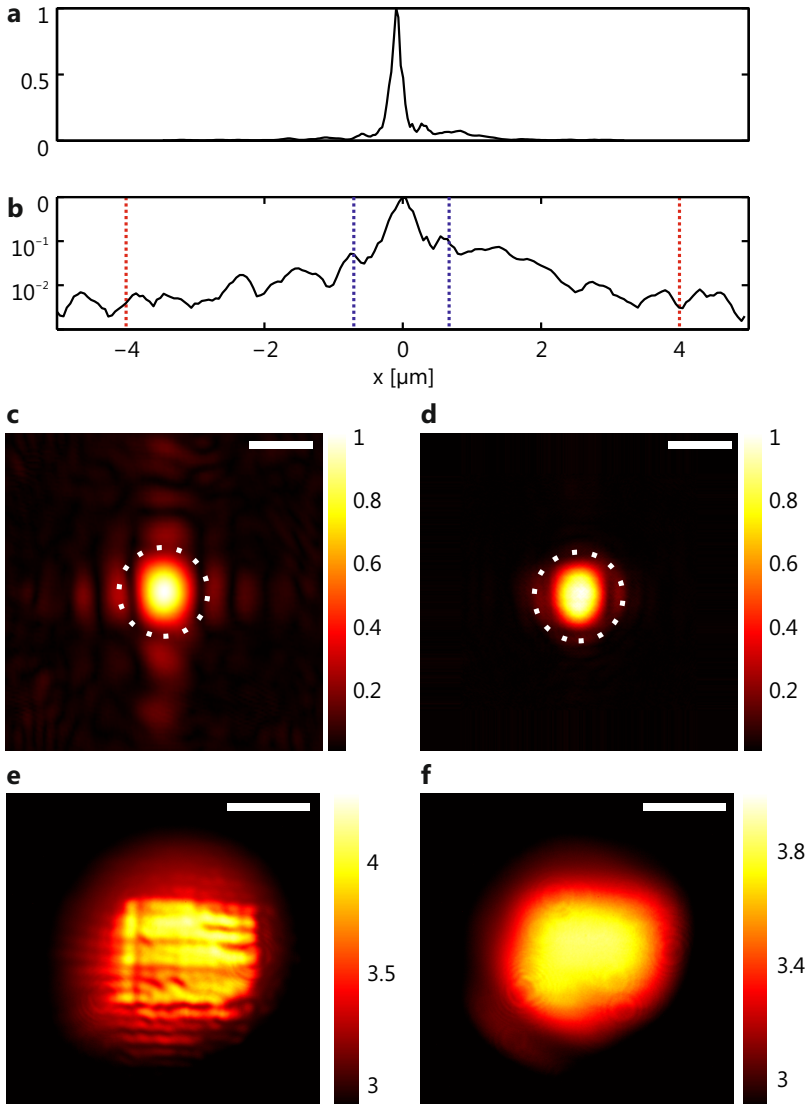


**Figure 4.9:** (a) Normalized intensity distribution in the focal plane of the KB mirrors obtained by scanning a one-dimensional waveguide slice through the focus along the horizontal direction. (b) Logarithmic scaling reveals residual intensity in the tails of the focus. Red and blue lines indicate the diameter of the pinholes used for low-pass filtering. (c,d) Reconstructed normalized amplitude in the focal plane obtained by ptychography [66]. A pinhole of (c)  $8 \mu\text{m}$  diameter and (d)  $1.4 \mu\text{m}$  diameter was placed close to the focal plane. The dashed circles have a diameter of  $1.4 \mu\text{m}$ . (e,f) Measured far field intensity distributions in logarithmic color coding. Scale bars, (a)  $1 \mu\text{m}$ , (b)  $1 \text{ mm}$ .

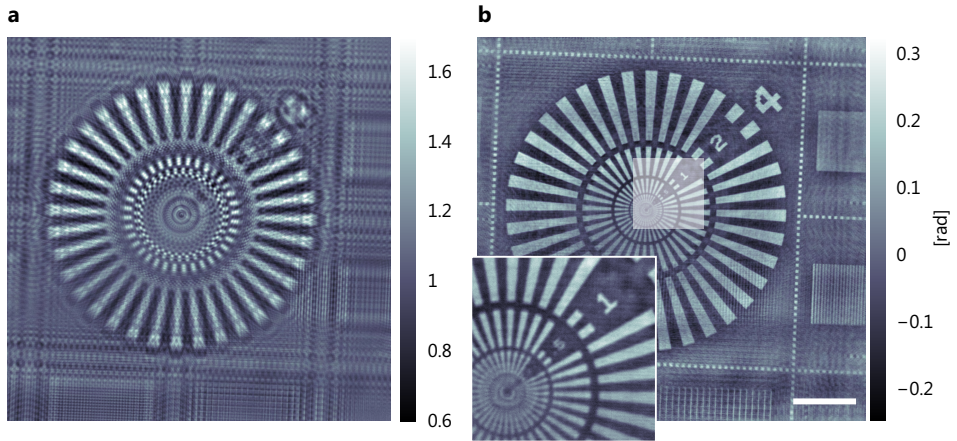


**Figure 4.10:** (a) Normalized intensity of a Tantalum test object recorded with a filtered KB beam ( $1.4\ \mu\text{m}$  pinhole) at a photon energy of  $13.8\ \text{keV}$ . (b) Phase reconstruction obtained by a combined approach of Holo-TIE and iterative refinement using homogeneity. Features down to  $200\ \text{nm}$  in size are visible. Scale bar,  $20\ \mu\text{m}$ .

of the wave field in the focal plane. Thus, high frequency variations in the far field correspond to non-vanishing intensity in the tails of the focus. Indeed, a scan with a one-dimensional x-ray waveguide through the focus along the horizontal direction reveals considerable residual intensity in the tails (**Fig. 4.9 b**) owing to figure errors of the elliptical shape and imperfections on the mirror surface as well as the rectangular window function represented by the mirrors and slits. To suppress high frequency variations in the KB far field a pinhole was inserted as a low-pass filter into the focal plane. An additional motorized  $xyz$  stage (MTS-65, Micos, Germany) was mounted on the optical table (T5) and a  $200\ \mu\text{m}$  thick Pt pinhole (Plano, Germany) with an  $8\ \mu\text{m}$  diameter polished by a focused ion beam was aligned in the beam  $3.95\ \text{mm}$  upstream of the focus. The complex wave field in the focal plane was obtained [66] by scanning x-ray diffraction and ptychographic reconstruction. In short, an object (ATN/XRESO-50HC, NTT-AT, Japan) made of Tantalum was moved laterally along the beam and Fraunhofer diffraction patterns were recorded at each position. The step size was chosen smaller than the object and illumination function dimensions. The resulting redundant information of the overlapping regions was used as a constraint to reconstruct the illuminating wave fields and the object transmission function simultaneously [201, 182, 181, 133].  $21 \times 21$  scan points with a step size of  $100\ \text{nm}$  and an exposure time of 1 second at each point were recorded. The primary beam was attenuated by roughly three orders of magnitude to protect the Pilatus detector from radiation damage. Coherent diffraction imaging requires a high degree of spatial coherence. To this end, slit system S5 was closed to  $100\ \mu\text{m} \times 100\ \mu\text{m}$  to ensure coherent illumination of the KB mirrors [66]. The reconstructed normalized amplitude in the focal plane

is shown in **Fig. 4.9 c**. Next to the central peak (the focus) residual intensity is visible. Therefore, the corresponding far field intensity measured within 10 seconds using the PCOx4 (**e**) shows variations on medium spatial frequencies. However, compared to the unfiltered beam (**Fig. 4.4 a**) high frequency variations are suppressed. The smaller lateral extent of the far field is a consequence of the closed slit system S5 needed for ptychography. Note that for propagation imaging the slit system was opened again. Next, a smaller pinhole with a  $1.4\ \mu\text{m}$  diameter milled by a focused ion beam (EMPA, Switzerland) into a  $200\ \mu\text{m}$  thick W foil was aligned in the beam  $0.5\ \text{mm}$  upstream of the focus. Ptychography was performed with an exposure time of 1.5 seconds per scan point and primary beam attenuation of roughly two orders of magnitude. The normalized amplitude (**d**) is now restricted to an area roughly corresponding to the pinhole diameter of  $1.4\ \mu\text{m}$ . As a result the KB far field appears to be what may be called “smooth”, i.e. only low frequencies carry substantial intensity.

Empty beam correction is now free of apparent artifacts (**Fig. 4.8 d-e**, here slits S5 were opened to  $150\ \mu\text{m} \times 300\ \mu\text{m}$ , h. $\times$ v.) enabling phase retrieval of recorded holograms [158, 117]. It is important to note that the filtered KB beam provides normalized holograms of sufficient quality to apply Holo-TIE, a phase reconstruction technique developed at the GINIX setup (see section 2.5 and [117]). **Fig 4.10 a** shows a normalized hologram of a  $500\ \text{nm}$  thick test object (ATN/XRESO-50HC, NTT-AT, Japan) made of Tantal. The sample was positioned at  $z_1 = 0.19\ \text{m}$  behind the focus and recorded within 5 seconds using the PCOx4 at  $z_2 = 5.42\ \text{m}$ . The photon energy was set to  $13.8\ \text{keV}$  and the slit system S5 was opened to the geometric acceptance of the KB mirrors ( $400\ \mu\text{m} \times 400\ \mu\text{m}$ ). A second hologram was recorded with the sample moved a distance  $\Delta z = 6\ \text{mm}$  along the optical axis (not shown, see [117]). The phase (shown in **b**) was reconstructed using the deterministic Holo-TIE approach and subsequent iterative refinement with a GS-type algorithm. The iterative algorithm utilized a coupling of amplitude and phase of the object transmission function [158] justified for a homogenous object, based on tabulated values of  $\delta$  and  $\beta$  for Ta [116]. Features down to  $200\ \text{nm}$  in size are resolved (inset in **b**) as expected for a KB focus of about  $200\ \text{nm}$ .

#### 4.4 Beamline ID22NI of the ESRF

The nano-imaging endstation ID22NI [137] of beamline ID22 [194] at the European Synchrotron Radiation Facility (ESRF, France) provides a high-flux nanoprobe [17, 16, 206] and the instrumentation for magnified x-ray propagation imaging [145, 126]. The U19 undulator is located at a high- $\beta$  section of the storage ring resulting in a highly asymmetric source with  $25\ \mu\text{m} \times 900\ \mu\text{m}$  (v. $\times$ h., FWHM) lateral extension [17]. A photon energy of  $17\ \text{keV}$  was selected corresponding to the first harmonic of the undulator [126]. While the vertical source size is comparable to the values of the P10 beamline, for small focus sizes and sufficient spatial coherence a virtual source is needed in the horizontal direction. To this end, high-heat-load slits  $27\ \text{m}$  away from the source can be closed to  $10 - 25\ \mu\text{m}$ , depending

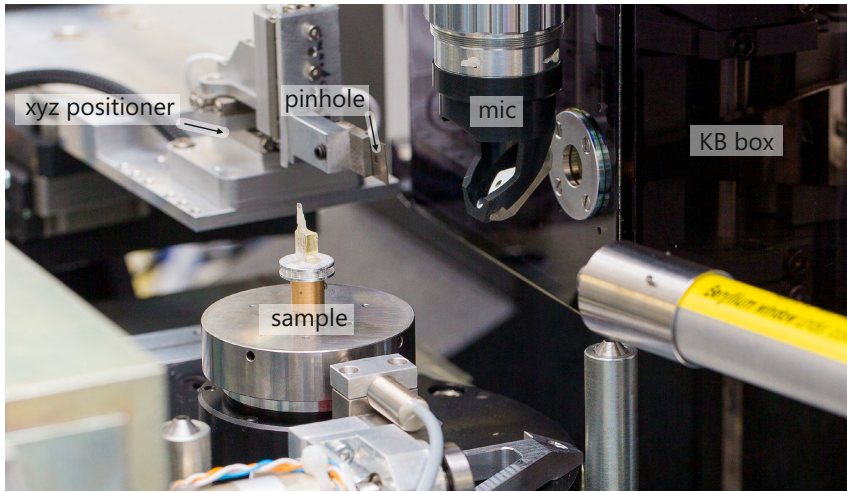


**Figure 4.11:** *Experimental setup at beamline ID22NI with KB box, sample stage and optical microscope (mic) with drilled mirror. The filtering scheme developed at GINIX was implemented by mounting a pinhole on a miniaturized xyz-positioner.*

on the photon flux and focus size needed for the experiment [114, 137]. The current experiment was performed with a  $25\ \mu\text{m}$  slit opening. The KB system is located 63 m from the undulator source and 36 m from the secondary source. It is composed of two graded  $\text{B}_4\text{C}/[\text{W}/\text{B}_4\text{C}]_{25}/\text{Cr}/\text{Si}$  multilayer coated surfaces which are bend by four actuators into elliptical shape [137], suitable for sub-100 nm focusing [93, 92, 148, 224]. The vertical and horizontal mirrors with a length of 112 mm and 76 mm focus the x-ray beam in a plane 180 mm and 83 mm from the mirror centres, respectively. Minimal focus sizes below  $60\ \text{nm} \times 60\ \text{nm}$  (FWHM) have been obtained with this mirror system [8]. To compensate for the loss in photon flux due to secondary source slits, no additional monochromator is inserted into the beam, i.e. the setup is operated in pink beam mode. Along with a mirror reflectivity of 73% this results in a photon flux of about  $10^{12}$  ph/s [114], however at the medium intrinsic monochromaticity of the undulator-multilayer system of  $\Delta E/E = 1.6 \cdot 10^{-2}$  [126]. A dedicated sample stage mounted on a granite block provides high precision movements on air pads over a distance of 320 mm along the optical axis. Sample rotation is facilitated by an air-bearing spindle with low radial and axial errors smaller than 50 nm. The FReLoN detector (see section 4.1) is available to record holograms at source-detector distances up to 1.6 m.

The endstation is routinely used for x-ray propagation imaging especially in combination with the holotomography reconstruction scheme. However, empty beam correction artifacts appear and degrade the image quality as expected for an unfiltered KB beam. **Fig 4.12 a** shows a normalized hologram of  $10\ \mu\text{m}$  polystyrene spheres (4210A, Duke Scientific Corporation) within a polyimide tube of 0.5 mm



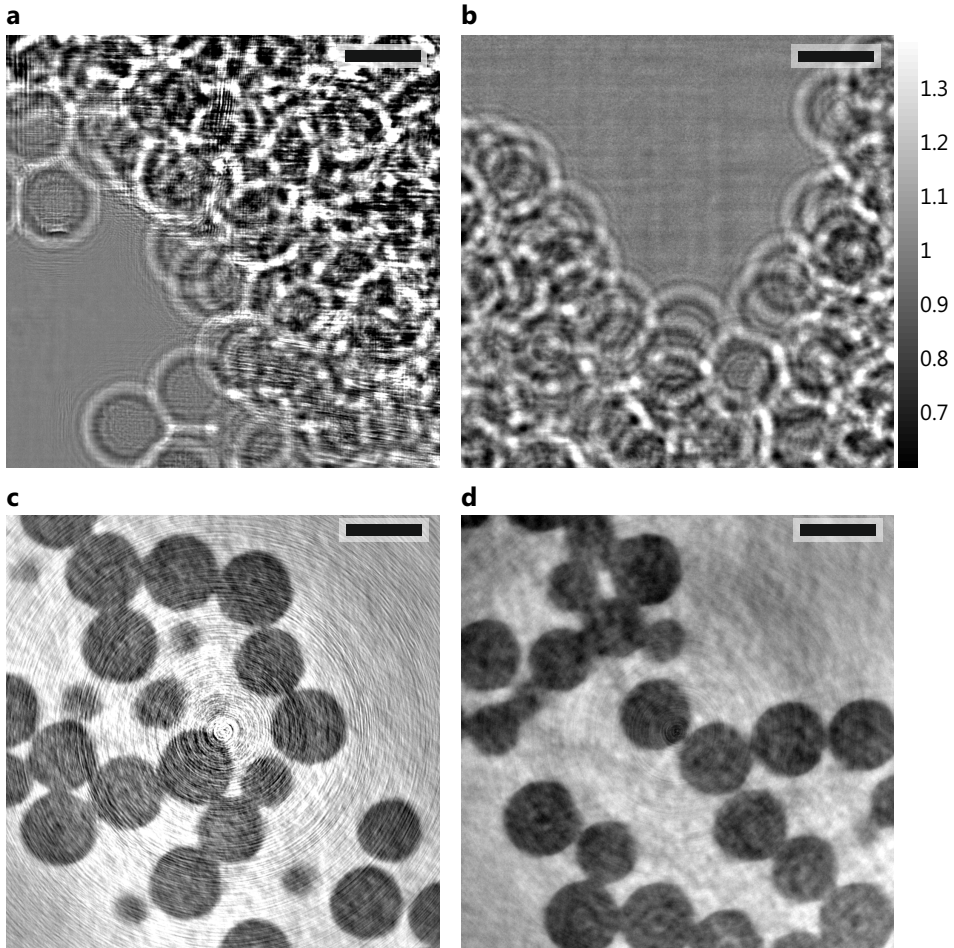


**Figure 4.12:** Normalized hologram of 10  $\mu\text{m}$  polystyrene spheres with (a) pure and (b) low-pass filtered KB beam. (c,d) Corresponding tomographic reconstruction of the electron density. Scalebars, 10  $\mu\text{m}$ .

diameter (Professional Plastics). The sample was placed at  $z_1 = 34.7$  mm, the FReLoN detector at  $z_2 = 526$  mm, resulting in an effective pixel size of 50 nm. Similar to the pure KB results at GINIX, strong artifacts appear, corresponding to stripes in the KB far field. The artifacts manifest as ring artifacts after phase (CTF-based) and tomographic reconstruction as can be seen in **c**. To improve empty beam correction, the filtering scheme developed at GINIX was implemented at the ID22NI. The 1.4  $\mu\text{m}$  diameter pinhole (see section 4.3.6) was aligned in the beam by means of  $xyz$  nano-positioners (SLC-1730, SmarAct, Germany) with crossed-roller slides and optical encoders (Fig. 4.11). The normalized hologram of 10  $\mu\text{m}$  polystyrene spheres with 60 nm effective pixel size shown in **b** exhibits



no high frequency artifacts. Accordingly, no ring artifacts are present after phase and tomographic reconstruction. Together with the results obtained at GINIX we conclude that significant improvements of KB-based x-ray propagation imaging can be achieved by applying the described filtering scheme. However, the rather improvised mounting of the pinhole at beamline ID22 resulted in unstable pinhole positioning. Hence, the pinhole was not used for tomograms of biological samples (see chapter 6).

## 4.5 Distance calibration

In x-ray propagation imaging it is important to know the geometric parameters  $z_1$  and  $z_2$  to determine magnification  $M$ , effective pixel size  $\Delta x$  and effective propagation distance  $z_{\text{eff}}$  accurately because they are needed for phase reconstruction schemes. Moreover, a correct pixel scaling in the sample plane is crucial for quantitative data analysis and interpretation.

### 4.5.1 Distance calibration with periodic structure

The distances  $z_1$  and  $z_2$  can be obtained by the following procedure. A periodic object with known period length  $\lambda_{\text{real}}$  is positioned in the beam at different unknown source-sample positions  $z_1 + n_z \cdot \Delta z_1$  with step size  $\Delta z_1$  and integers  $n_z$ . Holograms are recorded at each position by a detector placed at unknown distance  $z_2$  from the source. Next, the number of pixels per period  $n_{\text{pixel}}$  is determined for each hologram. To this end, all pixel values along the direction perpendicular to the periodic structure are summed up yielding a one-dimensional profile. A peak in the corresponding power spectral density at  $\nu_{\text{max}}$  corresponds to the spatial frequency of the periodic feature. Thus, the number of pixels per period is

$$n_{\text{pixel}} = \nu_{\text{max}}^{-1}. \quad (4.1)$$

The geometric magnification  $M$  can be calculated from the known period length  $\lambda_{\text{real}}$  and the physical pixel size  $\Delta x$  by

$$M = \frac{n_{\text{pixel}} \cdot \Delta x}{\lambda_{\text{real}}}. \quad (4.2)$$

The geometric magnification in turn can be written as

$$\begin{aligned} \frac{1}{M} &= \frac{z_1 + n_z \Delta z_1}{z_2} \\ &= \frac{z_1}{z_2} + \frac{\Delta z_1}{z_2} n_z \\ &= a + b \cdot n_z. \end{aligned} \quad (4.3)$$

Thus,  $a$  and  $b$  can be obtained by a linear fit and by  $z_2 = \Delta z_1/b$  and  $z_1 = a \cdot \Delta z_1/b$ , both distances can be calculated.

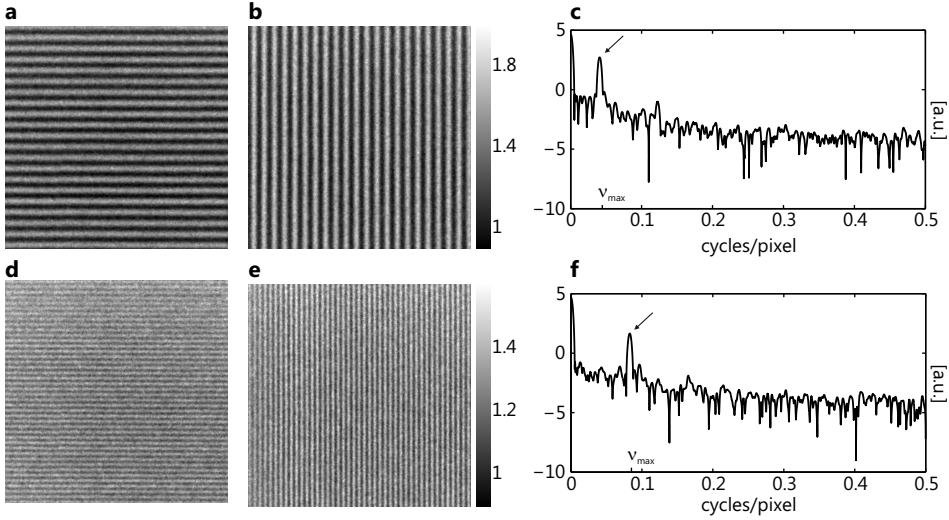


**Figure 4.13:** Normalized holograms of an object with periodic features ( $\lambda_{\text{real}} = 200 \text{ nm}$ ) aligned along (a) the horizontal and (b) vertical direction. (d,e) Holograms recorded with the object moved a distance  $130 \cdot \Delta z_1 = 6.5 \text{ mm}$  downstream. (c,f) Power spectral densities of one dimensional profiles obtained by summing up all pixel values along the direction perpendicular to the periodic structure.

**Fig. 4.13** illustrates the determination of  $M$  for a  $500 \text{ nm}$  thick object (ATN/XRESO-50HC, NTT-AT, Japan) made of Tantal. The periodicity was  $\lambda_{\text{real}} = 200 \text{ nm}$  and the step size was  $\Delta z_1 = 50 \mu\text{m}$ . Normalized holograms at two different planes separated by  $130 \cdot n_z = 6.5 \text{ mm}$  are shown, both for horizontally (a,d) and vertically (b,e) oriented lines. The PSDs (shown for the horizontal lines) of the one-dimensional profiles corresponding to both planes (c,f) demonstrate how the peak (small arrow) moves as the geometric magnification changes. **Fig. 4.14** shows linear fits as advised by equation (4.3) for the horizontal and vertical direction. Only distances where the peak in the PSD could be clearly identified were used for the fits. For the present example, one obtains  $z_{1,x} = 6.3805 \text{ mm}$  and  $z_{2,x} = 5.064 \text{ m}$  for the horizontal direction as well as  $z_{1,y} = 6.001 \text{ mm}$  and  $z_{2,y} = 5.075 \text{ m}$  for the vertical direction. The detector positions in both directions coincide within a relative deviation of  $0.2\%$ . The resulting difference between source-sample distances  $z_{1,x} - z_{1,y} = 379.5 \mu\text{m}$  fits very well to the separation of the two one-dimensional sources provided by the crossed x-ray waveguide (see section 4.3.3), since the second waveguide slice (aligned horizontally and confining the beam vertically) had a length of  $l_2 = 379 \mu\text{m}$  (XWG3).

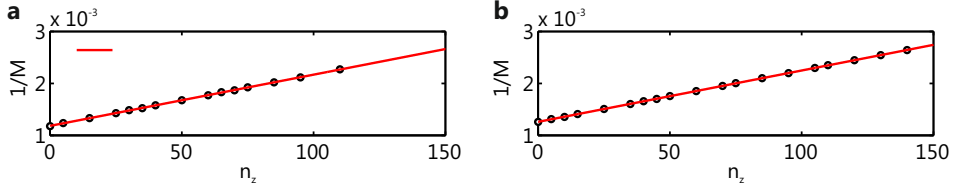


**Figure 4.14:** Linear fits of the form  $\frac{1}{M} = a + b \cdot n_z$  yield the source-sample distance  $z_1 a \cdot \Delta z_1 / b$  and the source-detector distance  $z_2 = \Delta z_1 / b$ .

#### 4.5.2 Distance calibration using holographic reconstruction

When a new sample is mounted in the beam,  $z_1$  has to be determined again.<sup>3</sup> The deterministic one step holographic reconstruction proves very helpful here. **Fig. 4.15** shows holographic reconstructions of a simulated hologram with  $F_{\text{sim}}^{10} = 0.5$  for different Fresnel number  $F^1 = [0.98, 1, 1.02] \cdot F_{\text{sim}}$ . Due to high sensitivity of the holographic reconstruction with respect to small deviations of  $F^1$ , the correct Fresnel number can be found accurately. We assume that the source-detector distance  $z_D = z_1 + z_2$  was already determined in a separate measurement (e.g. as described above) and use the relations

$$\begin{aligned} \Delta x &= \frac{\Delta p}{M}, \\ M &= z_D / z_1, \\ z_{\text{eff}} &= \frac{z_D - z_1}{M}, \\ F &= \frac{\Delta x^2}{\lambda z_{\text{eff}}}. \end{aligned}$$

Since  $z_D$ , detector pixel size  $\Delta p$  and  $\lambda$  are known, with Fresnel number  $F^1$  the source-sample distance  $z_1$  can be calculated as

$$z_1 = z_D / \left(1 + \frac{\Delta p^2}{F^1 z_D \lambda}\right).$$

Propagation of error for the common experimental case  $M \gg 1$  yields

$$\begin{aligned} \frac{\Delta z_1}{z_1} &= \frac{1}{1 + \frac{1}{M}} \frac{\Delta F^1}{F^1} \\ &\simeq \frac{\Delta F^1}{F^1}. \end{aligned}$$

Therefore,  $z_1$  can be determined with the same relative accuracy as the Fresnel number, neglecting the uncertainty of  $z_D$ .

<sup>3</sup> An alternative approach is to determine the axis of rotation of a tomographic sample tower once, e.g. by the method using a known period structure. Then, new samples are aligned into the axis of rotation.

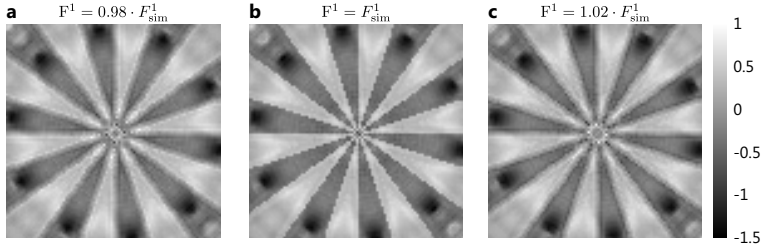


**Figure 4.15:** Determination of Fresnel number  $F^1_{\text{sim}} = \frac{\Delta x^2}{\lambda z_{\text{eff}}}$  for a simulated hologram at  $F^1_{\text{sim}} = 0.5$  (**Fig. 2.1 d**) of an object with maximum phase shift  $\pi/4$  and low maximal absorption of 0.8%, corresponding to  $\delta/\beta = 10^3$ . (a-c) Phase distribution of the holographic reconstruction for 2% deviation of the correct Fresnel number  $F^1 = [0.98, 1, 1.02] \cdot F^1_{\text{sim}}$ .

## 5 Three-dimensional imaging of rodent cochlea

The cochlea is the auditory end organ in the inner ear designed to encode sound into neuronal activity. To illustrate its main function, **Fig. 5.1** shows relevant anatomical parts of outer, middle and inner ear involved in the process of hearing. Sound waves travel along the external auditory canal and stimulate the ear drum which separates outer and middle ear. The middle ear contains the three ear bones (ossicles) hammer, anvil and stapes located in the air-filled tympanic cavity. They transmit the vibrations of the tympanic membrane to the fluid within the cochlea by the footplate of the stapes attached to the oval window. The cochlea itself is divided into three liquid-filled cavities: scala tympani, scala media and scala vestibuli. At the apex of the cochlea, scala tympani and scala vestibuli are connected by a minute hole called helicotrema. Scala media is separated from

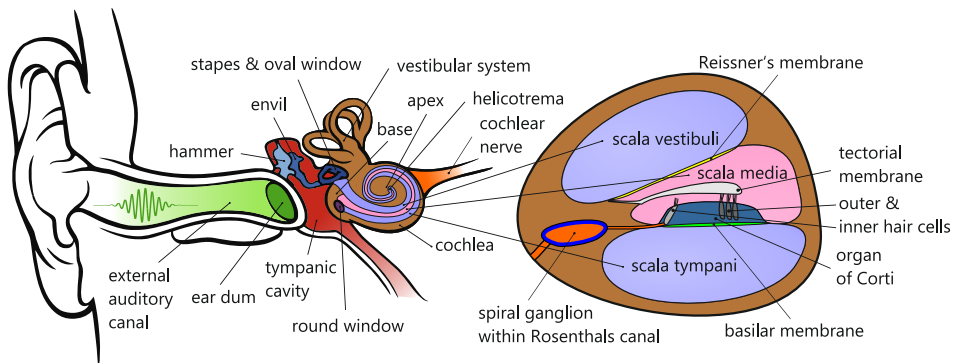


**Figure 5.1:** Anatomy parts relevant for hearing. Outer ear with external auditory canal and ear drum. Middle ear with tympanic cavity, hammer, anvil and stapes. The inner ear consists of vestibular system and cochlea. The footplate of the stapes is attached to the oval window near the base of the cochlea. The membrane of the round window separates middle ear and cochlea. The cavities scala tympani, scala vestibuli and scala media are separated by the basilar membrane and Reissner's membranes. Scalae tympani and vestibuli are connected at the apex by the helicotrema. The sound-sensitive Organ of Corti with outer and inner hair cells is located on the basilar membrane below the tectorial membrane. Neurons of the cochlear nerve, in synaptic contact with the inner hair cells, are located in the spiral ganglion within Rosenthal's canals. Drawing based on [30].

scala tympani and scala vestibuli by the basilar membrane and the thin Reissner membrane, respectively. Sound waves originating at the oval window travel along the scala vestibuli and excite vibrations of the basilar membrane. The freely oscillating membrane of the round window (separating scala tympani and the tympanic cavity) ensures movement of the fluid within the cochlea. The basilar membrane varies in thickness, stiffness and width from base to apex. This results in different resonant sound frequencies at different locations along the membrane. Therefore, the basilar membrane performs a Fourier analysis of the incoming sound wave with high frequency resonances located near the oval window and low frequency resonances near the helicotrema. The organ of Corti is located on the basilar membrane and acts as the interface between mechanical sound oscillations and auditory nervous system. Outer hair cells which are in contact to the tectorial membrane serve as local non-linear amplifiers of the vibrations. Inner hair cells respond to vibrations by releasing neurotransmitters which in turn trigger action potentials in corresponding nerve cells. The cell bodies of these neurons lie in the spiral ganglion within Rosenthals canal with their axons reaching to the central nervous system. Depending on their position relative to the basilar membrane the spiral ganglion neurons encode distinct sound frequencies. This relation between spatial position and sound frequency is called tonotopy. The brain interprets the nerve signal by a corresponding tonotopic map to evaluate the frequency of the perceived tone. When deafness is caused by malfunctioning hair cells, treatment by means of cochlear implants utilizes this tonotopic organisation. At first, a microphone records the sound which is decomposed into its frequency components. Next, electrodes implanted within scala tympani at different positions along the basilar membrane bypass the organ of Corti and directly stimulate the spiral ganglion neurons. The nerve activity is then interpreted by the brain as if the corresponding tone is being heard.

## 5.1 Challenges of cochlear imaging

Detailed knowledge about the delicate and complex cochlea morphology is necessary to understand malformations caused by genetic defects, improve the treatment of hearing diseases and optimize the design of cochlear implants [177, 127]. Therefore, three-dimensional visualization with sufficient contrast and resolution for functional soft tissues is required. Since cochlea morphology comprises soft tissue within surrounding bone (**Fig. 5.1**) most methods to determine its 3D, structure such as classical histology [129], optical coherence tomography [220], orthogonal-plane optical fluorescence [213] and magnetic resonance imaging [202], require invasive sample preparation (e.g. slicing [129], staining [129, 202, 213], dehydrating [129], opening the bony cochlea wall [220]) or lack sufficient contrast or spatial resolution. Specific advantages of x-ray imaging on the other hand concern the combination of high resolution and compatibility with unsliced, unstained and hydrated specimens. Hard x-ray microtomography based on absorption contrast has been used for non-destructive 3D structure determination of human cochleae

[212, 67, 127]. For small scale soft tissues e.g. within the mouse cochlea, absorption is weak and the interaction with x-rays results predominantly in a shifted phase. Therefore, coherent x-ray methods exploiting the phase shift induced by the sample are particularly well suited for cochlea imaging, as shown by recent synchrotron radiation studies [177, 176, 180]. However, these methods rely on the (limited) availability of third generation synchrotron facilities, inhibiting a routine use in the laboratory, which is needed for long-term biomedical research.

The goal of the present experiments was to implement 3D imaging of functional mouse cochlear soft tissue within the surrounding bone using compact laboratory microfocus x-ray sources. A specific application is the analysis and characterisation of optogenetic cochlear implants developed by the Inner Ear Lab of the University of Göttingen. Optogenetic stimulation of spiral ganglion neurons using light-gated ion channels is a novel promising approach to overcome the limited sound frequency resolution of current cochlear implants. In this research, a central challenge is the determination of position and orientation of light emitter(s) relative to the spiral ganglion. Grating based phase contrast imaging with compact sources is currently limited to spatial resolutions above  $30\ \mu\text{m}$  [170, 169, 115, 50, 13], a resolution range not suitable to identify small membranes or nerve fibres within the mouse cochlea. Therefore, a combination of cone-beam propagation based phase contrast and a fast Fourier-based phase reconstruction procedure (BAC, section 2.2.2) is presented in this chapter for biomedical tomography towards high resolution well below  $10\ \mu\text{m}$ .<sup>1</sup>

## 5.2 Experiment

### 5.2.1 Experimental setup

A series of experiments was performed at the laboratory instrument for phase-contrast microtomography JuLiA (section 4.2). Several tomographic phase-contrast datasets of mouse and rat cochleae were recorded using the solid target source configuration with geometric magnification  $M > 3$  (see **Fig. 5.2a**). The suitability of this compact and reliable setup was examined for 3D cochlea imaging and especially optogenetic cochlear implant research. The high-brilliance liquid-metal-jet x-ray source was then used (i) to decrease accumulation time and (ii) to increase spatial resolution using an optimized geometric arrangement of source, sample and detector (see **Fig. 5.2b**). To characterize the spatial resolution of a particular setup an absorbing test structure (RT RC-03, JIMA, Japan) was used. Polystyrene spheres with  $10\ \mu\text{m}$  diameter (Sigma-Aldrich, USA) on a  $200\ \mu\text{m}$  thick  $1.5 \times 1.5\text{mm}^2$   $\text{Si}_3\text{N}_4$  window (Silson, UK) served as phase contrast test samples. The experiments were carried out with different source and detector configurations as well as geometric parameters. A list of relevant parameters can be found in **Tab. 5.1** for cochlea datasets and in **Tab. 5.2** for measurements with test structures. If an increased signal-to-noise ratio was necessary several detector accumulations

---

<sup>1</sup> The work presented here has been published in a shorter form in [10] before.

were recorded and summed up. Since no drift correction was performed, for the sake of simplicity only the total accumulation time per projection is listed. For all datasets a corresponding empty beam intensity distribution was recorded.

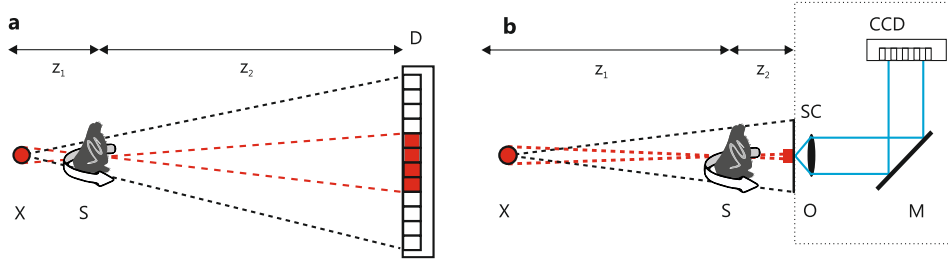


**Figure 5.2:** Experimental geometry for (a) high and (b) low geometric magnification. The sample ( $S$ ) is placed on a tomographic stage at a distance  $z_1$  behind the x-ray source ( $X$ ), the detector is placed at  $z_2$  behind the sample (penumbral blur shown in red). For low geometric magnifications a high resolution detector system is used (scintillation screen ( $SC$ ), objective ( $O$ ), mirror ( $M$ ), optical CCD, see section 4.1).

### 5.2.2 Sample preparation and mounting<sup>2</sup>

Different preparation methods were used, listed for each specimen in **Tab. 5.1**.

- (i) The spiral ganglion neurons of the cochleae which were used for optogenetic stimulation experiments were genetically rendered sensitive to light. A small window in the bony cochlear capsule (cochleostomy) was cut. Prior to the imaging experiment the spiral ganglion neurons were stimulated either by a high power LED put onto the cochleostomy or an optical fibre inserted through the cochleostomy. Subsequently, brainstem responses to light stimulation were recorded (see [90] for details on optogenetic experiments). After the optogenetic experiment, either the LED was removed or the fibre was fixed in place with dental cement. The cochlea was carefully dissected from the skull and chemically fixed. The organ was slowly perfused through the round and oval window with PFA 4% in phosphate buffer solution (PBS). Finally, the posterior semicircular canal was opened to facilitate the diffusion of the fixative in the endolymphatic space. The organ was maintained in fixative for 1 h, washed with PBS and then mounted for x-ray measurements (see below).
- (ii) For cochleae without cochleostomy, a small window in the bony capsule near the apex was cut to facilitate chemical fixation as described in (i)

<sup>2</sup> The preparation of mouse and rat cochleae as well as the optogenetic measurements were performed at the Inner Ear Lab of the University of Göttingen Medical Center. Victor Hernandez performed the preparation and measurements, Tobias Moser supervised the optogenetic implant study.



Figure	5.6 - 5.10	5.11	5.17 a		5.17 b
		5.15 a,c	5.15 b,d		
		5.16 a	5.16 b		
Detector	FDI	sCMOS	PCOx10	PCOx4	LCX
Pixel size [ $\mu\text{m}$ ]	6.54	6.54	0.74	1.85	20
$z_1$ [mm]	78	77	77	93	120
$z_2$ [mm]	116	168	18	8.5	460
$z_1 + z_2$ [mm]	194	245	95	101.5	580
$M$	2.49	3.18	1.23	1.09	4.83
$p_{\text{eff}}$ [ $\mu\text{m}$ ]	2.63	2.06	0.6	1.7	4.13
$z_{\text{eff}}$ [mm]	47	53	15	7.8	95
Metal target	Solid	Liquid	Liquid	Liquid	Solid
e-beam power [W]	4.2	40	40	42	4.2
Accumulation					
time [s]	20	2	90	40	44
BAC $\alpha$	0.05	0.07	0.03	-	0.3
BAC $\gamma$	0.15	0.16	0.25	-	0.17
Number of					
projections	916	916	916	1801	1831
Angular step	0.2	0.2	0.2	0.1	0.1
Total time [h]	5	0.5	23	20	22.4
Sample preparation	i	iii	iii	ii	ii

**Table 5.1:** Main experimental parameters used for cochlea datasets. The table is divided into detector and geometric parameters, x-ray source settings, phase reconstruction parameters, tomography measurement parameters and sample preparation with  $z_1$  source-sample distance,  $z_2$  sample-detector distance,  $M$  geometric magnification,  $p_{\text{eff}}$  effective pixel size,  $z_{\text{eff}}$  effective propagation distance, BAC  $\alpha$  and  $\beta$  parameters of Bronnikov Aided Correction.

Figure	5.13 a	5.13 d	5.13 b,c	5.13 e,f	5.14
Detector	FDI	PCOx10	LCX	PCOx20	PCOx20
Binning				2x2	2x2
Pixel size [ $\mu\text{m}$ ]	6.54	0.74	20	0.74	0.74
$z_1$ [mm]	72	95	70	65	82.4-65
$z_2$ [mm]	418	3	1930	20	2.6-20
$z_1 + z_2$ [mm]	490	98	2000	85	85
$M$	6.81	1.03	28.57	1.31	1.03-1.31
$p_{\text{eff}}$ [ $\mu\text{m}$ ]	0.96	0.72	0.7	0.57	0.72-0.57
$z_{\text{eff}}$ [mm]	61	3	68	15.3	2.5-15.3
Metal target	Liquid	Liquid	Liquid	Liquid	Liquid
e-beam power [W]	20	42	35	35	35
Accumulation time [s]	50	600	3600	3600	3600
BAC $\alpha$	-	-	0.01	0.01	0.01
BAC $\gamma$	-	-	0.16	0.15	0.15

**Table 5.2:** Main experimental parameters used for test structure measurements. The table is divided into detector and geometric parameters, x-ray source settings and phase reconstruction parameters with  $z_1$  source-sample distance,  $z_2$  sample-detector distance,  $M$  geometric magnification,  $p_{\text{eff}}$  effective pixel size,  $z_{\text{eff}}$  effective propagation distance, BAC  $\alpha$  and  $\gamma$  parameters of Bronnikov Aided Correction.

- (iii) For preparation of intact cochleae, mice between 4 and 6 weeks old were intracardially perfused with a fixative solution of PFA 4% in PBS in deep terminal anaesthesia following intraperitoneal injection of a mixture of Ketamine/Xylazin (0.125/5 mg/kg). A longitudinal incision was performed along the midline, from xiphoid cartilage to the pelvis to expose the abdominal cavity. The diaphragm was opened to allow access to the rib cavity and two parallel incisions were done following the lateral borders of the sternum. The bone was then retracted using forceps to expose the heart. A needle was inserted into the heart through a small nick in the apex of the left ventricle and the right auricle was cut. PBS solution was then slowly perfused until blood was cleared from body and the fixative solution was then injected. Directly afterwards, the cochlea was extracted, maintained in fixative for 1 h, washed with PBS and mounted for x-ray measurements.

During tomography measurements the extracted fixed cochlea was kept in air, facilitated by the holder shown in **Fig. 5.3 a**. The organ was glued with 2-

component epoxy resin adhesive (Plus sofortfest, UHU, Germany) onto a pipette tip (Eppendorf, Germany) which was cut to the desired length. Tip and cochlea were then glued onto a magnetic stainless steel goniometer base (GB-B1, MiTeGen, USA) which serves as a standard magnetic holder at the JuLiA instrument. The conical design of the pin allows to align the cochlea perpendicular to the base plate and therefore parallel to the rotation axis.

The height of the cochlea above the base was chosen to be identical to the height of a copper grid which was used to align the rotation axis and to determine the center of the x-ray beam (see section 5.2.3). The  $10\ \mu\text{m}$  thick copper alignment grid with a period of  $63.5\ \mu\text{m}$  (Square 400 mesh, Plano) was glued (Plus schnellfest, UHU, Germany) onto a  $8 \times 8\ \text{mm}^2$  polypropylene foil of about  $500\ \text{nm}$  thickness, mounted on a customized magnetic holder **Fig. 5.3 b**). Then, the holders can easily be placed onto a mount above the rotation stage which is equipped with a small magnet (Fig. 5.3 c).

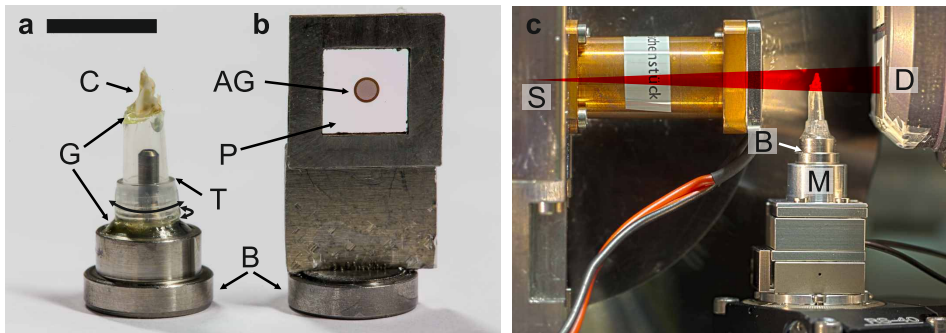


**Figure 5.3:** The cochlea (C) is glued (G) onto a pipette tip (T). The tip is then glued onto a magnetic stainless steel base (B). The copper alignment grid (AG) is glued onto a polypropylene foil (P) mounted on a stainless steel base (B). The magnetic bases can be placed onto a mount (M) above the rotation stage equipped with a small magnet and positioned between x-ray source (S) and detector (D).

### 5.2.3 Alignment of rotation axis

For an artifact free tomographic reconstruction the axis of rotation has to be aligned carefully with respect to angles  $\alpha$  and  $\beta$ . To this end, the copper alignment grid (Fig. 5.3 b) is mounted. For the following alignment procedure it is assumed that the  $sx$  positioner above the rotation stage is fabricated and mounted in such a way that it moves perpendicular to the axis of rotation (see section 4.2 for positioners configuration and notation).

- (i) The grid is moved into the axis of rotation, using the  $sx$  and  $sz$  positioners at rotation angles  $\theta = (0; 180)^\circ$  and  $\theta = (90; 270)^\circ$  (Fig. 5.4 a,b, indicated in orange), respectively.

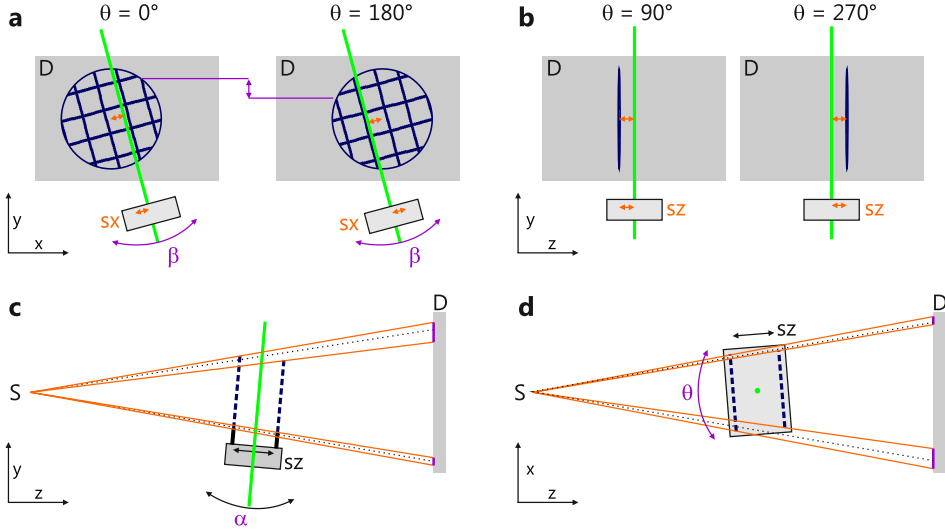


**Figure 5.4:** Alignment of rotation axis (green). A copper alignment grid (blue) is placed between x-ray source (S) and detector (D). (a,b) Alignment of the grid relative to the axis of rotation using positioners  $s_x$  and  $s_z$  (indicated in orange) and (a) alignment of angle  $\beta$  (indicated in purple). (c,d) Alignment of angles  $\alpha$  and  $\theta$  (indicated in purple) by moving the grid above the axis of rotation (for  $\theta = 0^\circ$ ).

- (ii) The axis of rotation is centered relative to the detector using the  $x$  translation below the rotation stage (see section 4.2).
- (iii) The grid is now centered relative to the rotation axis. Since it is only  $10\ \mu\text{m}$  thick it can be rotated  $180^\circ$  with respect to  $\theta$  without any cone-beam magnification effects. A linear fit to the  $(x, y)$  coordinates of corresponding grid intersections at  $\theta = 0^\circ$  and  $\theta = 180^\circ$  (**Fig. 5.4 a**, indicated in purple) yields the angle  $\beta$  which is then corrected by the motorized cradle below the rotation stage.
- (iv) The grid is moved by  $\pm 2\ \text{mm}$  above the rotation axis (at  $\theta = 0^\circ$ ) using the  $s_z$  positioner. In addition to the different geometric magnifications a lateral shift between the two grids exists (**Fig. 5.4 c**, indicated in purple) if the angle  $\alpha$  is not aligned correctly. The corresponding offset in  $\alpha$  is corrected by the motorized cradle below the rotation stage.
- (v) The lateral shift as described in (iii) is also used to determine  $\theta = 0^\circ$  (**Fig. 5.4 d**, indicated in purple).

To check the alignment, the grid is moved again by  $\pm 2\ \text{mm}$  above the rotation axis (at  $\theta = 0^\circ$ ) and images  $I_1(\mathbf{r}_\perp)$  and  $I_2(\mathbf{r}_\perp)$  are recorded, respectively. (**Fig. 5.5 a,b**). A pixelwise division  $I_1(\mathbf{r}_\perp)/I_2(\mathbf{r}_\perp)$  results in the image shown in **Fig.**

**5.5 c.** Since the contrast vanishes exactly at the center of the image, no lateral drift between  $I_1$  and  $I_2$  is present, apart from the differences in magnification due to cone-beam illumination. Note that due to spatial constraints, the pivot points of the cradles below the rotation stage do not coincide with the center of the illumination cone. Therefore, each rotation of  $\alpha$  and  $\beta$  has to be corrected for by a subsequent movement in  $x$  and  $y$  during alignment. Future upgrades of the instrumentation at JuLiA should aim at a sample mounting in the pivot point.

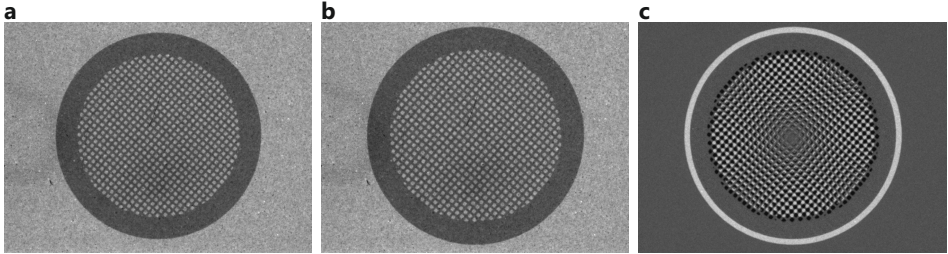


**Figure 5.5:** Image of the copper alignment grid moved (a) +2 mm ( $I_1$ ) and (b) -2 mm ( $I_2$ ) relative to the rotation axis using the  $sz$  positioner above the rotation stage resulting in different geometric magnifications (c) Pixelwise division  $I_1(\mathbf{r}_\perp)/I_2(\mathbf{r}_\perp)$  of the images shown in (a) and (b).

## 5.3 Data analysis

### 5.3.1 Phase and tomographic reconstruction

Phase reconstruction is illustrated for a particular configuration of the setup. While geometric parameters and therefore the degree of phase contrast may vary between the datasets, the same steps of analysis were performed for all datasets with slightly different reconstruction parameters (see **Tab. 5.1** and **5.2**). Due to the homogenous illumination the normalized intensity  $\bar{I}_\theta(\mathbf{r}_\perp, z_{\text{eff}})$  with a cochlea in the beam shows no artifacts (**Fig. 5.6 a**). Hence, no further image processing is needed prior to phase reconstruction. Corresponding to a Fresnel number of  $F_{10} \approx 80$  the data shows edge enhancement as can be seen in the profiles across the optical fibre (dashed lines in **Fig. 5.6**, profiles shown in **Fig. 5.7**). Compared to absorption imaging, this edge-enhancement allows higher contrast for low absorbing features and enables increased spatial resolution [139, 33]. However, tomography of such phase contrast images would result in disturbing edge-artifacts in the 3D data and consequently inhibit automatic segmentation. Contrarily, phase reconstruction circumvents those artifacts, simplifies the image segmentation process [219] and improves the signal-to-noise ratio in tomographic reconstructions [19]. Application of the MBA algorithm (equation 2.22) to the normalized intensity yields an approximation of the phase  $\phi(\mathbf{r}_\perp)$  of the object transmission function suitable for tomography (**Fig. 5.6 b**).

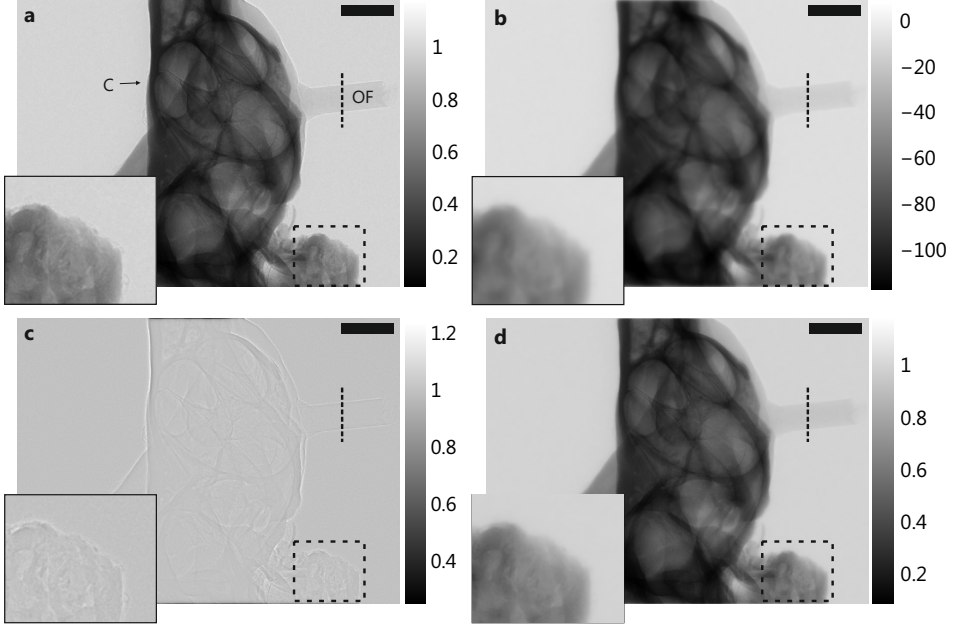


**Figure 5.6:** (a) Raw projection image  $\bar{I}_\theta(\mathbf{r}_\perp, z_{\text{eff}})$  of a mouse cochlea ( $C$ ) with implanted optical fibre ( $OF$ ) used for optogenetic characterisations. (b) Reconstruction of the phase  $\tilde{\phi}(\mathbf{r}_\perp)$  using modified Bronnikov algorithm (MBA). (c) Hypothetical pure phase contrast image  $C$  used to reconstruct (d) the amplitude  $I_\theta^0(\mathbf{r}_\perp)$  using Bronnikov aided correction (BAC). The insets show a magnified view of the region marked with the dashed rectangles. Scale bars, 500  $\mu\text{m}$ .

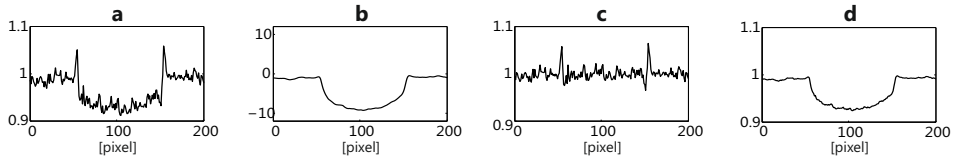


**Figure 5.7:** Profiles along the optical fibre corresponding to the dashed lines in Fig. 5.6 a-d). (a) Edge-enhancement for the projection image is clearly visible. The signal-to-noise ratio is increased by phase reconstruction as can be seen for (b) MBA and (d) BAC.

Note that the MBA reconstruction yields edge-artifact free tomographic reconstructions but shows significant blurring compared to the normalized intensity. Since the bony parts of the cochlea give rise to strong absorption, a subsequent reconstruction of the amplitude  $I_\theta(\mathbf{r}_\perp, 0)$  using the correction signal  $C(\mathbf{r}_\perp)$  of the BAC algorithm (equation 2.26) shown in **Fig. 5.6 c**, results in superior image quality (**Fig. 5.6 d**). Notably, the images are sharper compared to the MBA reconstruction and at the same time enable edge-artifact free tomographic reconstructions. The chosen parameters  $\alpha$  and  $\gamma$  of the algorithm are listed in **Tab. 5.1** for cochlea datasets and in **Tab. 5.2** for measurements with test structures. The amplitudes  $I_\theta(\mathbf{r}_\perp, 0)$  were reconstructed for  $\theta \in [0, 183]^\circ$  from 916 phase contrast projections (angular increment of  $0.2^\circ$ ). Cone-beam filtered backprojection (section 3.3) then yields the three-dimensional attenuation coefficients  $\mu(\mathbf{r})$  of the object.

### 5.3.2 Threshold based segmentation of bone

As a central result, no edge-artifacts disturb the 3D data quality (**Fig. 5.8**) owing to the applied phase reconstruction scheme and careful optimization of experimental parameters. This enables histogram-based segmentation of bony structures in contrast to previously reported in-line phase contrast studies of the cochlea which skipped the phase reconstruction step [177, 176]. An automatic segmentation of bony structures was achieved using a region growing operation in three dimensions. **Fig. 5.8** illustrates the process of segmentation for one slice of the reconstructed 3D volume of  $\mu(\mathbf{r})$ . A histogram for all values of  $\mu(\mathbf{r})$  in the complete dataset was computed with 256 bins. One of the two peaks that appear in the histogram corresponds to voxels with high attenuation attributable to bony structures. The lower threshold for the region growing operation (Magic Wand Tool, Avizo Fire) was therefore chosen between the peaks of the histogram. The seed voxel was manually chosen to be in the bony wall of the cochlea, which can readily be identified. Choosing the parameter “all slices” of the Magic Wand Tool results in a 6-connectivity<sup>3</sup> in 3D for the growing operation. The segmentation (shown in red in **Fig. 5.8b**) clearly distinguishes between bone and soft tissue structures. The histogram based segmentation is therefore fast and convenient, which is a key requisite for batch analysis of several cochleae as needed for the present case of a biomedical study.

<sup>3</sup> A voxel on a three dimensional cartesian grid has 6 direct neighbours with a voxel-voxel distance of one pixel.

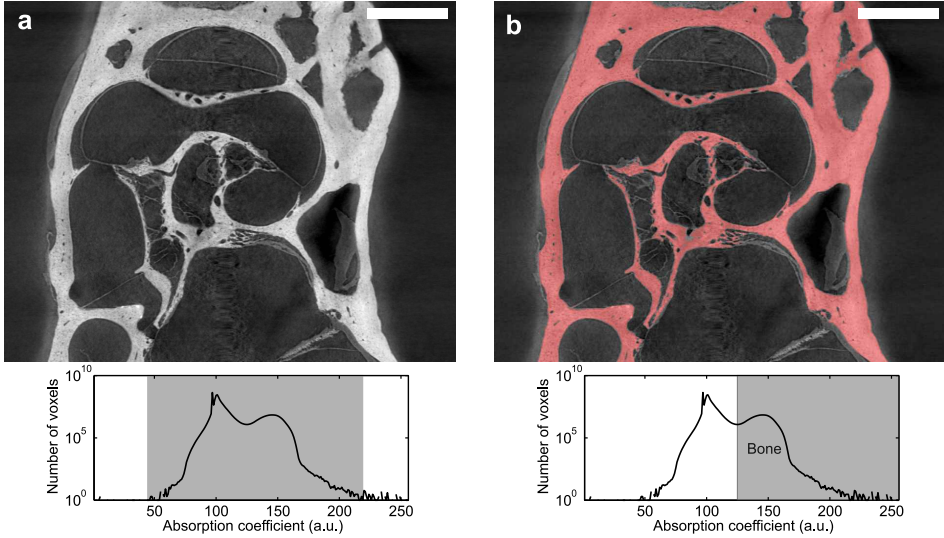


**Figure 5.8:** (a) Slice through the reconstructed 3D volume of a mouse cochlea along with the histogram of the attenuation coefficients. The gray area indicates the range of the applied colormap. (b) The same slice after application of a 3D region growing operation, segmentation is marked in red. The threshold for segmentation was chosen between the peaks of the histogram. Scale bars, 500  $\mu\text{m}$ .

## 5.4 Results

### 5.4.1 Solid target source

As part of an optogenetic study several mouse cochleae were investigated using the water-cooled solid target microfocuss configuration of the x-ray source (see section 4.2). The normalized intensity  $\bar{I}_\theta(\mathbf{r}_\perp, z_{\text{eff}})$  and corresponding phase reconstruction of the amplitude  $I_\theta(\mathbf{r}_\perp, 0)$  are shown in **Fig. 5.6** for one projection. Note that the effective pixel size of  $p_{\text{eff}} = 2.6 \mu\text{m}$  ( $z_1 = 78 \text{ mm}$ ,  $z_2 = 116 \text{ mm}$ ) is smaller compared to a recent tomographic synchrotron radiation study of the cochlea [176]. A slice through the reconstructed 3D volume (**Fig. 5.9**) reveals several functional structures. Notably, resolution and contrast are high enough to identify nerve tissue as well as the basilar membrane and the thin Reissner membrane. Therefore, all three cavities (scala tympani, scala vestibuli and scala media) can be identified. Basilar membrane, Reissner's membrane, Rosenthal's canal and the optical fibre were traced by manual segmentation and subsequent interpolation (Interpolate Slices, Avizo Fire). Visualisation in 3D (**Fig. 5.10 a**) was achieved using surface rendering of the segmented structures. A semi-transparency was chosen for bony structures. Manually segmented nerve tissue (**Fig. 5.10 b**) was visualized using volume rendering and shows how the nerve fibres of the spiral ganglion reach out



towards the basilar membrane where the organ of Corti and the sensory cells of hearing are located (not visible in the data). The colouring in **Fig. 5.10 b** was chosen identical to the one of **Fig. 5.1** for convenient comparison. The three-dimensional visualisation allows to readily evaluate the tonotopic position of the cochleostomy in the investigated cochleae. To this end, markers were set at different positions along the basilar membrane, a spline curve was fitted to the markers and was used to calculate the distance of the cochleostomy from the apex (not shown). Different positions along the basilar membrane correspond to different resonant sound frequencies. Therefore, the tonotopic position of the cochleostomy can be mapped to a certain sound frequency range of stimulated spiral ganglion neurons. As an important result it was found that the tonotopic position of the spiral ganglion neurons which were stimulated coincided with the tonotopic position of the cochleostomy (see [90] for details). Next, position and orientation of optical fibres relative to the tonotopic map of the cochlea were evaluated for several specimens based on 3D visualisations as shown in **Fig. 5.10 c-e**. Obviously, the orientation of the fibre varies strongly from specimen to specimen even though the cochleostomy was cut at roughly the same position. Therefore, x-ray phase contrast tomography was necessary to identify the tonotopic region of stimulated neurons, complementing the analysis of brainstem responses to light stimulation (see [90] for details on optogenetic experiments and results).

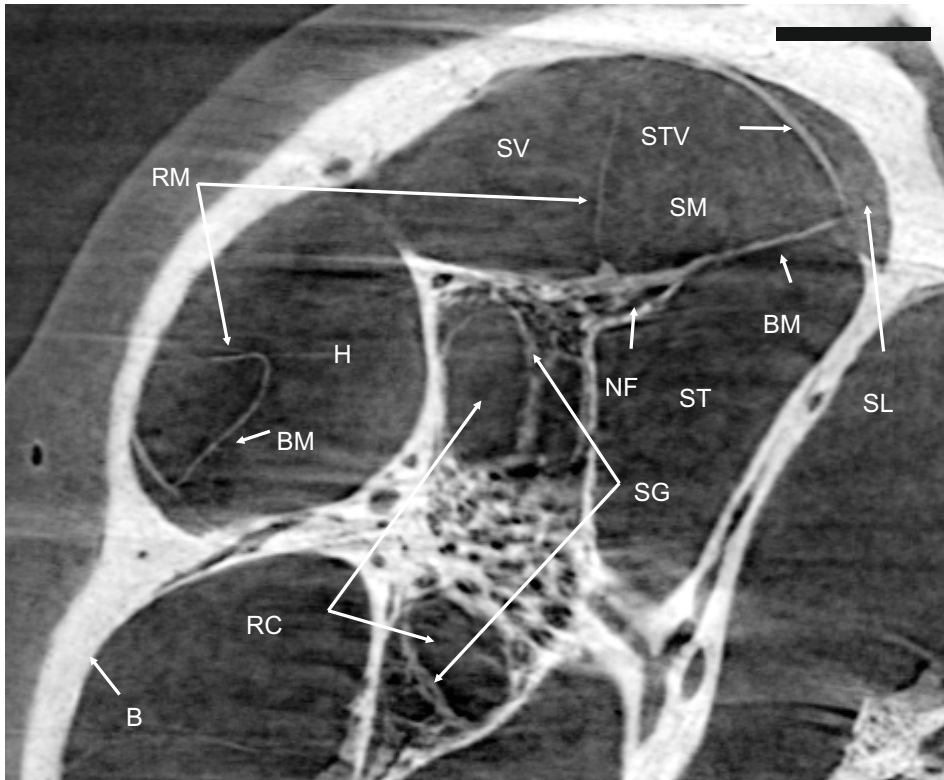


**Figure 5.9:** Slice through the reconstructed 3D volume of a mouse cochlea with basilar membrane (BM), Reissner's membrane (RM), scala tympani (ST), scala vestibuli (SV), scala media (SM), spiral ligament (SL), stria vascularis (STV), spiral ganglion (SG) within Rosenthal's canal (RC), nerve fibres (NF), helicotrema (H) and surrounding bone (B). Scale bar, 200  $\mu$ m.

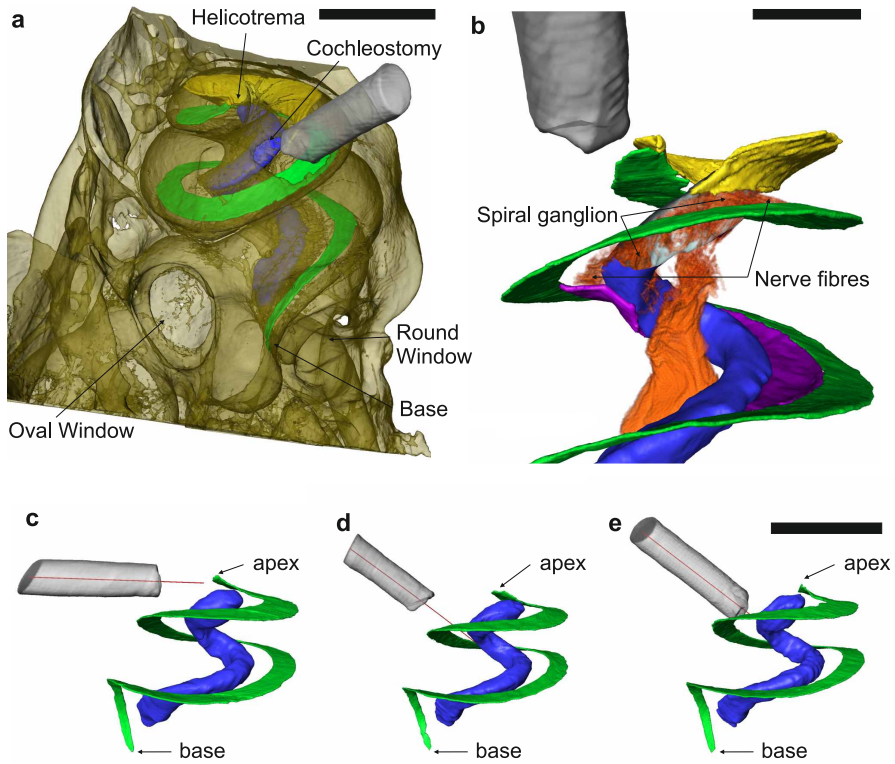


**Figure 5.10:** (a) 3D visualisation of bone (brown, semi-transparent), basilar membrane (green), Reissner's membrane (yellow), Rosenthal's canal (blue) and optical fibre (gray). Scale bar, 800  $\mu\text{m}$ . (b) Magnified view showing nerve tissue (orange). The nerve fibres of the spiral ganglion pass out between the two layers of the lamina spiralis ossea (bottom layer shown in magenta). Scale bar, 400  $\mu\text{m}$ . (c-e) Position and orientation of the optical fibre relative to the spiral ganglion in Rosenthal's canal for three different investigated mouse cochleae. The central cone of the stimulating optical light from the fibre illuminates the spiral ganglion neurons at different tonotopic positions. The tonotopic position is derived from the measured distance of the fibre from the apex along the basilar membrane (green). This information was used for optogenetic cochlear implant development, see main text. Scale bar, 1 mm.

### 5.4.2 Liquid metal jet source

A substantial reduction in accumulation time of about an order of magnitude could be achieved using the high-brilliance liquid-metal-jet x-ray source [132] (see section 4.2) and a fast sCMOS detector (see section 4.1). A tomogram with  $2\ \mu\text{m}$  voxel size was recorded within 30 minutes, compared to the typical exposure time of five hours using the solid target source (see also **Tab. 5.1**). Since the cochlea is kept in air during exposure, drying of the liquid-filled cavities and the attached soft tissue is difficult to avoid during long measurements. This may be the reason why the organ of Corti could not be observed in the long exposure tomograms (**Fig. 5.9**). Contrarily, in the fast acquisition dataset, soft tissue structures are visible in the region of the organ of Corti and the tectorial membrane (**Fig. 5.11a**). A subsequent replicate of the 30 minute measurement one hour later already shows that due to dehydration of the cochlear cavities, those soft tissue structures are not observed anymore and that Reissner's membrane ruptured at the basal turn (**Fig. 5.11b**). This is in agreement with the fact, that a recent synchrotron study (with intrinsic fast acquisitions) could visualize the organ of Corti [176], even though

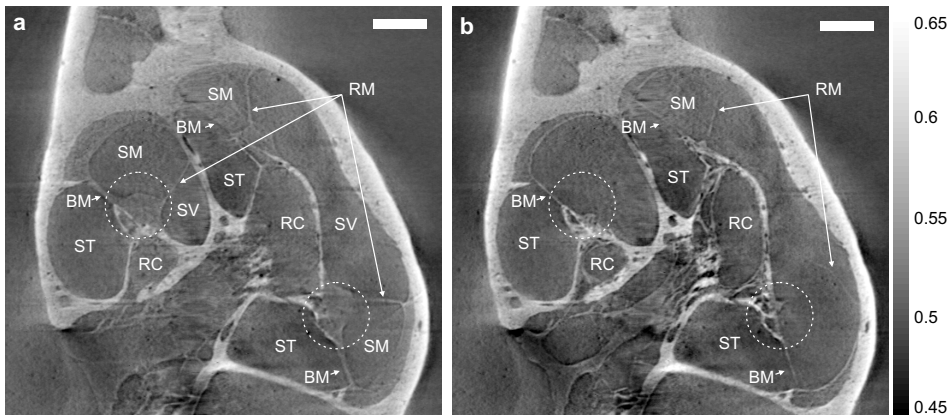


**Figure 5.11:** (a) Slice through the reconstructed 3D volume of a mouse cochlea obtained within 30 min exposure time using a liquid-metal-jet x-ray source and a fast sCMOS detector in conventional geometry showing basilar membrane (BM), Reissner's membrane (RM), Rosenthal's canal, scala tympani (ST), scala vestibuli (SV) and scala media (SM). The fast acquisition enables the observation of soft tissue structures in the region of the organ of Corti and the tectorial membrane (dashed circles). (b) The same tomogram was repeated one hour later. Due to dehydration of the cochlear cavities, those soft tissue structures could not be observed anymore (dashed circles) and Reissner's membrane ruptured at the basal turn. These observations illustrate the advantages of fast tomography using the liquid-metal-jet x-ray source and motivate agarose embedding for even better structure preservation. Scale bars,  $200\ \mu\text{m}$ .

the images appear to be of less quality (in terms of spatial resolution and contrast between bone and soft tissue) compared to the current results. These observations illustrate the advantages of fast tomography using a liquid- metal-jet x-ray source and motivate future work directed at improved structure preservation. Prevention of dehydration could be achieved using agarose embedding, which was successfully used in a current synchrotron study of *C. elegans* [158] and for 3D imaging of entire mouse nerves as presented in chapter 6. So far, the low photon energy of the current liquid-metal source (9.25 keV, Ga  $K_\alpha$ ) inhibits embedding due to very high resulting absorption effects. Note that beam hardening effects due to heavily absorbing bone already degrades the quality of the tomograms recorded with the liquid-metal source. Compared to the results of the solid target source with 17.5 keV photon energy (Mo  $K_\alpha$ ), the absorption coefficients  $\mu(\mathbf{r})$  are less uniform for bony structures (compare **Fig. 5.9** and **Fig. 5.11**). Since a 24 keV metal-jet has recently been developed [128] 3D cochlea imaging with short exposure times and improved structure preservation using compact laboratory sources may further be extended.

### 5.4.3 Optimizing spatial resolution

Propagation imaging of the cochlea can be further optimized for spatial resolution. The standard deviation  $\sigma_{\text{sys}}$  of the cone-beam imaging system point-spread function (PSF) in the sample plane can be written as

$$\sigma_{\text{sys}} = \sqrt{(M-1)^2 M^{-2} \sigma_{\text{src}}^2 + M^{-2} \sigma_{\text{det}}^2}, \quad (5.1)$$

where  $M = 1 + z_2/z_1$  is the geometric magnification and  $\sigma_{\text{src}}$  and  $\sigma_{\text{det}}$  indicate the standard deviation of the source intensity and detector PSF, respectively [78, 151]. Note the relation between full-width at half maximum (FWHM) and standard deviation of a Gaussian  $\text{FWHM} = 2\sqrt{2 \ln 2} \sigma$ . The MTF of a gaussian PSF drops to about 3% contrast for features with a full-period equal to the FWHM of the PSF (see section A.3). Therefore, the half-period resolution is equal to  $\text{FWHM}/2$ . For the imaging system, the PSF is constituted by the lateral source dimensions for high geometric magnifications ( $\sigma_{\text{sys}} \approx \sigma_{\text{src}}$ , if  $M \rightarrow \infty$ , **Fig. 5.2a**) and by the detector PSF for low geometric magnifications ( $\sigma_{\text{sys}} \approx \sigma_{\text{det}}$ , if  $M \rightarrow 1$ , **Fig. 5.2b**). By setting the derivative of equation (5.1) equal zero we find the optimal geometric magnification

$$\begin{aligned} M_{\text{opt}} &= 1 + \left( \frac{\sigma_{\text{det}}}{\sigma_{\text{src}}} \right)^2 \\ &= 1 + \left( \frac{\text{FWHM}_{\text{det}}}{\text{FWHM}_{\text{src}}} \right)^2, \end{aligned} \quad (5.2)$$

yielding the smallest imaging system PSF [151, 78], i.e. the highest spatial resolution

$$\sigma_{\text{opt,sys}} = \sqrt{\frac{\sigma_{\text{src}}^2 \sigma_{\text{det}}^2}{\sigma_{\text{src}}^2 + \sigma_{\text{det}}^2}}. \quad (5.3)$$

For  $\sigma_{\text{det}}/\sigma_{\text{src}} = 10$  (large detector PSF) the large optimal magnification  $M_{\text{opt}} = 101$  yields an imaging system resolution of  $\text{FWHM}_{\text{sys}} = 0.995 \cdot \text{FWHM}_{\text{src}}$ , dominated by the source size (**Fig. 5.12 a**). For  $\sigma_{\text{det}}/\sigma_{\text{src}} = 0.1$  (small detector PSF) the small optimal magnification  $M_{\text{opt}} = 1.01$  yields an imaging system resolution of  $\text{FWMM}_{\text{sys}} = 0.995 \cdot \text{FWHM}_{\text{det}}$ , dominated by the detectors resolution (**Fig. 5.12 b**). Typically, compact cone-beam setups use  $\sigma_{\text{det}} > \sigma_{\text{src}}$  and a high geometric magnification ( $z_1 < z_2$ ) to achieve spatial resolutions below the detector PSF [139]. We denote this configuration (used for the results in the previous sections) as the conventional geometry of compact microfocus cone-beam setups. However, using a high-resolution detector system with  $\sigma_{\text{det}} < \sigma_{\text{src}}$  in the low magnification geometry, a spatial resolution well below the source size was obtained, as can be seen for an absorbing test structure in **Fig. 5.13 a,d**.

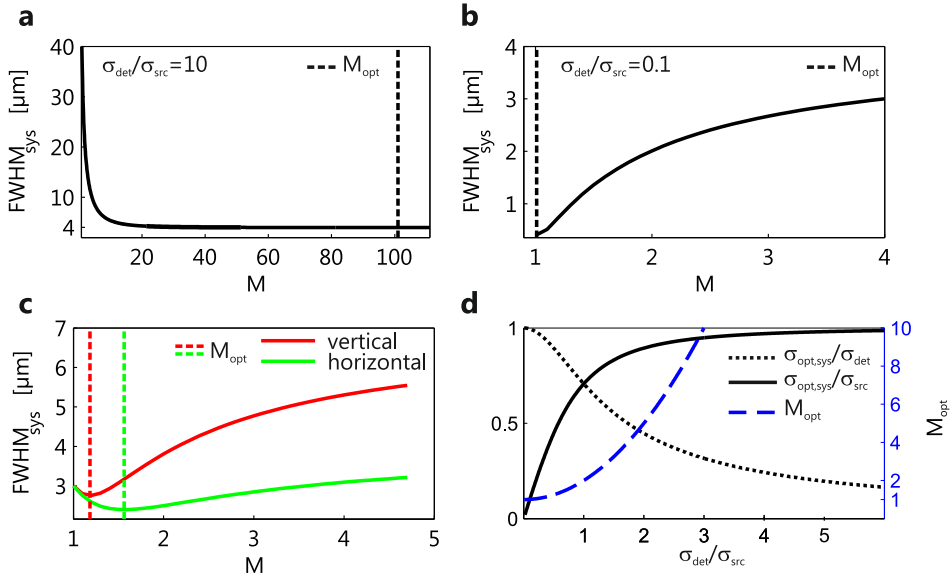


**Figure 5.12:** FWHM of the imaging system PSF (3% MTF contrast resolution) for different source and detector configurations along with the optimal magnification  $M_{\text{opt}}$  and resulting optimal  $\text{FWHM}_{\text{opt}}$ . (a)  $\sigma_{\text{src}} = 4 \mu\text{m}$ ,  $\sigma_{\text{det}} = 40 \mu\text{m}$ ,  $M_{\text{opt}} = 101$ ,  $\text{FWHM}_{\text{opt}} = 3.98 \mu\text{m}$ . (b)  $\sigma_{\text{src}} = 4 \mu\text{m}$ ,  $\sigma_{\text{det}} = 0.4 \mu\text{m}$ ,  $M_{\text{opt}} = 1.01$ ,  $\text{FWHM}_{\text{opt}} = 0.398 \mu\text{m}$ . (c)  $\sigma_{\text{src,h.}} = 4 \mu\text{m}$ ,  $\sigma_{\text{src,v.}} = 7 \mu\text{m}$ ,  $\sigma_{\text{det}} = 3 \mu\text{m}$ ,  $M_{\text{opt,h.}} = 1.56$ ,  $M_{\text{opt,v.}} = 1.18$ ,  $\text{FWHM}_{\text{opt,h.}} = 2.4 \mu\text{m}$ ,  $\text{FWHM}_{\text{opt,v.}} = 2.76 \mu\text{m}$ . (d) Increase in resolution relative to source size (solid black curve) and detector resolution (dashed black curve) at the optimal magnification (blue dashed curve) for different ratios  $\sigma_{\text{det}}/\sigma_{\text{src}}$ .

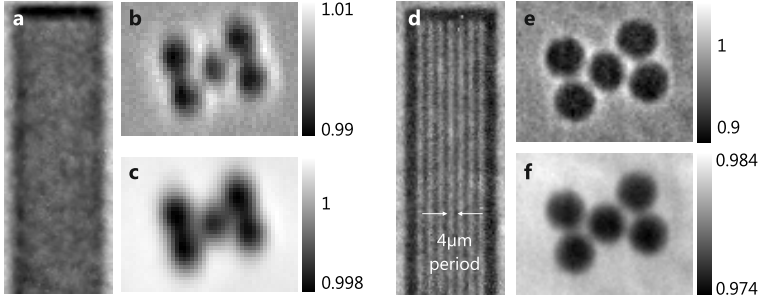


**Figure 5.13:** (a,d) Image of an absorbing test structure with  $2\ \mu\text{m}$  lines and  $2\ \mu\text{m}$  spaces along the direction corresponding to a source size of  $7\ \mu\text{m}$  (FWHM) recorded with (a) source-size limited ( $z_1 = 72\ \text{mm}$ ,  $z_2 = 418\ \text{mm}$ ,  $p_{\text{eff}} = 0.96\ \mu\text{m}$ ) and (d) detector PSF limited spatial resolution ( $z_1 = 95\ \text{mm}$ ,  $z_2 = 3\ \text{mm}$ ,  $p_{\text{eff}} = 0.72\ \mu\text{m}$ ). (b,e) Phase contrast image of  $10\ \mu\text{m}$  polystyrene spheres along with (c,f) the reconstructed amplitude (BAC) for conventional ( $z_1 = 70\ \text{mm}$ ,  $z_2 = 1930\ \text{mm}$ ,  $p_{\text{eff}} = 0.7\ \mu\text{m}$ ) and inverse ( $z_1 = 65\ \text{mm}$ ,  $z_2 = 20\ \text{mm}$ ,  $p_{\text{eff}} = 0.57\ \mu\text{m}$ ) geometry, respectively.

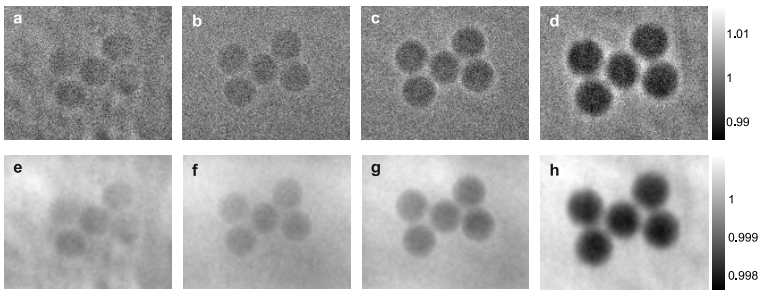


**Figure 5.14:** (a-d) Projection images of polystyrene spheres with  $10\ \mu\text{m}$  diameter. The sample-detector distance  $z_2$  is increased ( $2.6\ \text{mm}$  (a),  $5\ \text{mm}$  (b),  $10\ \text{mm}$  (c),  $20\ \text{mm}$  (d)) while the source-detector distance was kept constant at  $z_1 + z_2 = 85\ \text{mm}$ . (e-f) Reconstruction of the object transmission function using the BAC algorithm.

Due to the symmetry of the effective propagation distance  $z_{\text{eff}} = z_1 z_2 / (z_1 + z_2)$  with respect to  $z_1$  and  $z_2$ , phase contrast can also be exploited in this configuration given a sufficient resolution of the detector to resolve the phase contrast fringes [151, 78]. We denote this geometry ( $z_1 > z_2$ ) as the inverse geometry. Since  $z_{\text{eff}} \approx z_2$  for the low magnifications case ( $z_1 \gg z_2$ ), phase contrast arises for  $z_2 \gg 0$ . This effect is illustrated in **Fig. 5.14** for polystyrene spheres of  $10 \mu\text{m}$  diameter. The sample-detector distance  $z_2$  was gradually increased from  $2.6 \text{ mm}$  to  $20 \text{ mm}$  while the source-detector distance was kept constant at  $z_1 + z_2 = 85 \text{ mm}$ . The negligible attenuation of the x-ray beam due to the thin sample yields very little absorption contrast. By increasing  $z_2$  phase contrast arises and the object can be well recognized, however spoiled by edge-enhancement. With sufficient phase contrast the object transmission function can be reconstructed with a high signal-to-noise ratio using the BAC algorithm. Therefore, in the inverse geometry a high contrast due to phase sensitivity is combined with high spatial resolution below the x-ray spot size dimensions, yielding better results than in the conventional geometry case (compare **Fig. 5.13 c** and **f**). An asymmetric x-ray spot size affects the image resolution in the conventional geometry and creates a need for deconvolution [138]. The influence of the liquid-jet source size ( $4 \mu\text{m} \times 7 \mu\text{m}$ , h. $\times$ v.) is obviously reduced in the inverse geometry, however still defining the spatial coherence lengths. Note that the geometry  $z_1 > z_2$  is well known for synchrotron based imaging. In fact, the parallel beam geometry employed in most synchrotron tomography experiments (from early demonstrations [193, 31, 81] to recent cochlea studies [177, 176]) corresponds to the limit  $z_1 \gg z_2$ , as for typical beamlines the distance to the source is much larger than the distance between sample and detector. The terms *conventional* and *inverse geometry* are therefore used in view of compact cone-beam setups and do not reflect the historic development of phase contrast imaging at synchrotron sources, where the inverse geometry may be denoted as the conventional case. However, contrary to synchrotron instrumentation, for the case of compact microfocus setups  $z_1$  and  $z_2$  can easily and continuously be changed and optimized for contrast and resolution [78, 151]. **Fig. 5.12 c** illustrates this advantage in terms of spatial resolution for the source and detector parameters of the JuLiA setup. Importantly, at  $M_{\text{opt}}$  the imaging system resolution is simultaneously below both the lateral source dimensions and the detector resolution as expressed by

$$\frac{\sigma_{\text{opt,sys}}}{\sigma_{\text{src}}} = \sqrt{\frac{c^2}{c^2 + 1}} < 1, \quad (5.4)$$

$$\frac{\sigma_{\text{opt,sys}}}{\sigma_{\text{det}}} = \sqrt{\frac{1}{c^2 + 1}} < 1, \quad (5.5)$$

with  $c = \sigma_{\text{det}} / \sigma_{\text{src}}$ . The increase in resolution relative to source size and detector resolution is shown in **Fig. 5.12 d** depending on the ratio  $c$ . At the limiting cases ( $M_{\text{opt}} = 1$  and  $M_{\text{opt}} = \infty$ ) the ratios  $\sigma_{\text{opt,sys}} / \sigma_{\text{src}}$  and  $\sigma_{\text{opt,sys}} / \sigma_{\text{det}}$  reach their extrema (zero and unity). For the symmetric case of  $\sigma_{\text{det}} = \sigma_{\text{src}}$  the optimal magnification is  $M_{\text{opt}} = 2$  and the resolution increase is  $\sigma_{\text{opt,sys}} / \sigma_{\text{src}} = \sigma_{\text{opt,sys}} / \sigma_{\text{det}} = 1 / \sqrt{2}$ .



Despite these experimental design options, the vast majority of phase contrast tomography work at compact x-ray sources is based on  $z_1 < z_2$ , while only few authors have previously used  $z_2 < z_1$  [2]. The fact that the inverse geometry has not been exploited for tomography of biological samples may be due to the reduced efficiency of high-resolution scintillator-based detectors. However, the combination with a high-brilliance liquid-jet source renders this geometry a promising approach for phase contrast imaging applications. From the spatial frequencies corresponding to 3%–10% contrast, observed for the absorbing test structure at  $M \approx 1$  and  $M \gg 1$  (similar to **Fig. 5.2 a,b**, data not shown) the FWHM of the detector PSF and source intensity was estimated to  $\text{FWHM}_{\text{det}} = 3 \mu\text{m}$ ,  $\text{FWHM}_{\text{src,h.}} = 4 \mu\text{m}$  and  $\text{FWHM}_{\text{src,v.}} = 7 \mu\text{m}$  (asymmetric spot size for the liquid metal source), respectively. The x-ray spot size was previously imaged with a Fresnel zone plate yielding consistent values [9]. The parameters of source and detector result in optimal magnifications  $M_{\text{opt,h.}} = 1.56$  and  $M_{\text{opt,v.}} = 1.18$  along with optimal resolutions  $\text{FWHM}_{\text{opt,h.}} = 2.4 \mu\text{m}$  and  $\text{FWHM}_{\text{opt,v.}} = 2.76 \mu\text{m}$  for the vertical and horizontal direction, respectively. Phase contrast images of mouse cochlea (**Fig. 5.15**) were recorded at an intermediate value of  $M = 1.23$  as a compromise between optimal resolution in the vertical and horizontal direction. The images obtained in the inverse geometry exhibit higher spatial resolution when compared to conventional geometry results. Consequently, the corresponding 3D reconstruction reveals smaller features (**Fig. 5.16**), e.g. finer nerve fibres are resolved. The higher spatial resolution in 3D is confirmed by the corresponding azimuthally averaged power spectral density (**Fig. 5.16 c**). The (half-period) resolution for the inverse geometry setup is about  $1.75 \mu\text{m}$  (corresponding to three voxels), well below the dimensions of the x-ray spot and in agreement with the optimal (half-period) resolutions  $\text{FWHM}_{\text{opt,h.}}/2 = 1.2 \mu\text{m}$  and  $\text{FWHM}_{\text{opt,v.}}/2 = 1.4 \mu\text{m}$  of the setup.

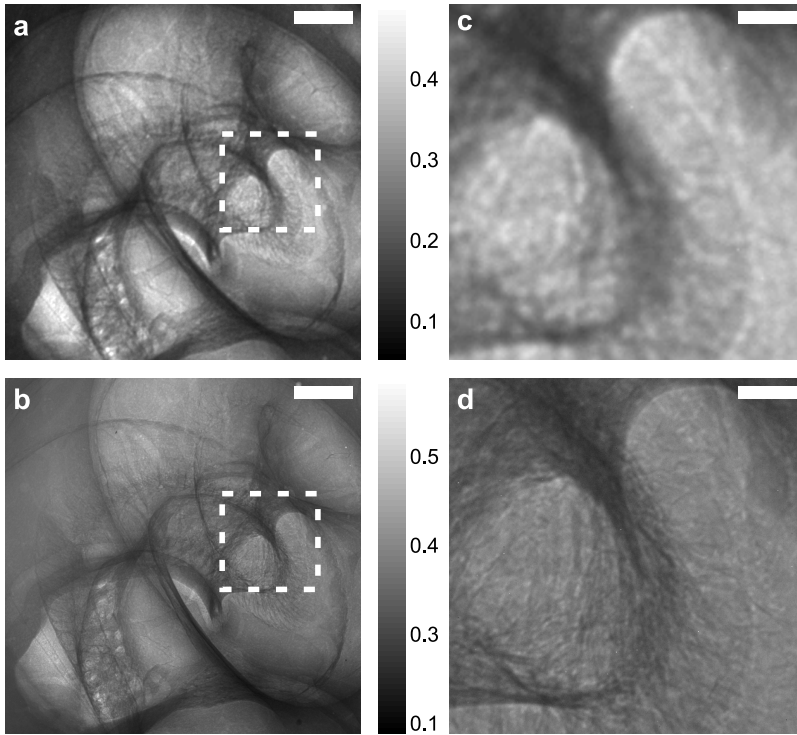


**Figure 5.15:** (a) Projection image of a mouse cochlea in (a) the conventional and (b) the inverse geometry. A higher spatial resolution is obtained in the inverse geometry, as can be seen in the (c,d) magnified views of the areas marked in (a,b). Scale bars, (a,b) 200  $\mu\text{m}$ , (c,f) 50  $\mu\text{m}$ .

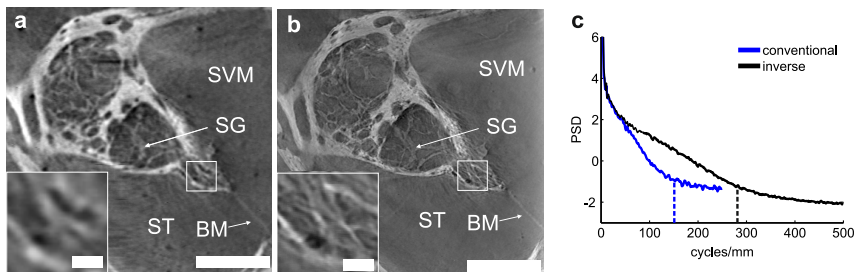


**Figure 5.16:** Slice (region of interest) through the reconstructed 3D volume obtained from data recorded in (a) the conventional and (b) the inverse geometry. (c) The azimuthally averaged power spectral densities indicate that by using the inverse geometry spatial frequencies up to 280  $\text{mm}^{-1}$  were reconstructed, compared to 150  $\text{mm}^{-1}$  in the conventional geometry. This corresponds to 1.75  $\mu\text{m}$ , which is well below the x-ray spot size dimensions. Scale bars, 200  $\mu\text{m}$  and 20  $\mu\text{m}$  (insets).

#### 5.4.4 Space estimation for intra-cochlear implants

As a next step towards optogenetic cochlear implants, the spiral ganglion neurons should be stimulated from within the cochlea rather than cutting a window into the bony capsule. To this end, miniaturized implants will be inserted through the round window of the cochlea in future experiments. The available space for such devices was estimated by analyzing intact mouse and rat cochleae. The basilar membrane, scala tympani and scala vestibuli et media were traced as described above, a surface rendering is shown in **Fig. 5.17**. Note that the datasets shown here were recorded during an early stage of the experimental optimizing for cochlea imaging. Therefore, source setting, choice of detector and geometric parameters are rather mixed and vary from the optimum settings described in the previous sections. The size of scala tympani along the basilar membrane was measured at different positions. The blue and black lines illustrate the measurements at one position. Blue represents the direction with largest width and black is the corresponding orthogonal direction. Both directions along with their geometric mean (effective diameter) are shown as a function of the distance from the base in **Fig. 5.18**. This information was used by the Inner Ear lab and collaborators for the design and development of miniaturized LED arrays.

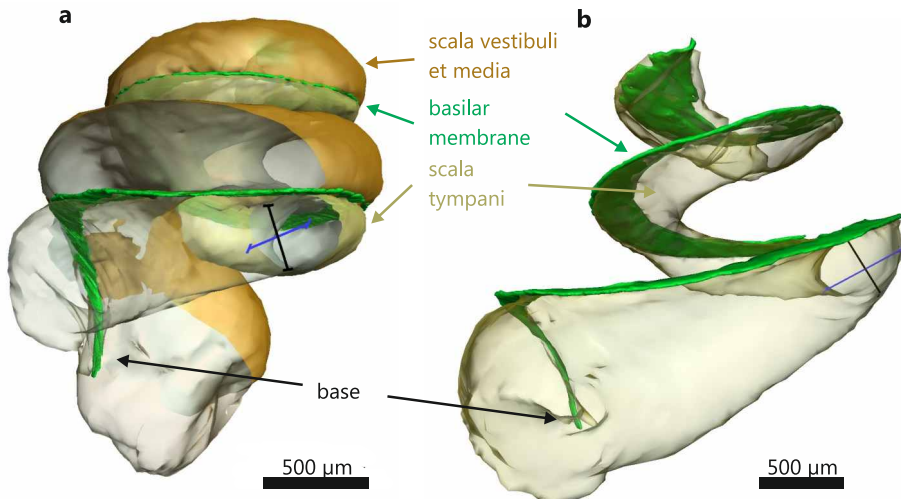


**Figure 5.17:** 3D visualisation of basilar membrane (green), scala tympani (fawn), scala vestibuli et media (brown, only traced in the mouse cochlea) for a (a) mouse and (b) rat cochlea. The size of scala tympani along the basilar membrane was measured at different positions, illustrated by the blue and black lines for one position.

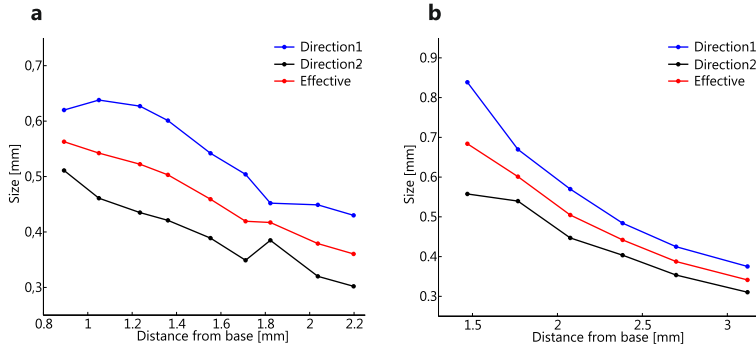


**Figure 5.18:** Estimation of available space for intra-cochlear implants in (a) mouse and (b) rat cochleae. Both directions (see Fig. 5.17) along with their geometric mean (red, effective diameter) are shown as a function of the distance from the base.

## 5.5 Summary

The results demonstrate that functional cochlear soft tissue within the surrounding bone can be imaged with unprecedented quality in 3D using compact laboratory microfocus x-ray sources. This was possible by means of optimized geometric parameters, matched to source and detector settings, in combination with suitable phase reconstruction algorithms. The phase retrieval algorithm based on the transport-of-intensity equation yields 3D data quality which allows for an automatic histogram-based segmentation between bone and soft tissue, while previously reported synchrotron based phase contrast studies of the cochlea skipped the phase reconstruction step [177, 176]. This enables fast and convenient data visualization and therefore, batch analysis of several cochleae as required by biomedical studies and demonstrated here for cochlear implant research. The additional advantage of using a novel liquid-metal-jet source is evidenced in terms of significantly reduced accumulation time as well as higher spatial resolution when combined with a high resolution detector in an optimized (inverse) geometry. The obtained 3D cochlea datasets were used to characterize brainstem responses to optogenetic stimulation and for design parameter estimations of future implants for mouse and rat cochleae. Note that biomedical phase contrast tomography applications have been demonstrated at compact laboratory instruments based on grating interferometry [170]. However, the current work provides a spatial resolution an order of magnitude higher than the resolution range of 30 – 200  $\mu\text{m}$  reported for grating based phase contrast [50, 170, 169, 115, 13]. For example, the thin membranes (basilar membrane, Reissner’s membrane) and the nerve fibres in the cochlea could not have been resolved with medium spatial resolution. The presented approach can be applied to a wide range of biological samples and may deliver 3D data with unprecedented spatial resolution and contrast for soft tissue.

## 6 Three-dimensional imaging of mouse nerves

To understand cellular networks in the nervous system and to map connectivity, three dimensional structural information of multi-cellular tissue over hundreds of micrometers is required with resolution and contrast high enough to resolve sub-cellular features. While multiple scattering, fluorescence staining and resolution issues pose a limit to visible light microscopy studies, preparation difficulties such as cutting and staining as well as limited penetration depth restrict the applications of electron microscopy. Serial block-face scanning electron microscopy was developed to image larger volumes with high resolution. The method is based on serial sections which are either cut with a diamond knife [42] or milled by focused ion beam [112]. Recently, this destructive technique was used to trace axons (nerve fibers) contained in a volume of roughly  $(80\ \mu\text{m})^3$  within a mouse brain [142]. However, the reported  $8\ \mu\text{s}$  dwell time for each scanning point corresponds to more than 17 hours for a dataset with  $2000^3$  voxels. Full-field x-ray tomography on the other hand offers the unique potential for non-destructive three dimensional imaging of large volumes within a reasonable amount of time. The goal of the present experiments was to explore whether x-ray propagation imaging can be applied to determine the three-dimensional structure of myelinated nerves. The myelin sheath is a concentric multilamellar membrane stack which is wrapped around axons of neurons [136]. The segmental structure of the insulating myelin sheath along the axon, with segments separated by so-called nodes of Ranvier (where myelin is lacking), enables the saltatory conduction of nerve impulses, needed for fast signal transduction [221, 214]. Three dimensional data of thousands of axons running parallel in the nerve along with their respective myelin sheath segments would allow to study if and how positions of the nodes of Ranvier in neighboring axons are correlated. In this chapter, x-ray propagation imaging of uncut saphenus, sciatic, and optical mouse nerves is presented.<sup>1</sup>

---

<sup>1</sup> The contents of this chapter is based on an unpublished manuscript [11].

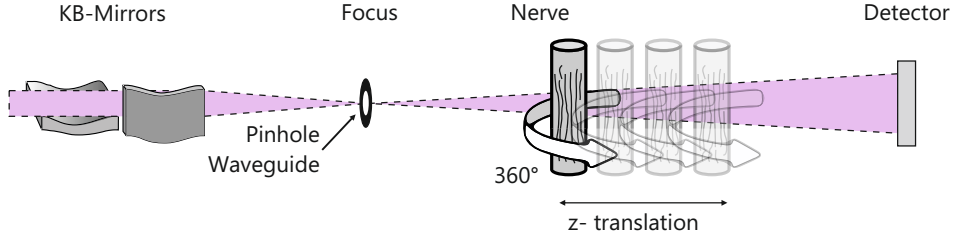


**Figure 6.1:** Sketch of the experimental setup. The nerve is placed into a divergent x-ray beam emerging from a (possible low-pass filtered) focus of two KB-mirrors or an x-ray waveguide. For different magnifications and for reasons of phase retrieval, the samples are placed at different positions along the optical axis and rotated for tomography.

## 6.1 Experiments

The experimental setup is sketched in **Fig. 6.1**. Experiments were carried out at the GINIX setup at PETRA III (see 4.3) and at the ID22 beamline of the ESRF (see section 4.4) with different configurations of detector, source and geometry as well as various sample preparation methods.

### 6.1.1 Experimental setup I

An unstained immersion fixated optical nerve (WT mouse, P47) in a glass capillary was imaged using the KB imaging configuration of GINIX (section 4.3.6) at a synchrotron ring current of 80 mA. The photon energy was set to 7.9 keV and the KB beam was filtered by a pinhole (Plano, Germany; polished with a focused ion beam) of 8  $\mu\text{m}$  diameter and 200  $\mu\text{m}$  thickness, positioned in the focal plane. The slits in front of the KB mirrors were closed to  $0.1 \times 0.1 \text{ mm}^2$  resulting in a focus size of  $345 \text{ nm} \times 550 \text{ nm}$  (h. $\times$ v.) as measured by ptychography (see section 4.3.6 and [66]) and a beam size of  $1.5 \times 1.2 \text{ mm}^2$  in the detection plane at  $z_2 = 5.51 \text{ m}$ . The x10 objective of the PCO detector resulting in a pixel size of  $p = 740 \text{ nm}$  was used with a  $1.5 \times 1.5 \text{ mm}^2$  field of view fitting the beam size. The sample was placed on the rear sample tower (T4 in **Fig. 4.3 d**) at a distance  $z_1 = 5.333 \text{ m}$  from the focus, behind the flight path (polyimide was used as window material) close to the PCOx10 detector in a quasiparallel geometry with geometric magnification  $M = 1.03$ , effective pixel  $p_{\text{eff}} = 718 \text{ nm}$ , effective propagation distance  $z_{\text{eff}} = 172 \text{ mm}$  and Fresnel number  $F^{10} \approx 2$ . For tomography 900 projections were recorded over 180 degrees with 0.2 degree step size and 10 second exposure time. For each projection the empty beam was recorded for 10 seconds.

### 6.1.2 Experimental setup II

An unstained immersion fixated saphenus nerve (WT mouse, P28) embedded in agarose between two polypropylene foils was imaged using the optimized WG imaging configuration of GINIX (section 4.3.4) at a synchrotron ring current of 100 mA. The x-ray beam was monochromatized to 13.6 keV and focused to  $380 \text{ nm} \times 420 \text{ nm}$  (h. $\times$ v.) as measured by scanning one-dimensional x-ray waveguides through the focus. A crossed multilayer x-ray waveguide with 59 nm guiding core dimensions (XWG3) was placed in the focal plane of the mirrors as a quasi point source with a maximum measured flux of  $5 \cdot 10^8$  ph/s. A  $1 \mu\text{m}$  thick  $\text{Si}_3\text{N}_4$  membrane was installed as entrance window of the vacuum flight path to reduce spurious phase contrast from polyimide windows used before. The sCMOS detector was installed at a distance  $z_2 = 5.127 \text{ m}$  and operated with gain factor 2. The sample was positioned at  $z_1 = 0.24 \text{ m}$  behind the focus (on sample tower T4 in **Fig. 4.3 c**) resulting in geometric magnification  $M = 21.1$ , effective pixel size  $p_{\text{eff}} = 309 \text{ nm}$ , Fresnel number  $F^{10} = 0.45$  and a field of view of  $585 \mu\text{m} \times 334 \mu\text{m}$  (h. $\times$ v.). For tomography, 838 holograms distributed among 180 degrees were recorded with an exposure time of 5 seconds. The missing wedge of 12.4 degrees resulted from the flat design of the sample holder. Empty beam intensities were recorded with  $60 \times 5$  seconds exposure time after every 150th projection (30 degrees).

### 6.1.3 Experimental setup III

Sciatic, optical and saphenus nerves prepared either by high pressure freezing or immersion fixation followed by agarose embedding in a polyimide tube were imaged at beamline ID22NI (section 4.4). The energy of the pink photon beam was set to 17 keV for the current experiment. The focus size was about  $80 \text{ nm} \times 80 \text{ nm}$  (FWHM) as determined by translating a gold edge of a nanofabricated test pattern (Xradia, USA) and recording both the transmitted intensity by a diode and the Au- $L_\alpha$  fluorescence emission line by a silicon drift detector (vortex-EX, SII NanoTechnology Inc., USA). Prior to tomographic measurements geometrical distortions due to aberrations of the focusing optics were measured using a grid with  $3 \mu\text{m}$  periodicity [145]. Tomographic datasets were recorded at different geometric magnifications and effective pixel sizes using the FReLoN detector system with a pixel size in the detection plane ( $z_2 = 526 \text{ mm}$ ) of  $p = 756 \text{ nm}$ . Low resolution datasets with effective pixel size  $p_{\text{eff}} = 430 \text{ nm}$  were recorded at a single distance, higher resolution datasets ( $p_{\text{eff}} = [100; 200] \text{ nm}$ ) were recorded using four planes with relative distances  $z_{1_2} - z_{1_1} = 1 \text{ mm}$ ,  $z_{1_3} - z_{1_1} = 5 \text{ mm}$  and  $z_{1_4} - z_{1_1} = 15 \text{ mm}$ . (see **Tab. 6.1**). For tomography 1499 projections distributed among  $360^\circ$  were recorded. The illumination time was altered between 0.1, 0.5 and 1 seconds for a single projection, depending on the focal distance and sample preparation method. For fast data acquisition and to minimize local tomography artifacts, tomograms were recorded in a continuous fashion with the rotation stage moving during accumulation. To minimize structural changes due to radiation damage, the x-ray

beam was attenuated by a factor  $f_{\text{att}} = 8$  using 1.5 mm thick aluminum for most samples.

### 6.1.4 Sample preparation and mounting

A careful sample preparation and suitable mounting is essential for x-ray propagation imaging. Aiming at near-native structure preservation simultaneous compatibility with three-dimensional imaging is an important issue. Different preparation and mounting methods have been investigated based either on immersion fixation of the nerves allowing wet environments or EPON-embedding allowing higher doses and possibly higher spatial resolution.<sup>2</sup>

#### 6.1.4.1 Immersion fixation

Wildtype C57Bl6/N mice were sacrificed by cervical dislocation. The optic nerves were carefully removed and fixed by immersion in 4% formaldehyde, 2.5% glutaraldehyde in phosphate buffer at the pH of 7.2 containing 0.5% NaCl according to [108] as described in [140]. Subsequently, the sciatic and saphenus nerves were prepared and fixed by immersion in the same fixing solution. For (optional) osmium tetroxide staining, after 18 hours of fixation at 4° C pieces of all the different nerves were postfixed in 2% OsO<sub>4</sub> in 0.1 M phosphate buffer pH 7.3 for two hours on ice and then washed several times in 0.1 M phosphate buffer.

#### 6.1.4.2 Mounting of immersion fixated samples

Immersion fixated mouse nerves had to be kept in a wet environment to prevent drying while keeping them spatially fixed. Several approaches were investigated for compatibility with 3D x-ray propagation imaging. In a first attempt, nerves were sucked into glass capillaries filled with phosphate buffer (**Fig. 6.2 a**). However, strong scattering from the glass-air interface at the capillary wall and relatively strong absorption of water and capillary degraded the quality of the phase reconstruction, especially since the nerves were close to the wall of the capillary with 0.5 mm diameter. A second approach used agarose embedding between two polypropylene foils on two metal rings [158] (**Fig. 6.2 b**). This preparation enables a kind of “contrast matching” by avoiding interfaces between air and strongly scattering sample parts improving phase reconstruction. However, the flat design of this holder imposes problems in tomographic reconstructions such as missing projections or varying absorption at different rotation angles. A third approach was developed as a merger of the first two which has proven an ideal sample container for three-dimensional imaging and phase reconstruction (**Fig. 6.3 a-e**). Strong absorption is circumvented by using a polyimide tube instead of a glass capillary. An increased diameter prevents capillary-air interfaces parallel to the optical axis to scatter, given the specimen is well centered within the tube and the illuminating beam is smaller than the capillary diameter. To position the nerve

<sup>2</sup> Immersion fixation, EPON-embedding and high pressure-freezing as well as optical and electron microscopy was performed by the Wiebke Möbius and colleagues, Max-Planck-Institut für Experimentelle Medizin, Göttingen, Germany.



Sample #	1	2	3	4	5			6	
Nerve	opt.	saph.	saph.	saph.	opt.			sci.	
Preparation	IF1	IF2	IF3	IF3	IF3			HPF	
OsO <sub>4</sub>				X	X			X	
$z_1 + z_2$ [mm]	5510	5127	526	526	526	526	526	526	526
$z_{1_1}$ [mm]	5333	240	300	300	300	138	69	300	69
$z_{1_2}$ [mm]	-	-	-	-	-	139	70	-	70
$z_{1_3}$ [mm]	-	-	-	-	-	143	74	-	74
$z_{1_4}$ [mm]	-	-	-	-	-	153	84	-	84
$p_{\text{eff}_1}$ [nm]	<b>718</b>	<b>309</b>	<b>430</b>	<b>430</b>	<b>430</b>	<b>198</b>	<b>99</b>	<b>430</b>	<b>99</b>
$p_{\text{eff}_2}$ [nm]	-	-	-	-	-	199	101	-	101
$p_{\text{eff}_3}$ [nm]	-	-	-	-	-	205	107	-	107
$p_{\text{eff}_4}$ [nm]	-	-	-	-	-	219	121	-	121
Time [s]	10	5	0.5	0.1	0.2	0.2	0.2	0.1	0.1
Attenuator	-	-	-	X	X	X	X	X	X
MBA $\alpha$	0.04	0.005	-	-	-	-	-	-	-
$N_{\text{it}}$ GS	-	4	-	-	-	-	-	-	-
CTF $\kappa$			150	9	9	-	-	9	25
CTF $\alpha_1$			0	0	0	$10^{-4}$	$10^{-4}$	0	0
CTF $\alpha_2$			0.2	0.2	0.2	0.01	0.01	0.2	0.01

**Table 6.1:** Main experimental parameters for 3D x-ray phase contrast imaging of nerve samples with source-detector distance  $z_1 + z_2$ , source-sample distance  $z_{1_m}$ , effective pixel size  $p_{\text{eff}_m}$ , accumulation time corresponding to a single projection at a single distance, attenuator settings (1.5 mm aluminum), and phase reconstruction parameter  $\alpha$  (for MBA),  $N_{\text{it}}$  (for GS),  $\kappa = \delta/\beta$ ,  $\alpha_1, \alpha_2$  (for CTF methods). Sample preparation is tabulated as IF1-3 (immersion fixation, different sample mounting and embedding) or HPF (high pressure freezing).

inside of the tube a mixture of 1% low melting point agarose (Agarose low EEO, AppliChem, Germany) was heated up to 60° C, degassed in an ultra sonic bath and kept at 45° C on a temperature controlled water bath on a hot plate. 2 ml agarose solution was filled into a small rectangular box, which got gelatinous after 2 minutes of cooling. A nerve kept in 50  $\mu$ l phosphate buffer (a) was deposited on the agarose and subsequently covered with additional 2 ml agarose solution. After cooling, a block of agarose gel was cut out which contained the nerve (b). A polyimide tube (Professional Plastics, USA) with 1.4 mm diameter was carefully stuck into the block with the nerve situated in the middle of the tube (c). Residual air in the lower part of the tube was replaced by agarose solution. Finally, the top end of the tube was closed with 2-component epoxy resin adhesive (Plus sofortfest, UHU, Germany) and the bottom end was glued onto the respective sample mount which consisted of a magnetic stainless steel goniometer base (GB-B1, MiTeGen, USA) at the GINIX setup (d) and a custom holder at the ID22NI beamline (e).

#### 6.1.4.3 EPON-embedding of immersion fixated samples

For electron microscopic analysis, immersion fixated nerves were embedded in EPON as described in [140]. In brief, after three washes in 0.1 M phosphate buffer pH 7.3, samples were postfixed with 2%  $\text{OsO}_4$  in 0.1 M phosphate buffer pH 7.3 at 4° C, followed by three washes in the same buffer. After dehydration in a graded ethanol series at 4° C, samples were incubated ( $3 \times 10$  minutes) in propylenoxide at room temperature followed by one hour incubations in propylenoxide/EPON 2:1 and 1:2 mixtures. After overnight infiltration with EPON, samples were transferred into embedding molds and polymerized for 24 hour at 60° C.

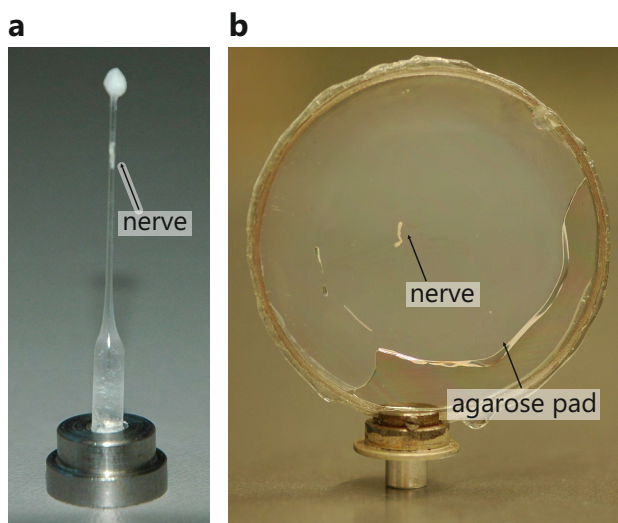


**Figure 6.2:** Immersion fixated nerve (a) in glass capillary with 0.5 mm diameter and (b) embedded in agarose between two polypropylene foils on metal rings.

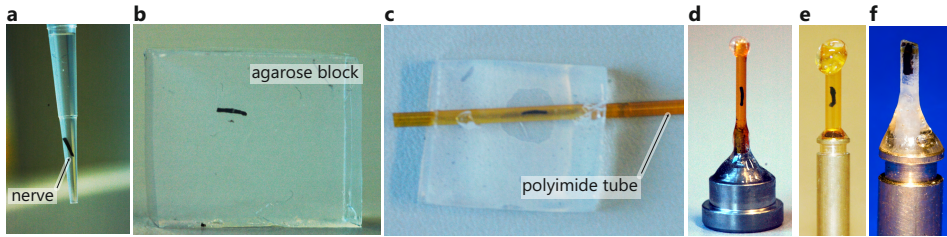


**Figure 6.3:** (a) Immersion fixated nerve (stained with osmium tetroxide) in 50  $\mu$ l phosphate buffer. (b) Block of agarose gel containing the nerve. (c) Polyimide tube stuck into the block. (d) Sample container glued onto the GINIX sample mount. Mounting for ID22 experiments of (e) immersion fixated and (f) high pressure frozen samples.

#### 6.1.4.4 High pressure freezing and EPON-embedding

For high-pressure-freezing, mice were sacrificed by cervical dislocation and optic nerves, sciatic and saphenus nerves were removed and placed in an aluminum specimen carrier with a 0.1 mm or 0.2 mm indentation (Leica, Austria). Remaining space was covered with 20% PVP (MW=10.000, Sigma-Aldrich), another aluminum carrier added as lid to assemble a sandwich and the sample was cryofixed in a high-pressure freezer (HPM100, Leica, Austria). Freeze-substitution was carried out in a Leica AFS (Leica, Austria) following the “tannic acid-OsO<sub>4</sub> protocol” as described in [140]. Briefly, samples were kept in tannic acid (Sigma-Aldrich) 0.1% in acetone at  $-90^{\circ}\text{C}$  for 100 hours first, washed with acetone ( $4 \times 30$  minutes,  $-90^{\circ}\text{C}$ ), and then transferred into OsO<sub>4</sub> (Science Services, Germany) 2% in acetone,  $-90^{\circ}\text{C}$  for 7 hours. The temperature was raised from  $-90^{\circ}\text{C}$  to  $-20^{\circ}\text{C}$  in increments of  $5^{\circ}\text{C}$  per hour, then kept unaltered at  $-20^{\circ}\text{C}$  for 16 hours, and then raised from  $-20^{\circ}\text{C}$  to  $+4^{\circ}\text{C}$  in increments of  $10^{\circ}\text{C}$  per hour. Afterwards, the samples were washed with acetone ( $3 \times 20$  minutes at  $4^{\circ}\text{C}$ ), allowed to adjust to room temperature (1 hour), and finally transferred into Epon (Serva) (50% Epon in acetone for 3 hours, 90% Epon in acetone for 18 hours, 100% Epon for 6 hours). The samples were placed in an embedding mold and polymerized ( $60^{\circ}\text{C}$ , 24 hours). The resulting robust EPON block was milled to a tube like shape and then mounted for imaging (Fig. 6.3 f).

#### 6.1.4.5 Light- and electron microscopy

For light microscopy, semithin sections (500 nm) of EPON-embedded samples were cut using a Leica Ultracut S ultramicrotome (Leica, Austria) equipped with a diamond knife ( $35^{\circ}$ , Diatome, Switzerland) and mounted on object slides. After drying and staining with Methylene blue/Azur II [179] for 1 minute on a hot plate at  $60^{\circ}\text{C}$ , coverslips were mounted using EUKITT® (Kindler, Germany) and images were taken at a Zeiss Axiophot microscope (Zeiss, Germany). For electron microscopic analysis, ultrathin sections (50 nm) were cut, mounted on copper grids (100 mesh hexagonal, Plano, Germany) and stained with an aqueous solution of

2% uranyl acetate (Merck, Germany) followed by lead citrate according to [178]. Electron micrographs were taken with a LEO912AB Omega electron microscope (Zeiss, Germany) equipped with an on-axis  $2048 \times 2048$  pixel CCD-camera (TRS, Germany).

## 6.2 Data analysis

### 6.2.1 Treatment of raw data

For experimental setup I, all diffraction patterns  $I(\mathbf{r}_\perp, z_{\text{eff}})$  were corrected by corresponding empty beam intensities  $I^{(\text{E})}(\mathbf{r}_\perp)$  and dark field recording  $I^{(\text{D})}(\mathbf{r}_\perp)$

$$\bar{I}(\mathbf{r}_\perp, z_{\text{eff}}) = \frac{I(\mathbf{r}_\perp, z_{\text{eff}}) - I^{(\text{D})}(\mathbf{r}_\perp)}{I^{(\text{E})}(\mathbf{r}_\perp) - I^{(\text{D})}(\mathbf{r}_\perp)}. \quad (6.1)$$

The dark field image represents detector read-out noise without any x-ray signal. **Fig. 6.4** shows diffraction pattern, empty beam and the corresponding normalized intensity for a single projection. Due to the filtering pinhole in the focal plane, there are no visible high frequency in the normalized intensity. The upper and lower part of the image corresponds to significantly lower photon flux of the illumination as can be seen in **(b)** and were not used for subsequent reconstruction steps. Tilt of the pixel columns of the detector against the rotation axis were corrected by numerically rotating all corrected intensity distributions by the corresponding angle **(d)**.

The same steps were performed for experimental setup II. Due to the fact that movements of the sample tower out of the beam resulted in a misaligned waveguide, empty beam intensities were recorded every 150th projection and averaged from 60 individual 5 second exposures. The waveguide was then realigned again. **Fig. 6.5** shows diffraction pattern, empty beam and the corresponding normalized intensity for a single projection. Note the smooth illumination provided by the waveguide. However, medium frequency features (horizontal stripes) of the waveguide beam persist after empty beam correction in addition to residual low frequency variations. This may be due to instabilities of the storage ring orbit and drift of the waveguide relative to the focus in combination with the rather large time interval between diffraction pattern and empty beam recording. Low frequency variations were effectively removed by dividing the intensity distribution by a profile obtained from the mean profile of the upper 200 rows of the image and subsequent application of a moving average filter with 200 pixel kernel. The resulting corrected intensity pattern is shown in **(d)**.

Data processing for experimental setup III was performed using a software package (based on Octave, ImageJ and PyHST) installed at the ID22 beamline server which was remotely accessible. All holograms were corrected by corresponding empty beam intensity and dark field recordings and normalized to a mean value of one. The diffraction pattern  $I(\mathbf{r}_\perp, z_{\text{eff}})$  for a single projection and the empty beam is shown in **Fig. 6.6**, the normalized intensity in **Fig. 6.9 a**. Empty beam intensities

were summed up from 21 individual recordings to increase statistics, recorded every 200th or 400th projection (depending on the dataset) of the tomographic scan. The dark field image was summed up over 20 individual recordings. KB mirror focusing induces wavefront aberrations which yield geometrical distortions of the recorded holograms. A grid with  $3\ \mu\text{m}$  periodicity was placed in the beam at respective  $z$  positions of the actual tomographic scans and used as a simple wavefront sensor to calculate and approximately remove these distortions [145]. Aberrations induced by the detector system were corrected based on characterisations performed earlier by the beamline staff.

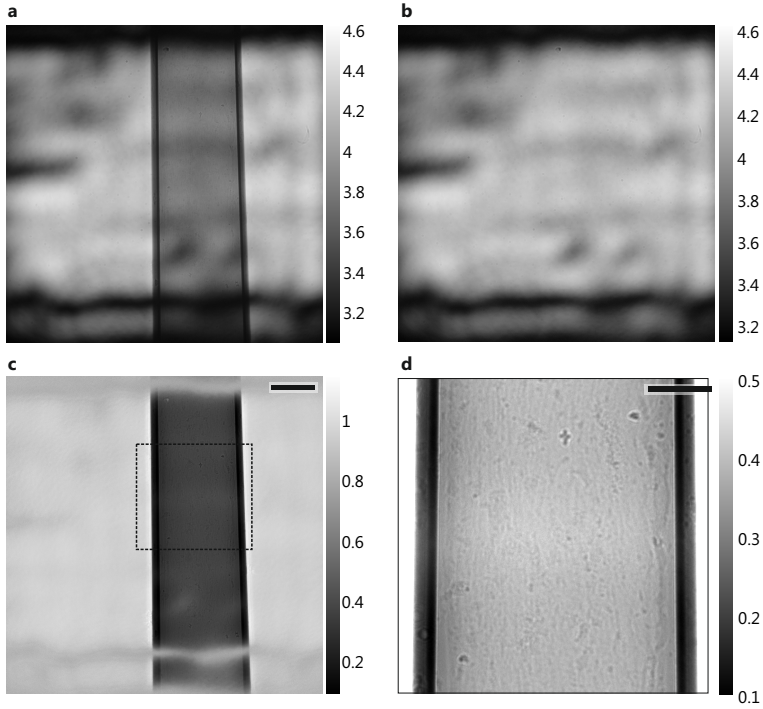


**Figure 6.4:** (a) Measured intensity distribution  $I(\mathbf{r}_{\perp}, z_{\text{eff}})$  with an immersion fixated optical nerve (sample 1, see **Tab. 6.1**) placed in the beam for experimental setup I, logarithmic color scaling. (b) Empty beam intensity distribution  $I^{(E)}(\mathbf{r}_{\perp})$ , logarithmic color scaling. (c) Corresponding normalized diffraction pattern  $\tilde{I}(\mathbf{r}_{\perp}, z_{\text{eff}1})$ . (d) Magnified view of the region indicated by the dashed rectangle in (c), corrected for detector rotation against tomographic axis. Scale bars, (c)  $200\ \mu\text{m}$ , (d)  $100\ \mu\text{m}$ .

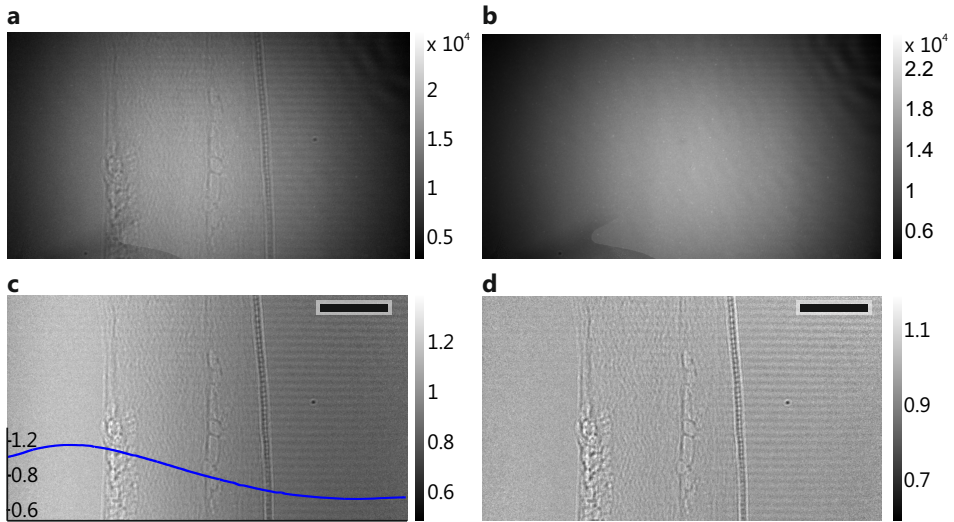


**Figure 6.5:** (a) Measured intensity distribution  $I(\mathbf{r}_\perp, z_{\text{eff}})$  with an immersion fixated saphenus nerve (sample 2 see **Tab. 6.1**) placed in the beam for experimental setup II. (b) Empty beam intensity distribution  $I^{(\text{E})}(\mathbf{r}_\perp)$ , average from 60 individual recordings. (c) Corresponding normalized diffraction pattern  $\bar{I}(\mathbf{r}_\perp, z_{\text{eff}_1})$ . Low frequency variations were removed by dividing the intensity distribution by the overlaid profile. (d) Corresponding corrected hologram. Scale bars, 100  $\mu\text{m}$ .

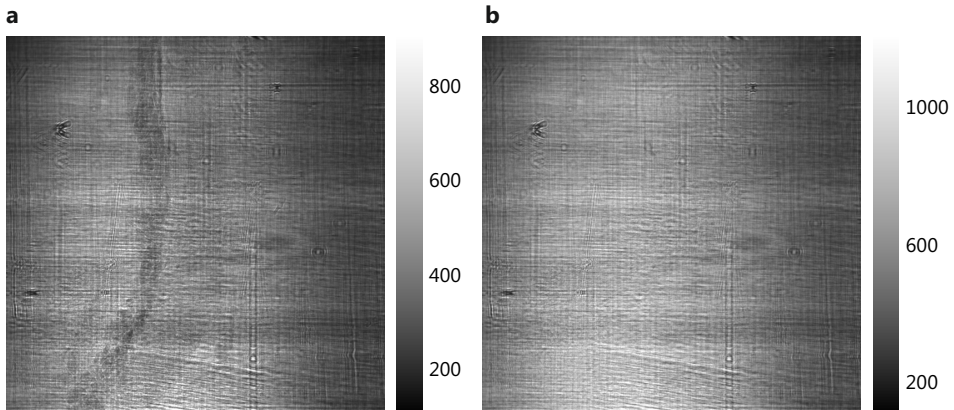


**Figure 6.6:** Raw data treatment. (a) Intensity distribution  $I(\mathbf{r}_\perp, z_{\text{eff}})$  recorded within 0.1 seconds with an immersion fixated and osmium tetroxide stained saphenus nerve (sample 4, see **Tab. 6.1**) in the beam. (b) Corresponding empty beam intensity  $I^{(\text{E})}(\mathbf{r}_\perp)$ . The corrected normalized hologram  $\bar{I}(\mathbf{r}_\perp, z_{\text{eff}_1})$  is shown in **Fig. 6.9 a**.

### 6.2.2 Phase retrieval

### 6.2.3 Single-distance phase retrieval

For experimental setup I, phase retrieval was performed using the modified Bronnikov algorithm (MBA, 2.22) with regularisation parameter  $\alpha = 0.04$  as shown in **Fig 6.7** for sample 1 (see **Tab. 6.1**). The diffraction patterns were padded by 100 pixels using mirror reflections in both directions prior to reconstruction.

For experimental setup II, a combined reconstruction method [76, 158, 117] yielded the best results. First, the phase distribution  $\varphi(\mathbf{r}_\perp)$  was reconstructed approximately using the MBA with regularisation parameter  $\alpha = 0.005$  and 500 pixel padding. Due to the small Fresnel number  $F^{10} = 0.45$  the recovered phase distribution is blurred. A subsequent iterative refinement based on the Gerchberg-Saxton algorithm assuming a pure phase object was able to remove the blurr. The algorithm was initialized with an object transmission function guess of

$$O(\mathbf{r}_\perp) = \exp[i\varphi(\mathbf{r}_\perp)] \quad (6.2)$$

and was run for  $N_{it} = 4$  iterations with a noise parameter of  $D = 0.02$ . The final phase reconstruction for a single projection of sample 2 (see **Tab. 6.1**) along with the corresponding normalized intensity is shown in **Fig. 6.8**.

For experimental setup III, lower resolution tomograms of entire nerves were recorded at a single distance to save acquisition time and to minimize dose. The relatively small Fresnel number  $F_{10} \approx 2$  according to source-sample distance  $z_1 = 0.3\text{m}$  and effective pixel size  $p_{\text{eff}} = 430\text{nm}$  resulted in rather blurred reconstructions using a single distance TIE-based approach (see section 2.2). However, the CTF-based approach assuming homogeneity ( $\kappa = \delta/\beta$ ) described by equation (2.40) yielded phase reconstructions  $\varphi(\mathbf{r}_\perp)$  of high quality. For immersion fixated nerves stained with osmium tetroxide as well as high-pressure frozen nerves,  $\kappa = 9$  gave the best results as evaluated by visual inspection. **Fig. 6.9** shows phase reconstruction and normalized intensity for an immersion fixated saphenus nerve (sample 4, see **Tab. 6.1**). For immersion fixated nerves which were not stained, a substantial higher  $\kappa = 150$  was chosen, corresponding to the weaker absorption compared to stained samples. The frequency-dependent regularisation parameter (equations 2.32,2.33)

$$\alpha(\nu) = \alpha_1 \cdot f(\nu) + \alpha_2 \cdot (1 - f(\nu)) \quad (6.3)$$

with

$$f(\nu) = (1 - \text{erf}[(\nu - \nu_{\text{cut}})/\sigma_\alpha]) / 2 \quad (6.4)$$

was set to  $\alpha_2 = 0.2$  for radial spatial frequencies  $\nu = \sqrt{\nu_x^2 + \nu_y^2}$  larger than the offset  $\nu_{\text{cut}} = 0.1$  cycles/pixel. Lower spatial frequencies were sufficiently regularized by the cosine terms in (2.34) corresponding to absorption, and  $\alpha_1 = 0$  could be chosen. The steepness of transition at  $\nu_{\text{cut}}$  is described by  $\sigma_\alpha = 0.01$ .

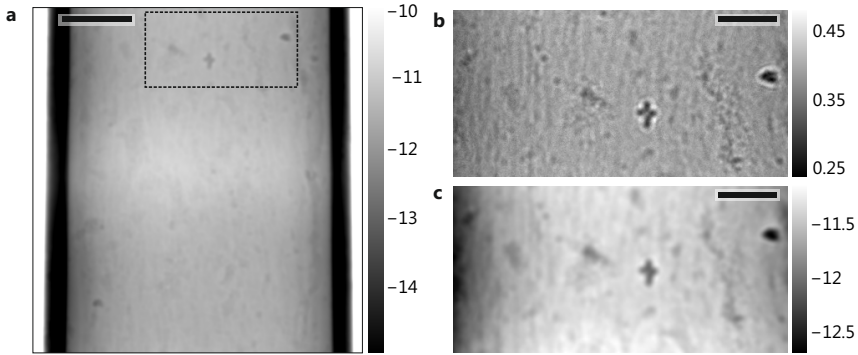


**Figure 6.7:** (a) Phase reconstruction corresponding to the intensity distribution shown in **Fig. 6.4 d** using the modified Bronnikov algorithm. Magnified view of (b) intensity and (c) phase reconstruction of the region indicated by a dashed rectangle in (a). Scale bars, (a) 100  $\mu\text{m}$ , 50  $\mu\text{m}$ .

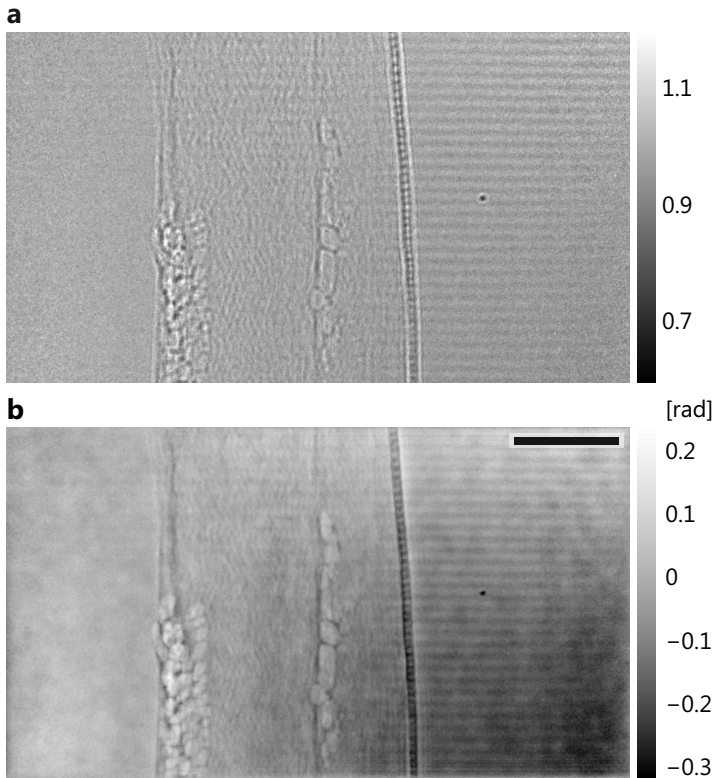


**Figure 6.8:** (a) Normalized intensity distribution  $\bar{I}(\mathbf{r}_{\perp}, z_{\text{eff}})$  of an immersion fixated saphenus nerve (sample 2, see **Tab. 6.1**). (b) Corresponding phase reconstruction obtained by a combined approach of a direct TIE based method and iterative refinement. Scale bar, 100  $\mu\text{m}$ .



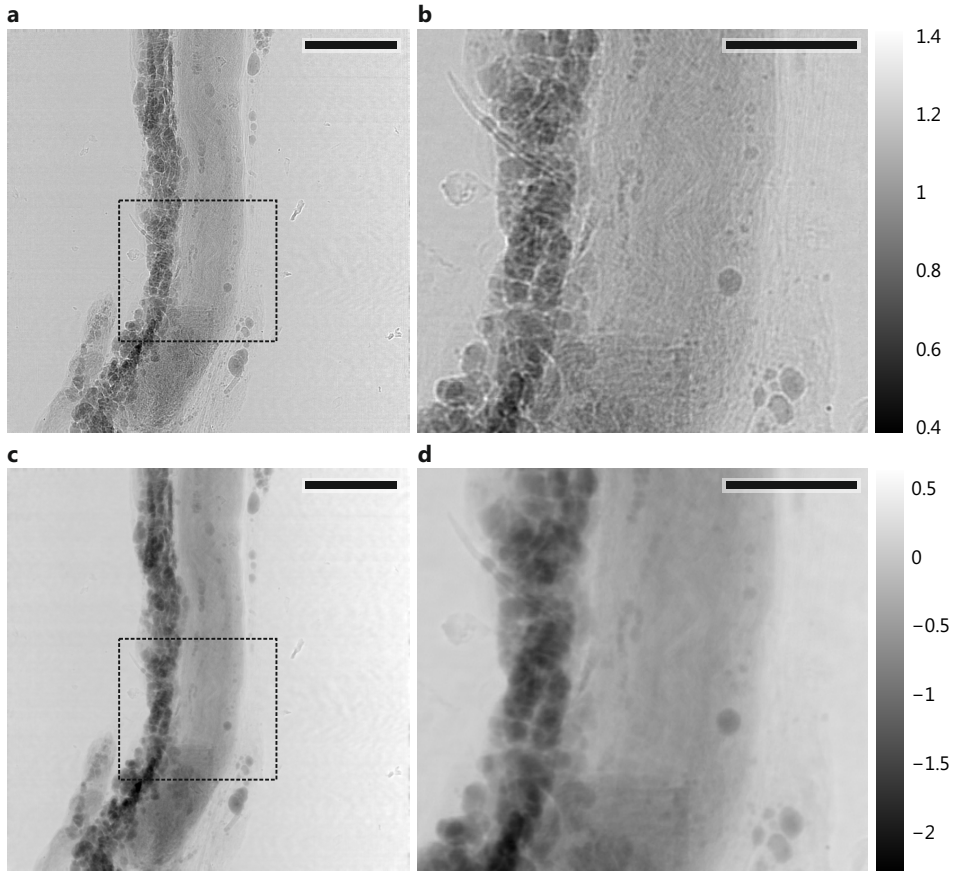


**Figure 6.9:** (a) Normalized intensity  $I(\mathbf{r}_{\perp}, z_{\text{eff}})$  of an immersion fixated saphenus nerve stained with osmium tetroxide (sample 4, see **Tab. 6.1**) for experimental setup III. (b) Magnified view of the region marked by the dashed rectangle in (a). (c) Phase reconstruction  $\tilde{\varphi}(\mathbf{r}_{\perp})$  corresponding to the hologram shown in (a) using the CTF-based approach assuming homogeneity with  $\kappa = \delta/\beta = 9$ . (d) Magnified view of the region marked by the dashed rectangle in (c). Scale bars, (a,c) 200  $\mu\text{m}$ , (b,d) 100  $\mu\text{m}$ .

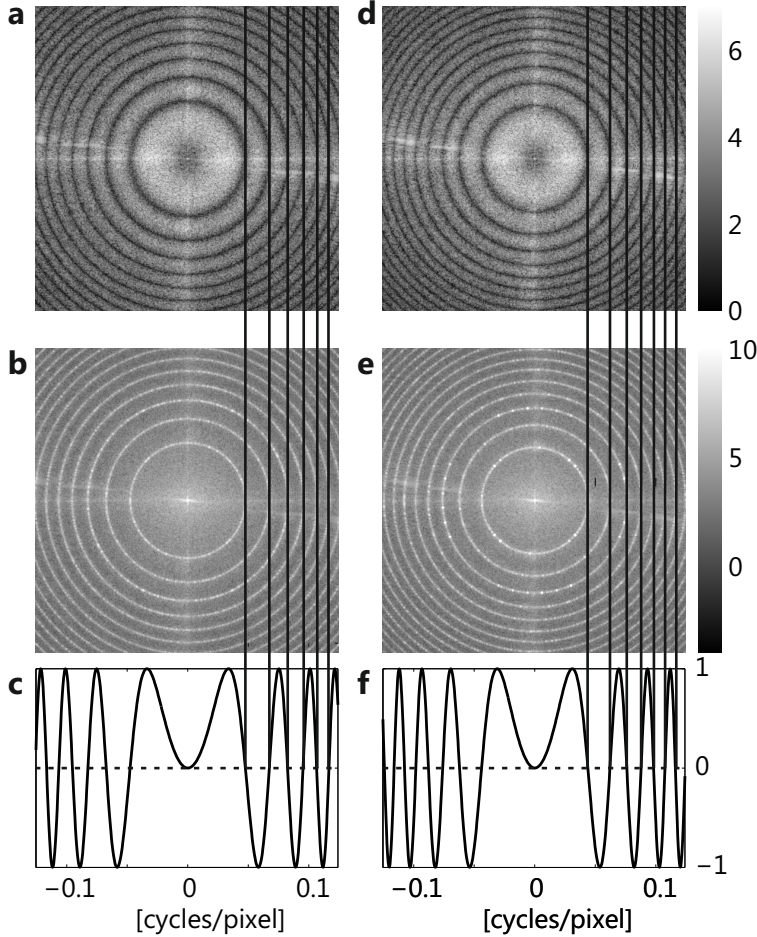


**Figure 6.10:** (a) PSD of the holographic reconstruction of sample 6 placed at  $z_{1_1}$  (Tab. 6.1). (b) PSD of a single-distance CTF-based reconstruction. (c) Corresponding phase contrast transfer function. (e-f) The same as obtained by placing sample 6 at a distance  $z_{1_4}$  (Tab. 6.1).

#### 6.2.4 Multi-distance phase retrieval

Higher resolution datasets recorded with experimental setup III at  $z_1 = 0.137$  m and  $z_1 = 0.069$  m with effective pixel sizes  $p_{\text{eff}} = 200$  nm and  $p_{\text{eff}} = 100$  nm correspond to Fresnel numbers  $F^{10} \approx 0.5$  and  $F^{10} \approx 0.2$ , respectively. At these Fresnel numbers the contrast transfer functions exhibits several zero crossings. **Fig. 6.10a** shows the power spectral density (PSD) of the holographic reconstruction from a single normalized hologram of sample 6 (**Fig. 6.12 a**) recorded with an effective pixel size of 99 nm (Tab. 6.1). Zeroes in the PCTF (c) manifest as missing infor-

mation in the PSD. Accordingly, single-distance CTF-based reconstruction shows maxima in the PSD (**b**) since the sinusoidal term in the denominator of equation (2.35) vanishes at zeroes of the PCTF. For larger effective propagation distances zero crossings appear at different spatial frequencies as shown in (**d-f**) for the sample positioned at  $z_{1_4}$  (**Tab. 6.1**). To minimize missing information  $N > 1$  distances were recorded.  $N = 4$  was chosen as a recommended compromise between reconstruction quality and applied dose [222]. Prior to phase reconstruction, the holograms  $\bar{I}_m(\mathbf{r}_\perp, z_{\text{eff}_m})$  with  $m = 1 \dots N$  were scaled to a common pixel size (corresponding to the highest magnification) and aligned with respect to each other by cross-correlation methods. **Fig. 6.11** shows the PSDs of phase reconstructions obtained by using 1-4 holograms recorded with the object (sample 6) placed at different distances. By increasing the number of regarded distances, artificial maxima in the PSD are removed more effectively. For immersion fixated nerves the

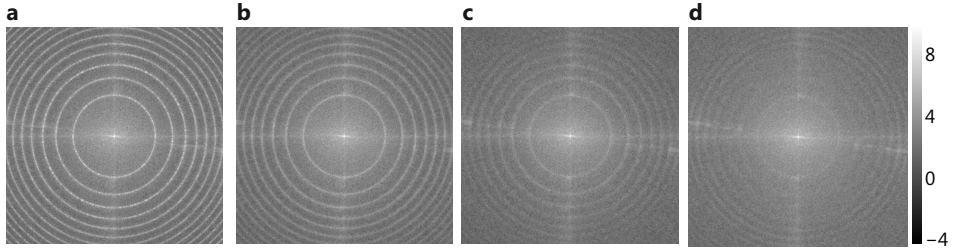


**Figure 6.11:** PSD of the phase distribution for a single projection of sample 6 as obtained by incorporating (a) one, (b) two (c) three and (d) four different  $z_{1_m}$  distances into the phase reconstruction.

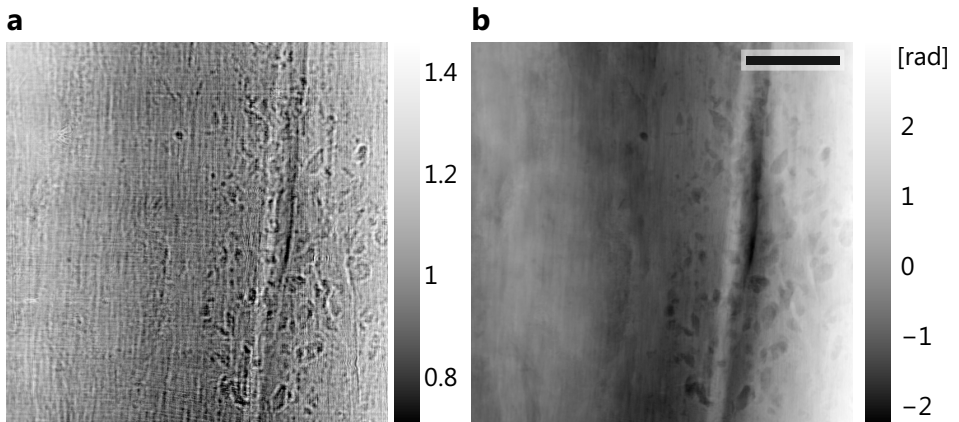


**Figure 6.12:** (a) Normalized hologram of a high pressure frozen sciatic nerve with effective pixel size  $p_{\text{eff}_1} = 99 \text{ nm}$  (sample 6, see **Tab. 6.1**) (b) Phase reconstruction obtained by using all four distances in a CTF-based phase reconstruction approach. Scale bar,  $50 \mu\text{m}$ .

phase  $\varphi(\mathbf{r}_\perp)$  was reconstructed using the CTF-approach assuming a pure phase object, described by equation (2.34). The frequency dependent regularisation parameter  $\alpha(\nu)$  (6.3) was defined by  $\alpha_1 = 10^{-4}$ ,  $\alpha_2 = 0.01$ ,  $\nu_{\text{cut}} = 0.1$  cycles/pixel and  $\sigma_\alpha = 0.01$ . For high pressure frozen samples embedded in EPON, the CTF approach assuming homogeneity ( $\kappa = \delta/\beta$ ) described by equation (2.39) yielded superior reconstructions, with  $\kappa = 25$ . The regularisation parameter was altered at low spatial frequencies compared to the pure phase object case since sufficient regularisation is provided by the absorption dependent cosine terms in (2.34), allowing for  $\alpha_1 = 0$ . **Fig. 6.12 b** shows the reconstructed phase distribution of a single projection for sample 6.

### 6.2.5 Tomographic reconstruction

For all datasets, phase distributions were obtained from all projections using the respective phase reconstruction method, yielding (1.91)  $\bar{\delta}_\theta(\mathbf{r}_\perp) = -\varphi_\theta(\mathbf{r}_\perp)/k$ . All phase projections corresponding to an angular range of  $\theta=0^\circ\dots180^\circ$  were aligned with respect to each other by cross-correlation methods for experimental setup I and II. To align the individual projections recorded with experimental setup III, every 200th or 400th projection (depending on the dataset, same as for empty images) a hologram was recorded as a reference with the rotation stage not moving, as opposed to the otherwise continuous data acquisition procedure. After all projections had been acquired, holograms at the reference angles were recorded again and used to determine and correct for drifts during the tomographic scan. Projections in between two reference angles were shifted by means of interpolation. After alignment of the individual phase projections, filtered backprojection (3.16) was performed using Ultra Fast Cone-Beam reconstruction software for setup I and II and PyHST for setup III. As a result, the three-dimensional decrement  $\delta(\mathbf{r})$  of the refractive index was reconstructed which is proportional to the electron density (1.67).

## 6.3 Results

### 6.3.1 Unstained nerves

A volume of  $0.6 \times 0.6 \times 1 \text{ mm}^3$  with a voxel size of 718 nm was reconstructed from 900 individual phase reconstructions (MBA) of sample 1 (experimental setup I). **Fig. 6.13 a** shows a slice through the reconstructed 3D electron density. The unstained nerve within the glass capillary is clearly identified and a substructure of point like features is visible. For comparison, an optical micrograph of an EPON-embedded optical nerve is shown in **Fig. 6.13 b** which allows to attribute these features to glial cells. Individual axons are not visible in the data due to medium spatial resolution and axon diameters below  $5 \mu\text{m}$ . As a next step, the zooming capability of cone-beam x-ray propagation imaging was exploited to achieve higher spatial resolution (experimental setup II) and a saphenus nerve with thicker axons was

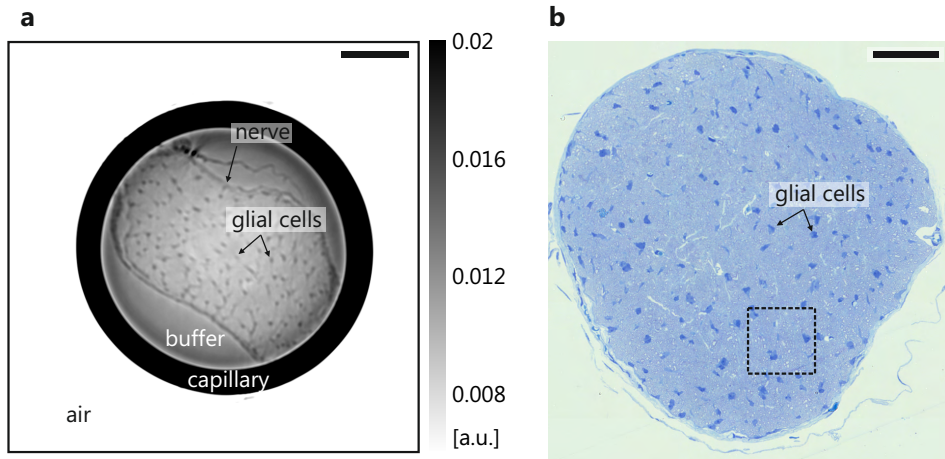


**Figure 6.13:** . (a) Slice through the reconstructed 3D electron density ( $848 \times 848$  pixel) showing the unstained nerve within the glass capillary. Substructures attributable to neuroglia are visible. (b) Optical micrograph of a semithin section of an EPON-embedded optical nerve. Size, quantity and distribution of glial cells matches the structures visible in the tomographic x-ray data. Scale bars, (a)  $100 \mu\text{m}$ , (b)  $50 \mu\text{m}$ .

prepared. Replacing the strongly absorbing glass capillary with agarose embedding between two polypropylene foils and switching to higher photon energies (from  $7.9 \text{ keV}$  to  $13.6 \text{ keV}$ ) justified the use of a pure phase object Gerchberg-Saxton type reconstruction scheme. This was necessary since higher spatial resolution is achieved by larger magnification corresponding to smaller effective pixel sizes in the sample plane, which in turn results in smaller Fresnel numbers where single-distance TIE based methods fail. A volume of  $463 \times 463 \times 463 \mu\text{m}^3$  with a voxel size of  $309 \text{ nm}$  was reconstructed from 838 individual phase reconstructions of sample 2. A slice through the reconstructed 3D electron density (**Fig. 6.14**) shows the nerve and adjacent fat. A closer view (inset in **a**) reveals substructures that could be related to axons. A vertical slice through the volume (**b**) shows structures that resemble filaments and form a shevron pattern. These structures may be attributed to axons, even though contrast and resolution do not suffice to clearly resolve individual axons. To consolidate the results, osmium tetroxide as a myelin stain was examined in a follow-up experiment.

### 6.3.2 Osmium tetroxide stain

The effect of osmium tetroxide staining on image contrast and axon visibility was investigated using experimental setup III. Phase and tomographic reconstruction were performed for a specimen without staining (sample 3) and for a specimen with staining (sample 4). Experimental parameters were identical for both mea-

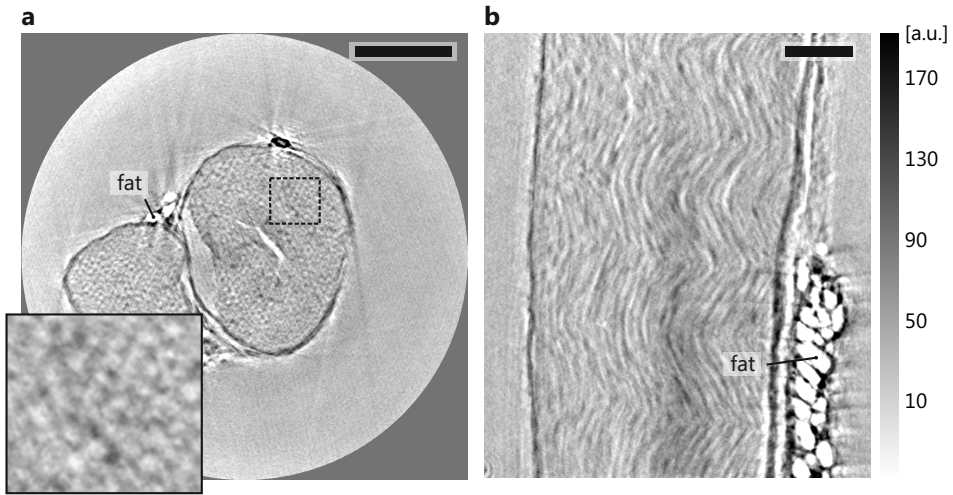


**Figure 6.14:** (a) Slice through the reconstructed 3D electron density ( $1500 \times 1500$  pixel) of a saphenus nerve showing sub-structures (inset) attributable to axons. (b) Vertical slice through the volume revealing structures that form a shevron pattern and can be attributed to axons. Scale bars, (a)  $100 \mu\text{m}$ , (b)  $50 \mu\text{m}$ .

surements (see **Tab. 6.1**) apart from attenuator settings and accumulation time. The first dataset (sample 3) without attenuators and 0.5 seconds accumulation time revealed that shrinkage and movements of the sample were induced by the high incident x-ray beam intensity. Based on this observation all other measurements at this setup were performed with the x-ray beam attenuated by a factor  $f_{\text{att}} = 8$  using 1.5 mm thick aluminum and reduced accumulation time of 0.1 or 0.2 seconds. As a result, data obtained for sample 4 did not show strong drifts and enabled a high quality tomographic reconstruction. **Fig. 6.15** shows a slice through the reconstructed 3D electron density for both samples. In addition to drifts, low frequency artifacts are introduced during the phase reconstruction process for sample 3 due to the fact that the nerve was situated close to the strongly scattering air-capillary interface (**a**). Sample 4 was well centered in the capillary and allows artifact free phase and tomographic reconstructions (**b**). Obviously, osmium staining has a huge effect on contrast. Staining of lipids with electron dense osmium reverses the relative electron density contrast of lipids against water as can be seen for fat (**c,d**). Without staining, electron dense nuclei of Schwann cells are visible while axons are at most vaguely identifiable. On the contrary, staining allows to visualize axons unambiguously since surrounding myelin is resolved (**f**). To confirm these observations, optical microscopy of EPON-embedded saphenus nerves was performed. **Fig. 6.16** shows an optical micrograph of a semithin section. Structures and most importantly axons which are visible in the tomographic data can readily be identified. In contrast to optical microscopy based



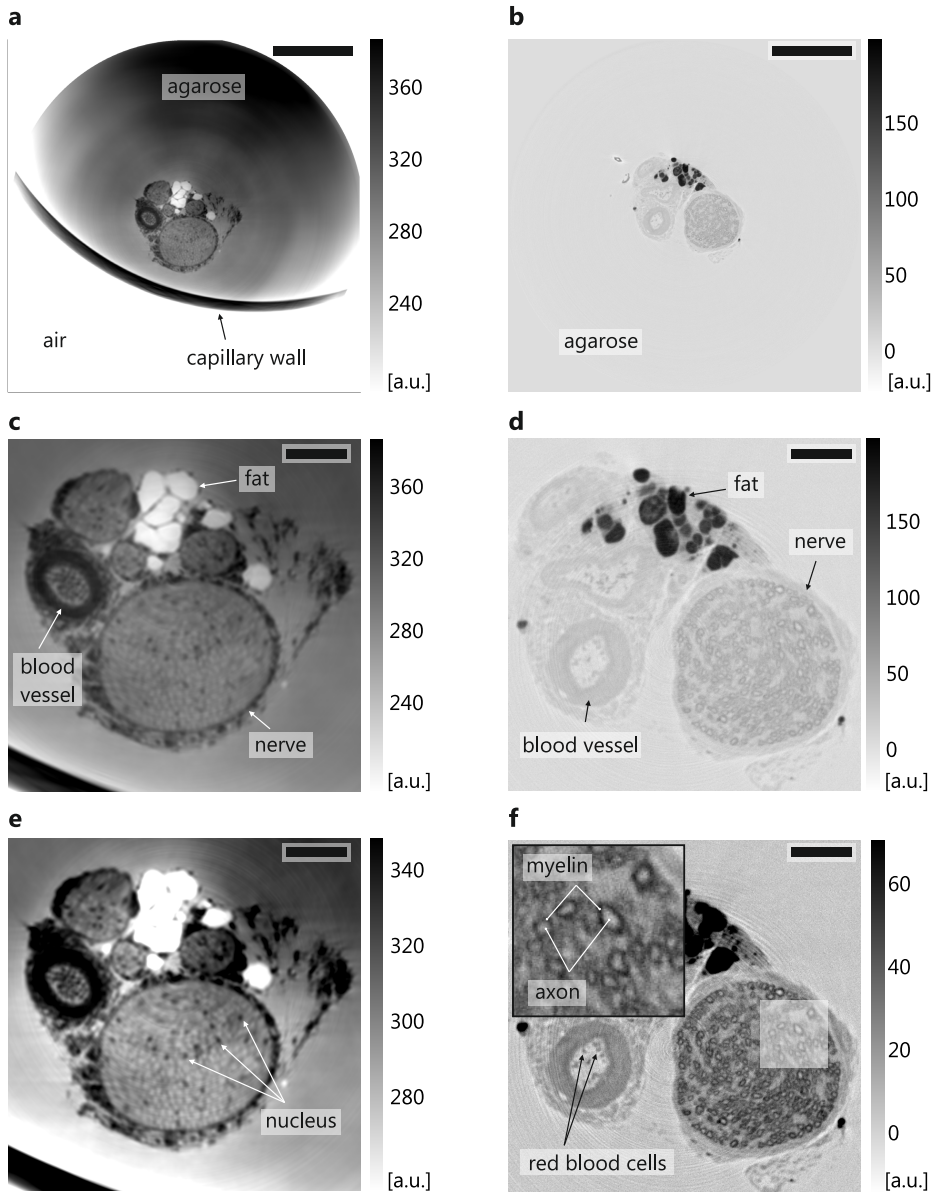


**Figure 6.15:** Slice through 3D electron density of immersion fixated saphenus nerves (a) without and (b) with osmium tetroxide stain. (c,d) Magnified view showing nerve, blood vessel and fat. Staining of lipids with electron dense osmium reverses the relative electron density contrast of lipids against water. (e,f) Adjusted contrast of the images shown in (c,d). Without staining only electron dense nuclei of Schwann cells are visible while staining allows to see axons surrounded by myelin (inset of (f)). Red blood cells are also visible. Scale bars, (a,b) 200  $\mu\text{m}$ , (c-f) 50  $\mu\text{m}$ .

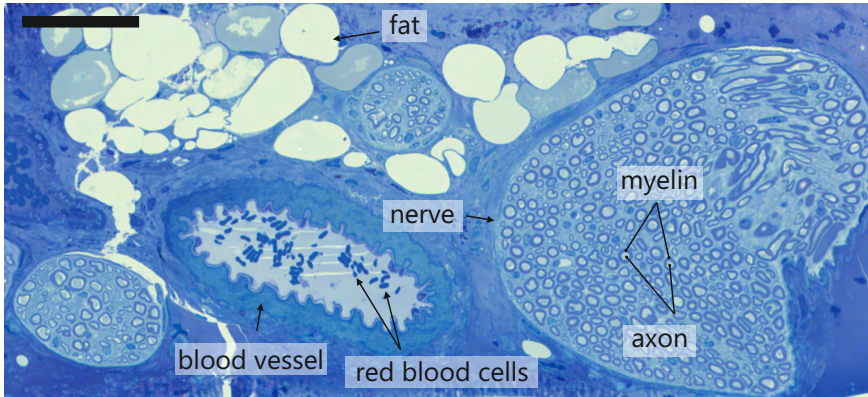


**Figure 6.16:** Optical micrograph of a semithin section of an EPON-embedded saphenus nerve. Nerve, fat, blood vessel, red blood cells, axon and myelin can be identified and readily correlated with the structures visible in the tomographic x-ray data (Fig. 6.15). Scale bar, 50  $\mu\text{m}$ .

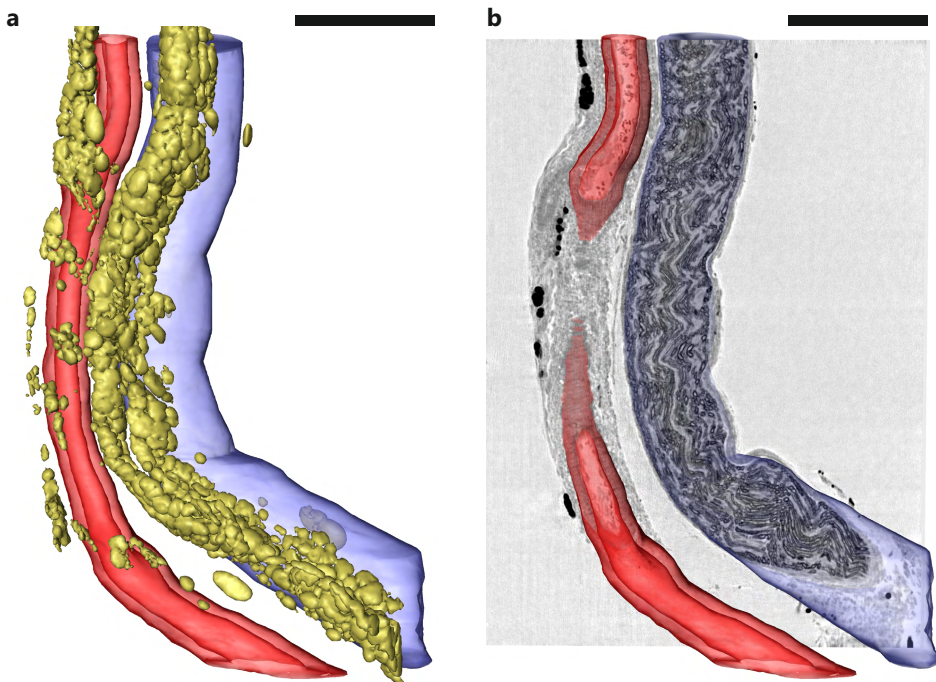


**Figure 6.17:** (a) three-dimensional visualisation of an immersion fixated specimen with nerve (blue), fat (yellow) and blood vessel (red). (b) A slice through the reconstructed 3D volume was added to the visualisation revealing how axons follow the direction of the nerve.



on sectioning, x-ray tomography provides a complete 3D dataset. Here, a volume of  $880\ \mu\text{m} \times 880\ \mu\text{m} \times 880\ \mu\text{m}$  was reconstructed which enables the visualisation of a large portion of the nerve as shown in **Fig. 6.17**. The dataset shows nerve, blood vessel and adjacent fat (**a**). Importantly, it reveals how axons follow the nerve and consistent to the previous experiment, a shevron pattern is observed (**b**). This strengthens the presumption of the previous experiment that unstained axons can be visualized by means of x-ray phase contrast. Future studies should analyze whether the shevron pattern is due to sample preparation, linked to the fact that the nerve may have relaxed from a stretched conformation after being cut out of the mouse or if it indeed is a native intrinsic pattern of the nerve.

### 6.3.3 Higher spatial resolution for imaging of optical nerves

The results of the previous section demonstrate that it is possible to image entire nerves in 3D with spatial resolution and contrast high enough to resolve single axons by means of x-ray phase contrast imaging. However, axons of the saphenus nerve in the peripheral nervous system (PNS) are relatively thick and more strongly myelinated than axons of the optical nerve in the central nervous system (CNS). To this end, another approach to image optical nerves was followed, based on the experience gained in the previous experiment concerning staining. A tomogram of an immersion fixated and osmium stained optical nerve (sample 5, see **Tab. 6.1**) was recorded and reconstructed with identical settings as used for the osmium stained saphenus nerve (**Fig. 6.18 a,d**). Obviously, only few axons are vaguely visible in contrast to the clearly resolved axons of the saphenus nerve (**Fig. 6.15 f**) owing to their smaller diameters. To increase spatial resolution, two additional tomographic scans were recorded and reconstructed based on the CTF approach (2.34) with  $N = 4$  distances at effective pixel sizes  $p_{eff_1} = 198\ \text{nm}$  and  $p_{eff_1} = 99\ \text{nm}$ , respectively (see **Tab. 6.1**). A slice through the reconstructed 3D electron density is shown in **Fig. 6.18** for both scans. Here, smaller pixel sizes result in increased visibility of axons (compare **d-f**). Moreover, increased photon flux density incident on the sample for smaller source-sample distances  $z_1$  yields increased contrast. However, the higher photon flux at smaller  $z_1$  and the need for multiple distances induced shrinkage and movements of sample or surrounding agarose. Alignment of the  $N = 4$  holograms with respect to each other as well as alignment of the resulting phase maps with respect to the reference images (see sections 6.2.4, 6.2.5) resulted in reasonable data quality near the axis of rotation. Away from the center, artifacts are clearly visible. In **b** low frequency artifacts at the border of the nerve arise while in **c** the data is severely blurred (see inset). An optical micrograph of an EPON-embedded optical nerve was recorded (**Fig. 6.19**) verifying the structures and their sizes observed by x-ray phase contrast tomography. As an important result, the tomogram with  $p_{eff_1} = 99\ \text{nm}$  allows to identify axons with a diameter down to  $1\ \mu\text{m}$  (inset in **Fig. 6.18 f**).

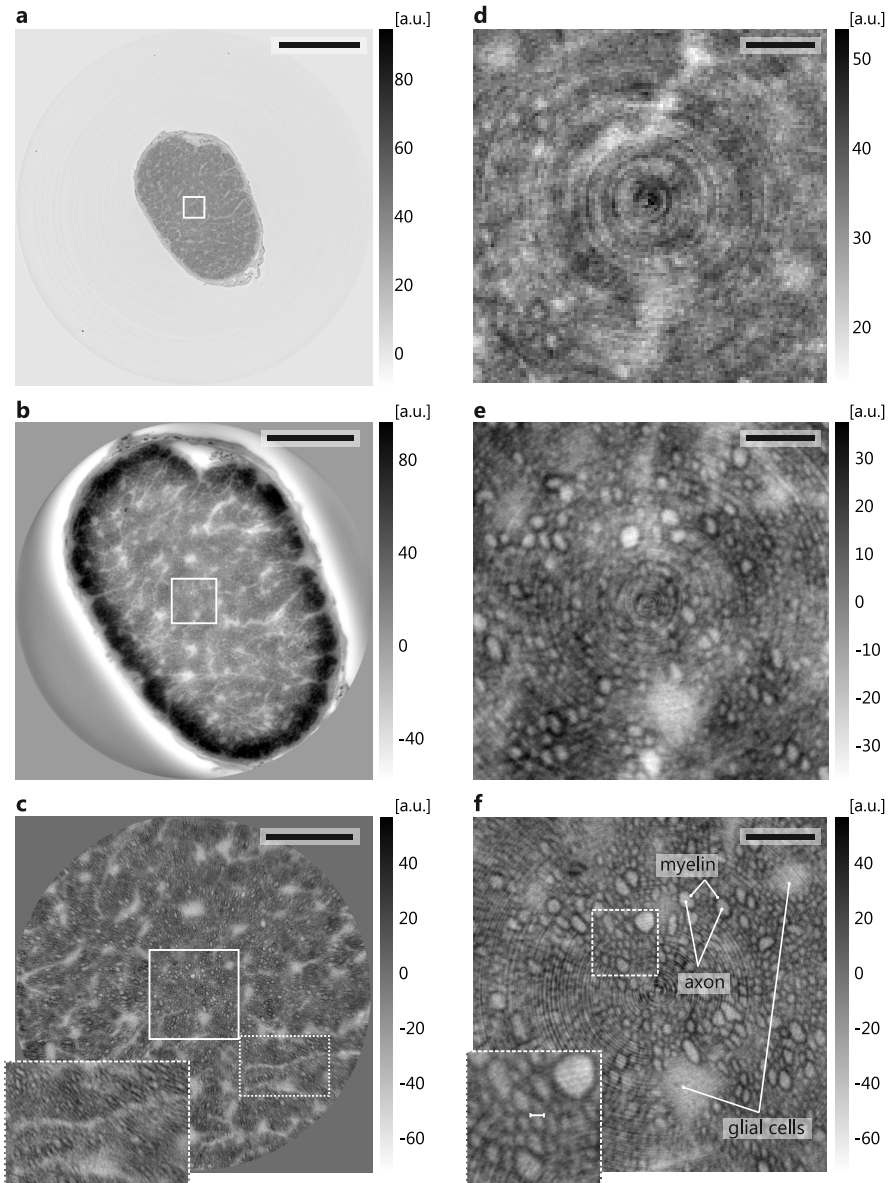


**Figure 6.18:** Slice through 3D electron density of an immersion fixated and osmium stained optical nerve obtained from (a) single-distance and (b,c) multi-distance recordings with (a) 430 nm, (b) 198 nm and (c) 99 nm voxel size. (d-f) Magnified views of the regions indicated by the rectangles in (a-d) corresponding roughly to the same volume within the sample. Smaller pixel sizes correspond to increased visibility of axons. (f) Axons surrounded by myelin are clearly resolved for axons with a diameter down to 1  $\mu\text{m}$  (scale bar in inset). Scale bars, (a) 200  $\mu\text{m}$ , (b) 100  $\mu\text{m}$ , (c) 50  $\mu\text{m}$  and (d-f) 10  $\mu\text{m}$ .

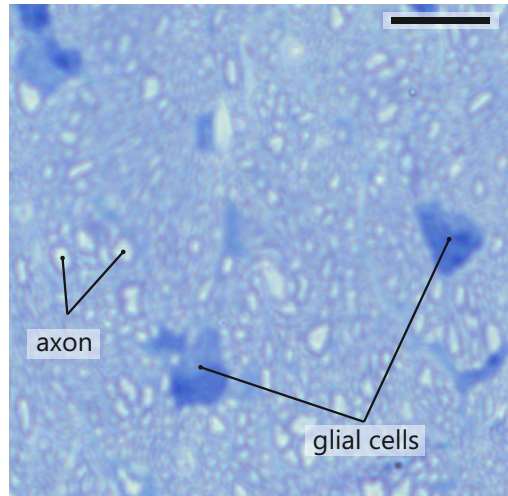


**Figure 6.19:** Optical micrograph of a semithin section of an EPON-embedded optical nerve. Magnified view of the region indicated by the dashed rectangle in **Fig. 6.13 b** with lateral extent corresponding to regions shown in **Fig. 6.18 d-f**. Axons and neuroglia can be identified and readily correlated with the structures visible in the tomographic x-ray data (**Fig. 6.18 f**). Scale bar, 10  $\mu\text{m}$ .

### 6.3.4 High resolution imaging using high pressure freezing

The results of the previous sections demonstrate the zooming capabilities of cone-beam x-ray propagation imaging [145]. However, structure preservation for immersion fixated nerves remains an issue, so far preventing artifact free high resolution imaging. For this reason, high pressure frozen EPON-embedded sciatic nerves were investigated. **Fig. 6.20** shows a slice through the reconstructed electron density of a high pressure frozen sciatic nerve (sample 6, see **Tab. 6.1**) with 99 nm voxel size and an optical micrograph of a corresponding semithin section. Axons and surrounding myelin are clearly visible. Moreover, resolution and contrast of the x-ray data is sufficient to identify Schmidt-Lantermann incisures [86] as shown in **Fig. 6.21**. In **a-c** the region corresponding to the rectangle in **Fig. 6.20 a** is shown for three slices separated from each other by 5  $\mu\text{m}$ . The myelin sheath transforms from a solid ring into a hollow donout and back. The same axon is shown as a vertical cut through the 3D data in **d**. The three planes used in **a-c** are indicated by small arrows. Comparison with an electron micrograph (e) suggests that this feature corresponds to a Schmidt-Lantermann incisure. **Fig. 6.22** depicts a vertical slice through the reconstructed volume showing several axons with myelin sheath and characteristic regions where the myelin sheath does not exist. A magnified view of such a region is shown in **b**. Comparison with an electron micrograph (c) strongly suggests to assign these structures to nodes of Ranvier. The huge ad-

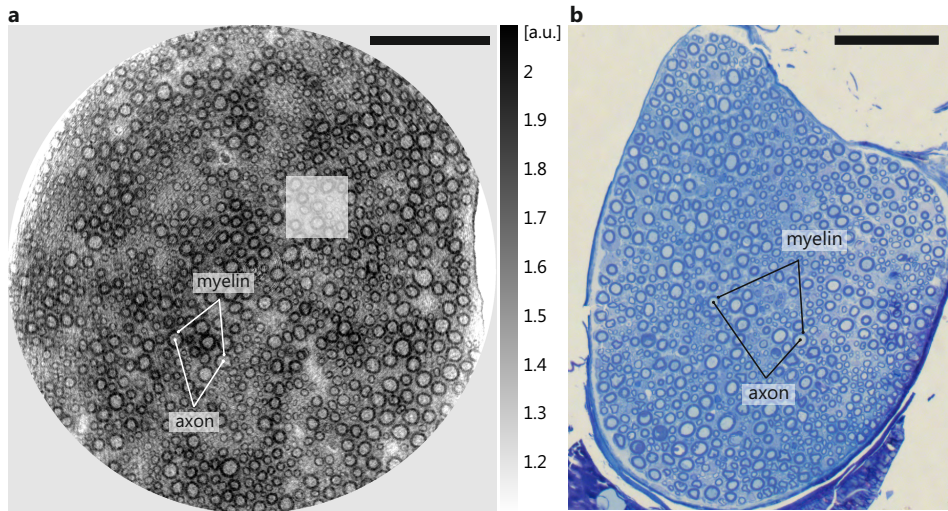


**Figure 6.20:** (a) Slice through the reconstructed electron density of a high pressure frozen sciatic nerve with 99 nm voxel size. (b) Optical micrograph of a semithin section of an EPON-embedded sciatic nerve. Axons with myelin sheath can readily be identified in both images. Scale bars, (a) 50  $\mu\text{m}$ , (b) 100  $\mu\text{m}$ .

vantage of the obtained dataset is its combination of a large field of view of more than  $200\ \mu\text{m} \times 200\ \mu\text{m} \times 200\ \mu\text{m}$  with sufficient spatial resolution and contrast to identify axons, the myelin sheath with Schmidt-Lantermann incisures and nodes of Ranvier. A three-dimensional rendering of 20 axons along with a slice through the volume is shown in **Fig. 6.23**. Myelin incisures are rendered green and nodes of Ranvier red. Next to the unique information content of three-dimensional visualisations one can envision several measures that could be drawn from the data. Examples are the thickness of axons, thickness of the myelin sheath and the corresponding g-ratio (ratio of both), internodal length, node length or the number of incisures per internode. As an important feature, the three-dimensional distribution, orientation and relative location of features can be evaluated. An example of 13 axons is shown in **Fig. 6.24** (different axons than in **Fig. 6.23** were rendered). The visualisation suggests that Schmidt-Lantermann incisures may predominately be found in the vicinity of nodes of Ranvier belonging to neighbouring axons. It is not the purpose of this study to draw this conclusion but the example illustrates how new insights may be inferred from quantitative three-dimensional x-ray phase contrast tomograms.

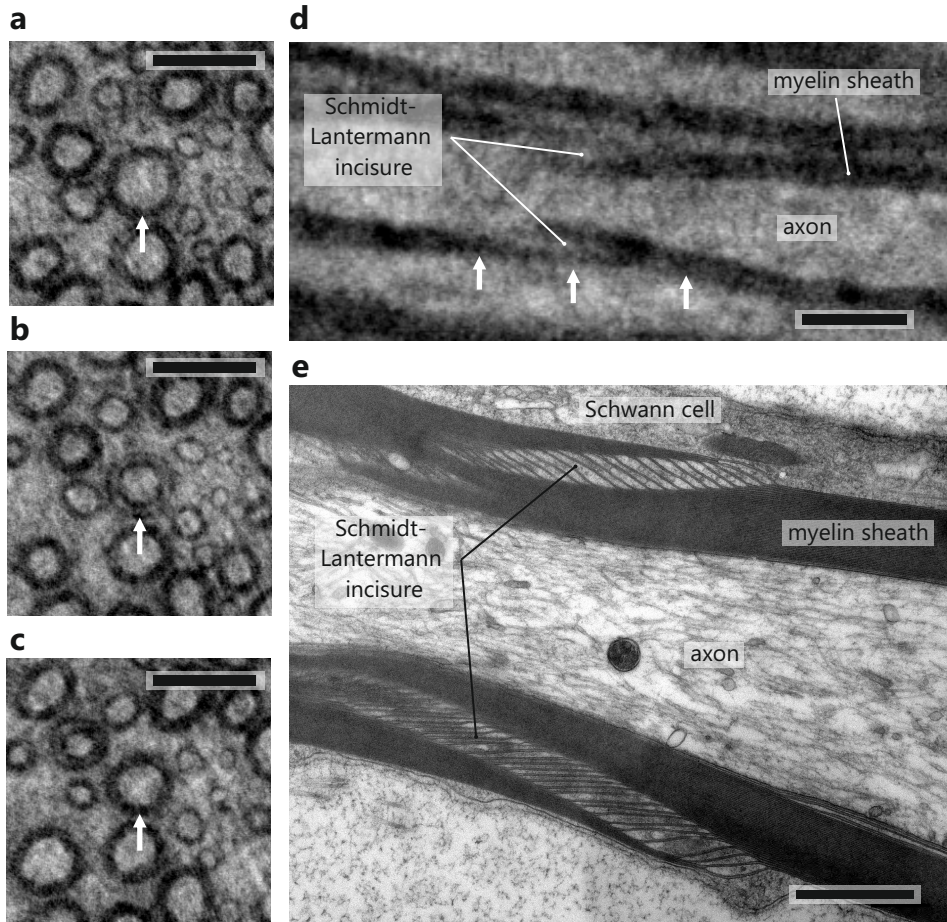


**Figure 6.21:** (a-c) Magnified view of the region corresponding to the rectangle in Fig. 6.20 a. for three different slices separated from each other by  $5\ \mu\text{m}$ . The myelin sheath surrounding the axon changes to a hollow donut and back (see arrows). (d) Vertical slice of the same axon. The position of the slices shown in (a-c) are indicated by arrows. (e) Electron micrograph (adjusted contrast) of a similar nerve suggesting that the observed structure is a Schmidt-Lantermann incisure. Scale bars, (a-c)  $1\ \mu\text{m}$ , (d)  $5\ \mu\text{m}$ , (e)  $1\ \mu\text{m}$ .



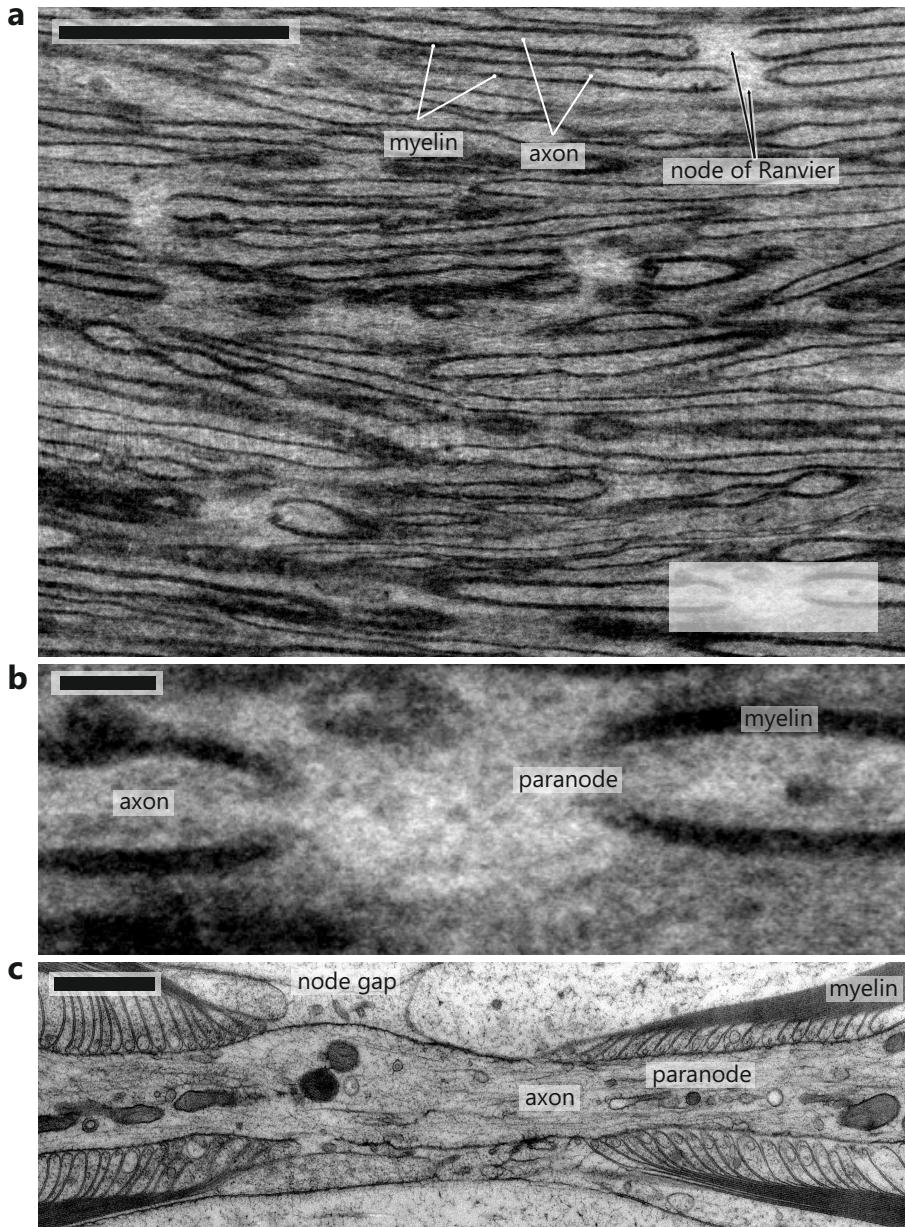


**Figure 6.22:** (a) Vertical slice through the reconstructed 3D electron density showing several axons surrounded by myelin. (b) Magnified view of the region indicated by the rectangle in (a). Comparison with an electron micrograph (c, adjusted contrast) suggests that the structure is a node of Ranvier. Scale bars, (a) 50  $\mu\text{m}$ , (b) 5  $\mu\text{m}$ , (c) 1  $\mu\text{m}$ .

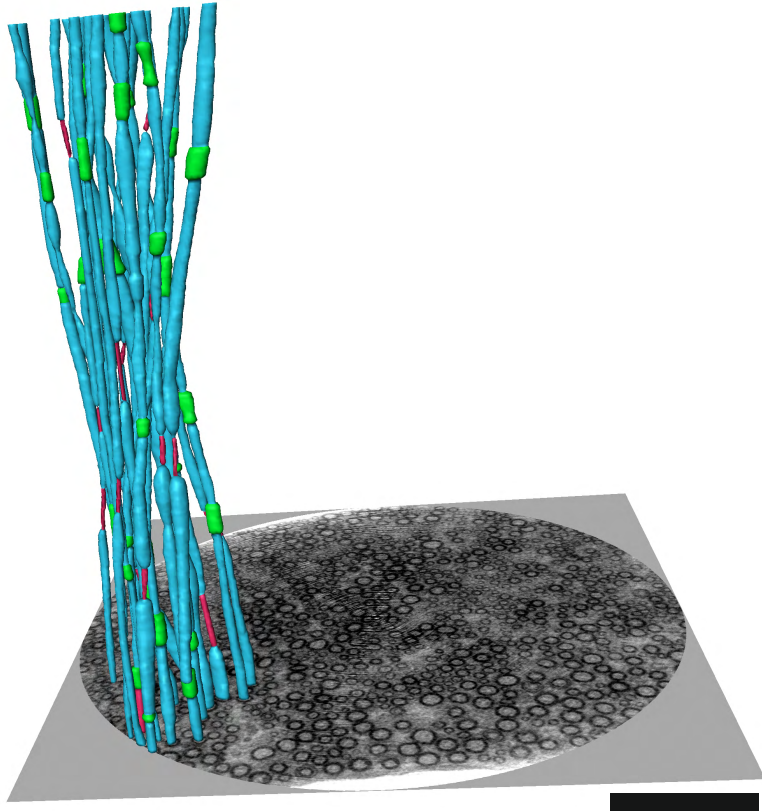


**Figure 6.23:** Three-dimensional visualisation of 20 axons (turquoise) along with a slice through the data. Nodes of Ranvier are rendered red, Schmidt-Lantermann incisures green. Scale bar, 100  $\mu\text{m}$ .

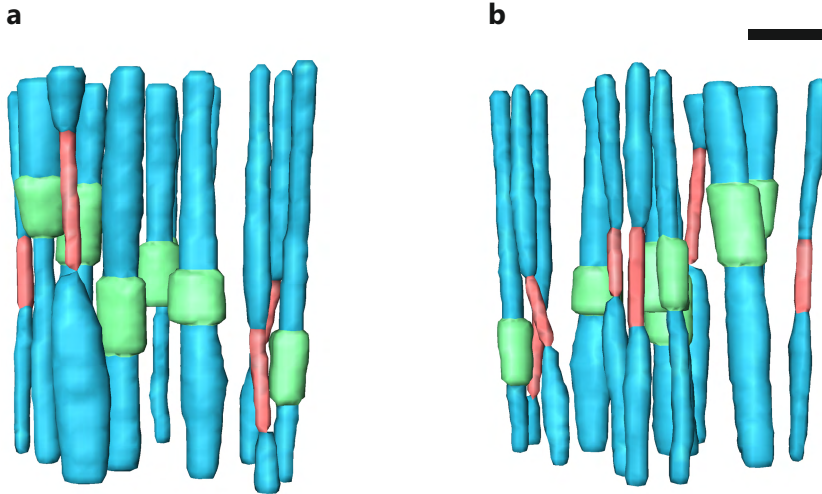


**Figure 6.24:** *Three-dimensional visualisation of 13 axons (turquoise) with nodes of Ranvier (red) and Schmidt-Lantermann incisures (green). (b) Different orientation of the same objects. Next to nodes of Ranvier, Schmidt-Lantermann incisures of neighbouring axons can be found. Scale bar, 20  $\mu\text{m}$ .*

## 6.4 Summary

Three-dimensional hard x-ray propagation imaging of uncut nerves was presented for mouse nerves of the central as well as peripheral nervous system. Different preparation and mounting approaches were investigated and phase retrieval was adapted to the respective experimental conditions. While sub-structure in the nerve was visible without staining, it was found that an osmium tetroxide stain helps to visualize myelin. Immersion fixation was sufficient for high resolution imaging, but artifacts associated with movements or shrinkage were observed. High pressure freezing turned out to be particularly useful for high resolution imaging. A large volume of more than  $(200 \mu\text{m})^3$  with isotropic voxel size of 100 nm was reconstructed from a sciatic nerve and more than 1000 single axons could be identified. Importantly, contrast and resolution were sufficient to resolve the myelin sheath, nodes of Ranvier and Schmidt-Lantermann incisures. The data suggests that Schmidt-Lantermann incisures may predominate be found in the vicinity of nodes of Ranvier belonging to neighbouring axons. Importantly, the presented approach is highly compatible with electron and optical microscopy in terms of sample preparation allowing correlative measurements. Once the setup is aligned and optimal phase reconstruction parameters are determined, batch measurements and reconstruction of several samples is in principle straight forward, and would enable to investigate several nerves as part of a biomedical study.



## 7 Three-dimensional density contrast of *Deinococcus radiodurans*

Optical nanoscopy based on visible light fluorescence is becoming an important tool for three-dimensional imaging of biological cells at the nanoscale [98, 167]. However, not all biological problems can be addressed based on the distribution of fluorescence markers. Therefore, additional and complementary contrast mechanisms are needed. Coherent x-ray imaging and tomography offers a unique potential for quantitative three-dimensional density determination at scalable resolution by means of quantitative phase reconstruction schemes [35, 100, 131, 153, 189, 195, 216]. Quantitative density measurements and density based discrimination is important in many biological applications but typically associated with destructive separation of components. Non-destructive determination of density distribution within the sample as obtained by 3D coherent x-ray imaging along with reconstructed volumes, shapes and topologies therefore equips biophysical research with an 'ultracentrifuge' at the organelle level.

The goal of the present experiment was to implement quantitative 3D imaging of unstained and unsliced cells of *Deinococcus radiodurans*. Density contrast may help to understand the bacterium's extraordinary resistance to high doses of ionizing radiation based on the structural arrangement of its nucleoid [49, 48, 144]. Coherent diffraction x-ray imaging was previously used to derive the *projected* electron density of *Deinococcus radiodurans* [65], providing thus a contrast complementary to electron microscopy studies [47, 130]. In order to obtain the locally resolved electron and mass density rather than just projected values, this work has to be extended from 2D to 3D. However, for biological samples the applied dose is a crucial parameter in view of structural changes and radiation damage during the imaging process as observed in a current 3D ptychographic CDI study of *Deinococcus radiodurans* [216]. Radiation damage of samples is considered to be the ultimate limitation in x-ray microscopy, if resolution due to the characteristics of sources, optical components, reconstruction algorithms and detection is successfully scaled down [97]. Therefore, minimizing the dose for a given image resolution and contrast is a primary challenge for x-ray optics. To this end, propagation based phase contrast imaging using x-ray waveguides is a promising approach, as recently presented for two-dimensional imaging of biological cells [63]. Moreover, in view of 3D imaging a full field approach based on scanning only one degree of freedom (rotation axis) in contrast to ptychographic tomography which involves scanning two translations and one rotation [216, 43] produces

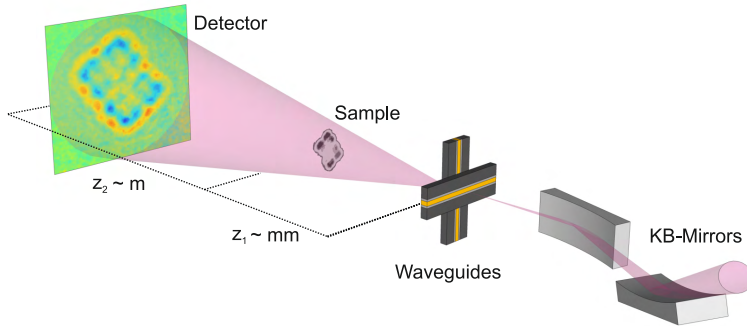


**Figure 7.1:** Sketch of the experimental setup. A system of two crossed planar waveguides is positioned in the focal plane of two KB mirrors, illuminated by a monochromatic x-ray synchrotron beam. The sample is placed at a distance  $z_1$  behind the waveguide exit. The holographic intensity distribution is recorded by an area pixel detector placed at a distance  $z_2$  behind the sample.

less overhead time in data acquisition and imposes less restrictive requirements on mechanical accuracy and longterm vibrational stability. However, an extension of waveguide-based phase contrast imaging to three dimensions requires a synchrotron endstation which provides the degrees of freedom needed for waveguide alignment and sample positioning. The present experiment was performed at the GINIX setup (see section 4.3) which provides the required instrumentation for 3D waveguide-based imaging. The measurements constitute the first demonstration of waveguide-based phase contrast tomography as well as the first tomographic experiment performed at this recently installed instrument.<sup>1</sup>

## 7.1 Experiment

### 7.1.1 Experimental setup

The experiment was performed at the original waveguide configuration of the GINIX setup (see section 4.3.4). The undulator beam was monochromatized to 13.8 keV and focused to a size of  $D_h = 370 \text{ nm}$  and  $D_v = 200 \text{ nm}$  full width at half maximum (FWHM). The total flux was  $2.4 \times 10^{11}$  counts per second at 70 mA storage ring current, as measured by a Pilatus pixel detector (see section 4.1) positioned at 5.29 m in the widened far-field of the KB beam. The waveguide system (XWG1, see **Tab. 4.1**) consisted of two crossed planar waveguide slices of lengths  $l_1 = 400 \mu\text{m}$  and  $l_2 = 207 \mu\text{m}$ , each with a transmission optimized sputtered thin film sequence Ge/Mo/C/Mo/Ge, with 35 nm amorphous C as the guiding layer [119, 120]. The near-field intensity distribution in the effective focal

<sup>1</sup> The work presented here has been published in a shorter form in [12] before.

plane obtained by phase reconstruction using the ER algorithm reveals a beam confinement of about  $10\text{ nm} \times 10\text{ nm}$  (FWHM), respectively (see **Fig. 4.6 e** and **Tab. 4.1**). The small quasi-point source provided by the waveguide is evidenced by the large divergence angle of its far-field intensity distribution (**Fig. 4.6 a**), measured at 15 keV by a Pilatus pixel detector positioned at 5.29 m. The relatively homogenous part of the waveguide far-field intensity distribution as indicated by the dashed rectangle was used for imaging. The sample was placed at a (defocus) distance  $z_1 = 8\text{ mm}$  from the WG exit plane on the dedicated sample tower (T2 in **Fig. 4.3 b**). The holograms were recorded with a Maxipix detector placed at about 5 m from the WG exit. The geometric magnification of  $M \simeq 660$  results in an effective detector pixel size of 83 nm and an effective propagation distance of  $z_{\text{eff}} = 8\text{ mm}$ . For tomographic imaging the sample was aligned into the axis of rotation by use of the second on-axis video microscope (see section 4.3) and subsequent refinement in the x-ray beam. Then, 83 projection images  $I_\theta(\mathbf{r}_\perp, z_{\text{eff}})$  were collected over 162 degrees with a total exposure time of 10 minutes for each angle  $\theta$ , distributed over  $N = 15$  detector accumulations. The empty beam intensity distribution  $I^{(\text{E})}(\mathbf{r}_\perp)$  was recorded during 40 minutes.

### 7.1.2 Sample preparation and mounting<sup>2</sup>

Cells of the *Deinococcus radiodurans* wild-type strain were cultivated from freeze-dried cultures (DSM No. 20539 by the German Collection of Microorganisms and Cell Cultures) for one day at 37°C on petri dishes covered with nutrient medium (corynebacterium agar: 10 g/l casein peptone, 5 g/l yeast extract, 5 g/l glucose, 5 g/l NaCl, 15 g/l agar). Prior to preparation, the actively growing cells were washed of the culturing medium with about 1.5 ml buffer solution (2 g/l  $\text{KH}_2\text{PO}_4$ , 0.36 g/l  $\text{Na}_2\text{HPO}_4 \cdot 2\text{H}_2\text{O}$ , pH 7.2). After placing a droplet of cell suspension onto the substrate, a  $\text{Si}_3\text{N}_4$ -foil (Silson, UK) of 1  $\mu\text{m}$  thickness and  $5 \times 5\text{ mm}^2$  lateral dimensions, the cells were allowed to adhere for 60 seconds. The remaining buffer was blotted, the frame cryoplunged into liquid ethane to prevent crystallization [45] and afterwards lyophilized in a home-built freeze-drier. **Fig. 7.2** shows an optical micrograph of the freeze-dried cells and the investigated cellular structure (inset). Mounting and orientation of the substrate with respect to the axis of rotation ensures that no structures next to the investigated region move into the field of view during tomographic scans.

<sup>2</sup> Sample preparation was performed by Marius Priebe, Institute for X-ray physics, University of Göttingen, Germany.

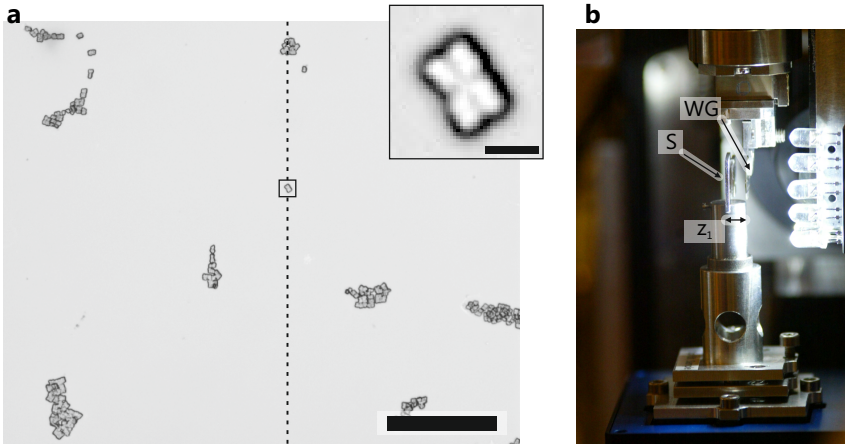


**Figure 7.2:** (a) Optical micrograph of freeze-dried *Deinococcus radiodurans* cells on a  $\text{Si}_3\text{N}_4$  substrate. A rectangle marks the investigated cellular structure, shown with a higher magnification in the inset. The chosen orientation of the sample with respect to the axis of rotation (dashed line) ensures that no structures next to the investigated region move into the field of view during tomographic scans. Scale bars,  $100\ \mu\text{m}$  and  $4\ \mu\text{m}$  (inset). (b) The substrate ( $S$ ) mounted a distance  $z_1$  from the waveguide ( $WG$ ) at the GINIX setup.

## 7.2 Data analysis

### 7.2.1 Treatment of raw data

**Fig. 7.3** shows the intensity distribution obtained by summing up all  $N = 15$  accumulations, the empty beam intensity and the normalized intensity for the projection at angle  $\theta = 80^\circ$ . The data corresponds to one module of the Maxipix detector with  $254 \times 254$  pixels. The module has certain hot and cold pixels which do not measure the correct intensity. For each dataset the values of those pixels were replaced by the average of local neighbours. The prominent lines in the upper left part of the module can be attributed to the Maxipix detector itself, since they were fixed to certain pixel positions when moving the detector sideways in the beam. Unfortunately, they still appeared in the normalized intensity (**c**). Therefore, the sample was positioned in a way that its diffracted intensity was centered in the lower right corner of the detector. During the 10 minute exposure lateral drift between waveguide exit and sample occurred and resulted in a blurring of the hologram. To minimize the effects of this drift, the  $N = 15$  intensity distributions  $I_\theta^{(n)}$ , each collected with 40 second dwell time, were aligned by cross-correlation with respect to each other prior to summation. To achieve an accurate registration, the analysis protocol has to be sensitive to the sample signal rather than to the

illumination function or other features in the recorded intensity distribution. The following procedure was found to fulfill this condition.

1. For each of the  $N$  accumulations  $I_\theta^{(n)}$  the following operations were performed yielding filtered accumulations  $I_\theta^{(n,\text{flt})}$ :
  - (a) Normalization of the raw data  $I_\theta^{(n)}$  by the empty beam  $I^{(\text{E})}$  intensity distribution.
  - (b) Application of a 3-by-3 median filter.
  - (c) Removal of residual stripes, e.g. of those shown in **Fig. 7.3 c** by means of division by the intensity fluctuations in the regions outside the cellular area, independently for the vertical and horizontal direction (averaged over 50 rows or columns, respectively) [63].
  - (d) Application of a Fourier bandpass filter .
  - (e) Removal of residual stripes (see c).
2. The relative shifts  $S$  between the  $N$  filtered accumulations  $I_\theta^{(n,\text{flt})}$  were calculated using a cross-correlation method with sub-pixel accuracy [74] (up-sampling factor 100).
3. The (unfiltered) accumulations  $I_\theta^{(n)}$  were shifted according to  $S$ , yielding registered accumulations  $I_\theta^{(n,\text{reg})}$ .
4. All shifted accumulations  $I_\theta^{(n,\text{reg})}$  were summed up yielding the intensity distribution  $I_\theta = \sum_n I_\theta^{(n,\text{reg})}$ .

The procedure was implemented in MATLAB and was used to automatically register the accumulations for each projection angle  $\theta$ . Then, the normalized intensity distribution was calculated as  $\bar{I}_\theta(\mathbf{r}_\perp, z_{\text{eff}}) = I_\theta(\mathbf{r}_\perp, z_{\text{eff}})/I^{(\text{E})}(\mathbf{r}_\perp) \cdot 40 \text{ min}/10 \text{ min}$ . **Fig. 7.4 a,b** illustrates the effect of aligning the accumulations prior to summation. Holographic fringes which were not visible when summing up the raw data appeared and are indicated by small arrows. However, drifts during the individual accumulations of 15 second exposure time were still present in the holograms and may have degraded the reconstruction quality and resolution. As a next step, low frequency variations were effectively removed (**Fig. 7.4 c**) by applying a Gaussian highpass filter and a subsequent stripe removal (see 1. c). Note that a first approximate phase reconstruction was used to determine the cellular area (for support determination see next section) which was then used for a second refined stripe removal. The hologram was finally normalized in a way that the area outside of the sample support had a mean value of one, as expected for the area without sample scattering in a normalized hologram.

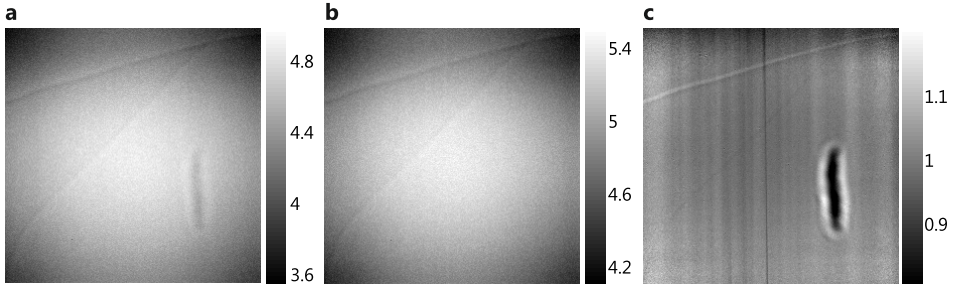


**Figure 7.3:** (a) Intensity distribution recorded with *D. radiodurans* cells in the beam (projection angle  $\theta = 80^\circ$ ). Data obtained by summing up  $N = 15$  accumulations, each with 40 second exposure time.  $254 \times 254$  pixels, gray values shown on a decadic logarithmic scale. (b) Empty beam intensity distribution, same color scaling as in (a). (c) Corresponding normalized intensity distribution intensity without application of corrections, linear color scaling.

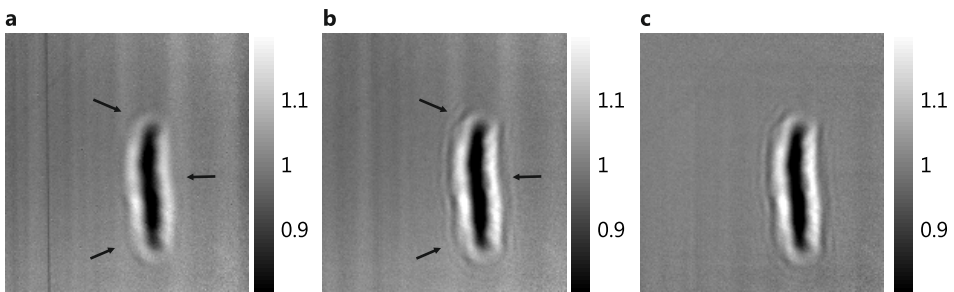


**Figure 7.4:** Normalized intensity distribution (a) without drift correction and (b) with correction of the relative shifts between the individual  $N = 15$  accumulation. Arrows indicate the appearance of additional holographic fringes compared to (a). (c) Normalized intensity after application of low spatial frequency filtering and stripe removal.

### 7.2.2 Phase retrieval and automatic support determination

The sample plane constraint of the modified HIO algorithm (mHIO, section 2.4.1.3) requires a support area of the sample  $\mathcal{S} \subset \mathbb{R}^2$  in the sample plane. For the initial experimental demonstration of the mHIO [63] the support area for a single hologram was extracted manually from the holographic reconstruction. However, in order to allow a convenient analysis for tomographic datasets, it is crucial to determine  $\mathcal{S}$  for all projections automatically and accurately. To achieve this, as a first step the same rectangular support was chosen for all projections as an initial guess, as shown in **Fig. 7.5 a** for the projection corresponding to  $\theta = 0^\circ$ . Using 150 iterations of the mHIO algorithm an approximate phase reconstruction of the sample transmission function is obtained (**Fig. 7.5 b**). By application of a threshold ( $-0.08$  rad) to the reconstructed phase a binary mask is generated which is refined by subsequent morphological operations. To remove isolated pixels of the mask, erosion followed by dilation is performed. To fill holes in the mask, dilation followed by erosion is performed (erosion and dilation are non-linear operations and not mutual inversions). Using the resulting support area (**Fig. 7.5 c**) in a subsequent run of the mHIO algorithm, one obtains a refined phase reconstruction (**Fig. 7.5 d**) which can in turn be used to further refine the support area. By repeating the steps described above twice, an accurate support area for all projections was found. The described process is similar to the Shrink-Wrap algorithm known for CDI experiments [135]. For the final phase reconstruction the algorithmic feedback parameters of the mHIO were set to  $\beta = \gamma = 0.2$ . An initial guess of the sample transmission function was generated as proposed in [61]

$$\psi_0 = \begin{cases} 1 + a_0 R_1 \exp(i\varphi_0 R_2) & (x, y) \notin \mathcal{S} \\ 1 + a_0 R_1 \exp(i\varphi_0 R_2 - 0.1) & (x, y) \in \mathcal{S} \end{cases}, \quad (7.1)$$

with  $a_0 = \varphi_0 = 0$  and equally distributed pseudo-random numbers  $R_{1/2}$  on the interval  $[-0, 5, 0.5]$ . A median filter using a 3-by-3 neighborhood was applied to the normalized holograms prior to phase reconstruction which yielded superior results.

## 7.3 Results

### 7.3.1 2D phase reconstruction

Phase reconstructions of *Deinococcus radiodurans* for two different rotation angles  $\theta$  along with the corresponding normalized holograms are shown in **Fig. 7.6**. They were obtained by averaging the complex reconstructions from 50 independent runs of the mHIO algorithm (each with a different random initialization), which stopped at an average iteration number of  $N_{\text{it}} = 2000$  and showed a very small distribution of the resulting phase values  $\varphi(\mathbf{r}_\perp)$  with a standard deviation below  $5 \cdot 10^{-4}$  rad in each pixel. The algorithm stops as soon as the misfit  $d$  between the reconstructed and measured holographic intensity distribution is smaller than a

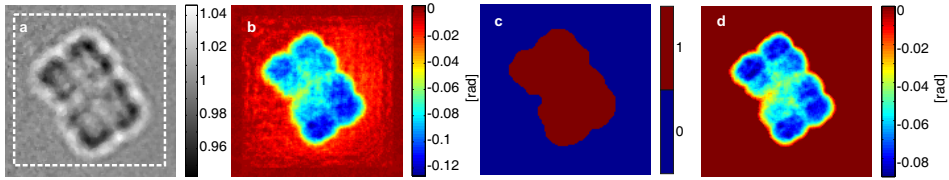


**Figure 7.5:** Automatic support determination shown for projection angle  $\theta = 0^\circ$ . (a) Normalized intensity distribution. The initial guess of the support area is indicated by the dashed rectangle. (b) Approximated phase reconstruction after 150 iterations of the modified HIO algorithm. (c) New support guess generated by thresholding of the phase shown in (b) and subsequent morphological operations (erosion and dilation). (d) Refined phase reconstruction after another 150 iterations of the modified HIO. By repeating the steps shown in (c-d) an accurate support can automatically be determined.

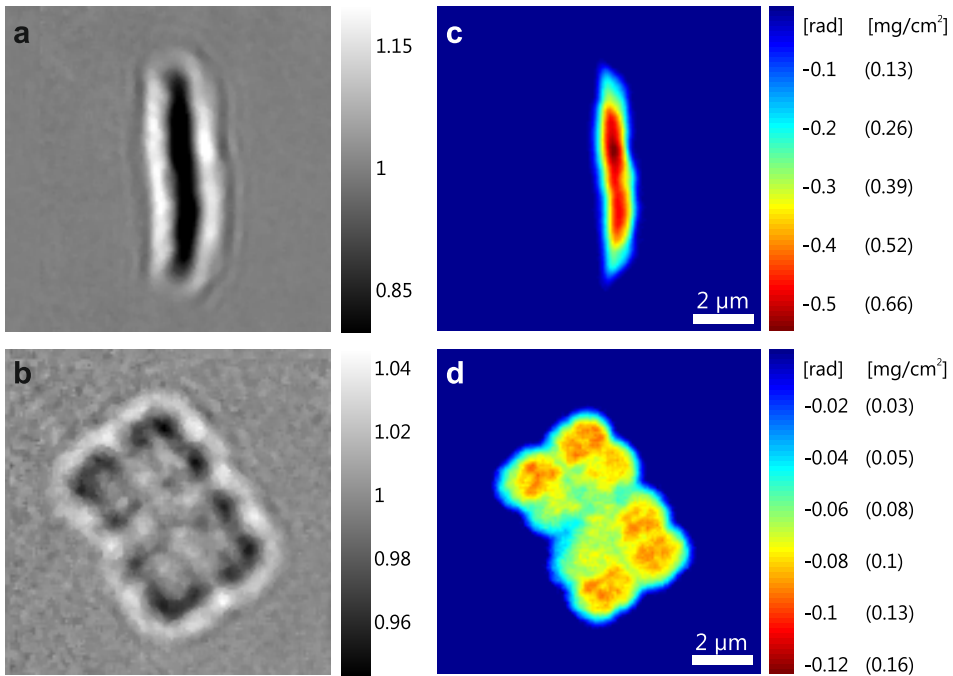


**Figure 7.6:** Normalized holographic intensity diffraction from freeze-dried *D. radiodurans* at projection angle (a)  $\theta = 0^\circ$  and  $\theta = 80^\circ$  (b). (c, d) Corresponding reconstructions of phase distributions and projected mass density maps (see colorbar scaling), obtained by averaging the complex reconstructions from 50 independent runs of the modified HIO algorithm.



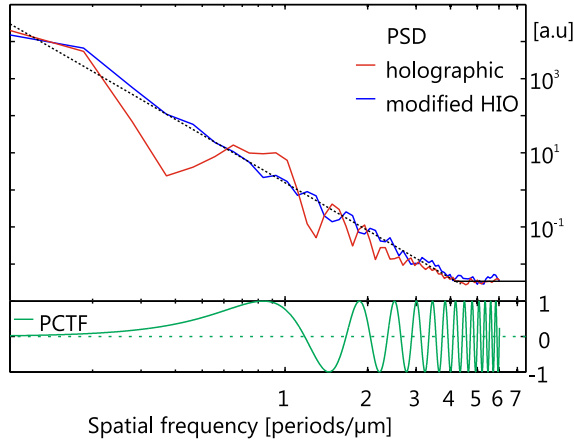


**Figure 7.7:** Azimuthally averaged power spectral density (PSD, blue curve) of the phase reconstruction at projection angle  $\theta = 0^\circ$  (shown in **Fig. 7.6 d**) together with the phase contrast transfer function (PCTF, green curve). In comparison to the PSD of a single-step holographic reconstruction (red curve), spatial frequencies are recovered where the PCTF is zero. At  $4 \mu\text{m}^{-1}$  the fit of an exponential power law to the PSD in the interval  $[0.1, 3] \mu\text{m}^{-1}$  (dashed black line) crosses over into the noise plateau (solid black line).

given parameter  $D$  (see section 2.4.1.3). An optimum value for  $D$  depends on the noise statistics of the experimental data. For the present analysis, a median filter was applied prior to phase reconstruction influencing the noise characteristics of the normalized hologram. Still, a natural choice for the threshold parameter  $D$  is the standard deviation  $\tilde{\sigma}$  of the normalized intensity distribution outside the cellular area (see section 2.4.1.3 and [63]). The smallest  $D$ , for which convergence in the sense defined above could be achieved within a reasonable amount of time (about 2000 iterations on average), was found to be in the interval of  $D = [0.9, 1.1]\tilde{\sigma}$  for all projections. Using relation (1.90), the projected decrement of the refractive index  $\bar{\delta}(\mathbf{r}_\perp)$  was calculated from the reconstructed phase distributions

$$\bar{\delta}(\mathbf{r}_\perp) = -\varphi(\mathbf{r}_\perp)/k. \quad (7.2)$$

The relation (1.69) between decrement of the refractive index and mass density of the sample also holds for the *projected* mass density. Using this relation, projected mass density maps were obtained (see additional colorbar scaling in **Fig. 7.6**), with a density range well in agreement to what has been found before for cells of *Deinococcus radiodurans* [65]. **Fig. 7.7** shows the azimuthally averaged power spectral density (PSD) of the phase reconstruction corresponding to angle  $\theta = 0^\circ$ . Notably, zeroes in the phase contrast transfer function at certain spatial frequencies (green curve, see section 1.3.1) which are visible in the PSD of the holographic reconstruction (red curve, reconstruction not shown) are less pronounced

in the modified HIO reconstruction (blue curve, see section 2.4.1.3 and [63] for a discussion on the recovery of lost information by the modified HIO). Fitting the PSD to an exponential power law in the interval  $[0.1, 3] \mu\text{m}^{-1}$ , a transition to the noise plateau was found at  $4 \mu\text{m}^{-1}$ , indicating an upper limit of the obtained (half-period) spatial resolution at 125 nm.

### 7.3.2 Three-dimensional mass density

83 phase distributions were reconstructed from data collected at angles distributed over 162 degrees and used to calculate projections  $\bar{\delta}(\mathbf{r}_\perp)$  of the decrement of the refractive index. As described in chapter 3, the decrement  $\delta(\mathbf{r})$  could be reconstructed in three dimensions using filtered backprojection. Equation (1.69) was finally used to generate the 3D effective mass density distribution  $\rho_m(\mathbf{r})$

$$\rho_m(\mathbf{r}) \simeq \frac{k^2 u}{\pi r_e} \delta(\mathbf{r}). \quad (7.3)$$

In **Fig. 7.8** different visualizations (using Avizo Fire) of the effective mass density distribution of the cellular structure are shown. The density ranges used for direct volume renderings are indicated in the histogram shown in **Fig. 7.9**. The histogram was calculated for all the interior voxels as defined by the surface in **Fig. 7.8 b** (surface rendering with a threshold of  $0.75 \text{ g/cm}^3$ ), corresponding to a cellular volume of  $V = 14.8 \mu\text{m}^3$  with a total mass of 15.8 pg. The presumed position of the  $\text{Si}_3\text{N}_4$  substrate is indicated as a dashed rectangle in **Fig. 7.8 b**, where the structure of the cells is nearly flat. A combined direct volume and surface rendering **Fig. 7.8 c**, obtained by a virtual cut through the three-dimensional dataset, allows to visualize the distribution of distinct spatial patterns with density maxima attributable to DNA rich regions within the cellular structure. These regions exhibit densities in the range of  $1.2\text{--}1.65 \text{ g/cm}^3$ , in agreement to the value of  $1.6 \text{ g/cm}^3$  found in a ptychographic CDI study of freeze-dried *Deinococcus radiodurans* [216].

### 7.3.3 Dose and resolution

The support generated for each projection was used to precisely calculate the fluence incident on the sample from the measured holographic intensities, based on the single photon counting characteristic of the Maxipix detector. The average photon flux density at the sample was  $7.3 \cdot 10^3 \text{ ph}/\mu\text{m}^2/\text{s}$  and the total fluence for each projection was about  $F = 4.4 \cdot 10^6 \text{ photons}/\mu\text{m}^2$  on average. This corresponds to a dose of  $D = 1.9 \cdot 10^3 \text{ Gy}$  per projection based on calculations presented in [97]. The total dose applied during the tomographic scan was about  $D_{\text{tot}} = 1.6 \cdot 10^5 \text{ Gy}$ . These values are several orders of magnitude below the values reported in previous x-ray coherent diffractive imaging (CDI) studies of *D. radiodurans* cells [131, 65, 216]. However, dose values have to be discussed in view of the obtained spatial resolution. A rather conservative assumption of  $d = 166 \text{ nm}$  (two pixels) for the (half-period) resolution of the present propagation imaging

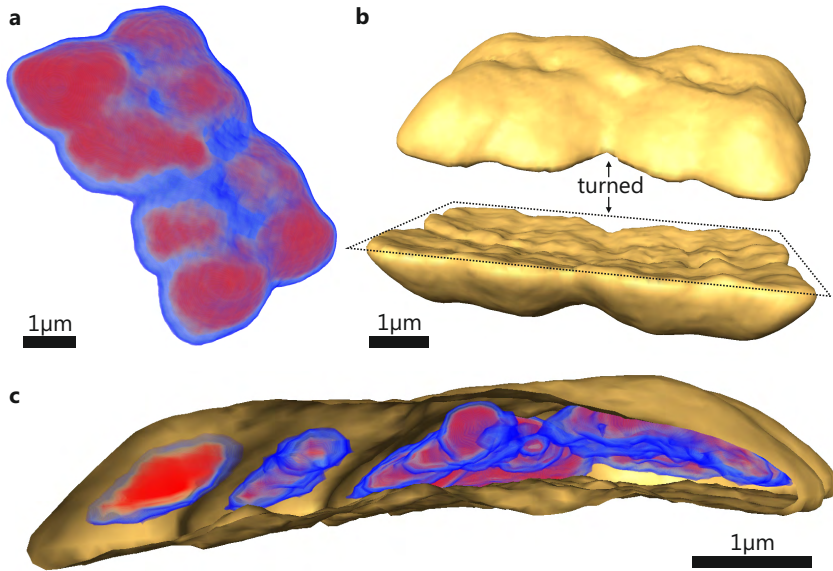


**Figure 7.8:** (a) Direct volume rendering of the 3D effective mass density of freeze-dried *D. radiodurans* cells. The coloring indicates densities from  $0.8 \text{ g/cm}^3$  (blue) to  $1.2 \text{ g/cm}^3$  (red). (b) Surface rendering obtained by choosing  $0.75 \text{ g/cm}^3$  as a threshold value. The cells are shown from above and turned upside-down. The presumed position of the substrate is shown as a dashed rectangle at the bottom of the cells where the structure is nearly flat. (c) Combined direct volume ( $1.15 - 1.25 \text{ g/cm}^3$ ) and surface ( $>0.75 \text{ g/cm}^3$ ) rendering.

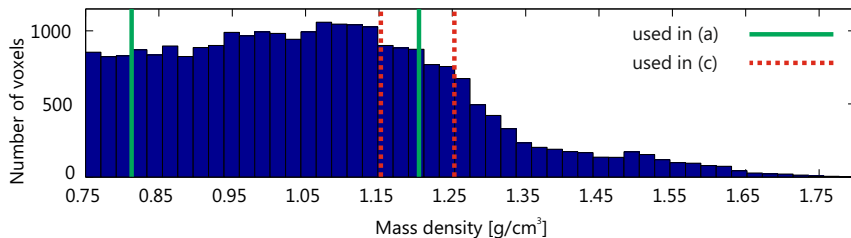


**Figure 7.9:** Histogram of the effective mass density of freeze-dried *D. radiodurans* cells inside the surface shown in Fig. 7.8 b, corresponding to the volume occupied by the cells. The limits used for direct volume rendering in Fig. 7.8 a, c are indicated by solid green and dashed red lines, respectively.

reconstructions in 2D and a (half-period) resolution of  $d_{\text{pty}} = 46$  nm (one pixel) for a recent ptychographic study of freeze-dried *D. radiodurans* cells [216] results in a ratio of  $d/d_{\text{pty}} = 3.6$ . As proposed in [97], the dose applied to the sample (and therefore the respective fluence) increases with the forth power of the obtained resolution. Scaling the resolution of the current experiment to 46 nm would therefore correspond to a fluence of  $F_{46} = 3.6^4 \cdot F = 7.5 \cdot 10^8$  photons/ $\mu\text{m}^2$ . This is below the reported value  $F_{\text{pty}} = 2.3 \cdot 10^9$  photons/ $\mu\text{m}^2$  of the ptychographic study [216] and indicates an advantage of x-ray propagation imaging compared to ptychography in terms of dose-efficiency. The important question, whether the presented approach can be extended towards higher spatial resolution is discussed in the next chapter. However, the fact that consistent phase reconstructions were even possible at these low dose values (with the corresponding medium resolution) is an advantage of the full-field propagation imaging approach. The threshold for photon fluence at which the algorithm yields a meaningful reconstruction is far below what is reported for far field (scanning) coherent x-ray imaging results.

## 7.4 Summary

Propagation based phase contrast tomography using x-ray waveguides was presented for the first time. The three-dimensional effective mass density distribution in *Deinococcus radiodurans* cells was computed, showing characteristic density maxima attributable to DNA rich regions. Density contrast may help to understand the bacterium's extraordinary resistance to high doses of ionizing radiation based on the structural arrangement of its nucleoid [49, 48, 144]. The presented approach enabled low dose imaging with medium resolution in the range of 125 – 200 nm. The total dose applied during the tomographic scan was about  $1.6 \cdot 10^5$  Gy, corresponding to  $1.9 \cdot 10^3$  Gy per projection. Despite the low dose which is several orders of magnitude below the values reported in previous x-ray coherent diffractive imaging (CDI) studies of *Deinococcus radiodurans* [131, 65, 216], phase reconstruction was successful. This was possible by means of a highly coherent beam with curved wavefronts [185], emitted by a 2D x-ray waveguide system [120, 119] and an iterative reconstruction scheme which takes photon noise effects into account [61]. The relatively long exposure times per projection resulted in residual artifacts in the normalized holographic intensities which therefore had to be corrected with rather elaborate raw data processing. An increased waveguide transmission, vibrational stability and an optimized detector-geometry configuration should render these steps superfluous and enable higher spatial resolutions, as discussed in the next chapter.

## 8 Towards higher resolution

So far, x-ray propagation imaging experiments with waveguides have been restricted to spatial (half-period) resolutions above 100 nm (see chapter 7 and [63]). In this chapter we investigate how spatial resolution can be further tuned by addressing the photon flux, beam stability and sample drifts as well as geometric and detector parameters. All experiments were carried out at the GINIX setup (see section 4.3.4) with different samples, varying configurations of waveguide, photon energy, detector and geometry parameters.

### 8.1 Imaging of *Dictyostelium discoideum* cells

*Dictyostelium discoideum* are eukaryotic cells which are capable to perform movements. The cytoplasm forms a protusion, a so called pseudopodium, based on constant reformation of the actin cytoskeleton and allows the amoebae to crawl [109].

#### 8.1.1 Sample preparation<sup>1</sup>

Freeze-dried *Dictyostelium discoideum* cells of the wild-type strain AX2-214 were investigated. Microfabricated polyimide foils of 10 – 20  $\mu\text{m}$  thickness and with about 300  $\mu\text{m}$   $\times$  800  $\mu\text{m}$  lateral dimensions (Mitegen, USA) were used as sample holders. Rapid freezing and freeze-drying were performed in a similar way as described for bacterial cells in chapter 7. Details on the preparation process are described in [63, 62, 61]. **Fig. 8.1** shows an optical micrograph of freeze-dried *Dictyostelium discoideum* cells as used for imaging.

#### 8.1.2 Experimental setup

The experiment was performed with the original waveguide configuration (see section 4.3.4). The undulator beam was monochromatized to 13.8 keV and focused to a size of  $D_h = 370$  nm and  $D_v = 150$  nm full width at half maximum (FWHM). The total flux was  $4.1 \times 10^{11}$  counts per second at 100 mA storage ring current as measured with a PIN diode. To achieve larger transmission, the crossed planar waveguide slices of the waveguide system (XWG2, see **Tab. 4.1**) with a transmis-

---

<sup>1</sup> Sample preparation was performed by Marius Priebe, Institute for X-ray physics, University of Göttingen, Germany.

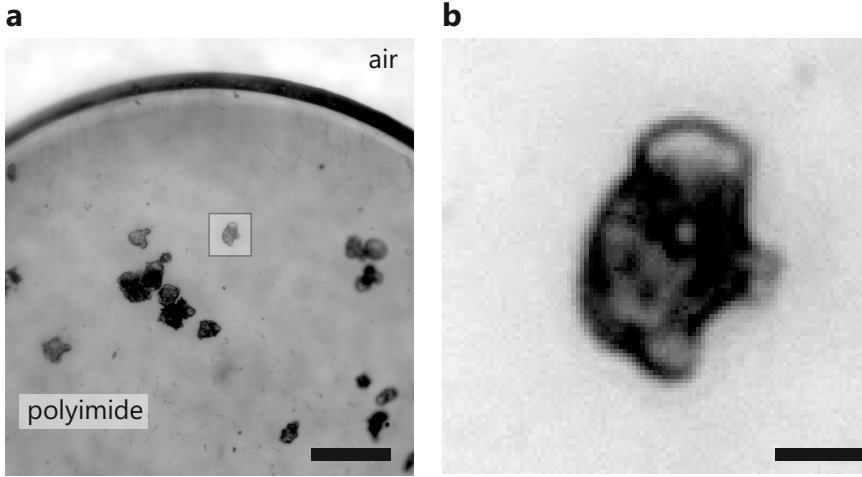


**Figure 8.1:** (a) Optical micrograph of *Dictyostelium discoideum* cells on a polyimide foil. (b) Magnified view of the investigated cell, as marked in (a). Scale bars, (a) 50  $\mu\text{m}$ , (b) 5  $\mu\text{m}$ .

sion optimized sputtered thin film sequence Ge/Mo/C/Mo/Ge, with 35 nm guiding layer [119, 120] had lengths of only  $l_1 = 270 \mu\text{m}$  and  $l_2 = 220 \mu\text{m}$ . As a consequence, the maximum photon flux exiting the waveguide system was  $1 \cdot 10^8 \text{ ph/s}$  as measured by a Pilatus pixel detector [120]. Similar to XWG1, the small quasi-point source provided by the waveguide is evidenced by the large divergence angle of its far-field intensity distribution (**Fig. 4.6 b**). The near-field intensity distribution in the effective focal plane obtained by phase reconstruction using the ER algorithm reveals a beam confinement of about  $11 \text{ nm} \times 11 \text{ nm}$  (FWHM), respectively (see **Fig. 4.6 f** and **Tab. 4.1**). The relatively homogenous part of the waveguide far-field intensity distribution as indicated by the dashed rectangle in **Fig. 4.6 b** was used for imaging. The sample was placed on the dedicated sample tower (T2 in **Fig. 4.3 b**) at at  $N_{\text{planes}} = 2$  different distances  $z_{1,x} = 5.9 \text{ mm}$  (first sample plane) and  $z_{1,x} = 6.9 \text{ mm}$  (second sample plane) from the exit surface of the second waveguide slice. Holograms were recorded with a Maxipix detector placed at a distance  $z_{1,x} + z_{2,x} = 5.09 \text{ m}$  behind the waveguide exit.

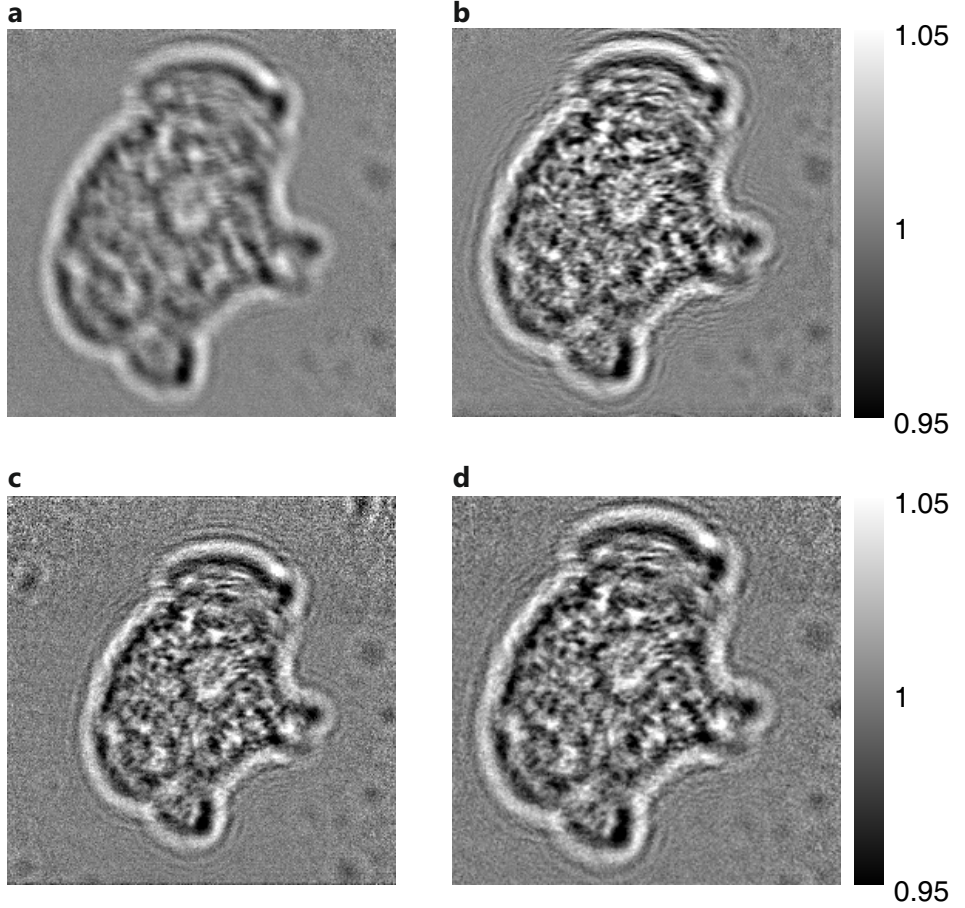


**Figure 8.2:** (a) Normalized hologram of a *Dictyostelium discoideum* cell for 600 individual recordings at  $z_1 = 5.9$  mm. Normalized hologram after drift correction at (b)  $z_1 = 5.9$  mm and (c)  $z_1 = 6.9$  mm. (d) The hologram shown in (c) after rescaling to the same pixel size as the hologram shown in (b).

### 8.1.3 Empty beam and drift correction

In chapter 7, elaborate raw data processing was necessary prior to phase reconstruction. Due to long exposure times of 10 minutes, the illumination function provided by the waveguide changed significantly between empty beam and hologram recording. As a consequence, residual low frequency variations were present after empty beam division. Improved empty beam correction can be expected, if hologram  $I(\mathbf{r})$  and empty beam  $I^{(E)}(\mathbf{r})$  are subject to identical fluctuations of the waveguide beam. In an experiment this can be achieved approximately by taking an alternating series of shorter accumulations ( $I_1, I_1^{(E)}, I_2, I_2^{(E)} \dots I_N, I_N^{(E)}$ ) with and

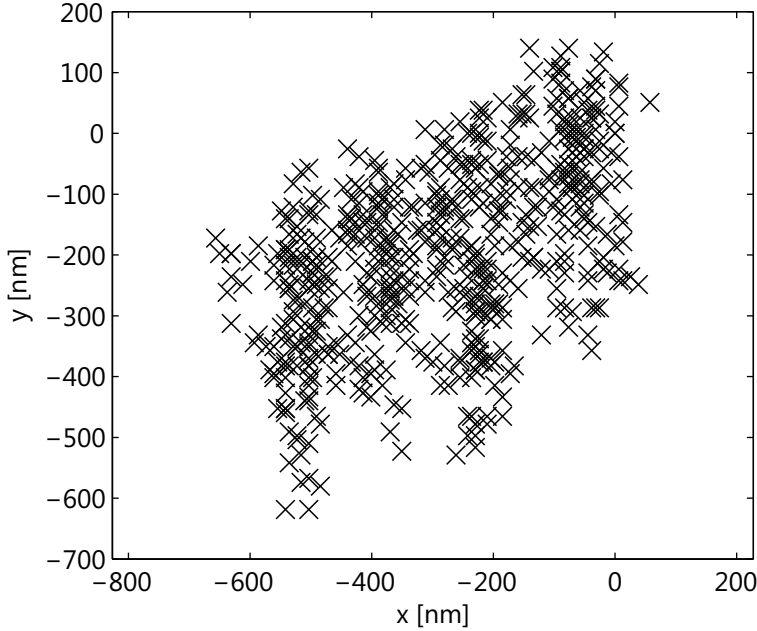


**Figure 8.3:** Lateral shifts between  $I_1$  and  $I_n$  with  $n = 2 \dots N$ , as obtained by cross correlation for  $N = 600$  individual recordings. The standard deviation is  $\sigma_x = 174$  nm,  $\sigma_y = 149$  nm in horizontal and vertical direction, respectively.

without the sample placed in the x-ray beam [63]. Then, the normalized intensity can be computed as

$$\bar{I}(\mathbf{r}) = \frac{\sum_{n=1}^N I_n(\mathbf{r})}{\sum_{n=1}^N I_n^{(E)}(\mathbf{r})}. \quad (8.1)$$

For the first sample plane at  $z_{1,x} = 5.9$  mm the accumulation was distributed among  $N = 600$  individual recordings, each with a dwell time of three seconds. For the second sample at distance  $z_{2,x} = 5.9$  mm a total of  $N = 190$  empty beam intensity distributions and holograms were recorded. Owing to the fast read-out of the Maxipix detector and the fast piezo stage, the overhead time between two consecutive recordings was 0.6 s or equivalently 20%. **Fig 8.2 a** shows the normalized intensity  $\bar{I}(\mathbf{r})$  for distance  $z_{1,x} = 5.9$  mm. Importantly, no low-frequency variations disturb the data. However, moving the specimen in and out of the beam several times, in addition to thermal drifts and vibrations, may have resulted in different lateral positions of the sample with respect to detector and waveguide beam. As a consequence, the final normalized intensity is blurred and holographic fringes are smeared. To correct for drift, the method developed in section 7.2.1 was applied in a modified version. For each individual shift of a raw hologram  $I_n$ , the corresponding empty beam recording  $I_n^{(E)}$  also has to be shifted by



Position	$z_{1,x}$	$z_{1,y}$	$M_x$	$M_y$	$\Delta x$	$\Delta y$	$F_x^{10}$	$F_y^{10}$
	[mm]	[mm]	-	-	[nm]	[nm]	-	-
1	5.90	6.17	863	825	63.7	66.7	0.77	0.80
2	6.90	7.17	738	710	74.6	77.4	0.90	0.93

**Table 8.1:** Geometric parameters for two different sample positions along the optical axis with source-sample distance  $z_{1,x/y}$ , geometric magnification  $M_{x/y}$ , effective pixel side length  $\Delta x/y$  and Fresnel number  $F_{x/y}^{10}$  for the horizontal and vertical direction, respectively.

the same amount, in order to ensure correct empty beam division using the final summed-up data. Due to the recording of an alternating series of holograms and empty beam intensities, the stripe removal steps (1.b and 1.e in section 7.2.1) were dispensable. The obtained shift values for all 600 recordings are shown in **Fig. 8.3**. Shifts of several hundred nanometers are large for a targeted resolution below 100 nm. Hence, the result of drift correction as shown in **Fig. 8.2 b** for distance  $z_{1,x} = 5.9\text{mm}$  has a huge influence and provides an obvious improvement. Notably, several holographic fringes appear in contrast to the normalized intensity obtained by simply summing up all accumulations.

#### 8.1.4 Astigmatism

For higher spatial resolutions, the astigmatism created by the two one-dimensional waveguide slices in serial arrangement has to be taken into account. The current waveguide system (XWG2) was mounted in a way that the second lamella with length  $l_2$  was oriented vertically, i.e. confining the beam horizontally. Therefore, the source-sample distance in vertical direction is given by  $z_{1,y} = z_{1,x} + 270\ \mu\text{m}$ , with the distance  $z_{1,x}$  between sample and exit surface of the second lamella. As a result, one obtains different magnifications  $M_x$  and  $M_y$ , different effective propagation distances  $z_{\text{eff},x}$  and  $z_{\text{eff},y}$  as well as effective pixels with rectangular rather than squared dimensions  $\Delta x$  and  $\Delta y$  for the horizontal and vertical direction, respectively. The current values are listed in **Tab. 8.1**. According to equation (1.56) Fresnel diffraction can numerically be implemented for different Fresnel numbers  $F_x^1$  and  $F_x^2$  in both directions. Hence, all Gerchberg-Saxton-Fienup-type algorithms were implemented for astigmatic illumination. TIE-based and CTF-based methods rely on filtering in Fourier space and were adapted by using the reciprocity relations (1.52, 1.53). For multi-distance CTF-based phase retrieval, intensity distributions obtained at different sample positions along the optical axis need to be brought to the same magnification. For the present case of astigmatic illumination, this was achieved by rescaling the intensity distributions along both directions by the respective ratios of magnifications  $M_{x,1}/M_{x,m}$  and  $M_{y,1}/M_{y,m}$ , for sample planes  $m = 2 \dots N_{\text{planes}}$ . To achieve highest possible sampling, the pixel dimensions were scaled down to the pixel size of the plane corresponding to largest

geometric magnification. **Fig 8.2 c** shows the drift-corrected normalized intensity for sample plane 2. After rescaling (**d**), the hologram appears at the same size as for plane 1 (**b**) with a different interference pattern and location of fringes as expected for different Fresnel numbers.

### 8.1.5 Phase reconstruction

**Fig. 8.4** shows holographic reconstructions as well as single-distance CTF reconstructions based on equation (2.35) for both sample planes. The assumption of a pure phase object is well justified for a thin biological cell and hard x-rays. For example, generic biological material consisting of  $H_{50}C_{30}N_9O_{10}S_1$  and mass density  $1.35/\text{gcm}^3$  [97] with thickness  $t = 5\ \mu\text{m}$  has an amplitude transmission of  $a = |O| = \exp(-k\beta t) = 0.9993$  for a photon energy of  $13.8\ \text{keV}^2$ . For CTF-based reconstruction, the holograms were padded symmetrically by 200 pixels (replicate of border values). The frequency dependent regularization parameter was set to  $\alpha_1 = 10^{-3}$  for low radial spatial frequencies  $\nu = \sqrt{\nu_x^2 + \nu_y^2}$  below  $\nu_{\text{cut}} = 0.1$  cycles/pixel. Higher spatial frequencies were regularized by  $\alpha_2 = 0.05$  for sample plane 2, higher fluence for sample plane 1 allowed to set  $\alpha_2 = 0.01$ . The holographic reconstructions (**a,b**) are severely disturbed by the twin image, even though the rim of the cell can be recognized. The CTF-based reconstructions (**c,d**) on the other hand clearly show the cell and reveal sub-cellular structure, which is reconstructed consistently for both sample planes. Missing information due to zeroes of the PCTF give rise to artifacts, which are more pronounced for the dataset with less total fluence and larger  $\alpha_2$  (sample plane 2, **c**). By using the information of both intensity distributions (**Fig. 8.2 b,d**), a reconstruction based on equation (2.34) with  $\alpha_1 = \alpha_2 = 10^{-3}$  yields a phase distribution with less artifacts (**Fig. 8.4 e**). As expected from simulations (section 2.3), mainly low frequency variations remain. Next, a support  $\mathcal{S}$  was defined manually based on the single-distance reconstruction shown in **d** and phase reconstruction was performed for sample plane 1 with the modified HIO algorithm (section 2.4.1.3). The measured normalized intensity was embedded in a larger array (by a factor of two, padding by replicate of border values) to allow sufficient sampling of the complex exponential (1.56) of the Fresnel diffraction operator. A mask with the size of the original array was defined and the amplitude constraint was restricted to the area of that mask. The noise parameter was set to  $D = 9.5 \cdot 10^{-3}$ , feedback parameters were set to  $\beta = \gamma = 0.5$  and the algorithm was initialized with the phase distribution shown in **d**. The result is shown in **f**, as obtained after the algorithm has stopped at  $N_{\text{it}} = 710$  iterations. Initialization with a random guess as defined by equation (2.50) or with the result of the holographic reconstruction yielded essentially the same result with deviations in the order of  $10^{-3}$  radian. However, a larger number of iterations was needed ( $N_{\text{it}} = 2950$  for random and  $N_{\text{it}} = 2035$  for holographic initialization). The combination of CTF-based initial guess and mHIO reconstruction therefore proves to be efficient for pure phase ob-

<sup>2</sup> Data taken from [89].

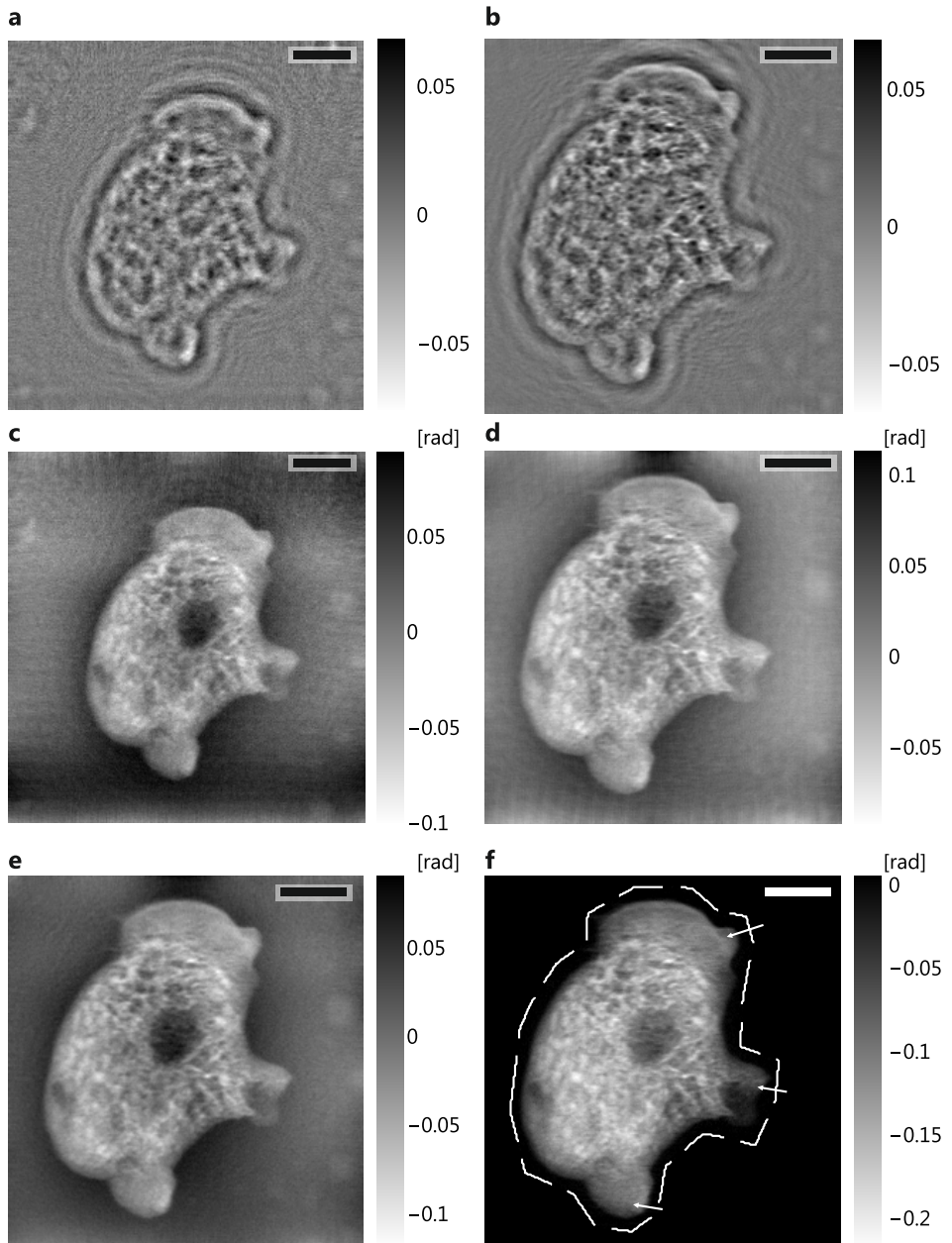


**Figure 8.4:** (a,b) Holographic reconstruction based on the normalized intensity distributions shown in **Fig. 8.2 b,c**. (c,d) Single-distance CTF-based reconstruction of the same holograms. (e) CTF reconstruction using two sample planes. (f) Phase reconstruction using the mHIO scheme. The support is indicated as a dashed line. Scale bars, 3  $\mu\text{m}$ .

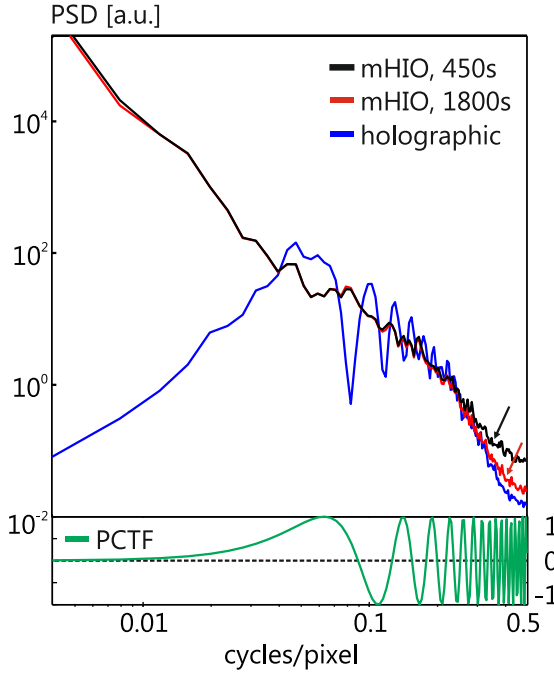


**Figure 8.5:** Azimuthally power spectral density (PSD) of the holographic reconstruction (blue curve) along with mHIO reconstructions based on total accumulation times of 450 seconds (black) and 1800 seconds (red). The latter corresponds to the reconstruction shown in **Fig. 8.4 f**.

jects with compact support. It is important to note that apart from artifacts all described methods reconstruct cellular features consistently as judged by visual inspection. The cell exhibits bulges which can be tentatively attributed to the formation of pseudopodia (indicated by arrows in **f**). In addition, several organelles within the cell are visible. The prominent large round spot in the centre could be the nucleus.

### 8.1.6 Dose and resolution

To assess the spatial resolution of the mHIO reconstruction we turn to the azimuthally averaged power spectral density (PSD) shown in **Fig. 8.5** (the image was scaled to a symmetric pixel size before computing the PSD). The mHIO reconstruction (red curve) recovers the phase of the object transmission function at spatial frequencies of zero contrast transfer (green curve) as opposed to the holographic reconstruction (blue curve). Using only 150 of the recorded 600 individual accumulations (corresponding to 450s against 1800s total exposure time) one obtains a reconstruction which is more noisy (black curve, phase reconstruction not shown). The azimuthal average of the power spectrum is expected to be

flat for spatial frequencies which do not carry information about the sample but contain only random fluctuations. The transition to the noise plateau is at about 0.3 cycles per pixel (black arrow, position of the kink). With more photon fluence the reconstruction exhibits structures at higher spatial frequencies and the noise transition point moves to higher spatial frequencies. The kink at about 0.4 cycles per pixel (red arrow) corresponds to a half-period resolution of 1.25 pixels and therefore to about 80 nm. The flux density was  $4 \cdot 10^4$  ph/ $\mu\text{m}^2$ /s at the sample plane and the total dose for all 600 accumulations was  $D = 3.1 \cdot 10^4$  Gy, according to a fluence of  $7.2 \cdot 10^7$  ph/ $\mu\text{m}^2$ . All values are higher than the corresponding values of the 3D dataset in chapter 7 and, in combination with improved drift and empty beam corrections, have resulted in higher spatial resolution. However, even though XWG2 showed a higher maximal total beam intensity compared to XGW1, and regardless of the fact that the sample was positioned closer to the waveguide, the average flux density was only increased by a factor of two. This is caused by unstable waveguide positioning using the minaturized goniometer tower (see section 4.3.4), resulting in huge variations of the beam intensity (**Fig. 4.7 a**).

## 8.2 Optimized waveguide configuration

Driven by the insights gained during the experiments outlined in the previous chapter, an optimized waveguide configuration was developed. Maximal photon flux, beam stability, field of view and effective pixel sizes were optimized by a well-matched waveguide-detector combination and a more robust waveguide positioning system as described in section 4.3.5.

### 8.2.1 Imaging of a test structure at 13.8 keV

To investigate the capabilities of the optimized waveguide configuration, a nanofabricated test structure milled by focused ion beam into a 200 nm thick gold layer on a 200 nm thick  $\text{Si}_3\text{N}_4$  membrane was imaged.

#### 8.2.1.1 Experimental setup

The undulator beam was monochromatized to 13.6 keV and focused to a size of  $D_h = 370$  nm and  $D_v = 350$  nm full width at half maximum (FWHM). The total flux was  $2.8 \times 10^{11}$  counts per second at 80 mA storage ring current as measured with a PIN diode. To achieve higher transmission, the C guiding layer of the sputtered thin film sequence Ge/Mo/C/Mo/Ge of each waveguide lamella was increased to  $d = 59$  nm (XWG3, see **Tab. 4.1**) [120] As a consequence, the maximum photon flux exiting the waveguide system was  $5 \cdot 10^8$  ph/s as measured by a Pilatus pixel detector. The flux enhancement compared to XWG2 is higher than what could be expected based solely on geometric considerations ( $5 > (59 \text{ nm}/35 \text{ nm})^2 = 2.84$ ). This is expected since for a larger guiding core the relative intensity which is lost in the cladding is smaller [186]. Increased influence

of real structure effects such as roughness [160] for smaller guiding cores may also contribute to this effect. Compared to XWG1 and XWG2, the divergence of the far-field intensity distribution of XWG3 (**Fig. 4.6 c**) is smaller, owing to a larger source size of about  $14\text{ nm} \times 11\text{ nm}$  (FWHM) as obtained by phase reconstruction using the ER algorithm (see **Fig. 4.6 g** and **Tab. 4.1**). The anisotropy of the source can be explained by the sequential arrangement of the crossed waveguide slices with rather thick lamella of about  $380\text{ }\mu\text{m}$  for XWG3. Note that the divergence of the smooth central cone of the waveguide beam is well matched to the active area of the sCMOS detector (see dashed rectangle in **Fig. 4.6 c** and **Fig. 4.4 b**) and was used for imaging. The waveguide was mounted on the robust sample tower (T2 in **Fig. 4.3 c**) yielding improved stability (**Fig. 4.7**). The nanofabricated test structure was mounted on a miniaturized  $xyz$  nano-positioner (T3 in 4.3). The sample was placed at a distance  $z_{1,y} = 4.93\text{ mm}$  and the detector at a distance  $z_{1,y} + z_{2,y} = 5.07\text{ m}$  behind the exit surface of the second waveguide slice.

### 8.2.1.2 Raw data treatment

An alternating series of shorter accumulations ( $I_1, I_1^{(E)}, I_2, I_2^{(E)} \dots I_N, I_N^{(E)}$ ) with and without the sample placed in the x-ray beam was recorded and the normalized intensity was computed as described in section 8.1.3. The accumulation was dis-

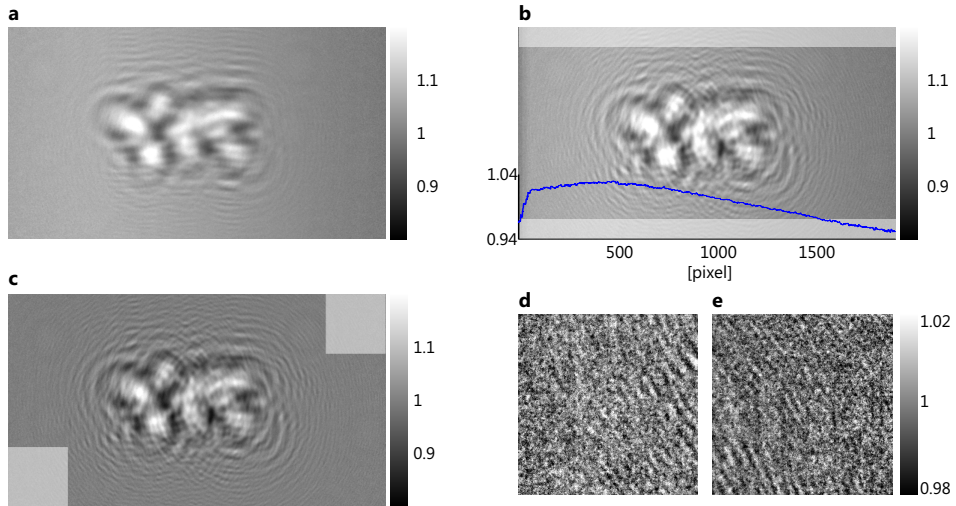


**Figure 8.6:** (a) Normalized hologram obtained by summation of 10 individual 20 second holographic and empty beam recordings. (b) Normalized hologram after drift correction. A remaining gradient in horizontal direction can be corrected by the profile shown in blue. It was obtained by averaging the 100 uppermost and 100 lowest rows of the diffraction pattern. (d) Final hologram. (e,f) Magnified views of (e) the lower left and (f) the upper right  $300 \times 300$  pixel domain with adjusted contrast.

tributed among  $N = 10$  individual recordings, each with a dwell time of 20 seconds. As presented in the previous sections, motor movements between individual recordings resulted in position inaccuracies and washed out holographic fringes (**Fig. 8.6 a**). The sample was moved horizontally for empty beam recordings and consequently, fringes in this direction are blurred most. By application of the developed drift correction procedure, one recovers a sharp diffraction pattern (**Fig. 8.6 b**) with several well-sampled holographic fringes. However, a small residual horizontal gradient remains after empty beam correction. Compared to the fast accumulation with the sensitive Maxipix detector used for the cellular imaging in section 8.1, the scintillator-based sCMOS detector requires longer exposure times. To achieve optimal signal-to-noise ratio for a single accumulation, the gain factor of the detector was set to the minimal value of one. Hence, 20 second accumulations were recorded and yielded small low frequency differences between the total raw holographic data  $\sum_{n=1}^N I_n(\mathbf{r})$  and the total empty beam intensities  $\sum_{n=1}^N I_n^{(E)}(\mathbf{r})$  (**b**). However, due to the smooth shape of the waveguide far-field, the resulting deviation constitutes a small and smooth gradient along the horizontal direction with no apparent variations along the vertical direction. By taking the mean of the 100 uppermost and 100 lowest pixel rows (semi-transparent rectangles in **b**) one obtains the profile shown as a blue curve in **b**. The steep slope at the first columns is a result of the drift correction, which uses symmetric boundaries, i.e. if a diffraction pattern is moved by  $j$  pixels to the right, the excess pixels appear on the left side of the image. The final hologram after division by the profile and subsequent normalization to a mean intensity value of unity is shown in (**c**). Holographic fringes extent all the way to the corners of the diffraction pattern as can be seen in (**d,e**) for magnified views with adjusted contrast for the lower left and upper right corner (300-by-300 pixel), respectively.

$z_{1,x}$	$z_{1,y}$	$M_x$	$M_y$	$\Delta x$	$\Delta y$	$F_x^{10}$	$F_y^{10}$
[mm]	[mm]	-	-	[nm]	[nm]	-	-
5.31	4.93	955	1028	6.9	6.4	$10^{-2}$	$9 \cdot 10^{-3}$

**Table 8.2:** Geometric parameters used for imaging of a nanofabricated test structure with source-sample distance  $z_{1,x/y}$ , geometric magnification  $M_{x/y}$ , effective pixel side length  $\Delta x/y$  and Fresnel number  $F_{x/y}^{10}$  for the horizontal and vertical direction, respectively.

### 8.2.1.3 Phase reconstruction

For phase reconstruction, the astigmatism created by the two one-dimensional waveguide slices in serial arrangement was taken into account as described in section 8.1.4. The current waveguide system (XWG3) was mounted in a way that the second lamella with length  $l_2$  was oriented horizontally, i.e. confining the beam vertically. Therefore, the source-sample distance in horizontal direction is given by  $z_{1,x} = z_{1,y} + 379 \mu\text{m}$ , with the distance  $z_{1,y}$  between sample and exit surface of the second lamella. The values of magnifications  $M_x$  and  $M_y$ , effective propagation distances  $z_{\text{eff},x}$  and  $z_{\text{eff},y}$  as well as effective pixels dimensions  $\Delta x$  and  $\Delta y$  are listed in **Tab. 8.2**. Note that the configuration enabled an effective pixel size below 7 nm and a field of view of  $1920 \times 1080$  pixels. The holographic reconstruction (**Fig. 8.7 a**) already reveals the object (a map of the world), however severely disturbed by the twin image. A single-distance CTF reconstruction (**b**) with regularization parameters  $\alpha_1 = 0.01$  and  $\alpha_2 = 0.1$  as well as 1500 pixel padding (replicate of boundary values) shows only minor artifacts. To illustrate the importance of taking the astigmatism into account, (**c**) shows a CTF reconstruction with identical parameters as in (**b**) for the assumption of a single x-ray source plane for both directions. To further increase image quality and resolution, the mHIO scheme was applied. The support  $\mathcal{S}$  was determined automatically as follows. The phase distribution shown in (**b**) was converted to a binary mask using a treshold of 0.02 radian (**Fig. 8.8 a**). Subsequent application of morphological operations (erosion with a 5 pixel disk kernel followed by dilation with a 30 pixel kernel) yielded a suitable support (**b**). The measured normalized intensity was embedded in a larger array (with edge length  $2 \cdot 1080 = 2160$  pixel, replicate padding) to allow sufficient sampling of the complex exponential (1.56) of the Fresnel diffraction operator. A mask with the size of the original array was defined, and the amplitude constraint was restricted to the area of that mask. The noise parameter was set to  $D = 3 \cdot 10^{-3}$ , feedback parameters were set to  $\beta = \gamma = 0.5$  and the algorithm was initialized with unit intensity and the phase distribution shown in **b**. Due to the large array size of  $2160^2$  pixels, the algorithm was implemented on a GPU (using GPUmat<sup>3</sup>). The resulting phase distribution after  $N_{\text{it}} = 1000$  iterations is shown in **c**. The features of the world map exhibit sharp edges and uniform gray values. A 100-by-100 pixel domain with mean  $\mu_\varphi = 0.18 \text{ rad}$  and standard deviation  $\sigma_\varphi$  showed a coefficient of variation of about  $\sigma_\varphi / \mu_\varphi = 3\%$ .

<sup>3</sup> GPUmat is a free C/C++ engine for MATLAB based on CUDA [154]. CUDA (Compute Unified Device Architecture) is a parallel computing platform implemented on graphics processing units (GPU), developed by NVIDIA.



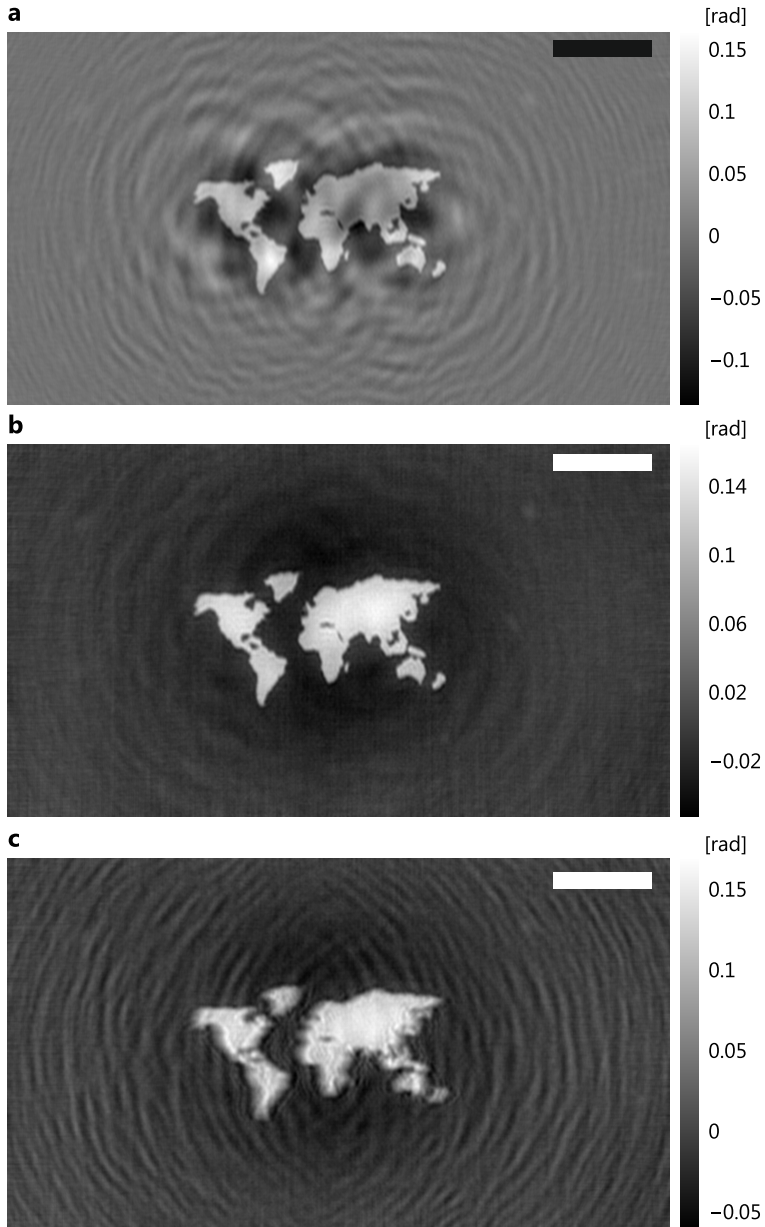


**Figure 8.7:** (a) Holographic reconstruction. Prior to backpropagation the hologram was embedded in a larger (three times) array (replicate padding). (b) Single-distance CTF reconstruction ( $\alpha_1 = 0.01$ ,  $\alpha_2 = 0.1$ , 1500 pixel replicate padding). (c) CTF reconstruction with identical parameters as in (b), neglecting astigmatism. Scale bars, 2  $\mu\text{m}$ .

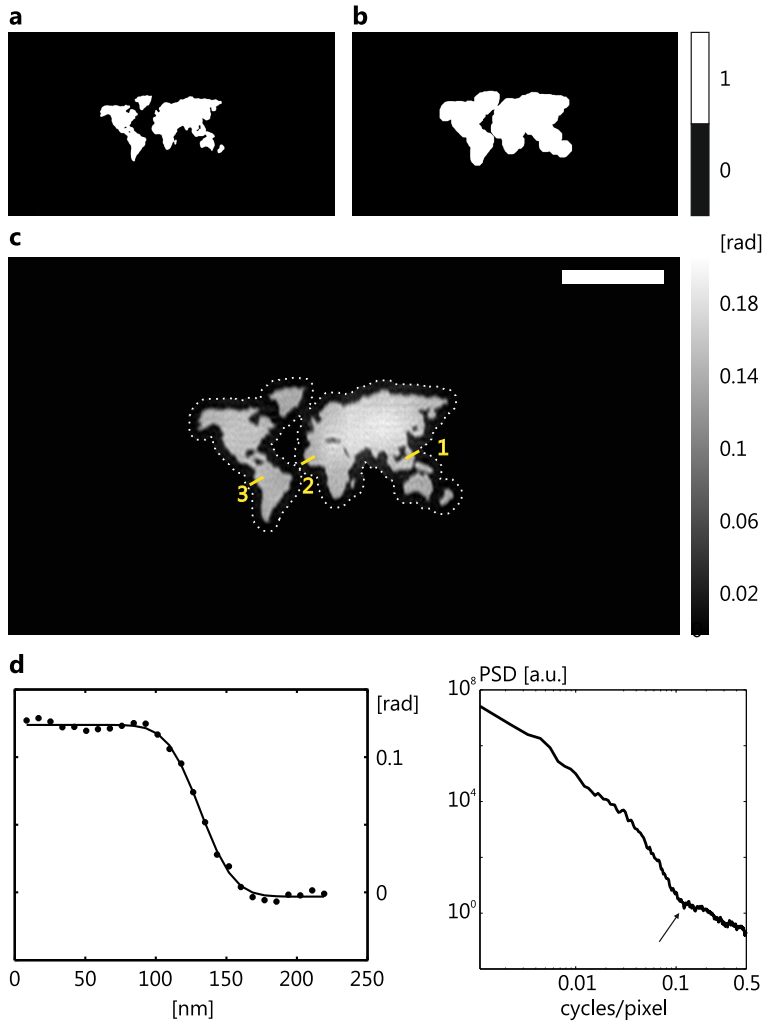


**Figure 8.8:** (a) Binary mask obtained applying a threshold of 0.02 radian to the phase reconstruction show in **Fig. 8.7 b**. (c) Support for the mHIO scheme obtained from (a) by erosion with a 5 pixel disk kernel followed by dilation with a 30 pixel kernel. (c) mHIO phase reconstruction after 1000 iterations using the CTF reconstruction (**Fig. 8.7 b**) as initial guess. (d) Profile along the first yellow line in (c) along with an error function fit. The fit result corresponds to the standard deviation of a Gaussian linespread function. Fit results are listed in **Tab. 8.3**. (e) Azimuthally averaged power spectral density (PSD). The cross-over to noise is at 0.12 cycles/pixel (kink, arrow), corresponding to a half-period of 27 nm.

Edge	FWHM, CTF [nm]	FWHM, mHIO [nm]
1	44	39
2	46	44
3	54	47

**Table 8.3:** Results of error function fits to profiles along the lines shown in **Fig. 8.8 c** for CTF and mHIO phase reconstruction.

#### 8.2.1.4 Resolution

The steepness of edges was measured at three different positions (indicated by yellow lines in **Fig. 8.8 c**). The profile along the first line is shown in **d** along with the edge-spread function (ESF) of the form

$$ESF(x) = a \cdot erf\left(\frac{x-c}{\sqrt{2}\sigma}\right), \quad (8.2)$$

with real numbers  $a, c, \sigma$  and

$$erf\left(\frac{x}{\sqrt{2}\sigma}\right) = \int_0^x \exp\left(-\frac{x^2}{2\sigma^2}\right). \quad (8.3)$$

The line-spread function (LSF) is the derivative of the edge-spread function, which in the present case results in

$$LSF(x) = \frac{derf\left(\frac{x}{\sqrt{2}\sigma}\right)}{dx} = \exp\left(-\frac{x^2}{2\sigma^2}\right). \quad (8.4)$$

Therefore, the line-spread function is a Gaussian with  $FWHM = 2\sqrt{2\ln 2}\sigma$  and standard deviation  $\sigma$ . For a Gaussian LSF the modulation transfer function (MTF) drops to about 3% for features with a half-period of  $r = FWHM/2$ , which we define as the resolution (see section A.3). The values for all profiles along the lines shown in **c** are listed in **Tab. 8.3** along with results of identical profiles for the CTF reconstruction (**Fig. 8.7 b**). The mHIO reconstruction exhibits sharper edges compared to the CTF reconstruction. Values below 50 nm (FWHM) were obtained for all three lines, while the best value is 39 nm. These results indicate a spatial half-period resolution between 20 nm and 30 nm. The azimuthally averaged power spectral density (the image was scaled to a symmetric pixel size before computing the PSD) exhibits a prominent kink at 0.12 cycles per pixel (**e**). This corresponds to a half-period of 27 nm in agreement to the line scan results.

#### 8.2.2 Imaging of *Deinococcus radiodurans* at 13.8 keV

Next, we exploit whether high-resolution imaging as presented for the nanofabricated world map can be achieved for biological cells. To this end, the same experimental setup as for the test structure was used to image freeze-dried *Deinococcus radiodurans* cells.

### 8.2.2.1 Experimental setup and raw data treatment

Sample preparation was performed as described in chapter 7<sup>4</sup>. The specimen was placed at three different distances along the optical axis, resulting in different magnifications  $M_x$  and  $M_y$ , effective propagation distances  $z_{\text{eff},x}$  and  $z_{\text{eff},y}$  as well as effective pixel dimensions  $\Delta x$  and  $\Delta y$  as listed in **Tab. 8.4**. For optimal empty beam correction, the sCMOS detector gain was set to 3 and an alternating series of 400 individual holograms and empty beam intensities with 1.5 seconds exposure time were recorded at each position. The normalized hologram  $I_1$  corresponding to the first sample position is shown in **Fig. 8.9 a**. It is free of any artifacts and due to the total dwell time of 10 minutes without significant noise. The high quality of the obtained holograms is evidenced by the difference images  $I_1 - I_2$  (**b**) and  $I_2 - I_3$  (**c**). Prior to subtraction, the normalized intensity distributions for sample position 2 and 3 were scaled to the pixel size  $\Delta x = 18.5 \text{ nm}$  and  $\Delta y = 18 \text{ nm}$  of the first sample plane, taking into account the astigmatism as described in section 8.1.4. Due to lateral shifts, the resulting holograms were cropped to  $980 \times 1900$  pixels as indicated by the dashed rectangle in (**a**). The difference images (**b,c**) illustrate how holographic fringes change with increasing Fresnel numbers and at the same time confirm that there are no residual variations in the holograms.

Position	$z_{1,x}$	$z_{1,y}$	$M_x$	$M_y$	$\Delta x$	$\Delta y$	$F_x^{10}$	$F_y^{10}$
	[mm]	[mm]	-	-	[nm]	[nm]	-	-
1	14.3	13.93	354	364	18.5	18.0	$2.62 \cdot 10^{-2}$	$2.55 \cdot 10^{-2}$
2	14.61	14.23	347	356	18.8	18.4	$2.67 \cdot 10^{-2}$	$2.61 \cdot 10^{-2}$
3	14.75	14.38	343	353	19.0	18.6	$2.70 \cdot 10^{-2}$	$2.63 \cdot 10^{-2}$

**Table 8.4:** Geometric parameters for three sample positions along the optical axis for cellular imaging of *Deinococcus radiodurans*, with source-sample distance  $z_{1,x/y}$ , geometric magnification  $M_{x/y}$ , effective pixel side length  $\Delta x/y$  and Fresnel number  $F_{x/y}^{10}$  for the horizontal and vertical direction, respectively.

### 8.2.2.2 Phase reconstruction

The rescaled and aligned holograms  $I_1$ ,  $I_2$  and  $I_3$  were used for multi-distance CTF phase retrieval based on equation (2.34). The frequency-dependent regularization parameter was specified by  $\alpha_1 = 2 \cdot 10^{-5}$  and  $\alpha_2 = 10$ . Prior to reconstruction the holograms were symmetrically padded with 1500 pixels (replicate of bordered values). **Fig. 8.10 a** shows the obtained phase reconstruction. A group of *Deinococcus radiodurans* cells is visible and can easily be recognized on the corresponding optical micrograph (**b**). At the lower left and upper right corners of the image

<sup>4</sup> Sample preparation was performed by Robin Wilke, Institute for X-ray physics, University of Göttingen, Germany.

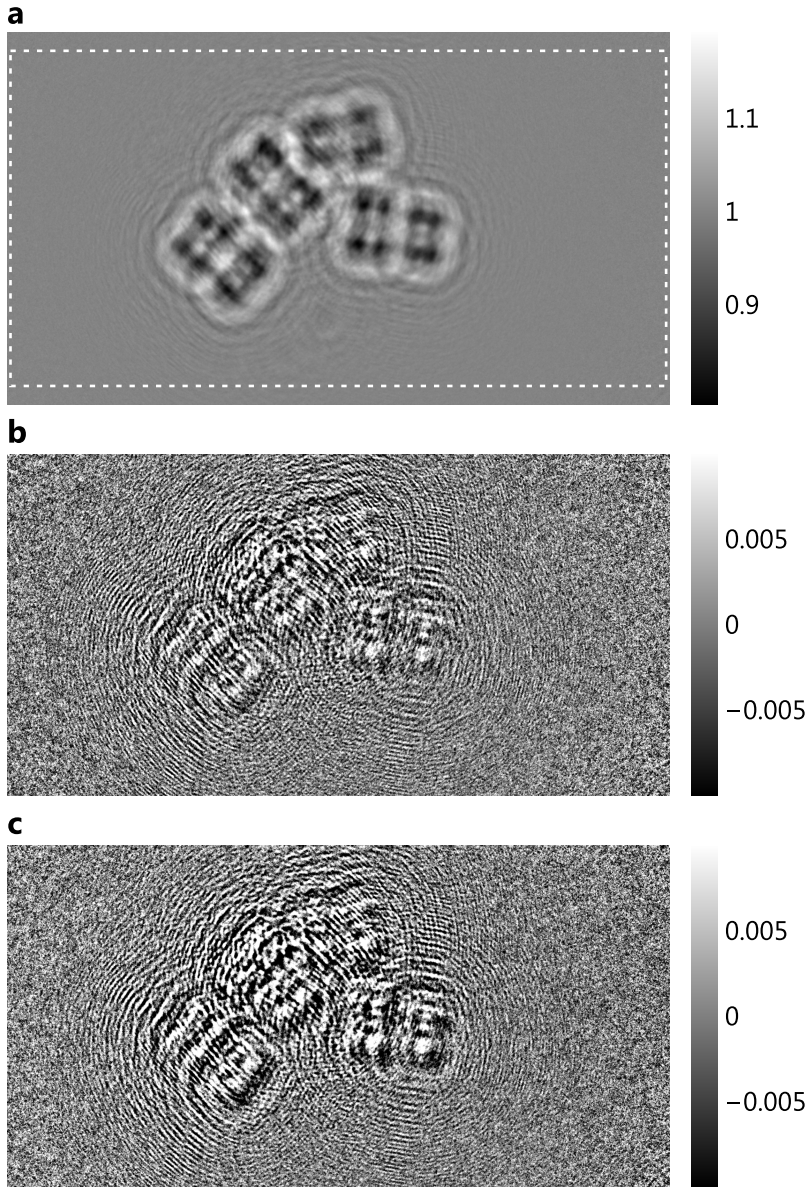


**Figure 8.9:** (a) Normalized hologram corresponding to the first sample position. No further corrections were applied. The holograms scaled to a common pixel size were cropped to 980x1900 pixels as indicated by the dashed rectangle. The difference images (b)  $I_1 - I_2$  and (c)  $I_1 - I_3$  confirm the high quality of the obtained holograms, as differences in holographic fringes are evident while no disturbing variations are visible.

two bright spots appear as reconstruction artifacts. However, the central region where the cells are located (marked with a dashed rectangle and magnified in **c**) exhibits no artifacts and shows a clean and detailed reconstruction of the phase distribution in the sample plane. This region corresponds to a field of view of  $17.5\ \mu\text{m} \times 17.5\ \mu\text{m}$ . Sub-cellular structures are clearly visible but the typical tetrad structure of *Deinococcus radiodurans* is not as clearly recognized as in a recent ptychographic study [216], similar to earlier ptychographic results [65]. This may be due to the fact that prior to preparation the cell stadium was not monitored, i.e. it is not clear whether the investigated cells were actively growing or in the stationary phase where *Deinococcus radiodurans* carries four copies of its genome [130]. Nonetheless, dark regions are attributable to DNA rich regions. The reconstructed phase distribution shows isolated islands around the group of cells (see small arrows). These features are also visible in the optical micrograph (**b**) and are most likely residues of buffer solution or nutrient medium. Thus, for the present sample the definition of a support is not straight forward and the chosen reconstruction technique based on multiple distances a reasonable choice. The fact that the residues are clearly visible in the reconstruction substantiates the high contrast provided by the current implementation of x-ray propagation imaging.

### 8.2.2.3 Dose and resolution

To assess the spatial resolution, we turn to the azimuthally averaged power spectral density (PSD) shown in **Fig. 8.11** (the image was scaled to a symmetric pixel size before computing the PSD). As expected, the multi-distance CTF reconstruction (blue curve) recovers spatial frequencies where a single distance holographic reconstruction suffers from missing information (dips in the black curve). The cross-overs to the noise plateau nearly coincide for holographic and CTF reconstruction. A prominent kink is visible at about 0.37 cycles per pixel (black arrow) corresponding to a half-period resolution of 1.35 pixels and therefore to about 25 nm, in agreement with the resolution achieved for the nanofabricated test structure. The flux density was  $3.9 \cdot 10^6\ \text{ph}/\mu\text{m}^2/\text{s}$  at the first sample plane and the total dose for all  $3 \times 450 = 1350$  accumulations was  $D = 3 \cdot 10^5\ \text{Gy}$ , according to a fluence of  $7 \cdot 10^8\ \text{ph}/\mu\text{m}^2$ .<sup>5</sup> These values are an order of magnitude higher compared to the imaging experiments with *Dictyostelium discoideum* (see section 8.1) at an identical total exposure time of 30 minutes, owing to the increased photon flux exiting XWG3. Compared to recent ptychographic study on freeze-dried *Deinococcus radiodurans* cells with reported half-period resolution of 85 nm [65] and 46 nm [216] at respective dose values of  $1.3 \cdot 10^5\ \text{Gy}$  [65] and  $4.9 \cdot 10^6\ \text{Gy}$ , the present results constitute a more dose-efficient approach to high resolution coherent lensless x-ray imaging of biological cells.

<sup>5</sup> Note that the flux densities in sample plane 2 and 3 are even smaller than in the first sample plane.

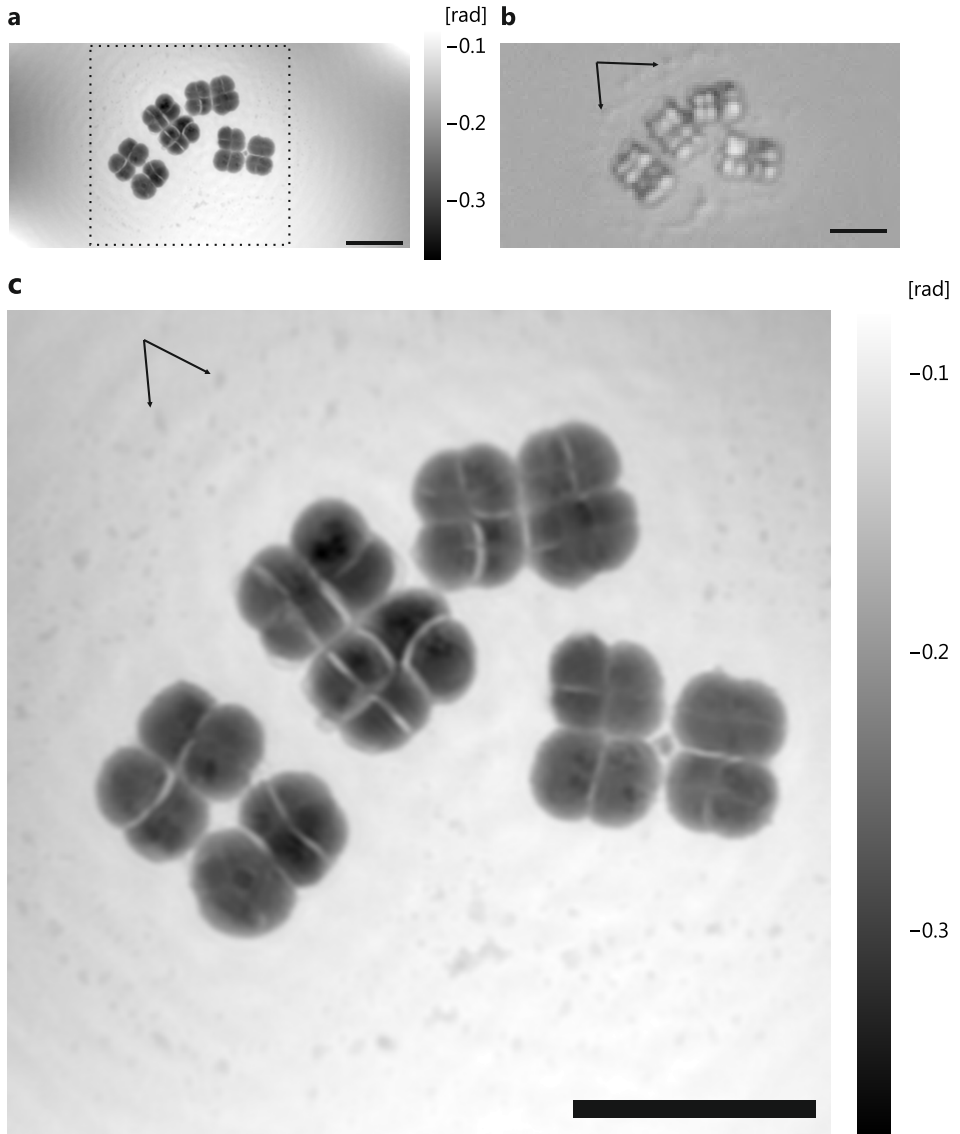


**Figure 8.10:** (a) CTF reconstruction based on three normalized holograms ( $\alpha_1 = 2 \cdot 10^{-5}$ ,  $\alpha_2 = 10$ , 1500 pixel replicate padding). The field of view is about  $35.5 \mu\text{m} \times 17.5 \mu\text{m}$  with  $1920 \times 980$  pixels. A group of *Deinococcus radiodurans* cells is visible and can be recognized in (b) the corresponding optical micrograph. (c) Magnified view of the region marked in (a) by a dashed rectangle, corresponding to  $17.5 \mu\text{m} \times 17.5 \mu\text{m}$ . Scalebars,  $5 \mu\text{m}$ .

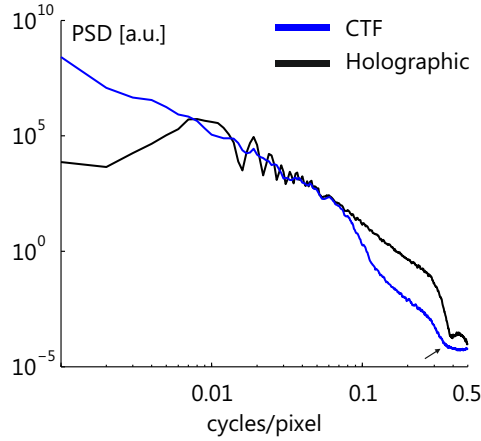


**Figure 8.11:** Power spectral density (PSD) of the CTF-based phase reconstruction shown in **Fig. 8.10 c** along with the PSD of a holographic reconstruction based on the diffraction pattern of the first sample position (reconstruction not shown). The kinks at 0.37 cycles/pixel (arrow) mark the cross-over to the noise plateau and indicate a half-period resolution of 25 nm.

### 8.2.3 Imaging of *Deinococcus radiodurans* at 7.9 keV

Recent progress in fabrication of lithographic bonded channel waveguides [85, 64, 152] enables waveguide-based imaging at GINIX with lower photon energies. Since the phase shift induced by the sample is increased at lower photon energies, the potential of cellular imaging at 7.9 keV photon energy is assessed in this section for freeze-dried cells of *Deinococcus radiodurans*.

#### 8.2.3.1 Experimental setup and raw data treatment

Experiments were performed with a similar configuration as used for 13.8 keV photon energy. The undulator beam was monochromatized to 7.9 keV and focused to a size of  $D_h = 400$  nm and  $D_v = 250$  nm full width at half maximum (FWHM). The total flux was  $6 \times 10^{11}$  counts per second at 100 mA storage ring current as measured with a PIN diode. For lower x-ray energies air-filled channel waveguides are well-suited. A 1 mm long bonded Si-waveguide (BWG) with lateral dimensions  $d_1 \times d_2 = 120$  nm  $\times$  65 nm was mounted (BWG, see **Tab. 4.1**) [85]. The maximum photon flux exiting the waveguide system was  $2 \cdot 10^9$  ph/s as measured by a Pilatus pixel detector, which is the highest flux of all waveguides used in this work. Compared to XWG1-3, the far-field intensity distribution (**Fig. 4.6 d**) has a smaller divergence, owing to a source size of about 20 nm  $\times$  17 nm (FWHM) as obtained by phase reconstruction using the ER algorithm (see **Fig. 4.6 h** and **Tab. 4.1**). The anisotropy of the source is due to the rectangular shape of the channel (see **Fig. 4.5 d**). The divergence of the smooth central cone of the waveguide beam



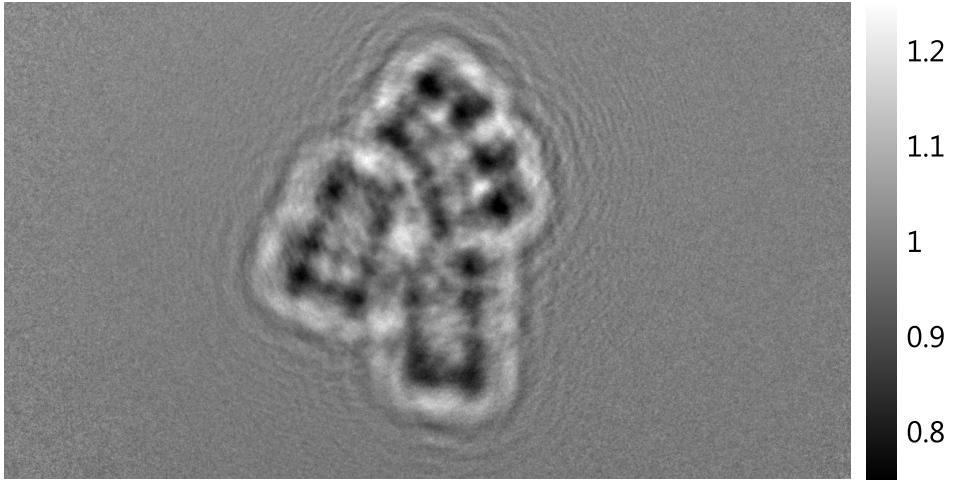


**Figure 8.12:** Normalized diffraction pattern corresponding to the first sample position for *Deinococcus radiodurans* cells, obtained by a single recording with 8 second dwell time (and corresponding empty beam recording).

is well matched to the active area of the sCMOS detector (see dashed rectangle in **Fig. 4.6 d**) and was used for imaging. The waveguide was mounted on the robust sample tower (T2 in **Fig. 4.3 c**) and freeze-dried *Deinococcus radiodurans* were mounted on a miniaturized *xyz* nano-positioner (T3 in 4.3). Sample preparation was performed as described in chapter 7<sup>6</sup>. In contrast to the previous section, the cells were known to be in the stationary phase, since cells of the same batch were imaged with ptychography and clearly showed a tetrad structure [216]. The sample was placed at four different distances separated by 0.5 mm along the optical axis, resulting in different magnifications  $M$ , effective propagation distances  $z_{\text{eff}}$  as well as effective pixels sizes  $\Delta x$  as listed in **Tab. 8.5**. Due to the high photon flux, the sCMOS detector gain was set to 1 and only a single recording with 8 second dwell time was recorded for each position, along with four corresponding empty beam intensity distributions. No further corrections were applied to the normalized diffraction patterns  $I_1 - I_4$ . **Fig. 8.12** shows the normalized hologram corresponding to the first sample position which exhibits no low-frequency variations. Due to the relatively large channel dimensions, the waveguide beam was less sensitive to lateral movements between waveguide and KB focus and thus allowed a temporal separation between hologram and empty beam recording of about 10 seconds.

<sup>6</sup> Sample preparation was performed by Robin Wilke, Institute for X-ray physics, University of Göttingen, Germany.

Position	$z_1$	$M_x$	$\Delta x$	$F_x$
	[mm]	-	[nm]	-
1	15.9	322	20.3	$1.65 \cdot 10^{-2}$
2	16.4	312	20.9	$1.70 \cdot 10^{-2}$
3	16.9	303	21.6	$1.76 \cdot 10^{-2}$
4	17.4	294	22.2	$1.81 \cdot 10^{-2}$

**Table 8.5:** Geometric parameters for four sample positions along the optical axis used for cellular imaging of *Deinococcus radiodurans*, with source-sample distance  $z_1$ , geometric magnification  $M_x$ , effective pixel size  $\Delta x$  and Fresnel number  $F^{10}$ .

### 8.2.3.2 Phase reconstruction

**Fig. 8.13** shows CTF reconstructions based on the first (**a**) and all four (**b**) sample positions. The diffraction patterns were padded by 500 pixels (replicate bordered values) prior to phase reconstruction. The regularization parameter was characterized by  $\alpha_1 = 10^{-2}$  and  $\alpha_2 = 3$  for the single distance and by  $\alpha_1 = 10^{-3}$  and  $\alpha_2 = 0.3$  for the four-distance reconstruction. Both reconstructions reveal a group of *Deinococcus radiodurans* cells. Importantly, disk-shaped domains with large relative phase shifts of up to  $-0.3$  radian can clearly be identified and attributed to the bacterial nucleoid. To further increase image quality and resolution, the mHIO scheme was applied to the diffraction data of the first sample position. The support  $\mathcal{S}$  was determined automatically as described in section 8.2.1.3 by setting a (lower) threshold of  $-0.07$  radian<sup>7</sup>. The measured normalized intensity was embedded in a larger array (with edge length  $2 \cdot 1080 = 2160$  pixel, replicate padding) to allow sufficient sampling of the complex exponential (1.56) of the Fresnel diffraction operator. A mask with the size of the original array was defined, and the amplitude constraint was restricted to the area of that mask. The noise parameter was set to  $D = 8.2 \cdot 10^{-3}$ , the feedback parameters were set to  $\beta = \gamma = 0.5$  and the algorithm was initialized with unit intensity and the phase distribution shown in **a**. Due to the large array size of  $2160^2$  pixels the algorithm was implemented on a GPU. The resulting phase distribution after  $N_{\text{it}} = 741$  iterations is shown in **c**. Low frequency artifacts visible in the CTF reconstruction (**a,b**) are effectively removed, while the same details within the cells remain visible. However, the iterative reconstruction seems to be affected more strongly by photon shot noise and detector read-out noise than the deterministic CTF approach. This may be linked to the fact that noise characteristics are not incorporated explicitly in the mHIO scheme and that a single parameter  $D$  is set globally for all  $10^6$  pixels (see section 2.4.1.3). As an alternative, it was investigated whether iteratively regularized Gauss-Newton methods (IRGN) yield better

<sup>7</sup> The sign of the phase is flipped for the test structure since it was milled into gold while the cells are placed on top of a membrane.

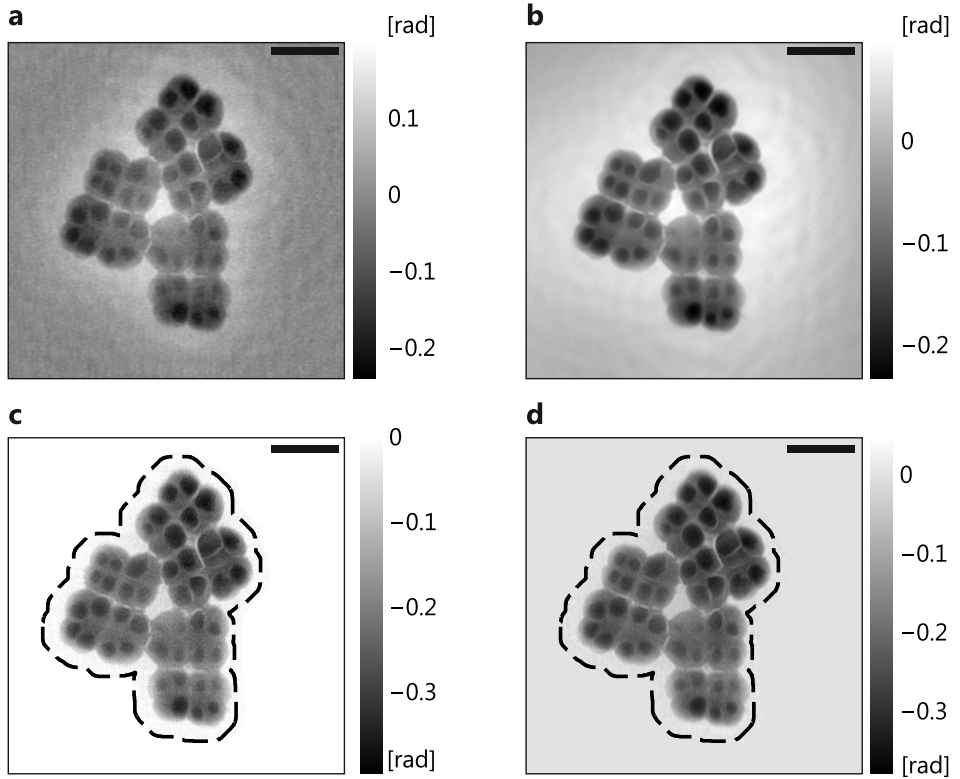


**Figure 8.13:** CTF reconstruction based on holograms corresponding to (a) the first sample position ( $\alpha_1 = 10^{-2}, \alpha_2 = 3$ , 500 pixel replicate padding) and (b) all four sample positions ( $\alpha_1 = 10^{-3}, \alpha_2 = 0.3$ , 500 pixel replicate padding). (c) mHIO reconstruction ( $D = 8.2 \cdot 10^{-3}$ ) and (d) IRGM reconstruction using the same support (dashed line) and initial guess (shown in a). The field of view is  $20 \mu\text{m} \times 20 \mu\text{m}$ . Scale bars,  $4 \mu\text{m}$ .

results in terms of high frequency noise. To this end, the algorithm described in section 2.4.2 was applied to the padded diffraction pattern. It was initialized with the same guess as for the mHIO scheme, namely the single-distance CTF reconstruction shown in (a), as well as with identical support  $\mathcal{S}$ . The regularization parameter  $\alpha_n = \alpha_0 C_{\text{dec}}^{-n}$  was characterized by  $\alpha = 0.1$  and  $C_{\text{dec}} = 3/2$ . The maximum number of iterations for the inner conjugate gradient loop was set to  $N_{\text{CG}} = 100$  and 50 Newton steps were performed. The result (d) is consistent to what was obtained with the mHIO approach. Visual inspection reveals that the phase reconstruction indeed exhibits less high frequency noise. This observation is confirmed by comparison of the azimuthally averaged power spectral densities (PSD) for both reconstruction approaches (Fig. 8.14). While cross-over to the noise plateau is at about 0.19 cycles per pixel for both reconstructions, the phase distribution obtained by the IRGN exhibits a lower plateau as expected for a reconstruction with less high-frequency noise. This result was approved by a second dataset with higher total photon fluence. Instead of one single 8 second exposure, 20 individual one second accumulations were summed up<sup>8</sup> to improve statistics. Phase reconstructions obtained by mHIO and IRGN (not shown) based on this dataset resulted in PSDs (solid lines in Fig. 8.14) with a similar behaviour as for the shorter accumulation. Hence, we conclude that application of an iteratively regularized Gauss-Newton method with an initial guess provided by a deterministic CTF method improved phase reconstruction compared to the mHIO algorithm. In view of automatic phasing needed for tomographic data, it is noteworthy that the same regularization parameters could be used for the IRGN method for both datasets, while the optimal choice of  $D$  was found manually ( $D = 6.9 \cdot 10^{-3}$  for the present case). In combination with the deterministic CTF approach yielding initial guess and support, this approach has a huge potential for three-dimensional x-ray propagation imaging.

### 8.2.3.3 Resolution and dose

The cross-over to the noise plateau at about 0.19 cycles per pixel corresponds to a half-period resolution of about 53 nm. Flux density at the first sample plane was  $5 \cdot 10^5$  ph/ $\mu\text{m}^2$ /s and the total dose for a single 8 second exposure was  $D = 5.2 \cdot 10^3$  Gy, according to a fluence of  $4 \cdot 10^6$  ph/ $\mu\text{m}^2$ . For the four-distance reconstruction and the 20 second exposure single-distance dataset, dose and fluence values are higher by a factor of 4 or 2.5, respectively. Once more, we compare these values to a recent ptychographic study with similar reported half-period resolution of 46 nm at a dose of and  $4.9 \cdot 10^6$  Gy [216]. Therefore, the current experiment enabled phase reconstruction at similar spatial resolution with almost three orders of magnitude less dose. Photon energies of both experiments were similar (7.9 keV and 6.2 keV), cells of the same batch were used and features visible in the respective phase reconstructions are similar (compare Fig. 8.13 with Fig. 4 a in [216]). Therefore, we conclude that cone-beam propagation imaging based on x-ray waveguides has proven to be more dose-efficient than ptychography for imaging of biological cells

<sup>8</sup> The sCMOS detector gain was set to 2.

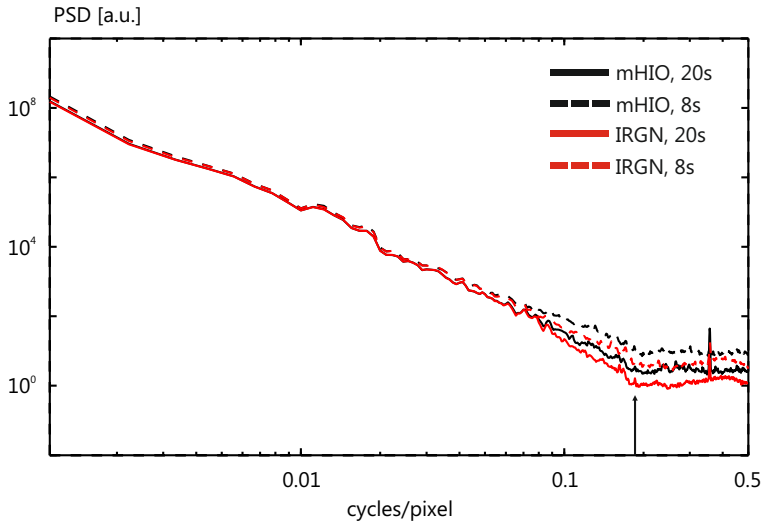


**Figure 8.14:** Azimuthally averaged power spectral density (PSD) of the mHIO reconstruction for the 8 second (dashed black line) and 20 second (solid black line) exposure dataset. The corresponding IRGN reconstructions (red curves) exhibit a lower noise level at high spatial frequencies. The kink at 0.19 cycles/pixel (arrow) corresponds to a half-period of 53 nm.

at a resolution of about 50 nm. At the same time, the reconstructed field of view of  $20\ \mu\text{m} \times 20\ \mu\text{m}$  is larger for the presented approach and the total accumulation time of 16 seconds (including empty beam recording) is much shorter than the value of about 1 minute reported in [216].

### 8.3 Summary

X-ray propagation imaging of biological cells using waveguides as quasi-point sources [63] was extended to sub-100 nm spatial resolution both for eukaryotic cells of *Dictyostelium discoideum* as well as bacterial cells of *Deinococcus radiodurans* with unprecedented image quality. For a nanofabricated test object, spatial resolution below 30 nm was achieved by means of an optimized configuration of the GINIX setup with a well-matched waveguide-detector combination and stable waveguide positioning system. For high-resolution imaging, it was essential to perform drift correction and to take astigmatism into account for crossed multilayer x-ray waveguides. Freeze-dried *Deinococcus radiodurans* cells were imaged at a resolution below 30 nm with x-rays of 13.8 keV photon energy. The obtained spatial resolution is higher (better) than a recent ptychographic study of *Deinococcus radiodurans* and notably, at lower dose values. Imaging of *Deinococcus radiodurans* at a photon energy of 7.9 keV was achieved by means of lithographic channel waveguides. Photon flux and beam stability were sufficient to image cells within a single

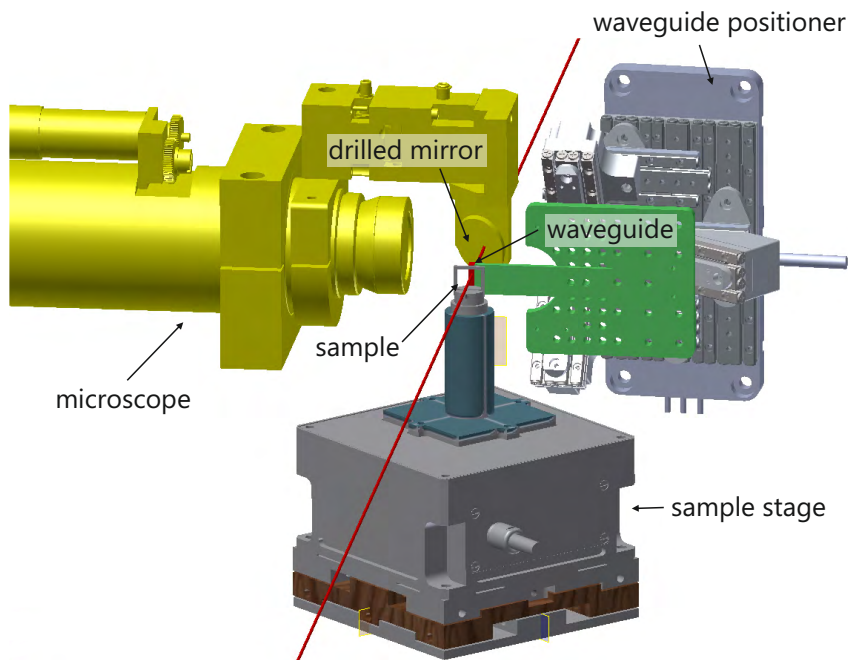


**Figure 8.15:** Sketch of the foreseen GINIX configuration for optimized waveguide-based three-dimensional x-ray propagation imaging. The optical axis is shown in red.

8 second accumulation (plus 8 second empty beam recording). Consistent phase reconstructions of the large  $20\ \mu\text{m} \times 20\ \mu\text{m}$  field of view were achieved using CTF-based methods, a modified HIO scheme and iteratively regularized Gauss-Newton methods. The latter has proven to yield least noise at high spatial frequencies. Altogether, waveguide-based x-ray propagation imaging has proven its potential for fast, dose-efficient quantitative imaging of biological samples. However, the optimized configuration of GINIX did not allow tomographic measurements so far, due to missing degrees of freedom. **Fig. 8.15** shows the sketch of an upgrade that is foreseen at GINIX to circumvent this limitation. A compact goniometer (SmarPod, SmarAct, Germany) will be used as waveguide positioner. Compared to the stacking of positioners in the original waveguide configuration, this design is expected to provide stable waveguide positioning. Then, the sample will be placed at the dedicated sample tower for high-precision tomographic scans in order to extend the current two-dimensional high-resolution results to three dimensions.

## Conclusion

The goal of this work was the optimization of x-ray propagation imaging in terms of contrast, spatial resolution and field of view for three-dimensional imaging of biological samples. The investigated objects ranged in size from a few micrometers for single cells over several hundred micrometers for multi-cellular nerve tissue up to a few millimeters for whole mouse organs. While the underlying concept of image formation remained unaffected, requirements on the experimental implementation of x-ray propagation imaging, sample preparation and data analysis varied significantly from specimen to specimen.

The first series of experiments targeted soft tissue visualisation within entire mouse and rat cochlea. It was demonstrated that by combination of a microfocus x-ray source with a phase retrieval algorithm suitable for strong absorption, functional soft tissue within the bony capsule of the cochlea can be visualized in 3D with unprecedented image quality. In contrast to previously reported x-ray tomography of mouse cochlea, the obtained data enabled automatic segmentation between bone and soft tissue structures. Contrast and resolution were sufficient to visualize small membranes and nerve tissue. The obtained 3D datasets were used to characterize brainstem responses to otogenic stimulations and to estimate design parameters for prosthetic mouse and rat cochlea implants. Fast tomography was achieved by means of novel liquid-metal-jet x-ray technology. To increase spatial resolution, an optimized configuration of detector and imaging geometry was exploited which allowed phase-contrast tomography with sub-source size resolution of about  $2\ \mu\text{m}$ . The approach can easily be applied to a wide range of biological samples.

The second branch of experiments was devoted to three-dimensional synchrotron-based imaging of uncut mouse nerves of the central and peripheral nervous system. Various experimental configurations, sample preparation techniques and phase reconstruction approaches were assessed for imaging of optical, sciatic and saphenus nerves. While sub-structure within unstained nerves was visible, it was found that an osmium tetroxide stain increases myelin visibility drastically. Immersion fixation and agarose embedding was used to image axons surrounded by myelin within saphenus nerves at a voxel size of  $430\ \text{nm}$ . High-resolution imaging with  $100\ \text{nm}$  voxel size of immersion fixated optical nerves was feasible but artifacts appeared. High-pressure freezing and EPON-embedding proved optimal for high-resolution nerve imaging. A large three-dimensional volume of more than  $(200\ \mu\text{m})^3$  was reconstructed with an isotropic voxel size of  $100\ \text{nm}$ , revealing more than 1000 axons running in parallel within the nerve. Contrast and resolution were sufficient to identify nodes of Ranvier and Schmidt-Lantermann incisures. A three-dimensional

rendering suggests that incisures may predominately be found in the vicinity of nodes belonging to neighbouring axons. The approach is highly compatible with electron and optical microscopy in terms of sample preparation and therefore allows correlative measurements. Compared to serial block-face scanning electron microscopy, data is recorded much faster with total scan times below one hour. This allows biological studies where several samples have to be investigated.

Another experiment aimed at quantitative density contrast of bacterial cells. Quantitative cellular imaging using x-ray waveguides was previously reported in 2D yielding *projected* effective mass density maps. The goal was to extend this approach to three dimensions. To this end, waveguide-based tomographic x-ray propagation imaging was developed at the GINIX setup of PETRA III. The three-dimensional effective mass density distribution within freeze-dried bacterial *Deinococcus radiodurans* was computed from quantitative phase maps as obtained by an iterative phase retrieval approach. Characteristic density maxima were identified and attributed to DNA rich regions. A medium spatial resolution in the range of 125 – 200 nm was obtained, however, at very low dose values compared to other lensless x-ray coherent imaging techniques.

The fourth series of experiments was designed to improve spatial resolution of waveguide-based x-ray propagation imaging at GINIX. To this end, different waveguides were examined in order to achieve higher photon flux, the waveguide positioning system was altered yielding increased beam stability and different detectors were investigated. As a result, freeze-dried eukariotic cells of *Dictyostelium discoideum* could be imaged with sub-100 nm resolution. By means of an optimized waveguide-detector configuration sub-30 nm resolution was achieved both for a test structure and for freeze-dried bacterial cells of *Deinococcus radiodurans* at a photon energy of 13.8 keV. Compared to coherent diffraction imaging studies the approach has proven to be very dose-efficient. For lower photon energies, propagation imaging was achieved using novel lithographic channel waveguides. Due to increased photon flux, stability and increased beam-sample interaction at 7.9 keV photon energy, a single 8 second exposure yielded an artifact-free phase reconstruction of *Deinococcus radiodurans* cells which clearly showed the bacterial nucleoids. The reconstruction exhibited a field of view of  $(20\ \mu\text{m})^2$  at about 50 nm spatial resolution and very low dose values compared to coherent diffraction imaging techniques.

In conclusion, x-ray propagation imaging was applied to a variety of biological specimens both at laboratory sources and synchrotron storage rings. Resolution and field of view are scalable by three orders of magnitude, provided suitable instrumentation and phase retrieval. Results of high resolution two-dimensional cellular imaging hold out the prospect for fast and dose-efficient quantitative three-dimensional imaging of weakly scattering and radiation sensitive samples.



# Appendix

## A.1 Fourier analysis

Fundamentals of Fourier analysis relevant for this work are summarized in this section. The reader is referred to standard textbooks for a profound description and mathematically rigorous derivations [20, 68, 26]. All relations are presented here for the case of one dimension, while analogous relations exist for higher dimensions.

### A.1.1 Fourier transform

The **Fourier transform**  $\mathcal{F}[f]$  of an integrable function  $f \in L^1(\mathbb{R}^n)$  is defined as

$$\mathcal{F}[f](k) := \tilde{f}(k) := \frac{1}{(2\pi)^{n/2}} \int_{\mathbb{R}^n} f(x) \exp(-ikx) dx. \quad (\text{A.1})$$

The **inverse Fourier transform**  $\mathcal{F}^{-1}[g]$  of a function  $g \in L^1(\mathbb{R}^n)$

$$\mathcal{F}[g](x) := \tilde{g}(x) := \frac{1}{(2\pi)^{n/2}} \int_{\mathbb{R}^n} g(k) \exp(ikx) dk \quad (\text{A.2})$$

yields the **Fourier theorem**

$$\mathcal{F}^{-1}[\mathcal{F}[f]] = f. \quad (\text{A.3})$$

For a square-integrable function  $f \in L^2(\mathbb{R}^n)$  the Fourier transform defines a bijective mapping and one speaks of the **Fourier pair**

$$f(x) \leftrightarrow \tilde{f}(k). \quad (\text{A.4})$$

### A.1.2 Properties of the Fourier transform

#### Linearity

The Fourier transform  $\mathcal{F}$  is a linear operator

$$\mathcal{F}[af + bg] = a\mathcal{F}[f] + b\mathcal{F}[g]. \quad (\text{A.5})$$

### Shifting

Shifting in real space results in a multiplication with a complex exponential in Fourier space

$$f(x - x_0) \leftrightarrow \tilde{f}(k) \exp(-ikx_0), \quad (\text{A.6})$$

$$f(x) \exp(ik_0x) \leftrightarrow \tilde{f}(k - k_0). \quad (\text{A.7})$$

### Scaling

Scaling in real space translates to inverse scaling in Fourier space

$$f(\alpha x) \leftrightarrow \frac{1}{|\alpha|} \tilde{f}\left(\frac{k}{\alpha}\right). \quad (\text{A.8})$$

for  $\alpha \in \mathbb{R} \setminus \{0\}$ .

### Derivatives

Derivatives in real space result in multiplication with the reciprocal coordinate in Fourier space

$$\frac{d^m}{dx^m} f(x) \leftrightarrow (ik)^m \tilde{f}(k), \quad (\text{A.9})$$

for  $m \in \mathbb{N}$ .

### Convolution theorem

The Fourier transform of the convolution

$$(f \otimes g)(x) := \int f(\tau)g(x - \tau)d\tau = \int f(x - \tau)g(\tau)d\tau = (g \otimes f)(x) \quad (\text{A.10})$$

of two functions  $f$  and  $g$  is given by the point-wise multiplication of their individual Fourier transforms

$$(f \otimes g)(x) \leftrightarrow (2\pi)^{n/2} \tilde{f}(k) \tilde{g}(k), \quad (\text{A.11})$$

and vice versa

$$f(x)g(x) \leftrightarrow \frac{1}{(2\pi)^{n/2}} (\tilde{f} \otimes \tilde{g})(k), \quad (\text{A.12})$$

### Cross-correlation theorem

The cross-correlation

$$(f \oplus g)(x) := \int f(\tau)g^*(x + \tau)d\tau, \quad (\text{A.13})$$

of two functions  $f$  and  $g$  is related to their Fourier transforms by

$$(f \oplus g)(x) \leftrightarrow (2\pi)^{n/2} \tilde{f}(k) \tilde{g}^*(k), \quad (\text{A.14})$$

with  $*$  denoting the complex conjugation.

### Auto-correlation theorem

The Fourier transform of the auto-correlation  $f \oplus f$  of a function  $f$  is related to the power spectral density  $|\tilde{f}(k)|^2$  by

$$(f \oplus f)(x) \leftrightarrow (2\pi)^{n/2} |\tilde{f}(k)|^2. \quad (\text{A.15})$$

### Complex conjugate

$$f^*(x) \leftrightarrow \tilde{f}(-k) \quad (\text{A.16})$$

### A.1.3 Fourier transform of the Dirac delta function

The Dirac delta function (distribution)  $\delta_D$

$$\delta_D(x) = \begin{cases} +\infty, & x = 0 \\ 0, & x \neq 0 \end{cases} \quad (\text{A.17})$$

obeys

$$\int \delta_D(x) dx = 1. \quad (\text{A.18})$$

It has the important property

$$\int \delta_D(x - x_0) f(x) dx = f(x_0) \quad (\text{A.19})$$

for any continuous compactly supported function  $f$  and the scaling property

$$\delta_D(\alpha x) = \frac{\delta_D(x)}{|\alpha|}. \quad (\text{A.20})$$

One finds the following Fourier pairs for the Dirac delta function:

$$\delta_D(x) \leftrightarrow \frac{1}{(2\pi)^{n/2}} \quad (\text{A.21})$$

$$1 \leftrightarrow (2\pi)^{n/2} \delta_D(k). \quad (\text{A.22})$$

## A.2 Free space propagation of conjugate objects

Free space propagation of a wave field  $f(\mathbf{r}_\perp)$  can be written as

$$\mathcal{D}_z [f(\mathbf{r}_\perp)] = \mathcal{F}_\perp^{-1} [H(\mathbf{k}_\perp, z) \mathcal{F}_\perp [f(\mathbf{r}_\perp)]], \quad (\text{A.23})$$

with

$$H(\mathbf{k}_\perp, z) = \exp\left(iz\sqrt{k^2 - k_\perp^2}\right). \quad (\text{A.24})$$

With

$$H^*(\mathbf{k}_\perp, z) = H(\mathbf{k}_\perp, -z) \quad (\text{A.25})$$

and

$$H(-\mathbf{k}_\perp, z) = H(\mathbf{k}_\perp, z) \quad (\text{A.26})$$

the following holds:

$$\begin{aligned} \mathcal{D}_z [f(\mathbf{r}_\perp)]^* &= \mathcal{F}_\perp^{-1} [H(\mathbf{k}_\perp, z) \mathcal{F}_\perp [f(\mathbf{r}_\perp, 0)](\mathbf{k}_\perp)]^* (\mathbf{r}_\perp) \\ &= \mathcal{F}_\perp^{-1} [H^*(\mathbf{k}_\perp, z) \mathcal{F}_\perp [f(\mathbf{r}_\perp, 0)](\mathbf{k}_\perp)]^* (-\mathbf{r}_\perp) \\ &= \mathcal{F}_\perp^{-1} [H(\mathbf{k}_\perp, -z) \mathcal{F}_\perp [f^*(\mathbf{r}_\perp, 0)](-\mathbf{k}_\perp)] (-\mathbf{r}_\perp) \\ &= \mathcal{F}_\perp^{-1} [H(-\mathbf{k}_\perp, -z) \mathcal{F}_\perp [f^*(\mathbf{r}_\perp, 0)](\mathbf{k}_\perp)] (\mathbf{r}_\perp) \\ &= \mathcal{F}_\perp^{-1} [H(\mathbf{k}_\perp, -z) \mathcal{F}_\perp [f^*(\mathbf{r}_\perp, 0)](\mathbf{k}_\perp)] (\mathbf{r}_\perp) \quad (\text{A.27}) \\ &= \mathcal{D}_{-z} [f^*(\mathbf{r}_\perp)]. \quad (\text{A.28}) \end{aligned}$$

### A.3 Spatial resolution

The determination of spatial resolution is important for evaluating the quality of a given imaging system. Loosely speaking, one wants to know which are the smallest features that can be detected. To give a single parameter for the spatial resolution is only useful if the corresponding resolution criterion is stated. Otherwise the comparison between two imaging systems or different results is not possible. The Rayleigh criterion defines two point sources as just resolved if the maximum of the first Airy pattern (diffraction limited point-spread-function (PSF) due to circular aperture) lies on the minimum of the second Airy pattern [20]. If the distance between the two points is smaller, they are regarded as not resolved. While this criterion is useful for diffraction limited imaging systems, e.g. in visible light optics it has no counterpart for PSFs without minima as for the case of a Gaussian or an exponential. While the PSF contains complete information about the spatial resolution a natural *single* parameter to characterize the PSF while ignoring its shape is the standard deviation  $\sigma$ . While the PSF is a two dimensional function, the one-dimensional line-spread-function (LSF) describes how an idealized line is blurred. The line-spread function can be obtained by differentiation of the edge-spread-function (ESF) which can be measured. For a Gaussian PSD the LSF is also a Gaussian with identical standard deviation [192, 69]

$$\text{LSF}(x) = \frac{1}{\sigma\sqrt{2\pi}} \exp\left(-\frac{x^2}{2\sigma^2}\right) \quad (\text{A.29})$$

and full width at half maximum of

$$\text{FWHM} = 2\sqrt{2 \ln 2} \sigma. \quad (\text{A.30})$$

The modulation transfer function is the modulus of the Fourier transform of the LSF

$$\text{MTF}(\nu) = |\mathcal{F}(\text{LSF})| = \exp\left(-\frac{(2\pi\nu)^2 \sigma^2}{2}\right), \quad (\text{A.31})$$

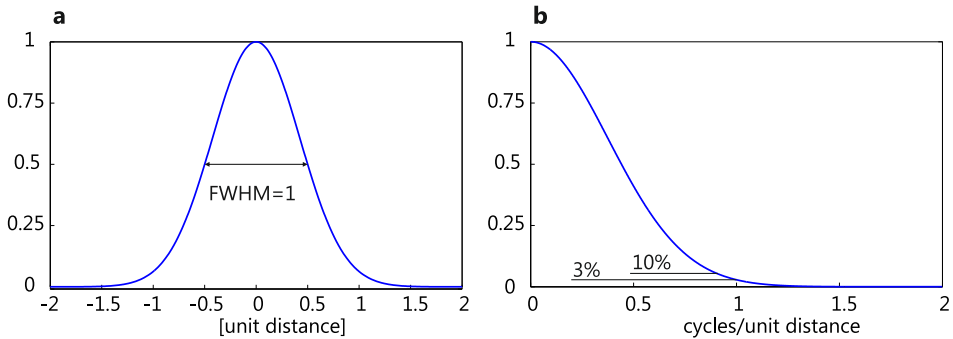


**Figure A.16:** (a) Gaussian PSF (identical to LSF) with  $\sigma = 1/2\sqrt{2\ln 2}$  (FWHM = 1). (b) Corresponding MTF. The 10%, 5% and 3% contrast levels correspond to 0.804, 0.917 and 0.993 cycles per unit distance, respectively.

with spatial frequency  $\nu$ . While each frequency is transmitted with a different contrast it is common to define the limiting spatial resolution as the feature size which is visible with a certain contrast value (typically 3%, 5% or 10%). For 3% contrast and a Gaussian LSF with FWHM=1 we get

$$3\% = \text{MTF}(\nu) = \exp\left(-\frac{(2\pi\nu)^2}{2} \frac{1}{(2\sqrt{2\ln 2}\sigma)^2}\right) \quad (\text{A.32})$$

$$\Rightarrow \nu = \sqrt{-\frac{4\ln(0.03) \cdot \ln(2)}{\pi^2}} \quad (\text{A.33})$$

$$= 0.993 \quad (\text{A.34})$$

Therefore, the MTF drops to 3% contrast at a spatial frequency of 0.993 cycles per unit distance. The 3% limiting full-period resolution is 1.008 and therefore almost (with 0.8 % deviation) the FWHM of the PSF. For 5% and 10% contrast the limiting resolution is 1.09 and 1.24 times the FWHM, respectively.



## Bibliography

- [1] J. Als-Nielsen and D. McMorrow. *Elements of Modern X-ray Physics*. John Wiley & Sons, Hoboken, NJ, 2001.
- [2] B. D. Arhatari and A. G. Peele. Optimisation of phase imaging geometry. *Optics Express*, 18:23727, 2010.
- [3] C. Badea, M. Drangova, D. W. Holdsworth, and G. Johnson. In Vivo Small Animal Imaging using Micro-CT and Digital Subtraction Angiography. *Physics in Medicine and Biology*, 7:R319, 2008.
- [4] A. B. Bakushinskii. The problem of the convergence of the iteratively regularized Gauss-Newton method. *Computational Mathematics and Mathematical Physics*, 32:1353, 1992.
- [5] A. B. Bakushinskii and M. Y. Kokurin. *Iterative Methods for Approximate Solution of Inverse Problems*. Springer, Berlin, 2004.
- [6] K. Balewski, W. Brefeld, W. Decking, H. Franz, R. Röhlberger, and E. Weckert. PETRA III: A low emittance synchrotron radiation source. Technical report, Deutsches Elektronen-Synchrotron DESY, 2004.
- [7] H. H. Barrett and K. J. Myers. *Foundations of image science (Wiley Series in Pure and Applied Optics)*. John Wiley & Sons, Hoboken, NJ, 2004.
- [8] R. Barrett, R. Baker, P. Cloetens, Y. Dabin, C. Morawe, H. Suhonen, R. Tucoulou, A. Vivo, and L. Zhang. Dynamically-figured mirror system for high-energy nanofocusing at the ESRF. *SPIE Proceedings*, 8139:813904, 2011.
- [9] M. Bartels. Phasenkontrast-Mikrotomographie an einer Laborröntgenquelle. Master's thesis, Georg-August-Universität Göttingen, 2010.
- [10] M. Bartels, V. H. Hernandez, M. Krenkel, T. Moser, and T. Salditt. Phase contrast tomography of the mouse cochlea at microfocus x-ray sources. *Applied Physics Letters*, 103:083703, 2013.
- [11] M. Bartels, W. Möbius, and T. Salditt. Hard x-ray phase contrast tomography of mouse nerves. *unpublished manuscript*.

- [12] M. Bartels, M. Priebe, R. N. Wilke, S. P. Krüger, K. Giewekemeyer, S. Kalbfleisch, C. Olendrowitz, M. Sprung, and T. Salditt. Low-dose three-dimensional hard x-ray imaging of bacterial cells. *Optical Nanoscopy*, 1:10, 2012.
- [13] M. Bech, T. H. Jensen, R. Feidenhans, O. Bunk, C. David, and F. Pfeiffer. Soft-tissue phase-contrast tomography with an x-ray tube source. *Physics in Medicine and Biology*, 54:2747, 2009.
- [14] D. H. Bilderback, P. Elleaume, and E. Weckert. Review of third and next generation synchrotron light sources. *Journal of Physics B: Atomic, Molecular and Optical Physics*, 38:773, 2005.
- [15] B. Blaschke, A. Neubauer, and O. Scherzer. On convergence rates for the Iteratively regularized Gauss-Newton method. *IMA Journal of Numerical Analysis*, 17:421, 1997.
- [16] P. Bleuet, P. Cloetens, P. Gergaud, D. Mariolle, N. Chevalier, R. Tucoulou, J. Susini, and A. Chabli. A hard x-ray nanoprobe for scanning and projection nanotomography. *Review of Scientific Instruments*, 80:056101, 2009.
- [17] P. Bleuet, A. Simionovici, L. Lemelle, T. Ferroir, P. Cloetens, R. Tucoulou, and J. Susini. Hard x-rays nanoscale fluorescence imaging of Earth and Planetary science samples. *Applied Physics Letters*, 92:213111, 2008.
- [18] M. Boone, W. Devulder, M. Dierick, L. Brabant, E. Pauwels, and L. V. Hoorebeke. Comparison of two single-image phase-retrieval algorithms for in-line x-ray phase-contrast imaging. *Journal of the Optical Society of America A*, 29:2667, 2012.
- [19] M. Boone, Y. D. Witte, M. Dierick, J. V. den Bulcke, J. Vlassenbroeck, and L. V. Hoorebeke. Practical use of the modified Bronnikov algorithm in micro-CT. *Nuclear Instruments and Methods in Physics Research Section B: Beam Interactions with Materials and Atoms*, 267:1182, 2009.
- [20] M. Born and E. Wolf. *Principles of optics: 7th (expanded) edition*. Cambridge University Press, Cambridge, 1999.
- [21] C. Broennimann, E. F. Eikenberry, B. Henrich, R. Horisberger, G. Huelsen, E. Pohl, B. Schmitt, C. Schulze-Briese, M. Suzuki, T. Tomizaki, H. Toyokawa, and A. Wagner. The PILATUS 1M detector. *Journal of Synchrotron Radiation*, 13:120, 2006.
- [22] A. V. Bronnikov. Reconstruction formulas in phase-contrast tomography. *Optics Communications*, 171:239, 1999.
- [23] A. V. Bronnikov. Theory of quantitative phase-contrast computed tomography. *Journal of the Optical Society of America A*, 19:472, 2002.



- [24] A. Burvall, U. Lundström, P. A. C. Takman, D. H. Larsson, and H. M. Hertz. Phase retrieval in X-ray phase-contrast imaging suitable for tomography. *Optics Express*, 19:10359, 2011.
- [25] L. D. Caro, C. Giannini, S. D. Fonzo, W. Yark, A. Cedola, and S. Lagomarsino. Spatial coherence of X-ray planar waveguide exiting radiation. *Optics Communications*, 217:31, 2003.
- [26] D. C. Champeney. *Fourier Transforms and their Physical Applications*. Techniques of Physics. Academic Press, Waltham, MA, 1973.
- [27] W. Chao, B. D. Harteneck, J. A. Liddle, E. H. Anderson, and D. T. Attwood. Soft X-ray microscopy at a spatial resolution better than 15nm. *Nature*, 435:1210, 2005.
- [28] H. N. Chapman, A. Barty, S. Marchesini, A. Noy, S. P. Hau-Riege, C. Cui, M. R. Howells, R. Rosen, H. He, J. C. H. Spence, U. Weierstall, T. Beetz, C. Jacobsen, and D. Shapiro. High-resolution ab initio three-dimensional x-ray diffraction microscopy. *Journal of the Optical Society of America A*, 23:1179, 2006.
- [29] S. Chilingaryan, A. Mirone, A. Hammersley, C. Ferrero, L. Helfen, A. Kopmann, T. dos Santos Rolo, and P. Vagovic. A GPU-Based Architecture for Real-Time Data Assessment at Synchrotron Experiments. *IEEE Transactions on Nuclear Science*, 58:1447, 2011.
- [30] L. Chittka and A. Brockmann. *Perception Space - The Final Frontier*, Fig. 1A. [Creative Commons Attribution License (<http://creativecommons.org/licenses/by/2.5/>)]. PLoS. Biol. 3, 2005.
- [31] P. Cloetens. *Contribution to Phase Contrast Imaging, Reconstruction and Tomography with Hard Synchrotron Radiation*. PhD thesis, Vrije Universiteit Brussel, 1999.
- [32] P. Cloetens, R. Barrett, J. Baruchel, J.-P. Guigay, and M. Schlenker. Phase objects in synchrotron radiation hard x-ray imaging. *Journal of Physics D: Applied Physics*, 29:133, 1996.
- [33] P. Cloetens, W. Ludwig, J. Baruchel, D. V. Dyck, J. V. Landuyt, J. P. Guigay, and M. Schlenker. Holotomography: Quantitative phase tomography with micrometer resolution using hard synchrotron radiation x rays. *Applied Physics Letters*, 75:2912, 1999.
- [34] P. Cloetens, W. Ludwig, J. Baruchel, J.-P. Guigay, P. Pernot-Rejmankova, M. Salome-Pateyron, M. Schlenker, J.-Y. Buffiere, E. Maire, and G. Peix. Hard x-ray phase imaging using simple propagation of a coherent synchrotron radiation beam. *Journal of Physics D: Applied Physics*, 32:A145, 1999.

- [35] P. Cloetens, R. Mache, M. Schlenker, and S. Lerbs-Mache. Quantitative phase tomography of Arabidopsis seeds reveals intercellular void network. *Proceedings of the National Academy of Sciences*, 103:14626, 2006.
- [36] W. Coene, G. Janssen, M. Op de Beeck, and D. Van Dyck. Phase Retrieval through Focus Variation for Ultra-Resolution in Field-Emission Transmission Electron Microscopy. *Physical Review Letters*, 69:3743, 1992.
- [37] A. M. Cormack. Representation of a Function by Its Line Integrals, with Some Radiological Applications. *Journal of Applied Physics*, 34:2722, 1963.
- [38] V. E. Cosslett and W. C. Nixon. The X-Ray Shadow Microscope. *Journal of Applied Physics*, 24:616, 1953.
- [39] J. Cowley. *Diffraction physics*. North Holland Publishing Company, Amsterdam, 1981.
- [40] C. David, B. Nohammer, H. H. Solak, and E. Ziegler. Differential x-ray phase contrast imaging using a shearing interferometer. *Applied Physics Letters*, 81:3287, 2002.
- [41] V. Davidoiu, B. Sixou, M. Langer, and F. Peyrin. Nonlinear phase retrieval based on Fréchet derivative. *Optics Express*, 19:176847, 2011.
- [42] W. Denk and H. Horstmann. Serial Block-Face Scanning Electron Microscopy to Reconstruct Three-Dimensional Tissue Nanostructure. *PLoS Biology*, 2:e329, 2004.
- [43] M. Dierolf, A. Menzel, P. Thibault, P. Schneider, C. M. Kewish, R. Wepf, O. Bunk, and F. Pfeiffer. Ptychographic X-ray computed tomography at the nanoscale. *Nature*, 467:436, 2010.
- [44] T. Donath, F. Pfeiffer, O. Bunk, C. Grünzweig, E. Hempel, S. Popescu, P. Vock, and C. David. Toward clinical X-ray phase-contrast CT: demonstration of enhanced soft-tissue contrast in human specimen. *Investigative Radiology*, 45:445, 2010.
- [45] J. Dubochet, M. , Adrian, J. Chang, J. Homo, L. J., A. McDowell, and P. Schultz. Cryo-electron microscopy of vitrified specimens. *Quarterly Reviews of Biophysics*, 21:129, 1988.
- [46] V. Elser. Phase retrieval by iterated projections. *Journal of the Optical Society of America A*, 20:40, 2003.
- [47] E. Eltsov and J. Dubochet. Fine Structure of the *Deinococcus radiodurans* Nucleoid Revealed by Cryoelectron Microscopy of Vitreous Sections. *Journal of Bacteriology*, 187:8047, 2005.
- [48] E. Eltsov and J. Dubochet. Rebuttal: Ring-Like Nucleoids and DNA Repair in *Deinococcus radiodurans*. *Journal of Bacteriology*, 188:6052, 2006.

- [49] E. Eltsov and J. Dubochet. Study of the *Deinococcus radiodurans* Nucleoid by Cryoelectron Microscopy of Vitreous Sections: Supplementary Comments. *Journal of Bacteriology*, 188:6053, 2006.
- [50] M. Engelhardt, J. Baumann, M. Schuster, C. Kottler, F. Pfeiffer, O. Bunk, and C. Davi. High-resolution differential phase contrast imaging using a magnifying projection geometry with a microfocus x-ray source. *Applied Physics Letters*, 90:224101, 2007.
- [51] H. M. L. Faulkner and J. M. Rodenburg. Movable Aperture Lensless Transmission Microscopy: A Novel Phase Retrieval Algorithm. *Physical Review Letters*, 93:023903, 2004.
- [52] L. A. Feldkamp, L. C. Davis, and J. W. Kress. Practical cone-beam algorithm. *Journal of the Optical Society of America A*, 1:612, 1984.
- [53] J. R. Fienup. Reconstruction of an object from the modulus of its Fourier transform. *Optics Letters*, 3:27, 1978.
- [54] J. R. Fienup. Phase retrieval algorithms: a comparison. *Applied Optics*, 21:2758, 1982.
- [55] H. Franz, O. Leupold, R. Röhlberger, S. V. Roth, O. H. Seeck, J. Spengler, J. Strempler, J. M. Tischer, Viefhaus, E. Weckert, and T. Wroblewski. PETRA III: DESY's new high brilliance third generation synchrotron radiation source. *Synchrotron Radiation News*, 19:25, 2006.
- [56] C. Fuhse. *X-ray waveguides and waveguide-based lensless imaging*. PhD thesis, Universität Göttingen, 2006.
- [57] C. Fuhse, C. Ollinger, and T. Salditt. Waveguide-Based Off-Axis Holography with Hard X Rays. *Physical Review Letters*, 97:254801, 2006.
- [58] C. Fuhse and T. Salditt. Finite-difference field calculations for two-dimensionally confined x-ray waveguides. *Applied Optics*, 45:4603, 2006.
- [59] D. Gabor. A New Microscopic Principle. *Nature*, 161:777, 1948.
- [60] R. W. Gerchberg and W. O. Saxton. A Practical Algorithm for the Determination of Phase from Image and Diffraction Plane Pictures. *Optik (Jena)*, 35:237, 1972.
- [61] K. Giewekemeyer. *A study on new approaches in coherent x-ray microscopy of biological specimens*. PhD thesis, Universität Göttingen, 2011.
- [62] K. Giewekemeyer, M. Hantke, C. Beta, R. Tucoulou, and T. Salditt. Fluorescence imaging of *Dictyostelium discoideum* with a hard X-ray nanoprobe. *Journal of Physics: Conference Series*, 186:012086, 2009.

- [63] K. Giewekemeyer, S. P. Krüger, S. Kalbfleisch, M. Bartels, C. Beta, and T. Salditt. X-ray propagation microscopy of biological cells using waveguides as a quasipoint source. *Physical Review A*, 83:023804, 2011.
- [64] K. Giewekemeyer, H. Neubauer, S. Kalbfleisch, S. P. Krüger, and T. Salditt. Holographic and diffractive x-ray imaging using waveguides as quasi-point sources. *New Journal of Physics*, 12:035008, 2010.
- [65] K. Giewekemeyer, P. Thibault, S. Kalbfleisch, A. Beerlink, C. M. Kewish, M. Dierolf, F. Pfeiffer, and T. Salditt. Quantitative biological imaging by ptychographic x-ray diffraction microscopy. *Proceedings of the National Academy of Sciences*, 107:529, 2010.
- [66] K. Giewekemeyer, R. Wilke, M. Osterhoff, M. Bartels, S. Kalbfleisch, and T. Salditt. Versatility of a hard X-ray Kirkpatrick-Baez focus characterized by ptychography. *Journal of Synchrotron Radiation*, 20:490, 2013.
- [67] R. Glueckert, H. Rask-Andersen, C. Sergi, J. Schmutzhard, B. Müller, B., F. Beckmann, O. Rittinger, L. H. Hoefsloot, A. Schrott-Fischer, and A. R. Janecke. Histology and synchrotron radiation-based microtomography of the inner ear in a molecularly confirmed case of CHARGE syndrome. *American Journal of Medical Genetics*, 152A:665, 2010.
- [68] J. W. Goodman. *Introduction to Fourier Optics*. Roberts & Company Publishers, Greenwood Village, CO, third edition, 2005.
- [69] U. Gopala Rao and V. Jain. Gaussian and Exponential Approximations of the Modulation Transfer Function. *Journal of the Optical Society of America*, 57:1159, 1967.
- [70] A. Groso, R. Abela, and M. Stampanoni. Implementation of a fast method for high resolution phase contrast tomography. *Optics Express*, 14:8103, 2006.
- [71] A. Groso, M. Stampanoni, R. Abela, P. Schneider, S. Linga, and R. Müller. Phase contrast tomography: An alternative approach. *Applied Physics Letters*, 88:214104, 2006.
- [72] J. Guigay. Fourier transform analysis of Fresnel diffraction pattern and inline holograms. *Optik (Stuttgart)*, 46:121, 1977.
- [73] J. P. Guigay, M. Langer, R. Boistel, and P. Cloetens. Mixed transfer function and transport of intensity approach for Phase retrieval in the Fresnel region. *Optics Letters*, 32:1617, 2007.
- [74] M. Guizar-Sicairos, S. T. Thurman, and J. R. Fienup. Efficient subpixel image registration algorithms. *Optics Letters*, 33:156, 2008.
- [75] T. Gureyev and S. Wilkins. On X-ray phase retrieval from polychromatic images. *Optics Communications*, 147:229, 1998.

- [76] T. E. Gureyev. Composite techniques for phase retrieval in the Fresnel region. *Optics Communications*, 220:49, 2003.
- [77] T. E. Gureyev, T. J. Davis, A. Pogany, S. Mayo, and S. W. Wilkins. Optical phase retrieval by use of first Born- and Rytov-type approximations. *Applied Optics*, 43:2418, 2004.
- [78] T. E. Gureyev, Y. I. Nesterets, A. W. Stevenson, P. R. Miller, A. Pogany, and S. W. Wilkins. Some simple rules for contrast, signal-to-noise and resolution in in-line x-ray phase-contrast imaging. *Optics Express*, 16:3223, 2008.
- [79] T. E. Gureyev, D. M. Paganin, G. R. Myers, Y. I. Nesterets, and S. W. Wilkins. Phase-and-amplitude computer tomography. *Applied Physics Letters*, 89:034102, 2006.
- [80] T. E. Gureyev, A. Pogany, D. M. Paganin, and S. W. Wilkins. Linear algorithms for phase retrieval in the Fresnel region. *Optics Communications*, 231:53, 2004.
- [81] T. E. Gureyev, C. Raven, A. Snigirev, I. Snigireva, and S. W. Wilkins. Hard x-ray quantitative non-interferometric phase-contrast microscopy. *Journal of Physics D: Applied Physics*, 32:563, 1999.
- [82] T. E. Gureyev, A. Roberts, and K. A. Nugent. Partially coherent fields, the transport-of-intensity equation, and phase uniqueness. *Journal of the Optical Society of America A*, 12:1942, 1995.
- [83] T. E. Gureyev, A. Roberts, and K. A. Nugent. Phase retrieval with the transport-of-intensity equation: matrix solution with use of Zernike polynomials. *Journal of the Optical Society of America A*, 12:1932, 1995.
- [84] T. E. Gureyev and S. W. Wilkins. On x-ray phase imaging with a point source. *Journal of the Optical Society of America A*, 15:579, 1998.
- [85] J. Haber. Herstellung und Charakterisierung optimierter lithographischer Röntgenwellenleiter: Die Verbesserung des Wafer-Bondings bei der Herstellung lithographischer Röntgenwellenleiter. Master's thesis, Universität Göttingen, 2013.
- [86] S. Hall and P. Williams. Studies on the "incisures" of Schmidt and Lanterman. *Journal of Cell Science*, 6:767, 1970.
- [87] O. Hemberg, M. Otendal, and H. M. Hertz. Liquid-metal-jet anode electron-impact x-ray source. *Applied Physics Letters*, 83:1483, 2003.
- [88] R. Henderson. The potential and limitations of neutrons, electrons and X-rays for atomic resolution microscopy of unstained biological molecules. *Quarterly Reviews of Biophysics*, 28:171, 1995.

- [89] B. Henke, E. Gullikson, and J. Davis. X-ray interactions: photoabsorption, scattering, transmission, and reflection at  $E=50\text{-}30000$  eV,  $Z=1\text{-}92$ . *Atomic Data and Nuclear Data Tables*, 54:181, 1993.
- [90] V. H. Hernandez, K. Reuter, Z. Jing, A. M. Schulz, G. Hoch, M. Bartels, H. Yawo, Y. Fukazawa, G. J. Augustine, E. Bamberg, S. Kügler, T. Salditt, N. Strenzke, and T. Moser. Optogenetic stimulation of the auditory pathway. *unpublished manuscript*.
- [91] M. R. Hestenes and E. Stiefel. Methods of Conjugate Gradients for Solving Linear Systems. *Journal of Research of the National Bureau of Standards*, 49:409, 1952.
- [92] O. Hignette, P. Cloetens, C. Morawe, C. Borel, W. Ludwig, P. Bernard, A. Rommeveaux, and S. Bohic. Nanofocusing at ESRF Using Graded Multilayer Mirrors. *AIP Conference Proceedings*, 879:792, 2007.
- [93] O. Hignette, P. Cloetens, G. Rostaing, P. Bernard, and C. Morawe. Efficient sub 100 nm focusing of hard x rays. *Review of Scientific Instruments*, 76:063709, 2005.
- [94] T. Hohage and F. Werner. Iteratively regularized Newton-type methods for general data misfit functionals and application to Poisson data. *Numerische Mathematik*, 123:754, 2013.
- [95] D. Holdsworth and M. M. Thornton. Micro-CT in small animal and specimen imaging. *Trends in Biotechnology*, 20:S34, 2002.
- [96] G. N. Hounsfield. Computerized transverse axial scanning (tomography): Part 1. Description of system. *British Journal of Radiology*, 46:1016, 1973.
- [97] M. Howells, T. Beetz, H. Chapman, C. Cui, J. Holton, C. Jacobsen, J. Kirz, E. Lima, S. Marchesini, H. Miao, D. Sayre, D. Shapiro, J. Spence, and D. Starodub. An assessment of the resolution limitation due to radiation-damage in X-ray diffraction microscopy. *Journal of Electron Spectroscopy and Related Phenomena*, 170:4, 2009.
- [98] B. Huang. Super-resolution optical microscopy: multiple choices. *Current Opinion in Chemical Biology*, 14:10, 2010.
- [99] X. Huang, H. Miao, J. Steinbrener, J. Nelson, D. Shapiro, A. Stewart, J. Turner, and C. Jacobsen. Signal-to-noise and radiation exposure considerations in conventional and diffraction x-ray microscopy. *Optics Express*, 17:13541, 2009.
- [100] X. Huang, J. Nelson, J. Kirz, E. Lima, S. Marchesini, H. Miao, A. M. Neiman, D. Shapiro, J. Steinbrener, A. Stewart, J. J. Turner, and C. Jacobsen. Soft X-Ray Diffraction Microscopy of a Frozen Hydrated Yeast Cell. *Physical Review Letters*, 103:198101, 2009.

- [101] A. Jarre, C. Fuhse, C. Ollinger, J. Seeger, R. Tucoulou, and T. Salditt. Two-Dimensional Hard X-Ray Beam Compression by Combined Focusing and Waveguide Optics. *Physical Review Letters*, 94:074801, 2005.
- [102] H. Jiang, C. Song, C.-C. Chen, R. Xu, K. S. Raines, B. P. Fahimian, C.-H. Lu, T.-K. Lee, A. Nakashima, J. Urano, T. Ishikawa, F. Tamanoi, and J. Miao. Quantitative 3D imaging of whole, unstained cells by using X-ray diffraction microscopy. *Proceedings of the National Academy of Sciences*, 107:11234, 2010.
- [103] A. C. Kak and M. Slaney. *Principles of computerized tomographic imaging*. IEEE Press, New York, New York, 1988.
- [104] S. Kalbfleisch. *A Dedicated Endstation for Waveguide-based X-Ray Imaging*. PhD thesis, Universität Göttingen, 2012.
- [105] S. Kalbfleisch, H. Neubauer, S. P. Krüger, M. Bartels, M. Osterhoff, D. D. Mai, K. Giewekemeyer, B. Hartmann, M. Sprung, and T. Salditt. The Göttingen Holography Endstation of Beamline P10 at PETRA III/DESY. *AIP Conference Proceedings*, 1365:96, 2011.
- [106] S. Kalbfleisch, M. Osterhoff, K. Giewekemeyer, H. Neubauer, S. P. Krüger, B. Hartmann, M. Bartels, M. Sprung, O. Leupold, F. Siewert, and T. Salditt. The holography endstation of beamline P10 at PETRA III. *AIP Conference Proceedings*, 1234:433, 2010.
- [107] B. Kaltenbacher, A. Neubauer, and O. Scherzer. *Iterative Regularization Methods for Nonlinear Ill-Posed Problems, Radon Series on Computational and Applied Mathematics 6*. de Gruyter, Berlin, 2008.
- [108] U. Karlsson and R. Schultz. Fixation of the Central Nervous System from Electron Microscopy by Aldehyde Perfusion. I. Preservation with Aldehyde Perfusates Versus Direct Perfusion with Osmium Tetroxide with Special Reference to Membranes and the Extracellular Space. *Journal of Ultrastructure Research*, 12:160, 1965.
- [109] R. H. Kessin. *Dictyostelium - Evolution, cell Biology, and the Development of Multicellularity*. Cambridge Univ. Press, Cambridge, 2001.
- [110] P. Kirkpatrick and A. V. Baez. Formation of Optical Images by X-Rays. *Journal of the Optical Society of America*, 38:766, 1948.
- [111] J. Kmetko, N. S. Husseini, M. Naides, Y. Kalinin, and R. E. Thorne. Quantifying X-ray radiation damage in protein crystals at cryogenic temperatures. *Acta Crystallographica Section D*, 62:1030, 2006.
- [112] G. Knott, H. Marchman, D. Wall, and B. Lich. Serial Section Scanning Electron Microscopy of Adult Brain Tissue Using Focused Ion Beam Milling. *The Journal of Neuroscience*, 28:2959, 2008.

- [113] A. Kohlstedt, S. Kalbfleisch, T. Salditt, M. Reiche, U. Gösele, E. Lima, and P. Willmot. Two-dimensional X-ray waveguides: fabrication by wafer-bonding process and characterization. *Applied Physics A: Materials Science & Processing*, 91:7, 2008.
- [114] E. Kosior, S. Bohic, H. Suhonen, R. Ortega, G. Deves, A. Carmona, F. Marchi, J. Guillet, and P. Cloetens. Combined use of hard X-ray phase contrast imaging and X-ray fluorescence microscopy for sub-cellular metal quantification. *Journal of Structural Biology*, 177:239, 2012.
- [115] C. Kottler, F. Pfeiffer, O. Bunk, C. Grünzweig, J. Bruder, R. Kaufmann, L. Tlustos, H. Walt, I. Briod, T. Weitkamp, and C. David. Phase contrast X-ray imaging of large samples using an incoherent laboratory source. *physica status solidi (a)*, 204:2728, 2007.
- [116] M. Krenkel. Quantitative Phasenkontrast-Mikrotomographie. Master's thesis, Universität Göttingen, 2012.
- [117] M. Krenkel, M. Bartels, and T. Salditt. Transport of intensity phase reconstruction to solve the twin image problem in holographic x-ray imaging. *Optics Express*, 21:2220, 2013.
- [118] S. P. Krüger. *Optimization of waveguide optics for lensless x-ray imaging*. PhD thesis, Universität Göttingen, 2010.
- [119] S. P. Krüger, K. Giewekemeyer, S. Kalbfleisch, M. Bartels, H. Neubauer, and T. Salditt. Sub-15 nm beam confinement by twocrossed x-ray waveguides. *Optics Express*, 18:13492, 2010.
- [120] S. P. Krüger, H. Neubauer, M. Bartels, S. Kalbfleisch, K. Giewekemeyer, P. J. Wilbrandt, M. Sprung, and T. Salditt. Sub-10 nm beam confinement by X-ray waveguides: design, fabrication and characterization of optical properties. *Journal of Synchrotron Radiation*, 19:227, 2012.
- [121] J. C. Labiche, J. Segura-Purchades, D. Brussel, and J. P.Moy. FRELON camera: FastReadLowNoise. *ESRF NewsLetter*, 25:41, 1996.
- [122] S. Lagomarsino, A. Cedola, P. Cloetens, S. Di Fonzo, W. Jark, G. Soullie, and C. Riekel. Phase contrast hard x-ray microscopy with submicron resolution. *Applied Physics Letters*, 71:2557, 1997.
- [123] M. Langer. Quantitative comparison of direct phase retrieval algorithms in in-line phase tomography. *Medical Physics*, 35:4556, 2008.
- [124] M. Langer, P. Cloetens, A. Pacureanu, and F. Peyrin. X-ray in-line phase tomography of multimaterial objects. *Optics Letters*, 37:2151, 2012.
- [125] M. Langer, P. Cloetens, and F. Peyrin. Regularization of Phase Retrieval With Phase-Attenuation Duality Prior for 3-D Holotomography. *IEEE Transactions on Image Processing*, 19:2428, 2010.



- [126] M. Langer, A. Pacureanu, H. Suhonen, Q. Grimal, P. Cloetens, and F. Peyrin. X-Ray Phase Nanotomography Resolves the 3D Human Bone Ultrastructure. *PLoS ONE*, 7:e35691, 2012.
- [127] A. Lareida, F. Beckmann, A. Schrott-Fischer, R. Glueckert, W. Freysinger, and B. Müller. High-resolution X-ray tomography of the human inner ear: synchrotron radiation-based study of nerve fibre bundles, membranes and ganglion cells. *Journal of Microscopy*, 234:95, 2009.
- [128] D. H. Larsson, P. A. C. Takman, U. Lundstrom, A. Burvall, and H. M. Hertz. A 24 keV liquid-metal-jet x-ray source for biomedical applications. *Review of Scientific Instruments*, 82:123701, 2011.
- [129] C.-F. Lee, G.-J. Li, S.-Y. Wan, W.-J. Lee, K.-Y. Tzen, C.-H. Chen, Y.-L. Song, Y.-F. Chou, Y.-S. Chen, and T.-C. Liu. Registration of Micro-Computed Tomography and Histological Images of the Guinea Pig Cochlea to Construct an Ear Model Using an Iterative Closest Point Algorithm. *Annals of Biomedical Engineering*, 38:1719, 2010.
- [130] S. Levin-Zaidman, J. Englander, E. Shimoni, A. K. Sharma, and K. W. Minton. Ringlike Structure of the *Deinococcus radiodurans* Genome: A Key to Radioresistance? *Science*, 299:254, 2003.
- [131] E. Lima, L. Wiegart, P. Pernot, M. Howells, J. Timmins, F. Zontone, and A. Madsen. Cryogenic X-Ray Diffraction Microscopy for Biological Samples. *Physical Review Letters*, 103:198102, 2009.
- [132] U. Lundström, D. H. Larsson, A. Burvall, L. Scott, U. K. Westermark, M. Wilhelm, M. A. Henriksson, and H. M. Hertz. X-ray phase-contrast CO<sub>2</sub> angiography for sub-10  $\mu\text{m}$  vessel imaging. *Physics in Medicine and Biology*, 57:7431, 2012.
- [133] A. M. Maiden and J. M. Rodenburg. An improved ptychographical phase retrieval algorithm for diffractive imaging. *Ultramicroscopy*, 109:1256, 2009.
- [134] S. Marchesini. Invited Article: A unified evaluation of iterative projection algorithms for phase retrieval. *Review of Scientific Instruments*, 78:011301, 2007.
- [135] S. Marchesini, H. He, H. N. Chapman, S. P. Hau-Riege, A. Noy, M. R. Howells, U. Weierstall, and J. C. H. Spence. X-ray image reconstruction from a diffraction pattern alone. *Physical Review B*, 68:140101, 2003.
- [136] R. E. Martenson. *Myelin: biology and chemistry*. CRC Press, Boca Raton, FL, 1992.
- [137] G. Martínez-Criado, R. Tucoulou, P. Cloetens, P. Bleuet, S. Bohic, J. Cauzid, I. Kieffer, E. Kosior, S. Labouré, S. Petitgirard, A. Rack, J. A. Sans, J. Segura-Ruiz, H. Suhonen, J. Susini, and J. Villanova. Status of the hard

- X-ray microprobe beamline ID22 of the European Synchrotron Radiation Facility. *Journal of Synchrotron Radiation*, 19:10, 2012.
- [138] S. Mayo, T. Davis, T. Gureyev, P. Miller, D. Paganin, A. Pogany, A. Stevenson, and S. Wilkins. X-ray phase-contrast microscopy and microtomography. *Optics Express*, 11:2289, 2003.
- [139] S. Mayo, P. Miller, S. Wilkins, T. Davis, D. Gao, T. Gureyev, D. Paganin, D. Parry, A. Pogany, and A. Stevenson. Quantitative X-ray projection microscopy: phase-contrast and multi-spectral imaging. *Journal of Microscopy*, 207:79, 2002.
- [140] W. Möbius, B. Cooper, W. Kaufmann, C. Imig, T. Ruhwedel, N. Snaidero, A. Saab, and F. Varoquaux. Electron microscopy of the mouse central nervous system. *Methods in Cell Biology*, 96:475, 2010.
- [141] J. Miao, P. Charalambous, J. Kirz, and D. Sayre. Extending the methodology of X-ray crystallography to allow imaging of micrometre-sized non-crystalline specimens. *Nature*, 400:342, 1999.
- [142] S. Mikula, J. Binding, and W. Denk. Staining and embedding the whole mouse brain for electron microscopy. *Nature Methods*, 9:1198, 2012.
- [143] H. Mimura, S. Handa, T. Kimura, H. Yumoto, D. Yamakawa, H. Yokoyama, S. Matsuyama, K. Inagaki, K. Yamamura, Y. Sano, K. Tamasaku, Y. Nishino, M. Yabashi, T. Ishikawa, and K. Yamauchi. Breaking the 10 nm barrier in hard-X-ray focusing. *Nature Physics*, 6:122, 2010.
- [144] A. Minsky, E. Shimoni, and J. Englander. Study of the *Deinococcus radiodurans* Nucleoid. *Journal of Bacteriology*, 188:6059, 2006.
- [145] R. Mokso, E. Cloetens, P. and Maire, W. Ludwig, and J. Buffiere. Nanoscale zoom tomography with hard x rays using Kirkpatrick-Baez optics. *Applied Physics Letters*, 90:144104, 2007.
- [146] A. Momose. Recent Advances in X-ray Phase Imaging. *Japanese Journal of Applied Physics*, 44:6355, 2005.
- [147] A. Momose and J. Fukada. Phase-contrast radiographs of nonstained rat cerebellar specimen. *Medical Physics*, 22:375, 1995.
- [148] C. Morawe, O. Hignette, P. Cloetens, W. Ludwig, C. Borel, P. Bernard, and A. Rommeveaux. Graded multilayers for focusing hard x rays below 50nm. *Proceedings of the SPIE*, 6317:63170, 2006.
- [149] C. Nave. Radiation damage in protein crystallography. *Radiation Physics and Chemistry*, 45:483, 1995.

- [150] P. D. Nellist and J. M. Rodenburg. Electron Ptychography. I. Experimental Demonstration Beyond the Conventional Resolution Limits. *Acta Crystallographica Section A*, 54:49, 1998.
- [151] Y. I. Nesterets, S. W. Wilkins, T. E. Gureyev, A. Pogany, and A. W. Stevenson. On the optimization of experimental parameters for x-ray in-line phase-contrast imaging. *Review of Scientific Instruments*, 76:093706, 2005.
- [152] H. Neubauer. *Ein Verfahren zur Herstellung zweidimensionaler Röntgenwellenleiter*. PhD thesis, Universität Göttingen, 2012.
- [153] Y. Nishino, Y. Takahashi, N. Imamoto, T. Ishikawa, and K. Maeshima. Three-Dimensional Visualization of a Human Chromosome Using Coherent X-Ray Diffraction. *Physical Review Letters*, 102:018101, 2009.
- [154] N.N. GPUMat: GPU toolbox for MATLAB.  
<http://sourceforge.net/projects/gpumat/>.
- [155] N.N. LCX datasheet.  
[http://www.princetoninstruments.com/Uploads/Princeton/Documents/Datasheets/Princeton\\_Instruments\\_PI\\_LCX\\_1300\\_Rev\\_C1.pdf](http://www.princetoninstruments.com/Uploads/Princeton/Documents/Datasheets/Princeton_Instruments_PI_LCX_1300_Rev_C1.pdf).
- [156] K. A. Nugent. Coherent methods in the X-ray sciences. *Advances in Physics*, 59:1, 2010.
- [157] K. A. Nugent, T. E. Gureyev, D. F. Cookson, D. M. Paganin, and Z. Barnea. Quantitative Phase Imaging Using Hard X Rays. *Physical Review Letters*, 77:2961, 1996.
- [158] C. Olendrowitz, M. Bartels, M. Krenkel, A. Beerlink, R. Mokso, M. Sprung, and T. Salditt. Phase-contrast x-ray imaging and tomography of the nematode *Caenorhabditis elegans*. *Physics in Medicine and Biology*, 57:5309, 2012.
- [159] C. Ollinger, C. Fuhse, S. Kalbfleisch, R. Tucoulou, and T. Salditt. Object localization with 10 nm accuracy by x-ray phase contrast projection imaging. *Applied Physics Letters*, 91:051110, 2007.
- [160] M. Osterhoff and T. Salditt. Real structure effects in X-ray waveguide optics: The influence of interfacial roughness and refractive index profile on the near-field and far-field distribution. *Optics Communications*, 282:3250, 2009.
- [161] M. Osterhoff and T. Salditt. Coherence filtering of x-ray waveguides: analytical and numerical approach. *New Journal of Physics*, 13:103026, 2011.
- [162] M. Otendal, T. Tuohimaa, U. Vogt, and H. M. Hertz. A 9 keV electron-impact liquid-gallium-jet x-ray source. *Review of Scientific Instruments*, 79:016102, 2008.

- [163] D. Paganin, S. Mayo, T. Gureyev, P. Miller, and S. Wilkins. Simultaneous phase and amplitude extraction from a single defocused image of a homogeneous object. *Journal of Microscopy*, 206:33, 2002.
- [164] D. M. Paganin. *Coherent X-Ray Optics*. Oxford Univ. Press, Oxford, 2006.
- [165] D. M. Paganin and K. A. Nugent. Noninterferometric Phase Imaging with Partially Coherent Light. *Physical Review Letters*, 80:2586, 1998.
- [166] D. Parker. Optimal short scan convolution reconstruction for fanbeam CT. *Med. Phys. Medical Physics*, 9:254, 1982.
- [167] G. H. Patterson. Fluorescence microscopy below the diffraction limit. *Seminars in Cell & Developmental Biology*, 20:886, 2009.
- [168] F. Pfeifer, O. Bunk, C. David, M. Bech, G. Le Duc, A. Bravin, and P. Cloetens. High-resolution brain tumor visualization using three-dimensional x-ray phase contrast tomography. *Physics in Medicine and Biology*, 52:6923, 2007.
- [169] F. Pfeiffer, C. Kottler, O. Bunk, and C. David. Hard X-Ray Phase Tomography with Low-Brilliance Sources. *Physical Review Letters*, 98:108105, 2007.
- [170] F. Pfeiffer, T. Weitkamp, O. Bunk, and C. David. Phase retrieval and differential phase-contrast imaging with low-brilliance X-ray sources. *Nature Physics*, 2:258, 2006.
- [171] A. Pogany, D. Gao, and S. W. Wilkins. Contrast and resolution in imaging with a microfocus x-ray source. *Review of Scientific Instruments*, 68:2774, 1997.
- [172] C. Ponchut, J. Clément, J.-M. Rigal, E. Papillon, J. Vallerger, D. LaMarra, and B. Mikulec. Photon-counting X-ray imaging at kilohertz frame rates. *Nuclear Instruments and Methods in Physics Research Section A: Accelerators, Spectrometers, Detectors and Associated Equipment*, 576:109, 2007.
- [173] C. Ponchut, J. M. Rigal, J. Clément, E. Papillon, A. Homs, and S. Petitdemange. MAXIPIX, a fast readout photon-counting X-ray area detector for synchrotron applications. *Journal of Instrumentation*, 6:C01069, 2011.
- [174] M. Poulsen, F. Jensen, O. Bunk, R. Feidenhans'l, and D. W. Breiby. Silicon waveguides produced by wafer bonding. *Applied Physics Letters*, 87:261904, 2005.
- [175] J. Radon. Über die Bestimmung von Funktionen durch ihre Integralwerte längs gewisser Mannigfaltigkeiten. *Berichte über die Verhandlungen der Königlich-Sächsischen Akademie der Wissenschaften zu Leipzig, Mathematisch-Physische Klasse*, 69:262, 1917.

- [176] C. Rau, M. Hwang, W.-K. Lee, and C.-P. Richter. Quantitative X-ray Tomography of the Mouse Cochlea. *PLoS ONE*, 7:e33568, 2012.
- [177] C. Rau, I. Robinson, and C.-P. Richter. Visualizing soft tissue in the mammalian cochlea with coherent hard x-rays. *Microscopy Research and Technique*, 69:660, 2006.
- [178] E. Reynolds. The use of lead citrate at high pH as an electron-opaque stain in electron microscopy. *The Journal of Cell Biology*, 17:208, 1963.
- [179] K. Richardson, L. Jarett, and E. Finke. Embedding in epoxy resins for ultrathin sectioning in electron microscopy. *Stain Technology*, 35:313, 1960.
- [180] C.-P. Richter, S. Shintani-Smith, A. Fishman, C. David, I. Robinson, and C. Rau. Imaging of cochlear tissue with a grating interferometer and hard X-rays. *Microscopy Research and Technique*, 72:902, 2009.
- [181] J. Rodenburg. Ptychography and Related Diffractive Imaging Methods. *Advances in Imaging and Electron Physics*, Volume 150:87, 2008.
- [182] J. M. Rodenburg and H. M. L. Faulkner. A phase retrieval algorithm for shifting illumination. *Applied Physics Letters*, 85:4795, 2004.
- [183] A. Ruhlandt, T. Liese, V. Radisch, S. P. Krüger, M. Osterhoff, K. Giewekemeyer, H. U. Krebs, and T. Salditt. A combined Kirkpatrick-Baez mirror and multilayer lens for sub-10 nm x-ray focusing. *AIP Advances*, 2:012175, 2012.
- [184] T. Salditt, K. Giewekemeyer, C. Fuhse, S. P. Krüger, R. Tucoulou, and P. Cloetens. Projection phase contrast microscopy with a hard x-ray nanofocused beam: Defocus and contrast transfer. *Physical Review B*, 79:184112, 2009.
- [185] T. Salditt, S. Kalbfleisch, M. Osterhoff, S. P. Krüger, M. Bartels, K. Giewekemeyer, H. Neubauer, and M. Sprung. Partially coherent nano-focused x-ray radiation characterized by Talbot interferometry. *Optics Express*, 19:9656, 2011.
- [186] T. Salditt, S. P. Krüger, C. Fuhse, and C. Bahtz. High-Transmission Planar X-Ray Waveguides. *Physical Review Letters*, 100:184801, 2008.
- [187] B. E. A. Saleh and M. C. Teich. *Fundamentals of Photonics*. John Wiley & Sons, Hoboken, NJ, 1991.
- [188] G. Schulz, T. Weitkamp, I. Zanette, F. Pfeiffer, B. F., D. C., S. Rutishauser, E. Reznikova, and B. Müller. High-resolution tomographic imaging of a human cerebellum: comparison of absorption and grating-based phase contrast. *Journal of the Royal Society Interface*, 7:1665, 2010.

- [189] D. Shapiro, P. Thibault, T. Beetz, V. Elser, M. Howells, C. Jacobsen, J. Kirz, E. Lima, H. Miao, A. M. Neiman, and D. Sayre. Biological imaging by soft x-ray diffraction microscopy. *Proceedings of the National Academy of Sciences*, 102:15343, 2005.
- [190] Q. Shen, I. Bazarov, and P. Thibault. Diffractive imaging of nonperiodic materials with future coherent x-ray sources. *Journal of Synchrotron Radiation*, 11:432, 2004.
- [191] B. Sixou, V. Davidoui, M. Langer, and F. Peyrin. Absorption And Phase Retrieval With Tikhonov And Joint Sparsity Regularizations. *Inverse Problems And Imaging*, 7:267, 2013.
- [192] S. W. Smith. *The Scientist & Engineer's Guide to Digital Signal Processing*. California Technical Publishing, San Diego, CA, 1997.
- [193] A. Snigirev, I. Snigireva, V. Kohn, S. Kuznetsov, and I. Schelokov. On the possibilities of x-ray phase contrast microimaging by coherent high-energy synchrotron radiation. *Review of Scientific Instruments*, 66:5486, 1995.
- [194] A. Somogyi, R. Tucoulou, G. Martinez-Criado, A. Homs, J. Cauzid, B. P., S. Bohic, and A. Simionovicia. ID22: a multitechnique hard X-ray microprobe beamline at the European Synchrotron Radiation Facility. *Journal of Synchrotron Radiation*, 12:208, 2005.
- [195] C. Song, H. Jiang, A. Mancuso, B. Amirbekian, L. Peng, R. Sun, S. S. Shah, Z. H. Zhou, T. Ishikawa, and J. Miao. Quantitative Imaging of Single, Unstained Viruses with Coherent X Rays. *Physical Review Letters*, 101:158101, 2008.
- [196] Y. Takahashi, A. Suzuki, N. Zettsu, Y. Kohmura, Y. Senba, H. Ohashi, K. Yamauchi, and T. Ishikawa. Towards high-resolution ptychographic x-ray diffraction microscopy. *Physical Review B*, 83:214109, 2011.
- [197] A. Tapfer, M. Bech, A. Velroyen, J. Meiser, J. Mohr, M. Walter, J. Schulz, B. Pauwels, P. Bruyndonckx, X. Liu, A. Sasov, and F. Pfeiffer. Experimental results from a preclinical X-ray phase-contrast CT scanner. *Proceedings of the National Academy of Sciences*, 109:15691, 2012.
- [198] M. R. Teague. Irradiance moments: their propagation and use for unique retrieval of phase. *Journal of the Optical Society of America*, 72:9, 1982.
- [199] M. R. Teague. Deterministic phase retrieval: a Green's function solution. *Journal of the Optical Society of America*, 73:1434, 1983.
- [200] P. Thibault. *Algorithmic methods in diffraction microscopy*. PhD thesis, University Microfilms International, Ann Arbor, Mich., 2008.

- [201] P. Thibault, M. Dierolf, O. Bunk, A. Menzel, and F. Pfeiffer. Probe retrieval in ptychographic coherent diffractive imaging. *Ultramicroscopy*, 109:338, 2009.
- [202] M. Thorne, A. N. Salt, J. E. DeMott, M. M. Henson, O. W. Henson, and S. L. Gewalt. Cochlear Fluid Space Dimensions for Six Species Derived From Reconstructions of Three-Dimensional Magnetic Resonance Images. *Laryngoscope*, 109:1661, 1999.
- [203] A. N. Tikhonov and V. Y. Arsenin. *Solution of Ill-posed Problems*. Winston & Sons, Washington, 1977.
- [204] J. B. Tiller, A. Barty, D. Paganin, and K. A. Nugent. The holographic twin image problem: a deterministic phase solution. *Optics Communication*, 183:7, 2000.
- [205] H. Toyokawa, C. Broennimann, E. Eikenberry, B. Henrich, M. Kawase, M. Kobas, P. Kraft, M. Sato, B. Schmitt, M. Suzuki, H. Tanida, and T. Uruga. Single photon counting pixel detectors for synchrotron radiation experiments. *Nuclear Instruments and Methods in Physics Research Section A: Accelerators, Spectrometers, Detectors and Associated Equipment*, 623:204, 2010.
- [206] R. Tucoulou, Martinez-Criado, P. G. Bleuet, I. Kieffer, P. Cloetens, S. Labouré, T. Martin, C. Guilloud, and J. Susini. High-resolution angular beam stability monitoring at a nanofocusing beamline. *Journal of Synchrotron Radiation*, 15:392, 2008.
- [207] L. Turner, B. Dhal, J. Hayes, A. Mancuso, K. Nugent, D. Paterson, R. Scholten, C. Tran, and A. Peele. X-ray phase imaging: Demonstration of extended conditions for homogeneous objects. *Optics Express*, 12:2960, 2004.
- [208] H. Tuy. An inversion formula for cone-beam reconstruction. *SIAM Journal on Applied Mathematics*, 43:546, 1983.
- [209] I. Vartanyants and I. Robinson. Partial coherence effects on the imaging of small crystals using coherent x-ray diffraction. *Journal of Physics: Condensed Matter*, 13:10593, 2001.
- [210] D. G. Voelz and M. C. Roggemann. Digital simulation of scalar optical diffraction: revisiting chirp function sampling criteria and consequences. *Applied Optics*, 48:6132, 2009.
- [211] P. Vogel. *Systemtheorie ohne Ballast*. Springer, Berlin, 2011.
- [212] U. Vogel. New approach for 3D imaging and geometry modeling of the human inner ear. *ORL: Journal for Oto-Rhino-Laryngology and its Related Specialties*, 61:259, 1999.

- [213] A. H. Voie. Imaging the intact guinea pig tympanic bulla by orthogonal-plane fluorescence optical sectioning microscopy. *Hearing Research*, 171:119, 2002.
- [214] S. Waxman. Determinants of conduction velocity in myelinated nerve fibers. *Muscle & Nerve*, 3:141, 1980.
- [215] T. Weitkamp, A. Diaz, C. David, F. Pfeiffer, M. Stampanoni, P. Cloetens, and E. Ziegler. X-ray phase imaging with a grating interferometer. *Optics Express*, 13:6296, 2005.
- [216] R. N. Wilke, M. Priebe, M. Bartels, K. Giewekemeyer, A. Diaz, P. Karvinen, and T. Salditt. Hard X-ray imaging of bacterial cells: nano-diffraction and ptychographic reconstruction. *Optics Express*, 20:19232, 2012.
- [217] R. N. Wilke, M. Vassholz, and T. Salditt. Enhancement of Dynamic Range in Ptychography by Use of KB Focusing and Semi-Transparent Central Stop. *submitted manuscript*.
- [218] S. W. Wilkins, T. E. Gureyev, D. Gao, A. Pogany, and A. W. Stevenson. Phase-contrast imaging using polychromatic hard X-rays. *Nature*, 384:335, 1996.
- [219] Y. D. Witte, M. Boone, J. Vlassenbroeck, M. Dierick, and L. V. Hoorebeke. Bronnikov-aided correction for x-ray computed tomography. *Journal of the Optical Society of America A*, 26:890, 2009.
- [220] B. J. F. Wong, J. F. de Boer, B. H. Park, Z. Chen, and J. S. Nelson. Optical coherence tomography of the rat cochlea. *Journal of Biomedical Optics*, 5:367, 2000.
- [221] L. M. N. Wu, A. Williams, A. Delaney, D. Sherman, and P. Brophy. Increasing Internodal Distance in Myelinated Nerves Accelerates Nerve Conduction to a Flat Maximum. *Current Biology*, 20:1957, 2012.
- [222] S. Zabler, P. Cloetens, J. Guigay, and J. Baruchel. Optimization of phase contrast imaging using hard x-rays. *Review of Scientific Instruments*, 76:073705, 2005.
- [223] F. Zernike. The concept of degree of coherence and its application to optical problems. *Physica*, 5:785, 1938.
- [224] L. Zhang, R. Baker, R. Barrett, P. Cloetens, and Y. Dabin. Mirror profile optimization for nanofocusing KB mirror. *AIP Conference Proceedings*, 1234:801, 2010.
- [225] A. Zozulya, S. Bondarenko, and M. Sprung. *P10 Coherence Beamline User Guide*. PETRA III at DESY, Hamburg, 2012.



- [226] A. V. Zozulya, S. Bondarenko, A. Schavkan, F. Westermeier, G. Grübel, and M. Sprung. Microfocusing transfocator for 1D and 2D compound refractive lenses. *Optics Express*, 20:18967, 2012.



## List of Publications

- S. Kalbfleisch, M. Osterhoff, K. Giewekemeyer, H. Neubauer, S. P. Krüger, B. Hartmann, M. Bartels, M. Sprung, O. Leupold, F. Siewert, and T. Salditt. The holography endstation of beamline P10 at PETRA III. *AIP Conference Proceedings*, 1234:433, 2010.
- S. P. Krüger, K. Giewekemeyer, S. Kalbfleisch, M. Bartels, H. Neubauer, and T. Salditt Sub-15 nm beam confinement by two crossed x-ray waveguides. *Optics Express*, 18:13492, 2010.
- S. Kalbfleisch, H. Neubauer, S. P. Krüger, M. Bartels, M. Osterhoff, D. D. Mai, K. Giewekemeyer, B. Hartmann, M. Sprung and T. Salditt. The Göttingen Holography Endstation of Beamline P10 at PETRA III/DESY. *AIP Conference Proceedings*, 1365:96, 2011.
- T. Salditt, S. Kalbfleisch, M. Osterhoff, S. P. Krüger, M. Bartels, K. Giewekemeyer, H. Neubauer, and M. Sprung. Partially coherent nano-focused x-ray radiation characterized by Talbot interferometry. *Optics Express*, 19:9656, 2011.
- K. Giewekemeyer, S. P. Krüger, S. Kalbfleisch, M. Bartels, C. Beta, and T. Salditt X-ray propagation microscopy of biological cells using waveguides as a quasipoint source. *Physical Review A*, 83:0238041, 2011
- M. Bartels, M. Priebe, R. N. Wilke, S. P. Krüger, K. Giewekemeyer, S. Kalbfleisch, C. Olendrowitz, M. Sprung, and T. Salditt. Low-dose three-dimensional hard x-ray imaging of bacterial cells. *Optical Nanoscopy*, 1:10, 2012.
- C. Olendrowitz, M. Bartels, M. Krenkel, A. Beerlink, R. Mokso, M. Sprung, and T. Salditt. Phase-contrast x-ray imaging and tomography of the nematode *Caenorhabditis elegans*. *Physics in Medicine and Biology*, 57:5309, 2012.
- R. N. Wilke, M. Priebe, M. Bartels, K. Giewekemeyer, A. Diaz, P. Karvinen, and T. Salditt. Hard X-ray imaging of bacterial cells: nano-diffraction and ptychographic reconstruction. *Optics Express*, 20:19232,2012.

- A. Beerlink, S. Thutupalli, M. Mell, M. Bartels, P. Cloetens, S. Herminghaus, and T. Salditt. X-Ray propagation imaging of a lipid bilayer in solution. *Soft Matter*, 8:4595, 2012.
- S. P. Krüger, H. Neubauer, M. Bartels, S. Kalbfleisch, K. Giewekemeyer, P. J. Wilbrandt, M. Sprung, and T. Salditt. Sub-10 nm beam confinement by X-ray waveguides: design, fabrication and characterization of optical properties. *Journal of Synchrotron Radiation*, 19:227, 2012.
- K. Giewekemeyer, R.N. Wilke, M. Osterhoff, M. Bartels, S. Kalbfleisch, and T. Salditt. Versatility of a hard X-ray Kirkpatrick–Baez focus characterized by ptychography. *Journal of Synchrotron Radiation*, 20:490, 2013.
- M. Krenkel, M. Bartels, and T. Salditt. Transport-of-intensity phase reconstruction to solve the twin image problem in holographic x-ray imaging. *Optics Express*, 21:2220, 2013.
- F. Döring, A.L. Robisch, C. Eberl, M. Osterhoff, A. Ruhlandt, T. Liese, F. Schlenkrich, S. Hoffmann, M. Bartels, T. Salditt, and H.U. Krebs. Sub-5 nm hard x-ray point focusing by a combined Kirkpatrick-Baez mirror and multilayer zone plate. *Optics Express*, 21:19311, 2013.
- M. Bartels, V. H. Hernandez, T. Moser, and T. Salditt. Phase contrast tomography of mouse cochlea at microfocus x-ray sources. *Applied Physics Letters*, 103:083703, 2013.

## Danksagung

Ganz herzlich möchte ich mich bei Prof. Dr. Tim Salditt für die ausgezeichnete Betreuung bedanken. Seine stets positive Einstellung und sein Enthusiasmus haben mich sehr beeindruckt. Die Möglichkeit, seit Beginn meiner Diplomarbeit Messzeiten und instrumentelle Aufbauten mitgestalten zu dürfen, habe ich immer als besondere Freiheit empfunden. Für das uneingeschränkt entgegengebrachte Vertrauen möchte ich mich ausdrücklich bedanken. Besonders genossen habe ich auch die stets entspannte Atmosphäre während unzähliger Messzeiten. Fachliche Diskussionen, zahlreiche Erläuterungen und nicht zuletzt seine Begeisterung für die Themen dieser Arbeit, haben mich immer wieder entscheidend vorangebracht und motiviert.

Ich bedanke mich bei PD Dr. Timo Aspelmeier und bei Prof. Dr. Martin Müller für die Bereitschaft, meine Doktorarbeit zu korreferieren. Ich danke Prof. Dr. Sarah Köster für die Bereitschaft, dem Betreuungsausschuss sowie der Prüfungskommission beizutreten. Desweiteren möchte ich mich bei Prof. Dr. Tobias Moser, Prof. Dr. Thorsten Hohage und PD Dr. Simone Techert bedanken, die sich bereit erklärt haben, der Prüfungskommission beizutreten.

Die Ergebnisse dieser Arbeit waren nur auf Grund ausgezeichneten Teamworks und toller Kollaborationen möglich. Ein besonderer Dank gebührt Dr. Sebastian Kalbfleisch, der durch sein umfassendes Technikwissen und seine Faszination für SPEC-Automatisierung bei mir das Interesse für Synchrotroninstrumentierung geweckt hat. In ganz besonderem Umfang hat seine Arbeit an der Gestaltung und Umsetzung des GINIX-Messplatzes zum Erfolg dieser Arbeit beigetragen. Zahlreiche Diskussionen bezüglich der GINIX-Konfiguration und gemeinsame Verbesserungsarbeiten habe ich stets genossen. Dr. Sven Philip Krüger danke ich für seine Arbeit an Röntgenwellenleitern, die schlussendlich die Grundlage für den Großteil der Ergebnisse bilden als auch für seinen Einsatz bei Messzeiten. In besonderem Maße hat der unermüdliche Einsatz von Bastian Hartmann, seine Konstruktionsarbeit am GINIX-Messplatz sowie am JuLiA-Instrument und vor allem seine Flexibilität, unmittelbar vor einer Messzeit noch entscheidende Veränderungen umzusetzen, zum Erfolg dieser Arbeit beigetragen. Hierfür möchte ich mich ausdrücklich bedanken. Bei Martin Krenkel möchte ich mich recht herzlich bedanken für die aufschlussreichen Diskussionen, den Einsatz während Messzeiten als auch für die Bereitschaft, die Pflege und die anstehende Erweiterung des JuLiA Messplatzes zu übernehmen. Die gemeinsame Entwicklung und Verbesserung zahlreicher MATLAB Programme haben in entscheidender Weise die Qualität der Phasenrekonstruktionen verbessert. I would like to thank Dr. Victor Hernandez for a great collaboration regarding

the cochlea project. I enjoyed fruitful discussions and I am very thankful for the preparation of the cochlea samples. Prof. Dr. Tobias Moser danke ich ebenfalls herzlich für die Initiierung dieses Projektes und die gute Zusammenarbeit.

Ein besonderer Dank gebührt Dr. Wiebke Möbius für eine tolle und konstruktive Zusammenarbeit im Rahmen des Nerv-Projektes. Für ihre immerwährende Bereitschaft, geeignete Proben zu präparieren sowie für die Hilfe bei der Interpretation der Ergebnisse möchte ich mich hiermit ausdrücklich bedanken. In diesem Zusammenhang danke ich auch Torben Ruhwedel, Aiman Saab und allen Mitgliedern der Elektronenmikroskopieabteilung des Max-Planck-Instituts für Experimentelle Medizin in Göttingen.

Robin Wilke danke ich recht herzlich für die Präparation von *D. radiodurans* Zellen, seinen Einsatz bei Messzeiten und sehr aufschlussreiche fachliche Diskussionen. Marius Priebe danke ich für die Präparation von *D. radiodurans* und *D. discoideum* Zellen. Dr. Christian Olendrowitz danke ich für die tolle Zusammenarbeit und seinen unermüdlichen Einsatz bei Messzeiten. Henrike Neubauer und Johann Haber danke ich für die Herstellung der lithographischen Wellenleiter. Dr. Markus Osterhoff gebührt mein Dank für fachliche Gespräche und in besonderem Maße für seine technischen Verbesserungen, die er zum GINIX-Messplatz beigetragen hat, sowie für kompetente Hilfe bei allen IT-Fragen.

Ein besonderer Dank geht an Dr. Michael Sprung, Sergej Bondarenko, Dr. Fabian Westermeier und Dr. Alexey Zozulya für exzellente Bedingungen an der Beamline P10 sowie für eine immer konstruktive und angenehme Atmosphäre. Zahlreiche Vorschläge und Erläuterungen von Dr. Michael Sprung haben zu meinem Verständnis der Beamlinekomponenten maßgeblich beigetragen und den Verlauf von Experimenten nicht selten entscheidend beeinflusst. Weiterhin möchte ich mich für herausragenden Einsatz während der Messzeiten ausdrücklich bedanken.

Mein Dank geht an Prof. Dr. Thorsten Hohage und Kollegen für die Umsetzung und Bereitstellung des MATLAB Programms zur Gauss-Newton Rekonstruktion. In diesem Zusammenhang bedanke ich mich besonders bei Carolin Homann für ihre ausführlichen Erläuterungen. I would like to thank Dr. Peter Cloetens and Dr. Heikki Suhonen for outstanding support during the ID22NI beamtime. Dr. André Beerlink danke ich zunächst für die Konfiguration des PCO Detektors. Darüber hinaus habe ich die zahlreichen fachlichen und außerfachlichen Gespräche während meiner gesamten Studien- und Promotionszeit sowie gemeinsame Messzeiten immer sehr genossen. Dr. Klaus Giewekemeyer danke ich für konstruktive fachliche Diskussionen sowie seinen Einsatz bei Messzeiten. Jan Goeman gebührt mein Dank für außerordentliche Unterstützung in allen IT-Fragen sowie für die Konfiguration von speziellen Tomographie- und Auswerterechnern. Bei Peter Nischalk und Carsten Wulff bedanke ich mich für die Fertigung von Komponenten des GINIX und JuLiA Messplatzes, vor allem für kurzfristige Umsetzungen bei nahenden Messzeiten. Ein besonderer Dank geht an Jochen Herbst, Mike Kanbach und Thorsten Gronemann für kompetente Unterstützung bei technischen Fragen und bei Probenpräparationen. Mike Kanbach und Thorsten Gronemann danke ich weiterhin für ihren Einsatz bei der Wellenleiterfertigung.

Schließlich geht mein herzlicher Dank an alle Mitarbeiter des Instituts für Röntgenphysik für die ausgesprochen freundliche und entspannte Atmosphäre im Institut und das große Engagement, das jeder täglich einfließen lässt.

Die Forschungsarbeit wurde vom Bundesministerium für Bildung und Forschung unter den Fördernummern *05KS7MGA* und *05K10MGA* sowie von der Deutschen Forschungsgemeinschaft durch den *SFB 755 Nanoscale Photonic Imaging* und das *Exzellenzcluster 171 Mikroskopie im Nanometerbereich und Molekularphysiologie des Gehirns* unterstützt.

Ein ganz besonderer Dank gilt meinen Eltern für ihre durchgehende Unterstützung. Franzi bin ich von ganzem Herzen dankbar für uneingeschränkte Unterstützung, Rückhalt und Verständnis, sowie für das Korrekturlesen der Arbeit.





# Curriculum vitae

Matthias Bartels

Geboren am 10. März 1985 in Nordhorn.

Staatsangehörigkeit: deutsch.

07/2004	Abitur, Gymnasium Nordhorn
07/2004-04/2005	Zivildienst, DRK Rettungsdienst Nordhorn
10/2005-09/2010	Physik-Studium, Georg-August-Universität Göttingen
10/2007-04/2012	BWL-Studium, Georg-August-Universität Göttingen
09/2010	Diplom in Physik, Titel der Arbeit: ‚Phasenkontrast-Mikrotomographie an einer Laborröntgenquelle‘
04/2012	Bachelor of Science in Betriebswirtschaftslehre, Titel der Arbeit: ‚Vergleich von Boardstrukturen europäischer Aktiengesellschaften‘
seit 10/2010	Wissenschaftlicher Mitarbeiter am Institut für Röntgenphysik, Georg-August-Universität Göttingen

**T**hree-dimensional information of entire objects can be obtained by the remarkable technique of computed tomography (CT). In combination with phase sensitive X-ray imaging high contrast for soft tissue structures can be achieved as opposed to CT based on classical radiography. In this work biological samples ranging from micrometer sized single cells over multi-cellular nerve tissue to entire millimeter sized organs are investigated by use of cone-beam propagation-based X-ray phase contrast. Optimization with respect to contrast, resolution and field of view is achieved by addressing instrumentation, sample preparation and phase reconstruction techniques. By using laboratory sources functional soft tissue within the bony capsule of mouse cochleae is visualized in 3D with unprecedented image quality. At synchrotron storage rings the technique reveals more than 1000 axons running in parallel within a mouse nerve and enables dose-efficient three-dimensional cellular imaging as well as two-dimensional imaging at high resolutions below 50 nm.



ISBN 978-3-86395-134-4  
ISSN 2191-9860

Universitätsverlag Göttingen